

# Northumbria Research Link

Citation: Yurduseven, Okan (2014) Integration of Microwave Antennas with Solar PV for Multiband and Wideband Mobile, WLAN and WiMAX Applications. Doctoral thesis, Northumbria University.

This version was downloaded from Northumbria Research Link:  
<https://nrl.northumbria.ac.uk/id/eprint/17466/>

Northumbria University has developed Northumbria Research Link (NRL) to enable users to access the University's research output. Copyright © and moral rights for items on NRL are retained by the individual author(s) and/or other copyright owners. Single copies of full items can be reproduced, displayed or performed, and given to third parties in any format or medium for personal research or study, educational, or not-for-profit purposes without prior permission or charge, provided the authors, title and full bibliographic details are given, as well as a hyperlink and/or URL to the original metadata page. The content must not be changed in any way. Full items must not be sold commercially in any format or medium without formal permission of the copyright holder. The full policy is available online: <http://nrl.northumbria.ac.uk/policies.html>

**Integration of Microwave Antennas with  
Solar PV for Multiband and Wideband  
Mobile, WLAN and WiMAX Applications**

Okan Yurduseven

This thesis is submitted to the University of  
Northumbria at Newcastle for the Degree of  
Doctor of Philosophy

Faculty of Engineering and Environment

May 2014

# Contents

Abstract.....	vii
List of Figures.....	viii
List of Tables.....	xviii
Glossary of Abbreviations.....	xx
Glossary of Symbols.....	xxii
Acknowledgements.....	xxiv
Declaration.....	xxv
Chapter 1 – Introduction.....	1
1.1 The History of Antennas.....	1
1.2 The History of Solar Cells.....	2
1.3 Research Motivation and Aims.....	3
1.4 Literature Review.....	5
1.5 Outline of the Thesis, Novelty and Publications.....	18
Chapter 2 – Background on Antennas.....	26
2.1 Introduction.....	26
2.2 Antennas.....	26
2.2.1 Antenna Parameters.....	26
2.2.1.1 Radiation Pattern.....	26
2.2.1.2 Beamwidth.....	28
2.2.1.3 Directivity, Gain and Antenna Efficiency.....	30
2.2.1.4 Bandwidth.....	31
2.2.1.5 Input Impedance.....	32
2.2.1.6 Polarisation.....	35
2.2.2 Photovoltaically Integrated Antennas.....	40
2.2.2.1 Microstrip Patch Antennas.....	41
2.2.2.1.1 Feed Methods.....	44
2.2.2.1.1.1 Microstrip Line Feed.....	44
2.2.2.1.1.2 Coaxial Probe Feed.....	45
2.2.2.1.1.3 Aperture-Coupled Feed.....	47

2.2.2.1.1.4 Proximity-Coupled Feed .....	48
2.2.2.1.2 Analysis Methods.....	49
2.2.2.1.2.1 Transmission Line Method .....	50
2.2.2.1.2.2 Cavity Method.....	53
2.2.2.2 Planar Inverted-F Antennas (PIFAs).....	61
2.3 Integration Process and Challenges from an RF Point of View.....	63
Chapter 3 – Background on Photovoltaics and Solar Cells .....	67
3.1 Introduction.....	67
3.1.1 Photovoltaics.....	67
3.2 Crystalline Silicon Solar cells .....	69
3.2.1 Structure of a crystalline silicon solar cell .....	69
3.2.1.1 Open-Circuit Termination.....	72
3.2.1.2 Short-Circuit Termination.....	73
3.2.1.3 I-V Characteristics .....	74
3.2.2 Efficiency and Loss.....	75
3.2.2.1 Efficiency.....	75
3.2.2.2 Losses.....	78
3.2.2.2.1 Losses due to Quantization of Energy in Photons.....	78
3.2.2.2.2 Optical Losses .....	78
3.2.2.2.3 Recombination Losses .....	81
3.2.2.2.4 Resistance Losses.....	81
3.3 Crystalline Silicon Solar Modules .....	83
3.3.1 Connection of Solar Cells .....	83
3.3.1.1 Series Connection .....	84
3.3.1.2 Parallel Connection.....	85
3.4 Integration Process and Challenges from a Photovoltaic Point of View .....	86
3.5 Solar Simulators.....	87
Chapter 4 – RF Ground Plane Solar Integration .....	93
4.1 Introduction.....	93
4.2 The Integration Topology .....	93
4.3 Transparent Solar Patch Antenna for 2.4 GHz band WLAN and 2.3/2.5 GHz band WiMAX Applications .....	95

4.3.1 Meshed Solar Patch Antenna .....	95
4.3.2 Solar Patch Antenna with Transparent Meshed Rectangular Radiating Patch Element ..	97
4.3.3 Effect of Photovoltaic Integration on the Resonance Characteristics of the Antenna ...	110
4.3.4 Effect of Meshing the Radiating Patch Element on the Photovoltaic Performance.....	114
4.4 A Meshed Multiband Solar Patch Array Antenna .....	116
4.4.1 Design and Fabrication of the Meshed Solar Patch Array Antenna .....	117
4.4.2 Measurement Results and Discussion.....	122
4.4.2.1 Antenna Measurements.....	122
4.4.2.2 Solar Measurements .....	128
4.5 UWB Meshed Solar Monopole Antenna .....	132
4.5.1 Meshed Solar Monopole Antenna Design .....	132
4.6 Summary .....	145
Chapter 5 – RF Radiating Element Solar Integration .....	146
5.1 Introduction.....	146
5.2 The Integration Topology .....	146
5.3 Suspended Solar Patch Antenna for 2.4 GHz Band WLAN and 2.5 GHz band WiMAX Applications .....	147
5.3.1 Solar Patch Antenna Design .....	147
5.3.2 Simulation and Measurement Results.....	149
5.3.3 Effect of Solar Integration on the Antenna Performance.....	153
5.3.3.1 Effect of DC Termination on the RF Antenna Response.....	155
5.3.3.2 DC/RF Isolation for DC Load Connection at the Radiating Edge .....	158
5.4 Cross-Coaxial Fed Wideband Solar Patch Antenna.....	163
5.4.1 Solar Patch Antenna Design .....	163
5.4.2 Simulation and Measurement Results.....	166
5.4.2.1 Antenna Performance.....	166
5.4.2.2 Solar Performance.....	173
5.5 Solar Illumination Intensity and the RF Antenna Performance .....	175
5.6 Summary .....	181
Chapter 6 – RF Stacked Parasitic Patch Element Solar Integration.....	183

6.1 Introduction.....	183
6.2 The Integration Topology .....	183
6.3 Solar Cell Stacked Modified Z-Double L-Slot Quad-Band PIFA .....	184
6.3.1 Solar PIFA Design .....	185
6.3.2 Simulation and Measurement Results.....	186
6.3.2.1 Antenna Performance.....	186
6.3.2.2 Solar Performance.....	193
6.3.2.3 The Effect of Solar Integration on PIFA Performance .....	194
6.3.2.4 The Effect of the DC connections on PIFA Performance.....	198
6.4 A Solar Cell Stacked Multi-Slot Quad-Band PIFA for GSM, WLAN and WiMAX Networks .....	199
6.4.1 Solar PIFA Design .....	200
6.4.2 Simulation and Measurement Results.....	202
6.4.2.1 Antenna Performance.....	202
6.4.2.3 The Effect of Solar Integration on PIFA Performance .....	204
6.4.2.2 Solar Performance.....	210
6.5 A Solar Cell Stacked Slot-Loaded Suspended Microstrip Patch Antenna for WLAN and WiMAX Networks.....	211
6.5.1 Slot-Loaded Stacked Solar Patch Antenna Design .....	211
6.5.2 Simulation and Measurement Results.....	213
6.5.2.1 Antenna Performance.....	213
6.5.2.2 The Effect of Solar Integration on Antenna Performance.....	218
6.5.2.3 Solar Performance.....	220
6.6 Solar Cell Stacked Dual-Polarised Patch Antenna for 5.8 GHz band WiMAX Network.....	220
6.6.1 Dual-Polarized Solar Patch Design.....	221
6.6.2 Simulation and Measurement Results.....	223
6.7 Beam Steering Solar Cell Stacked Dual-Polarised Microstrip Patch Array Antenna.....	230
6.7.1 Solar Array Antenna Design .....	231
6.7.2 Simulation Results .....	232
6.7.3 Beam Steering.....	235
6.8 Summary .....	240

Chapter 7 - Conclusions and Future Work.....	243
7.1 Conclusions.....	243
7.2 Future Work.....	246
References.....	248

# Abstract

The primary goal of this research is to investigate the existing photovoltaic antenna integration techniques and develop a new solar antenna integration topology in order to address the drawbacks of these techniques.

With the increasing demands for low-profile antennas and a growing move towards the microgeneration of electricity, primarily by photovoltaics, photovoltaic antennas are of increasing importance with a growing amount of research in this area being developed. At present there are a number of designs for photovoltaic antennas which could be divided into two distinct categories. The first type is the use of solar cells as an RF ground plane, whilst the second type involves the use of solar cells as an RF radiating element. Both techniques bring significant challenges if they are to be widely adopted. Considering the first technique, using a solar cell as an RF ground plane introduces an optical shading problem, which significantly reduces the solar efficiency of the solar antennas using this integration topology. To this end, meshing the RF radiating element is investigated in this thesis to achieve optical transparency at the expense of increasing the cost and complexity of the fabrication process of photovoltaic antennas. Conversely, using a solar cell as an RF radiating element limits the ability to modify the resonance response using traditional RF bandwidth enhancement techniques due to the fact that solar cells need to have a homogeneous structure to achieve optimum solar performance.

In order to address these challenges, a third solar antenna integration topology is proposed in this thesis. This method is based upon the use of solar cells as an RF stacked parasitic patch element suspended above the conventional RF radiating element of the integrated antennas. This integration topology enables the integrated solar cells to achieve an optimum solar efficiency due to their suspended position eliminating the shading problem. It also enables the RF radiating element to be modified to excite multiple  $TM_{mn}$  propagation modes to achieve enhanced resonance response for multiband and wideband applications. This new topology has been further developed and applied to design a dual-polarised photovoltaic antenna for polarisation diverse communication systems, which has been extended to produce a photovoltaic array antenna for beam steering applications.

This thesis addresses a major knowledge gap in the field of photovoltaic antennas. As a result of this, greater understanding of the design procedures of photovoltaic antennas and associated trade-offs from such designs is developed. Using this knowledge, novel designs that overcome the associated problems of current photovoltaic antennas are presented.

# List of Figures

Fig. 1.1: Project roadmap and research undertaken in this thesis.

Fig. 2.1: Radiation pattern of an antenna.

Fig. 2.2: FNBW and HPBW of an antenna.

Fig. 2.3: A dipole antenna in transmitting mode (a) dipole connected to a signal generator (b) circuit equivalent.

Fig. 2.4: A dipole in receiving mode (a) dipole connected to a load (b) circuit equivalent.

Fig. 2.5: Linear polarisation.

Fig. 2.6: Two linearly polarised dipole antennas oriented at right angle.

Fig. 2.7: Circular polarisation.

Fig. 2.8: Elliptical polarisation.

Fig. 2.9: A microstrip patch antenna with an arbitrary shaped radiating element.

Fig. 2.10: Different shapes of microstrip radiating patch elements.

Fig. 2.11: Microstrip line feed (a) patch fed by a feed line consisting of a  $\lambda/4$  line (b) patch fed by an inset feed line (c) Equivalent circuit of microstrip line feed.

Fig. 2.12: Coaxial probe feed (a) top view (b) side view (c) equivalent circuit of coaxial probe feed.

Fig. 2.13: Aperture-coupled feed (a) top view (b) side view (c) equivalent circuit of aperture-coupled feed.

Fig. 2.14: Proximity-coupled feed (a) top view (b) side view (c) equivalent circuit of proximity-coupled feed.

Fig. 2.15: Transmission line method (a) patch antenna with radiating slots (b) equivalent circuit model of the radiating slots.

Fig. 2.16:  $\vec{E}$  field distribution along the length of the patch (a) patch antenna with radiating slots (b) cross-section along the patch length.

Fig. 2.17: Fringing fields from a microstrip line (a) microstrip line (b) fringing field lines in air and dielectric.

Fig. 2.18: PEC walls of a conventional cavity.

Fig. 2.19: Cavity description of a patch antenna.

Fig. 2.20: Cavity description of a patch antenna with PEC and PMC walls.

Fig. 2.21: Cavity under patch with boundaries for homogeneous 2D wave equation.

Fig. 2.22: Field, voltage and current distributions along the length of the patch (a)  $TM_{10}$  (b)  $TM_{20}$  (c)  $TM_{30}$ .

Fig. 2.23: Voltage and current distribution with the impedance curve along the patch for fundamental ( $TM_{10}$ ) mode.

Fig. 2.24: Surface currents on PEC and PMC walls in the presence of an infinite ground plane.

Fig. 2.25: Surface currents on the PMC walls in the absence of the ground plane (image theory).

Fig. 2.26: A conventional microstrip patch operating at a half-wave mode.

Fig. 2.27: Patch short-circuited to the ground plane through a shorting edge at the centre.

Fig. 2.28: Planar inverted-F antenna.

Fig. 3.1: Simplified energy band diagram.

Fig. 3.2: Structure of a crystalline silicon solar cell and the movement of freed electrons.

Fig. 3.3: Tetrahedral structure of silicon atoms in a crystal lattice.

Fig. 3.4: Equivalent circuit model of an ideal cell.

Fig. 3.5: Equivalent circuit model of an ideal cell with an open-circuit termination.

Fig. 3.6: Equivalent-circuit model of an ideal cell with a short-circuit termination.

Fig. 3.7: Quadrants in the description of I-V characteristics.

Fig. 3.8: I-V curve in the dark and under illumination.

Fig. 3.9: I-V curve and Fill Factor (FF).

Fig. 3.10: Grid structure of the front contact of a solar cell.

Fig. 3.11: Antireflection coating.

Fig. 3.12: Texturization of the cell surface (a) texturized silicon surface (b) reflection from texturized silicon surface in comparison to flat silicon surface.

Fig. 3.13: Light trapping in a cell.

Fig. 3.14: The equivalent circuit model with series and shunt resistances.

Fig. 3.15: Equivalent circuit model with series resistance (a) circuit-diagram (b) I-V curve.

Fig. 3.16: Equivalent circuit model with shunt resistance in parallel (a) circuit-diagram (b) I-V curve.

Fig. 3.17: Series connection of solar cells in a module (a) top view (b) front view.

Fig. 3.18: Total I-V curve of the module consisting of  $N$  series connected solar cells.

Fig. 3.19: Parallel connection of solar cells in a module (a) top-view (b) front-view.

Fig. 3.20: Total I-V curve of the module consisting of  $M$  parallel connected solar cells.

Fig. 3.21: Metal halide solar simulator (a) without front cover (b) with front cover.

Fig. 3.22: Metal halide lamp (Osram Powerstar HQI-BT400W/D).

Fig. 3.23: Spectral power distribution of the Osram Powerstar HQI-BT400W/D metal halide solar lamps.

Fig. 3.24: Adjustable platform and the illumination map.

Fig. 3.25: Normalised illumination distribution scanning result in MATLAB.

Fig. 3.26: Abet Sun 2000 solar simulator.

Fig. 4.1: RF ground plane solar antenna integration topology.

Fig. 4.2: Suspended meshed solar patch antenna with non-optimised initially selected meshing parameters (a) overall view in CST Microwave Studio (b) side view ( $x$ - $z$  plane).

Fig. 4.3: Meshed solar patch antenna with varying meshing line widths (a) line width of 0.2 mm (optical transparency = 81.46%) (b) line width of 0.5 mm (optical transparency = 53.66%) (c) line width of 0.7 mm (optical transparency = 35.13%) (d) line width of 1 mm (optical transparency = 7.32%).

Fig. 4.4: Impedance response of the meshed solar patch antenna versus varying line widths (a) resistance (b) reactance.

Fig. 4.5: Impedance response of the meshed solar patch antenna versus varying number of vertical meshing lines (a) resistance (b) reactance.

Fig. 4.6: Impedance response of the meshed solar patch antenna versus varying number of horizontal meshing lines (a) resistance (b) reactance.

Fig. 4.7: Simulated current distribution across the optimised meshed radiating patch element.

Fig. 4.8: Optimised meshed solar patch antenna in CST Microwave Studio.

Fig. 4.9: Simulated  $S_{11}$  response of the meshed solar patch antenna.

Fig. 4.10: Simulated far-field radiation patterns of the meshed solar patch antenna (a) E-plane and H-plane far-field radiation patterns (b) 3D far-field radiation pattern.

Fig. 4.11: Solar patch antenna with a conventional solid radiating patch element.

Fig. 4.12: Impedance response of the solar patch antenna with the proposed meshed radiating patch element and the conventional solid radiating patch element, respectively (a) resistance (b) reactance.

Fig. 4.13: Far-field radiation patterns of the solar patch antenna with meshed and conventional solid patches, respectively (a) E-plane (b) H-plane.

Fig. 4.14: Meshed solar patch antenna (a) with solar cell (b) without solar cell (conventional copper ground plane).

Fig. 4.15: Simulated  $S_{11}$  patterns of the proposed meshed solar patch antenna with and without the encapsulated poly-Si solar cell operating as an RF ground plane.

Fig. 4.16: The effect of the encapsulation elements on the  $S_{11}$  performance of the meshed solar patch antenna.

Fig. 4.17: Proposed transparent meshed patch element placed upon a poly-Si solar panel for solar measurements in a solar chamber.

Fig. 4.18: Solid patch element placed upon a poly-Si solar panel for solar measurements in a solar chamber.

Fig. 4.19: A poly-Si solar panel without any elements placed upon for solar measurements in a solar chamber.

Fig. 4.20: Meshed solar patch array antenna (a) fabricated antenna (b) antenna geometry (c) feeding network.

Fig. 4.21: The meshed microstrip patch array antenna designed in CST Microwave Studio.

Fig. 4.22: Simulated  $S_{11}$  responses of the antenna versus varying distances between the meshed radiating patch elements within the array.

Fig. 4.23: Simulated  $S_{11}$  responses of the antenna versus varying patch tilt angle.

Fig. 4.24: Simulated and measured  $S_{11}$  patterns of the proposed meshed solar patch array antenna.

Fig. 4.25: Measured E-plane (normalized to maximum gain of 9.5 dBi) and H-plane (normalized to maximum gain of 6.2 dBi) far-field radiation patterns (a) E-Plane for GSM/UMTS bands (b) E-Plane for WiMAX and C-band (c) H-plane for GSM/UMTS bands (d) H-plane for WiMAX and C-band.

Fig. 4.26: Solar measurement of the meshed solar patch array antenna (a) solar simulator (b) measurement setup within the chamber.

Fig. 4.27: Measured I/V curves of the antenna.

Fig. 4.28: Meshed solar monopole antenna (a) fabricated antenna (b) technical overall view.

Fig. 4.29: Input impedance response of the monopole antenna versus varying meshing line widths (a) resistance response (b) reactance response.

Fig. 4.30: Input impedance response of the monopole antenna versus varying number of vertical meshing lines (a) resistance response (b) reactance response.

Fig. 4.31: Input impedance response of the monopole antenna versus varying number of horizontal meshing lines (a) resistance response (b) reactance response.

Fig. 4.32: Simulated surface current distribution (a) 3.1 GHz (b) 10.6 GHz.

Fig. 4.33: Simulated and measured  $S_{11}$  patterns of the meshed solar monopole antenna.

Fig. 4.34: Measured far-field radiation patterns of the meshed solar monopole antenna (a) E-plane (y-z) (b) H-plane (x-z) (c) maximum gain values across 3.1-10.6 GHz.

Fig. 4.35: Measured I/V curve of the meshed solar monopole antenna.

Fig. 5.1: RF radiating element solar antenna integration topology.

Fig. 5.2: Suspended solar patch antenna (a) design in CST Microwave Studio (b) top view (x-y plane) (c) side view (y-z plane).

Fig. 5.3: Simulated and measured  $S_{11}$  patterns.

Fig. 5.4: Silicon solar cell modelled in CST Microwave Studio.

Fig. 5.5: E-plane and H-plane far-field radiation pattern measurement set-up in anechoic chamber.

Fig. 5.6: Far-field radiation patterns (a) E-plane (b) H-plane.

Fig. 5.7: Suspended microstrip patch antenna consisting of conventional printed copper patch radiating element.

Fig. 5.8: DC load connection introduced at the non-radiating edge.

Fig. 5.9: Surface current distribution at 2.5 GHz (a) solar patch without the DC load (b) solar patch with the DC load attached at the non-radiating edge.

Fig. 5.10: DC load connection introduced at the radiating edge.

Fig. 5.11: Surface current distribution at 2.5 GHz (a) solar patch without the DC load (b) solar patch with the DC load connected at the radiating edge.

Fig. 5.12: DC/RF isolation circuit introduced at the radiating edge (a) design in CST Microwave Studio (b) fabricated prototype (c) equivalent circuit model of the proposed DC/RF isolation circuit.

Fig. 5.13: Surface current distribution at 2.5 GHz (a) solar patch without the DC load (b) solar patch with the DC load connected at the radiating edge through the proposed DC/RF isolation circuit.

Fig. 5.14: Measured  $S_{11}$  patterns with and without DC load.

Fig. 5.15: Cross-coaxial fed suspended solar patch antenna (a) top view (b) front view (c) back view.

Fig. 5.16: Equivalent circuit model of the proposed cross-coaxial feed (a) circuit element representation of the cross-coaxial feeding elements (b) equivalent circuit model.

Fig. 5.17: Measured  $S_{11}$  patterns with and without the copper insert forming the cross-coaxial feed structure.

Fig. 5.18: Simulated  $S_{11}$  patterns versus varying insert lengths.

Fig. 5.19: Simulated  $S_{11}$  patterns versus varying distance between the insert and the cell.

Fig. 5.20: Simulated  $S_{11}$  patterns with and without the shorting wire.

Fig. 5.21: Antenna far-field measurement set-up in the anechoic chamber.

Fig. 5.22: E-plane far-field radiation (a) measured normalised E-plane radiation patterns at 2.45, 2.6 and 3 GHz (b) measured E-plane gain values across the operational frequency band.

Fig. 5.23: H-plane far-field radiation (a) measured H-plane radiation patterns at 2.45, 2.6 and 3 GHz (b) measured H-plane gain values across the operational frequency band.

Fig. 5.24: Solar measurement of the cross-coaxial fed suspended solar patch antenna.

Fig. 5.25: Measured I/V curve of the solar antenna.

Fig. 5.26: Solar patch antenna terminated in a  $220\Omega$  DC load under varying illumination intensity.

Fig. 5.27: Transmission coefficient and reflection coefficient measurement set-up under varying illumination intensity.

Fig. 5.28: Portable solar simulator illuminating the photovoltaic microstrip patch antenna.

Fig. 5.29: TENMA 72-6693 light meter.

Fig. 5.30: Measured S-parameter responses versus varying illumination intensities (a)  $S_{11}$  patterns (b)  $S_{21}$  patterns.

Fig. 6.1: RF stacked parasitic patch element solar antenna integration topology.

Fig. 6.2: Z-double-L slot loaded solar PIFA (a) overall view (b) side view (c) back view (d) radiating PIFA element top view.

Fig. 6.3: Simulated and measured  $S_{11}$  patterns.

Fig. 6.4: Simulated surface current distributions on the Z-double-L slot loaded radiating PIFA element at the frequencies of (a) 1.79 GHz (b) 2.45 GHz (c) 3.4 GHz (d) 4.75 GHz.

Fig. 6.5: Measured E-plane (x-z) and H-plane (y-z) far-field radiation patterns at (a) 1.79 GHz (b) 2.45 GHz (c) 3.4 GHz (d) 4.75 GHz.

Fig. 6.6: Measured I/V curve of the solar PIFA.

Fig. 6.7: PIFA with the suspended stacked poly-Si solar cell.

Fig. 6.8: PIFA without the poly-Si solar cell.

Fig. 6.9: Simulated  $S_{11}$  patterns of the Z-double-L slot loaded PIFA with and without the stacked poly-Si solar cell.

Fig. 6.10: Simulated surface current distributions. At 1.79 GHz (a) PIFA with the stacked poly-Si solar cell (b) PIFA without the poly-Si solar cell; at 2.45 GHz (c) PIFA with the stacked poly-Si solar cell (d) PIFA without the poly-Si solar cell; at 3.4 GHz (e) PIFA with

the stacked poly-Si solar cell (f) PIFA without the poly-Si solar cell; at 4.75 GHz (g) PIFA with the stacked poly-Si solar cell (h) PIFA without the poly-Si solar cell.

Fig. 6.11: The introduction of the DC load at the (a) radiating edge (b) non-radiating edge.

Fig. 6.12: Measured  $S_{11}$  patterns obtained when the DC load is introduced at the non-radiating and radiating edges, respectively.

Fig. 6.13: Fabricated W-L slot loaded solar PIFA (a) fabricated solar PIFA, overall view (b) fabricated solar PIFA, back view (c) W-L slot loaded radiating PIFA element, top view.

Fig. 6.14: Simulated and measured  $S_{11}$  patterns.

Fig. 6.15: Surface current distribution on the W-L slot loaded radiating PIFA element (a) 1.8 GHz (b) 2.4 GHz (c) 3.4 GHz (d) 5.8 GHz.

Fig. 6.16: Measured normalised E-Plane and H-Plane far-field radiation patterns with and without the stacked poly-Si solar cell at (a) first resonance (b) second resonance (c) third resonance (d) fourth resonance.

Fig. 6.17: Measured I/V curve of the solar PIFA.

Fig. 6.18: Fabricated self-complementary shaped multiple-L slot loaded suspended microstrip patch antenna stacked with a poly-Si solar cell (a) Top view (b) back view (c) overall view. Dimensions (in mm):  $A=41.5$ ,  $B=18.3$ ,  $C=3.2$ ,  $D=0.38$ ,  $E=27.8$ ,  $F=21.1$ ,  $G=14.4$ ,  $H=7.6$ ,  $I=4.1$ ,  $J=10.8$ ,  $K=17.6$ ,  $L=24.3$ ,  $M=32$ ,  $N=40.5$ ,  $O=30.9$ ,  $P=22.3$ ,  $Q=13.8$ ,  $R=5.3$ ,  $S=9.5$ ,  $T=18.1$ ,  $U=26.6$ ,  $V=35.1$ ,  $W_1=60$ ,  $W_2=43$ ,  $L_1=90$ ,  $L_2=33$ ,  $h_1=6$ ,  $h_2=3$ , L-slot width=1.

Fig. 6.19: Simulated and measured  $S_{11}$  patterns.

Fig. 6.20: Simulated current distributions across the self-complementary shaped multiple-L slot loaded suspended microstrip patch together with the feed line at (a) 2.5 GHz (b) 3.3 GHz (c) 5.2 GHz (d) 5.8 GHz.

Fig. 6.21: Measured E-plane and H-plane far-field radiation patterns at (a) 2.5 GHz (b) 3.3 GHz (c) 5.2 GHz (d) 5.8 GHz.

Fig. 6.22: Measured  $S_{11}$  patterns with and without the stacked poly-Si solar cell.

Fig. 6.23: Measured  $S_{11}$  patterns with and without DC wires connected to the terminals of the stacked poly-Si solar cell.

Fig. 6.24: Dual-polarised microstrip patch antenna stacked with a poly-Si solar cell with a DC/RF isolation circuit (Dimensions in mm:  $A=4.25$ ,  $B=1.64$ ,  $C=0.37$ ,  $D=15.2$ ,  $W=60$ ,  $L=62$ ,  $h=2$ ).

Fig. 6.25: Measured S-parameters of the dual-polarised solar patch antenna (a) transmission coefficient ( $S_{12}$  and  $S_{21}$ ) (b) reflection coefficient ( $S_{11}$  and  $S_{22}$ ).

Fig. 6.26: Simulated surface current distributions (a, b) patch together with feed lines for  $+45^\circ$  and  $-45^\circ$  (with DC/RF isolation); (c, d) patch together with feed lines for  $+45^\circ$  and  $-45^\circ$  (no DC/RF isolation); (e, f) solar cell rear contact for  $+45^\circ$  and  $-45^\circ$  (no DC/RF isolation); (g, h) solar cell rear contact for  $+45^\circ$  and  $-45^\circ$  (with DC/RF isolation); (i, j) solar cell front grid for  $+45^\circ$  and  $-45^\circ$  (no DC/RF isolation); (k, l) solar cell front grid for  $+45^\circ$  and  $-45^\circ$  (with DC/RF isolation).

Fig. 6.27: Measured E-plane and H-plane far-field radiation patterns (a) antenna fed through port 1 ( $+45^\circ$  polarisation) (b) antenna fed through port 2 ( $-45^\circ$  polarisation).

Fig. 6.28: A communication target positioned differently from the direction of the Sun.

Fig. 6.29: Slant  $\pm 45^\circ$  dual-polarised microstrip patch array antenna stacked with an array of poly-Si solar cell.

Fig. 6.30: A dual-polarised microstrip patch stacked with a poly-Si solar cell within the array.

Fig. 6.31: Simulated  $S_{11}$  ( $+45^\circ$  polarisation, fed through port 1) and  $S_{22}$  ( $-45^\circ$  polarisation fed through port 2) patterns.

Fig. 6.32: Simulated far-field radiation patterns of the solar array antenna when no beam steering is applied (a) elevation (x-z) (b) azimuth (y-z).

Fig. 6.33: Simulated 3D far-field radiation pattern of the solar array antenna when no beam steering is applied.

Fig. 6.34: Distance between array elements (no beam steering is applied).

Fig. 6.35: Slant  $\pm 45^\circ$  dual-polarised microstrip patch array antenna with an external phase shift applied to each array element in order to steer the main lobe by  $10^\circ$  (phase shifters are highlighted).

Fig. 6.36: Simulated far-field radiation patterns of the solar patch array antenna when  $10^\circ$  beam steering is applied in the elevation plane (x-z plane) (a) elevation (b) azimuth.

Fig. 6.37: Simulated 3D far-field radiation pattern of the solar array antenna when 10° beam steering is applied.

# List of Tables

Table 2.1: Advantages and disadvantages of the microstrip line feed method.

Table 2.2: Advantages and disadvantages of the coaxial probe feed method.

Table 2.3: Advantages and disadvantages of the aperture-coupled feed method.

Table 2.4: Advantages and disadvantages of the proximity-coupled feed method.

Table 3.1: Recorded maximum solar cell efficiencies ( $1000 \text{ W/m}^2$ ,  $25^\circ\text{C}$ ).

Table 3.2: Advantages and disadvantages of the metal halide solar simulator.

Table 4.1: Solar performance readings.

Table 4.2: -10 dB impedance bandwidth performance of the meshed solar patch array antenna.

Table 4.3: Measured maximum E-plane and H-plane gain values across multiple resonance frequency bands.

Table 4.4: Measured DC solar performance characteristics.

Table 4.5: Measured maximum E-plane and H-plane gain values.

Table 5.1: Measured maximum E-plane and H-plane gain values.

Table 5.2: Comparison between the resonance characteristics of solar and conventional non-solar versions of the antenna.

Table 5.3: Measured maximum E-Plane gain values at selected frequencies.

Table 5.4: Measured maximum H-plane gain values at selected frequencies.

Table 5.5: Solar measurement readings.

Table 6.1: Analysis of the measured  $S_{11}$  performance.

Table 6.2: Slot types, contributed resonance bands and supported  $\text{TM}_{mn}$  propagation modes.

Table 6.3: Measured maximum gain values of the solar PIFA.

Table 6.4: Slot types, contributed resonance bands and supported  $\text{TM}_{mn}$  propagation modes.

Table 6.5: Effect of size and distance of the stacked poly-Si solar cell on the resonance characteristics of the solar PIFA.

Table 6.6: Measured maximum gain values of the PIFA with and without the stacked poly-Si solar cell.

Table 6.7: Measured  $S_{11}$  performance of the proposed solar patch antenna.

Table 6.8: Measured maximum gain values of the proposed solar patch antenna.

Table 6.9: Beam steering parameters for the array elements.

# Glossary of Abbreviations

AF	Array Factor
ARC	Anti-Reflective Coating
a-Si	Amorphous Silicon
AUT	Antenna Under Test
CW	Clockwise
CCW	Counter Clockwise
dB	Decibel
dB <sub>i</sub>	Decibel isotropic
dB <sub>i</sub> C	Decibel isotropic Circular
DC	Direct Current
EM	Electromagnetic
FCC	Federal Communications Commission
FF	Fill Factor
FR4	Flame Retardant 4 (Printed Circuit Board)
GSM	Global System for Mobile Communications
LHEP	Left Hand Elliptical Polarisation
LHCP	Left Hand Circular Polarisation
LTE	Long-Term Evaluation
MIC	Microwave Integrated Circuit
MMIC	Monolithic Microwave Integrated Circuit
Mono-Si	Monocrystalline Silicon
O/C	Open-circuit
PEC	Perfect Electric Conductor
PIFA	Planar Inverted-F Antenna
PMC	Perfect Magnetic Conductor
Poly-Si	Polycrystalline Silicon
PV	Photovoltaics
RHEP	Right Hand Elliptical Polarisation
RHCP	Right Hand Circular Polarisation
RF	Radio Frequency
S/C	Short-Circuit
SMA	SubMiniature version-A connector

TE	Transverse Electric
TM	Transverse Magnetic
UMTS	Universal Mobile Telecommunication System
UWB	Ultra Wide Band
VNA	Vector Network Analyser
WiMAX	Worldwide Interoperability for Microwave Access
WLAN	Wireless Local Area Network
WWAN	Wireless Wide Area Network

# Glossary of Symbols

$\mu_0$	Permeability of free space
$a_n$	Array weight
$D(\theta, \phi)$	Angular directivity
$D_{\max}$	Maximum directivity
$e_c$	Conductance efficiency
$e_{cd}$	Radiation efficiency
$e_d$	Dielectric efficiency
$E_G$	Bandgap
$e_t$	Total efficiency
$G(\theta, \phi)$	Angular gain
$G_{\max}$	Maximum gain
$G_R$	Gain of the AUT
$G_T$	Gain of the reference antenna
$h$	Substrate thickness
$I_D$	Diode current
$I_{MP}$	Cell current at the maximum power point
$I_{ph}$	Photogenerated current
$I_s$	Saturation current
$I_{SC}$	Short-circuit current
$J_m$	Magnetic surface current
$J_s$	Electric surface current
$k$	wave propagation vector
$L$	Patch Length
$L_{Cable}$	Cable loss
$L_{eff}$	Effective patch length
$n$	Array element number
$P_{in}$	Total input solar power
$P_{MP}$	Maximum power
$P_o$	Input power fed to the reference antenna
$P_R$	Power received by the AUT
$q$	Electric charge of an electron
$R$	Distance between the AUT and the receiving antenna

$R_L$	Loss resistance
$R_R$	Radiation resistance
$R_{sh}$	Shunt cell resistance
$R_{sr}$	Series cell resistance
$R_{Tot}$	Total radiation intensity
$S_{11}$	Reflection coefficient (port 1)
$S_{12}$	Transmission coefficient (from port 2 to port 1)
$S_{21}$	Transmission coefficient (from port 1 to port 2)
$S_{22}$	Reflection coefficient (port 2)
$T$	Temperature (K)
$\tan\delta$	Dielectric loss tangent
$V_{MP}$	Cell voltage at the maximum power point
$V_{oc}$	Open-circuit voltage
$W$	Patch Width
$W_{eff}$	Effective patch width
$Z_{in}$	Input impedance
$\epsilon_0$	Permittivity of free space
$\epsilon_r$	Relative permittivity
$\epsilon_{reff}$	Effective permittivity
$\eta$	Solar efficiency
$\lambda$	Wavelength
$\lambda_0$	Free space wavelength
$\lambda_{reff}$	Effective wavelength

# Acknowledgements

First and foremost, I would like to express my sincere gratitude to my supervisors, Professor David Smith and Professor Nicola Pearsall, for giving me the opportunity to pursue this Ph.D. and for the continued support throughout the course of this research.

My sincere thanks go to Dr. Michael Elsdon for his advice and fruitful discussions.

I am indebted to my parents, Sevda Yurduseven and Demirhan Yurduseven, and my wife Olena Aleksandrova, for their encouragement and patience throughout the duration of this research.

Finally, I would like to acknowledge and thank Northumbria University for the Ph.D. scholarship.

# Declaration

I declare that the work contained in this thesis has not been submitted for any other award and that is all my own work. I also confirm that this work fully acknowledges opinions, ideas and contributions from the work of others.

Word Count: 44,923

Name: Okan Yurduseven

Signature:

Date: May 2014

# Chapter 1 – Introduction

This chapter provides a brief outline of the historical evaluation of antennas and photovoltaics in section 1.1 and section 1.2, enabling the chapter to guide the reader through the history of these technologies. In section 1.3, the research motivation and aims for the integration of microwave antennas and photovoltaics is provided. Section 1.4 presents a detailed literature review, demonstrating existing research on the photovoltaic integration of microwave antennas. Section 1.5 demonstrates the outline of the thesis, highlighting the novelty of this research, together with associated publications.

## 1.1 The History of Antennas

The history of antennas and propagation dates back to 1864 when a Scottish physicist and mathematician James Clerk Maxwell unified the theory of electricity and magnetism and proposed the Electromagnetic Field theory [1]. In this work, Maxwell also explained the phenomenon of “electromotive force”. A German physicist, Heinrich Rudolf Hertz, validated and expanded the fundamental principles of Maxwell’s electromagnetic theory by performing experiments about the existence of the electromagnetic waves with engineering instruments, which led to a significant contribution to the area of wireless communications. In 1886, Hertz designed the first wireless communication system, a Hertz antenna receiver, and developed the first known antenna, a half-wavelength dipole [2]. A new era in radio communication was marked by the successful demonstration of the first transatlantic transmission performed between Poldhu, Cornwall-England and St. John’s Newfoundland by Marconi in 1903. The transmitted information was the Morse letter “S” [3]. It was also Marconi who introduced the term “antenna” in 1909 [4]. Wire antennas consisting of a single or an array of radiating elements were widely used until the World War II which would be the first war in which the concept of electronic warfare was used. The development of radar (radio detection and ranging) by the British and its successful use against German aircraft brought a significant development in the area of aperture antennas, such as open-ended waveguides, horn and reflector antennas, which are today widely used in modern communication and radar systems [5, 6]. In 1953, the first concept of a microstrip patch antenna was proposed by G. Dechamps whilst the practical applications would need to wait until the 1970s when R. E. Munson and J. Q. Howell designed and proposed the first practical microstrip patch antenna [7].

## 1.2 The History of Solar Cells

Although the history of solar technology spans from the 7<sup>th</sup> century B.C., the era when magnifying glass were used to concentrate the sunlight to make fire to cook and keep warm, the progression of photoelectricity dates back to 1839. In 1839, a French scientist, Edmund Becquerel, discovered the photovoltaic effect when he observed that an electrolytic cell consisting of two brass plates, a platinum anode and a cathode, in a liquid generates a continuous current when it is illuminated by sunlight. In 1873, an English electrical engineer, Willoughby Smith made one of the most significant observations in the historical evaluation of photoelectricity when he discovered the photoconductivity of selenium. In 1883, the first solar cell with an energy conversion efficiency of less than 1% was reported by an American inventor, Charles Fritts. For this design, Fritts used selenium wafers covered by a very thin gold plate and discovered that the resulting cell produced a continuous current when it was exposed to sunlight [8-10]. The major development which would result in potentially useful amounts of DC power being generated by photovoltaic devices would need to wait until the 1950s when the development of silicon wafers in good quality was achieved. In 1954, the first silicon solar cell was developed by Daryl Chapin, Calvin Fuller and Gerald Pearson at Bell Labs in the USA, within one year after the accidental discovery of the ability of p-n junction diodes to generate voltage when the room lights at Bell Labs were on by mistake [11]. The efficiency of the first silicon solar cell was 6% but the estimated production cost of \$200 per Watt prevented these cells from being an alternative to conventional power generation techniques for several decades [12, 13]. In 1956, a gallium arsenide (GaAs) p-n junction solar cell with an efficiency of 6% was designed by Radio Corporation of America (RCA) in the USA [12, 14]. The space program launched by the USA in 1958, Vanguard, and the satellites designed by the Soviet Union in 1957, Sputnik I and Sputnik II, created a new era where the use of solar cells became significantly popular in powering satellites in space [13]. In 1970s, the energy crisis triggered by the oil embargo imposed by the Arab countries resulted in a growing interest in alternative energy sources in industrialised countries which also boosted the support of governments, universities and industrial laboratories to encourage the use of solar energy. This resulted in the establishment of large photovoltaic companies, such as Solar Power in 1972, Solarex Corporation in 1973, Solar Technology International in 1975, and the US Solar Energy Research Institute in 1977. Despite the difficult economic climate in Europe, since the beginning of 1990s, the leadership within the field of photovoltaics has shifted to Europe and Asia as a direct result of the launch of a \$500m

“100,000 Solar Roofs” program by Germany in 1990 followed by a “70,000 Solar Roofs” program launched by Japan in 1994. Today, Germany and China remain as major forces in global photovoltaic market [12].

### **1.3 Research Motivation and Aims**

With global warming and increasing energy consumption combined with decreasing amount of fossil fuels, a change is required in the way that the energy demand should be met.

Today, there are two billion people who do not have the opportunity to use electricity due to the fact that there is no electric grid connection available where they live [15]. On the other hand, the use of fossil fuels results in a continuous rise in the level of carbon dioxide (CO<sub>2</sub>) emissions which play a significant role in global warming. As the industrialization grows continuously, especially in third world countries, energy demand keeps increasing and it is estimated that by the year 2025 the need for fuels will go up by 30% with the demand for electricity growing by 265% [16]. A recent research study suggests that the depletion times for oil, gas and coal are approximately 35, 37 and 107 years, respectively [17].

The use of alternative energy sources, primarily photovoltaics, to power communication systems in places where there is no electric grid connection available has received considerable attention due to the ability to meet the requirement of powering these systems without the necessity of using an electric grid. Due to the ability to be embedded as a power source in communication systems devoid of direct access to an external power grid, photovoltaics offer a significant potential to tackle this challenge.

Two solutions to address this challenge, both of which involve the use of photovoltaics as a power source, have been the subject of much study in the literature:

- Autonomous integration of microwave antennas with photovoltaics [18-34],
- “Full” integration of microwave antennas with photovoltaics [35-57].

The first technique, which is the introduction of solar cells in communication systems as a separate power source working independently from the antennas, requires an additional surface area for the solar cells which need to be situated at a considerable distance from the antennas to ensure that the solar cells have minimal effect upon the RF antenna performance [18-34]. This would suggest that this technique is not suitable for modern

low-profile communication systems, in which a limited surface area is available for photovoltaic integration.

The second technique, which is the “full” integration of microwave antennas with photovoltaics into a single multifunctional element smaller in size and lighter in weight, on the other hand, brings some potential advantages as demonstrated in this thesis. In this technique, rather than being used as a separate element, the integrated solar cells work as a part of the RF operation in addition to their photovoltaic function, which brings the multifunctionality in the proposed solar antenna designs studied in the research.

The aims of this research can be given as follows:

- This research aims to address the requirement of powering communication systems in places where there is no electric grid connection available.
- The autonomous integration of solar cells with microwave antennas to address this requirement brings the challenge of situating the solar cells at a considerable distance from the antennas in order to ensure that the solar cells have minimal effect upon the RF antenna performance. This would suggest that this type of integration is not suitable for today’s modern low-profile mobile, WLAN and WiMAX communication systems, in which significantly limited surface area is available for solar integration. This work aims to overcome this challenge by demonstrating the “full” integration of microwave antennas with solar cells into a single multifunctional low-profile structure. In this approach, the integrated solar cells work as a part of the RF operation contributing to the RF radiation rather than being used as a separate element whose effect upon the antenna response must be minimised to achieve stable RF characteristics.
- This work aims to propose a new solar antenna integration topology in order to address the drawbacks of the existing solar antenna integration topologies studied in the literature.
- This work aims to demonstrate the feasibility of multiband and ultra-wideband (UWB) photovoltaic antennas in comparison to the work carried out in the literature which mainly focuses on the demonstration of photovoltaic antennas with single narrowband resonance characteristics.
- This work aims to demonstrate the feasibility of dual-polarised solar antennas for polarisation diverse communication systems.

- Finally, this work aims to provide a further solution to the challenge of being able to communicate with the target which is positioned differently from the direction of the Sun, in which a solar antenna should be oriented to achieve optimum solar performance.

## 1.4 Literature Review

Powering communication systems in places where there is no electric grid connection available has been the subject of much research in recent years. Due to its ability to be embedded as a power source in communication systems devoid of direct access to an external power grid, photovoltaics offer a significant potential to address this challenge. Two solutions to this problem, both of which involve the use of photovoltaics as a power source, have been demonstrated in the literature.

The first technique is the introduction of solar cells in communication systems as a separate power source working independently from the antennas [18-34]. This type of autonomous integration requires an additional surface area for the solar cells which need to be situated at a considerable distance from the antennas to ensure that the solar cells have minimal effect upon the RF antenna performance. This would suggest that this technique is not suitable for modern low-profile communication systems.

The second technique, on the other hand, is the “full” integration of microwave antennas with solar cells into a single low-profile multifunctional element [35-57]. In view of this, the work demonstrated in the literature has been focused on the solar antenna integration topologies given below:

- The use of solar cells as an RF ground plane or as an additional element attached to an existing RF ground plane [35-47],
- The use of solar cells as an RF radiating element or as an additional element attached to an existing RF radiating element [48-57],
- Other: Photovoltaic integration of non-planar antennas, such as Yagi-uda [58] and reflectarray [56] (although a reflectarray has a planar geometry, the overall system is not due to the requirement of a feed horn).

The integration of microwave antennas with solar cells operating as an RF ground plane or as an additional element attached to an existing RF ground plane was proposed by a

number of authors [35-47]. Potential problems regarding the use of solar cells as an RF ground plane element can be given as follows:

- For solar antenna designs in which the radiating element is placed upon/above the solar cell (i.e. the RF ground plane) [35-39]: For this type of integration, the RF radiating element needs to be placed upon/above the solar cell operating as an RF ground plane. Due to the opaque structure of the radiating element, such as a microstrip copper patch, this type of alignment brings shading upon the integrated solar cell and therefore has the potential to significantly reduce the solar efficiency.
- For solar antenna designs in which the radiation is achieved through a slot cut in the solar cell operating as an RF ground plane [42]: This type of integration suggests that the RF radiation can be achieved through a slot cut in the solar cell operating as an RF ground plane. However, cutting a slot in the cell deforms and damages the cell structure, which ideally should be homogeneous for optimum solar operation performance, and therefore has the potential to significantly reduce the solar efficiency.
- For solar antenna designs in which the solar cells do not replace the RF ground plane but are simply attached to it as an additional element [43, 44] [46, 47]: In this type of integration, solar cells are not a part of the RF operation. For this reason, in this method, the integrated solar cells work in a manner which is more similar to the way that the solar cells operate in solar powered autonomous communication systems. Therefore, the solar cells in this method cannot be considered as fully integrated.

In order to address the shading problem, transparency techniques, such as meshing the RF radiating element and making the RF radiating element out of a transparent material were studied in the literature [40, 41] as well as in this thesis as demonstrated in chapter 4.

The integration of microwave antennas with solar cells operating as an RF radiating element or as an additional element attached to an existing RF radiating element was also given considerable attention [48-57]. The advantage of this topology is that it enables the integrated solar cells to operate without being shaded by any RF components of the antenna. This is due to the fact that in this integration topology the integrated cells are placed upon the RF antenna elements. However, this advantage comes at the cost of not being able to modify the RF radiating element, i.e. the solar cell, such as applying capacitive slot loading techniques [59-83], in order to achieve multiband and wideband

radiation characteristics. This is due to the requirement of the integrated solar cells to be homogeneous in structure to achieve optimum solar performance.

Other integration techniques, which were mainly applied for non-planar antennas, such as Yagi-uda [58] and reflectarray [56] antennas, are not the subject of this research due to the requirement for the solar antennas studied in this work to be planar and low-profile to be employed in today's modern mobile, WLAN and WiMAX systems.

Details of the work demonstrated on the integration of microwave antennas with solar cells in the literature can be given as below:

- Solar Antenna Integration Topology: The use of solar cells as an RF ground plane or as an additional element attached to an existing RF ground plane [35-47]:
  - Integration of an inset fed microstrip patch antenna with a polycrystalline (poly-Si) solar cell operating as an RF ground plane was carried out [35, 36]. It was reported in [35] that the proposed solar patch antenna resonates at 2.19 GHz (with a measured -10 dB bandwidth of 3.11%) and has a maximum gain of 1.23 dBi when the top grid electrodes of the solar cell are parallel to the direction of the surface current of the radiating patch. When the direction of the solar cell top grid electrodes is selected to be perpendicular to the direction of the surface current of the radiating patch, on the other hand, the solar patch antenna resonates at a slightly lower frequency given as 2.168 GHz (with a measured -10 dB bandwidth of 3.13%) and offers a measured maximum gain of 1.05 dBi. Similarly, the solar patch antenna proposed in [36] has measured impedance bandwidths of 2.98% and 2.8% when the direction of the solar cell top grid electrodes are selected to be parallel and perpendicular to the direction of the surface current of the radiating patch, respectively. For these configurations, the maximum gains of the antenna were measured as 2.75 dBi and 0.46 dBi, respectively. As reported in [35], the RF ground plane solar antenna integration topology studied in this work results in the radiating copper patch element, which is opaque in structure and printed on an opaque FR4 substrate that altogether has a surface area of 13.3 cm<sup>2</sup>, being mounted onto the RF ground plane (i.e. the solar cell) and shading 5.5% of the total surface area of the solar cell. The solar efficiency of the antenna was reported as 12.3% (the conditions under which the solar measurements were

taken are unknown). Moreover, the reported narrow band single frequency operation combined with poor gain performance makes the proposed antennas in [35, 36] not suitable for wideband and multiband communication systems. It should also be noted here that both antennas have linear polarisation and therefore cannot be employed for polarisation diverse applications.

- The same solar antenna integration topology as in [35, 36] was applied to different types of antennas, including a printed dipole antenna [37], a shorted quarter-wave metal plate antenna [38] and a shorted trapezoidal-shaped quarter-wave metal plate antenna [39]. The printed dipole antenna proposed in [37] was combined with a poly-Si silicon solar cell operating as an RF ground plane for the microstrip feed line and as a reflector for the dipole. The dipole is half-wavelength in length and was printed on an FR4 substrate that was suspended above the solar cell. The dipole was fed through a  $50 \Omega$  microstrip feed line printed on a separate FR4 substrate mounted onto the surface of the cell. A balun was also used in order to feed the dipole in a balanced manner. Similar to [35, 36], the orientation of the solar cell top grid electrodes was selected to be parallel and perpendicular to the direction of the surface current across the printed dipole arms, respectively. It was reported that while the solar dipole with the parallel cell top grid electrode orientation resonates at the centre frequency of 2.339 GHz (with a -10 dB impedance bandwidth of 15.8%), the solar dipole with the perpendicular cell top grid electrode orientation resonates at a slightly higher centre frequency, which is 2.3484 GHz (with a -10 dB impedance bandwidth 13.1%). Both of these solar dipole configurations have a gain of 8.60 dBi. In [38], the integration of a metal plate quarter-wave shorted suspended patch with a poly-Si solar cell operating as an RF ground plane was performed for Universal Mobile Telecommunications System (UMTS) base stations. In the proposed design, the suspended metal plate antenna was shorted to the cell top grid electrodes and together with the microstrip feed line printed on an FR4 substrate was placed upon the solar cell. Analyses were carried out with parallel and perpendicular cell top grid electrode orientations, respectively, and it was reported that the metal plate solar antenna resonates at 2.08 GHz (with a -10 dB impedance bandwidth of

16.6%) with parallel grid orientation and 2.064 GHz (with a -10 dB impedance bandwidth of 14.5%) with perpendicular grid orientation whilst the maximum gain values were measured as 3.9 dBi and 4 dBi, respectively. In [39], a quarter-wave shorted trapezoidal metal plate antenna combined with a poly-Si solar cell operating as an RF ground plane was demonstrated. The proposed solar antenna consists of a suspended trapezoidal-shaped metal plate fed through a  $50\Omega$  microstrip feed line printed on an FR4 substrate that altogether was placed upon the solar cell. The radiating suspended trapezoidal metal plate was short-circuited to the cell top grid electrodes in the corners and therefore has the advantage of operating at a quarter-wavelength mode similar to the metal plate antenna demonstrated in [38]. It was reported in [39] that the trapezoidal metal plate solar antenna resonates at a single frequency band of 1.957 GHz (with a -10 dB impedance bandwidth of 15.2%) and offers a gain of 4.5 dBi. The reduction in the solar cell efficiency due to the proposed solar antenna integration topology, which includes an opaque radiating metal plate element together with a feed line placed upon the cell, was reported as 3.46%. Although in [37-39] relatively low-profile radiating elements were selected for the solar integration, i.e. a dipole, a quarter-wave rectangular plate and a quarter-wave trapezoidal metal plate in comparison to [35, 36], the requirement for this integration topology that the RF radiating element needs to be placed upon/above the solar cell deteriorates the solar performance of these antennas. This is a significant challenge to be addressed in order to achieve optimum solar operation performance. Moreover, single band radiation response of the proposed solar antennas in [35-39] makes them not suitable for multiband applications. It should also be noted here that the solar antennas proposed in [35-39] have linear polarisation.

- In order to address this challenge, several techniques were studied in the literature including meshing the RF radiating element placed upon the cell operating as an RF ground plane [40] and making the RF radiating element placed upon the cell out of a transparent conductive material, such as AgHT-4 [41]. In [40], two types of meshed patch antenna prototypes were produced; wire mesh (offering a radiating patch element transparency of 93%) and ink mesh (offering a radiating patch element transparency of

61%). In both prototypes, the meshed radiating patch elements were attached to the solar cells operating as an RF ground plane on the top. While the ink meshed solar patch antenna operates at a single frequency band resonating at 2.61 GHz with a measured directivity of 8.4 dB, the wire meshed prototype offers a directivity of 8.2 dB. A decrease of 0.2 dB in the directivity was associated to the increased optical transparency of the radiating patch element. It should be noted here that in [40] it is unknown how effective the proposed meshing technique is in terms of the solar operation performance. The investigation of this technique from both antenna and photovoltaic perspectives is carried out in chapter 4 in detail. In [41], on the other hand, the integration of a transparent square microstrip patch made out of an AgHT-4 transparent film offering a minimum visible light transmission of 75% with an amorphous silicon (a-Si) solar cell operating as an RF ground plane was carried out. It was demonstrated in [41] that the proposed transparent patch antenna operates at a single frequency band with a -10 dB impedance bandwidth of 4.3% (154 MHz) and a peak gain of 3.96 dBi. It was reported in [41] that in comparison to the use of a conventional copper radiating patch element, the use of the proposed AgHT-4 transparent patch increases the solar efficiency by 4.8%. However, it should be noted that the use of a transparent conductive film as suggested in [41] is rather expensive. Moreover, both of the proposed solar antennas in [40, 41] have single band resonance characteristics making them impossible to be employed in multiband applications.

- The concept of using slot antennas combined with a-Si solar cells was investigated [42-44]. In [42], a dual-band H-slot antenna combined with an a-Si solar cell operating as an RF ground plane of the slot antenna was reported for 2.4/5.2 GHz band WLAN applications. The solar slot antenna is excited through a T-feed element printed on an FR4 substrate. As indicated in [42], the selection of the proposed slot geometry in order to minimise the effect of DC operation of the integrated solar cells on the RF performance of the antenna has the disadvantages of resulting in a narrow impedance bandwidth response and poor circular polarisation performance. Moreover, the effect of cutting an H-slot in the cell on the solar performance is unknown due to the fact that the solar measurements of the

proposed antenna were not carried out. The proposed H-slot solar antenna was reported to resonate at the frequencies of 2.465 GHz and 5.11 GHz, respectively, with measured -10 dB impedance bandwidths of 6.7% and 4.1%. In [43], a solar slot antenna, which is called “a fully-integrated SOLANT”, integrated with a-Si solar cells that were directly attached to an existing RF ground plane consisting of a slot excited through a microstrip feed line was proposed. As indicated in [43], as a result of using a slot antenna, a high cross-polarisation level, which was reported as -12 dB, was observed. The proposed solar slot antenna operates at a single frequency band, resonating at 4.14 GHz, with a measured maximum gain of 3.15 dBi. The open-circuit voltage of each cell was reported to be in the range of 0.82-0.87 V with a produced short-circuit current density of 10.2 mA/cm<sup>2</sup> resulting in a reported measured solar efficiency in the range of 5.6%-6% (the conditions under which the solar measurements were performed were not explained in this paper). The circularly polarised version of the linearly-polarised solar slot antenna demonstrated in [43] was proposed in [44]. The proposed SOLANT in [44] differs from the SOLANT in [43] that the ground plane consists of a cross-slot excited through a feed line at 45<sup>0</sup> with respect to the slot. The feed line is capable of being able enable two orthogonal propagation modes at the desired resonance frequency making it possible for the SOLANT to have circular polarisation when the modes are excited with the same amplitude and opposite phase. It was demonstrated in [44] that the proposed circularly-polarised SOLANT has an axial ratio (AR) of under 3 dB across the frequency band of 3.82-3.94 GHz with a -10 dB impedance band of 3.82-3.92 (3%) and a gain in the range of 9.7-11.6 dBi across the operational frequency band. Solar characteristics of the proposed SOLANT are unknown due to the lack of the solar measurements.

- Other work demonstrated in the literature on this solar antenna integration topology includes an internal LTE/WWAN solar handset antenna [45], a scalable solar antenna for integrated wireless sensor nodes [46], and a solar power active antenna as a beacon signal generator [47]. The solar handset antenna demonstrated in [45] has a printed short-circuited multiband radiating element consisting of a capacitive coupled-fed strip line. The proposed design consists of two ground planes with an array of eight series

connected solar cells between these ground planes. The solar cells were placed upon an FR4 substrate with an inverted-L metal strip coupled to the solar cells printed on the backside of the substrate. The radiating element was attached to the first ground plane. The use of the first ground plane enables the antenna to operate at the frequency of 1.63-2.77 GHz covering GSM 1800/1900, UMTS and LTE 2300/2500 applications. Activating the inverted-L metal strip between the ground planes, on the other hand, enables the solar cells to be coupled as an additional ground plane actively bridging between the first and second ground planes and therefore significantly extending the size of the overall ground plane, which enables the proposed antenna to have dual-band resonance characteristics operating at 660-990 MHz and 1.63-2.77 GHz covering LTE 700 and GSM 850/900 applications in addition to GSM 1800/1900, UMTS and LTE 2300/2500 applications. As the far-field radiation pattern and solar performance measurements were not carried out, the suitability of the proposed antenna for practical applications remains unknown. The proposed scalable solar antenna in [46] consists of four layers; a top layer (solar cell), a second layer (first RF ground plane), a third layer (RF feeding network) and a bottom layer (second RF ground plane). The solar cell was attached to the first RF ground plane (second layer) on the top and between the cell and the first RF ground plane a dielectric FR4 board lies. While the first RF ground plane is responsible for isolating the solar cell from the RF feeding network (third layer), the FR4 board prevents the solar cell from being in contact with the first RF ground plane. For this reason, the proposed design in [46] differs from the previous designs described above where the solar cell is a part of the RF operation as a result of the “full” solar integration. In view of this, the solar integration described in [46] can be seen more similar to the idea behind the autonomous solar powered communication systems in which solar cells and antennas are used separately. The RF feeding network (third layer) is responsible for carrying the RF signal and equally dividing it to be radiated from the slots, each placed symmetrically at the antenna edges resulting in omnidirectional monopole-like radiation characteristics for 2.4 GHz band autonomous integrated wireless sensor nodes. It was reported in [46] that the proposed solar antenna resonates at around 2.4 GHz

presenting a narrow impedance bandwidth calculated as 2.1% and has a gain of 0 dBi in free-space conditions. In [47], a coplanar waveguide (CPW) fed active printed folded-slot antenna fed through an oscillator powered by two flexible thin-film solar cells was proposed for wireless energy harvesting applications operating at 927 MHz. The oscillator circuit consists of thin-film solar cells powering the device, various parasitic circuit elements, an HJFET transistor and a low noise micropower regulator all of which were placed upon the CPW ground plane sharing the same surface of the substrate, Arlon 25N, with the folded-slot antenna. It was shown in the paper that the proposed folded-slot antenna operates across the frequency band of 800 MHz – 1.1 GHz and offers relatively wide E-plane and H-plane co-polarisation far-field radiation patterns.

- Solar Antenna Integration Topology: The use of solar cells as an RF radiating element or as an additional element attached to an existing RF radiating element [48-57]:
  - An autonomous wireless sensor node antenna for solar energy harvesting was studied in [48-50]. The work in [48-50] demonstrates a monopole antenna printed on an FR4 substrate and fed through a grounded CPW transmission line with a characteristic impedance of  $50\Omega$ . In order to widen the operational frequency band to be able to cover UWB applications (defined as 3.1-10.6 GHz by the Federal Communications Commission, FCC), the square monopole has a bevelled copper tab at the edge where it is connected to the feed line. A thin-film a-Si solar cell has been placed upon the square monopole and works as an RF radiating element in addition to its photovoltaic function. It was indicated in [48, 49] that the solar cell has an open-circuit voltage of 0.9 V and a short-circuit current density of  $13 \text{ mA/cm}^2$  resulting in a poor solar efficiency of 6.3% obtained under a solar illumination intensity of  $100 \text{ mW/cm}^2$  at  $25^\circ\text{C}$ . Low-pass filters were used in order to isolate the DC terminal connections of the solar cell from the RF operation. It was reported in the paper that up to 5 GHz, the proposed solar antenna offers similar far-field radiation characteristics to a conventional planar monopole antenna with an omnidirectional radiation pattern in the H-plane and bidirectional radiation pattern in the E-plane. The measured gain, on the other hand, was reported to be in the range of 0 dBi – 3 dBi up to 5

GHz. Although it was demonstrated in [48, 49] that the antenna is capable of covering UWB, the far-field radiation response beyond 5 GHz was not investigated. In [50], however, it was indicated that the far-field radiation patterns beyond 5 GHz start differentiating from the radiation patterns of a conventional planar copper monopole antenna. This was attributed to different reflections occurring at the input port and the losses caused by the solar cells. Due to typical polarisation characteristics of printed monopole antennas, it can be said that the solar monopoles demonstrated in [48-50] have linear-polarisation and therefore are not suitable for polarisation diverse applications.

- In [51], a UWB dipole antenna combined with a pair of thin-film a-Si solar cells capable of solar energy harvesting across UWB was presented. The dipole has coaxially-fed bow-tie shaped arms each consists of a square patch combined with a bevelled copper tab that together was printed upon an FR4 substrate with a DC/RF isolation circuit presented in [48-50] on the backside. Similar to [48-50], the solar cells were conductively glued to the square part of the bow-tie arms. The far-field radiation patterns of the proposed solar dipole antenna were indicated to have some differences in comparison to far-field radiation patterns of conventional planar bow-tie antennas at higher frequencies within UWB. This was attributed to the solar cell front and rear contacts with the additional layouts introduced in the design. Due to the typical polarisation characteristics of dipole antennas, it can be said that the proposed dipole antenna has linear polarisation. As the same a-Si solar cells in [48-50] were used in this solar dipole, the characteristics of the a-Si cell given in [51] are the same as in [48-50].
- The integration of a planar antenna consisting of a standard copper patch with GaAs solar cells was demonstrated in [52]. In the proposed solar antenna design, the conventional copper patch was replaced with a GaAs solar cell operating as an RF radiating element placed upon an FR4 substrate. In order to increase the total effective cell surface area, two more solar cells, one is on the left and the other is on the right of the radiating solar cell in the centre, were introduced as parasitic elements at the cost of increasing the cross-polarisation level, which was demonstrated as up to -5 dB in the paper. The radiating cell was fed through an excitation slot which

is in the centre of the ground plane printed on a separate FR4 layer with RF feed and DC lines on the backside. It was demonstrated that the antenna operates at a single frequency band of 2.753-2.983 GHz (with an impedance bandwidth of 8%) with a peak gain of 5.5 dBi at 2.75 GHz and therefore is not suitable for multiband applications. The solar response of the proposed solar antenna is unknown due to the fact that the solar measurements of the antenna were not carried out.

- The integration of a GPS planar antenna with photovoltaics for vehicular applications was demonstrated in [53]. The proposed solar planar antenna, called SOLPLANT in [53], consists of a central patch divided into four sub-patches with additional slots in between. These radiating sub-patches were replaced with monocrystalline silicon (mono-Si) solar cells operating as an RF radiating element in addition to the radiation from the slots between the cells. The ground plane underneath these solar patch cells have a cross-shaped aperture through which each of these solar cells was excited by a specially designed feeding network consisting of Wilkinson power dividers printed on an FR4 substrate. As a result of the use of the Wilkinson power dividers in the feeding network, the phase difference between each sub-patch was selected as  $90^{\circ}$  resulting in a circularly-polarised operation when the sub-patches are fed with a uniform amplitude distribution. It was indicated in [53] that each solar cell has an open-circuit voltage of 0.5 V and in order to increase the total open-circuit voltage output of the solar antenna to 18 V, a total of 36 solar cells were used in the design. While the core four solar patches in the centre were used as direct radiating elements, the other cells surrounding the central four were used as coupled parasitic elements. The electromagnetically coupled feeding network was selected in order to minimise the effect of the integration on the antenna performance which was reported to result in an enhanced axial ratio performance obtained from the proposed solar antenna. However, the proposed design consists of a rather complex and expensive DC/RF decoupling circuit which was realised by means of concentrated reactive elements. The demonstrated solar antenna has a maximum gain of 2 dBi. The voltage and current readings of the investigated GPS solar patch antenna at the maximum power point were recorded as 17.6 V and 0.87 A, respectively. In addition to the

SOLPLANT – GPS antenna demonstrated in [53], in [54] the design of a SOLPLANT – GSM antenna using the same solar antenna integration topology as in [53] was also discussed.

- Investigation into a wearable aperture-coupled shorted patch antenna integrated with flexible a-Si solar cells covering 902-928 MHz ISM band was carried out for remote tracking and monitoring applications [55]. In this proposed design, the patch, which was made out of Flectron (a copper coated nylon fabric), was printed on a flexible polyurethane foam substrate with a ground plane on the backside, which consists of an H-shaped slot, coupling a  $50\Omega$  microstrip feed line underneath to the Flectron patch. Two parallel-connected flexible a-Si solar cells, each generating a maximum DC power output of 48mW, were then glued onto the surface of the Flectron radiating patch. The I-V characteristics of the solar cells were measured in a solar simulator with an illumination intensity of  $100 \text{ mW/cm}^2$  (the temperature at which the solar measurements were taken is unknown) and an open-circuit voltage of 4.23 V with a short-circuit current of 26.25 mA was observed. At the maximum power point, on the other hand, the current and voltage readings were recorded as 3 V and 19.1 mA, respectively, resulting in a maximum DC power output of 57.3 mW, which drops to 48 mW as a result of the blocking Schottky diodes introduced in the design. During the on-body measurements, the solar antenna was placed on the chest of a human body and it was reported that the proposed solar antenna has a measured impedance bandwidth of 64 MHz and offers a gain of about 1.6 dBi (3 dBi in free space). Although the proposed wearable solar patch antenna seems to be a promising candidate to be employed in on-body applications, the obtained low-gain and single narrow band impedance bandwidth responses make it not suitable for multiband/wideband applications where adequate gain performance is required.
- In [56], a low-gain UHF solar cross-slot antenna was proposed for future Mars Rover applications. The proposed solar antenna has a microstrip patch radiator that originally consists of a four quarter-wavelength sub-patches each short-circuited to the ground plane at a single edge. The radiation was achieved through the slots between the sub-patches at the non-short-circuited edges. The solar cells were then placed upon the patches excluding

the areas where the radiating slots are. It was demonstrated in the paper that the proposed solar crossed-slot antenna has circular polarisation and offers a narrow -10 dB impedance bandwidth of 40 MHz with a maximum gain of 4.5 dBiC.

- A prototype of an array of printed-strip-slot-foam-inverted-patch (SSFIP) antennas combined with an a-Si solar cell powering a monolithic microwave integrated circuit (MMIC) amplifier was demonstrated in [57]. The proposed solar antenna, called SOLANT, was designed to operate at 4 GHz C-band for satellite communications. The antenna consists of an array of printed microstrip patches excited through slots etched in the ground plane with a printed microstrip RF distribution network underneath consisting of Wilkinson power dividers distributing the RF signal to feed the aperture coupled patches. The a-Si solar cells were glued onto the radiating patches and are responsible for powering the MMIC amplifier printed on the feedline, capable of providing a maximum gain of 20 dB in the received signal amplitude. It was demonstrated in [57] that the proposed solar antenna resonates at the centre frequency of 3.95 GHz (with an impedance bandwidth of 600 MHz – 15%) and has a gain of 13 dBi in passive mode without the MMIC amplifier and 30 dBi in active mode with the MMIC amplifier. As indicated in the paper, the solar measurements of the proposed SOLANT were performed under non-standard conditions and a short-circuit current of 98 mA with an open-circuit voltage of 6.755 V was obtained. At the maximum power point, on the other hand, the current and voltage readings were recorded as 63 mA and 4 V, resulting in a maximum DC power output of 252 mW. In the proposed design, the use of substrate surface, which was occupied by printed DC connections between the solar cells separated by a considerable distance from each other, significantly increases the size of the proposed SOLANT preventing it from offering a reasonable improvement in terms of size reduction.
- Solar Antenna Integration Topology: Other [56, 58]
  - In [56], the photovoltaic integration of a high-gain microstrip reflectarray antenna fed through a circularly-polarised conical feed horn antenna was also demonstrated for X-band deep space telecommunication applications in addition to the low-gain UHF solar cross-slot antenna described above. An

array of 204 solar cells was placed across the surface of the planar reflectarray with a coverglass on top operating as a substrate for the printed 408 cross dipoles. However, it was reported in [56] that the proposed solar reflectarray antenna has an aperture efficiency of only 10% which was attributed to the electrical characteristics of the crossed-dipoles and the effect of the inhomogeneous ground plane. Moreover, a significant problem with the presented approach is that the proposed reflectarray is central-fed and therefore the feed horn shades the solar cells in the solar array. This is a significant problem due to the fact that shading of a single cell in the proposed design would limit the overall electrical output of the 204 element solar array (the total current output if the cells in the array are connected in parallel or the total voltage output if the cells in the array are connected in series) to the electrical output of the shaded single cell in the array. As the photovoltaic measurements of the proposed reflectarray antenna were not carried out, the solar performance remains unknown.

- In [58], a Yagi-uda antenna consisting of a six linear elements (one reflector element, one driven element and four director elements) with a spacing of quarter-wavelength between the elements was integrated with solar cells for 435 MHz CubeSat platform. The solar cells were placed between the elements of the proposed Yagi-uda antenna and it was demonstrated that the solar antenna has a -10 dB impedance bandwidth of 53 MHz and a maximum gain of 11.5 dBi. The solar performance is unknown due to the lack of the solar measurements.

## **1.5 Outline of the Thesis, Novelty and Publications**

- In chapter 1, brief information about the historical evaluation of antennas and photovoltaics is given. The motivation of this research together with the aims for the integration of antennas with photovoltaics is explained. A rigorous literature review is performed to provide a detailed review of present methods of integrating microwave antennas with solar cells. The novelty of the work undertaken in this research is presented together with the associated publications.
- In chapter 2, a background on photovoltaically integrated antennas in this research is provided. In this chapter, the fundamental antenna parameters, such as radiation pattern, beamwidth, directivity, gain, antenna efficiency, bandwidth, input

impedance and polarisation, are explained in detail. Investigation into the background of microstrip patch antennas and Planar Inverted-F Antennas (PIFAs), covering the feed and analysis methods of these antennas, is performed. The photovoltaic integration process and the challenges of this process from an RF perspective are also investigated.

- In chapter 3, a background on photovoltaics and solar cells is given. This chapter provides the fundamentals of photovoltaics and crystalline silicon solar cells. It covers the I-V characteristics, efficiency and loss factors of crystalline silicon solar cells. It provides an outline on the photovoltaic integration process and the challenges of this process from a photovoltaic perspective. It also demonstrates the solar simulators used for the solar efficiency measurements of the photovoltaic antennas studied in this research.
- Chapter 4 provides a detailed investigation into the first type of solar antenna integration topology demonstrated in the literature, which is the use of solar cells as an RF ground plane or as an additional element attached to an existing RF ground plane. The limitations of this technique are investigated and novel designs to overcome these are developed.
- Chapter 5 investigates the second solar antenna integration topology studied in the literature, which is the use of solar cells as an RF radiating element or as an additional element attached to an existing RF radiating element. Moreover, in order to demonstrate the RF stability of solar antennas required to work under challenging/unpredictable weather conditions with varying solar illumination intensities, novel investigation into the effect of varying the solar illumination intensity on the RF antenna response is carried out and the results are demonstrated in this chapter.
- Chapter 6 builds upon the research in previous chapters and presents a new solar antenna integration topology. This approach is then used to develop further antenna designs. Full details of chapter 6 are outlined below:
  - It proposes a novel solar antenna integration topology. It explains how this proposed new solar antenna integration topology addresses the disadvantages of the existing solar antenna combination topologies investigated in chapter 4 and chapter 5.

- This chapter also demonstrates the novel integration of PIFAs with photovoltaics using the proposed new solar antenna integration topology. This brings the advantage of a considerable size reduction due to the quarter-wavelength mode operation capability of PIFAs in comparison to microstrip patch antennas operating at a half-wavelength mode.
  - Existing work in the literature mainly focuses on the photovoltaic integration of linearly-polarised microwave antennas, which are not suitable to be employed in polarisation diverse applications. To this end, in this chapter, the novel investigation into the integration of photovoltaics with a slant  $\pm 45^\circ$  dual-polarised microstrip patch antenna for polarisation diverse WiMAX systems is also demonstrated.
  - Moreover, in this chapter, a novel design of a microstrip solar patch array antenna using the proposed new solar antenna integration topology is presented for electronic beam steering applications. The proposed solar array antenna has a significant potential to be employed in applications where the user to be communicated with is positioned differently from the direction of the Sun, in which the solar antenna is required to be oriented to achieve optimum solar efficiency. Therefore the proposed antenna addresses the challenge of performing an electronic beam steering to achieve the RF coverage in the direction of the communication target whilst maintaining the physical position of the antenna for optimum solar performance.
- Chapter 7 concludes the thesis and suggests some future research directions.

Fig. 1.1 summarises the project roadmap and the research performed in this thesis.

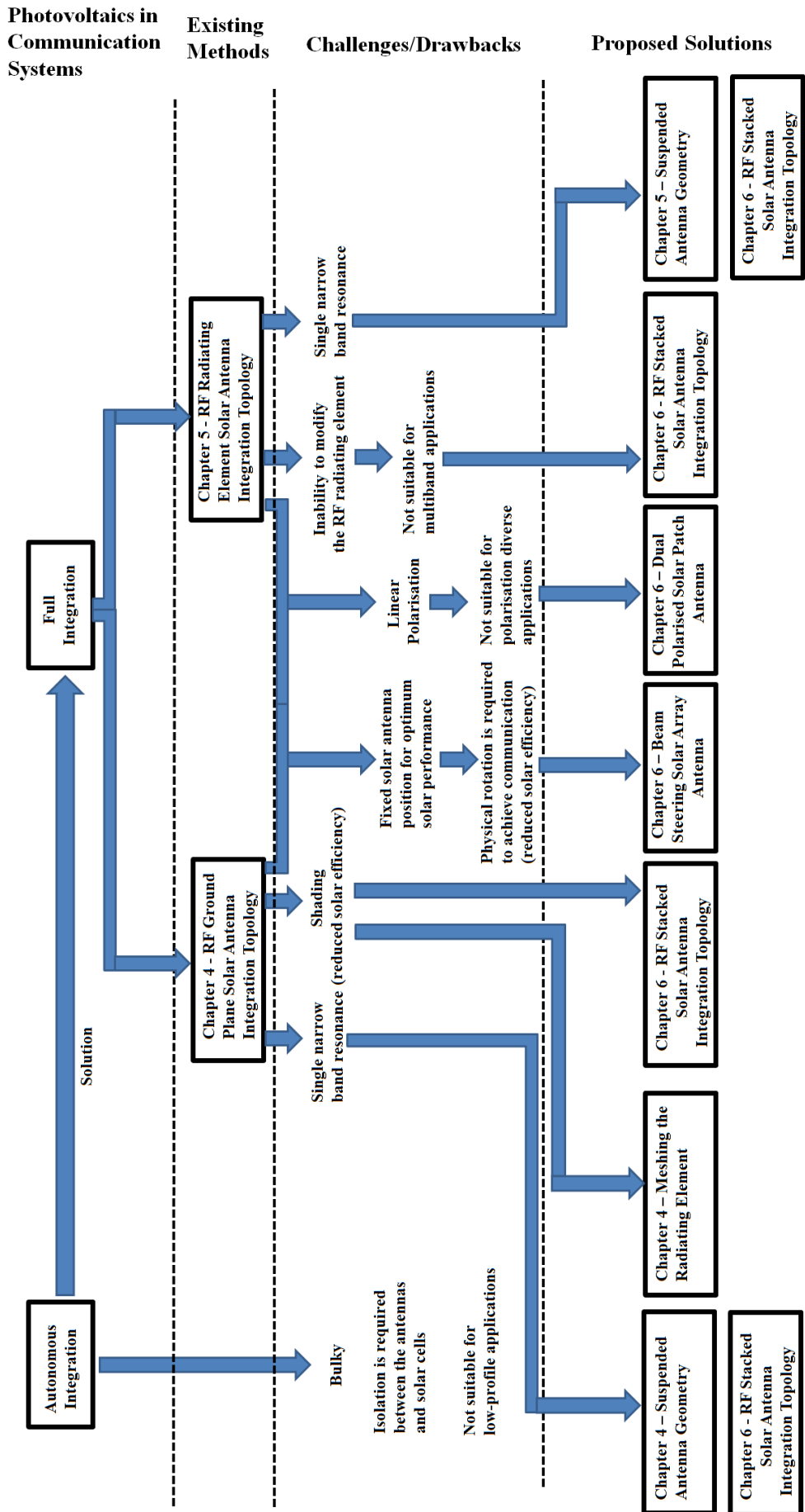


Fig. 1.1: Project roadmap and research undertaken in this thesis.

The work undertaken in the research has led to the following publications given below:

### **Journal Papers**

- Okan Yurduseven, “Reduced size photovoltaic patch antenna using metamaterial substrate for 2.3 GHz band WiMAX networks,” *IET Electronics Letters*, 2014 (under review).
- Okan Yurduseven, David Smith, and Michael Elsdon, “Dual-polarised photovoltaic array antenna for 5.8 GHz band WiMAX base stations,” *IET Electronics Letters*, 2014 (under review).
- Okan Yurduseven, David Smith, and Michael Elsdon, “Printed Slot Loaded Bow-Tie Antenna with Super Wideband Radiation Characteristics for Imaging Applications,” *IEEE Transactions on Antennas and Propagation*, vol. 61, no. 12, pp. 6206-6210, December 2013.
- Okan Yurduseven and David Smith, “A Solar Cell Stacked Multi-Slot Quad-Band PIFA for GSM, WLAN and WiMAX Networks,” *IEEE Microwave and Wireless Components Letters*, vol. 23, no. 6, pp. 285-287, 2013.
- Okan Yurduseven, David Smith, Nicola Pearsall, and Ian Forbes, “Solar Cell Stacked Slot Loaded Suspended Multiband Patch Antenna for WLAN and WiMAX Systems,” *Progress in Electromagnetics Research (PIER)*, vol. 142, pp. 321-332, 2013.
- Okan Yurduseven, David Smith, and Michael Elsdon, “UWB Meshed Solar Monopole Antenna,” *IET Electronics Letters*, vol. 49, no. 9, pp. 285-287, 2013.
- Okan Yurduseven and David Smith, “Solar Cell Stacked Dual-Polarised Patch Antenna for 5.8 GHz band WiMAX Network,” *IET Electronics Letters*, vol. 49, no. 24, pp. 1514-1515, 2013.
- Okan Yurduseven, “DC suppressed on-axis indirect microwave holographic imaging with reduced sampling,” *IEEE Transactions on Antennas and Propagation*, 2014 (under review).
- Okan Yurduseven, “Indirect microwave holographic imaging of concealed ordnance for airport security imaging systems,” *Progress in Electromagnetics Research*, vol. 146, pp. 7-13, 2014.
- David Smith, Okan Yurduseven, Bryan Livingstone, and Vladimir Schejbal, “Microwave Imaging using Indirect Holographic Techniques”, *IEEE Antennas and Propagation Magazine*, vol. 56, no. 1, February 2014 (in press).

- Michael Elsdon, Okan Yurduseven, and David Smith, “Early Stage Breast Cancer Detection using Indirect Microwave Holography,” *Progress in Electromagnetics Research (PIER)*, vol. 143, pp. 405-419, 2013.
- Okan Yurduseven, David Smith, Bryan Livingstone, Vladimir Schejbal, and Zhonghui You, “Investigations of Resolution Limits for Indirect Microwave Imaging”, *Wiley International Journal of RF and Microwave Computer Aided Engineering*, vol. 23, no. 4, pp. 410-416, 2013.

### **Conference Papers**

- David Smith, Okan Yurduseven, Bryan Livingstone, and Hu Zheng, “An outline of indirect holographic methods for antenna measurements and microwave imaging,” *Radioelektronika*, 2014 (invited paper).
- Okan Yurduseven, David Smith, and Michael Elsdon, “A Dual-Polarised Solar Cell Stacked Microstrip Patch Antenna with a  $\lambda/4$  DC/RF Isolation Circuit for 5.8 GHz band WiMAX Networks,” *European Conference on Antennas and Propagation (EuCAP)*, 2014 (accepted).
- Okan Yurduseven, David Smith, and Michael Elsdon, “A Transparent Meshed Solar Monopole Antenna for UWB Applications,” *European Conference on Antennas and Propagation (EuCAP)*, 2014 (accepted).
- David Smith, Okan Yurduseven, Bryan Livingstone, and Hu Zheng, “Object reconstruction from indirect intensity measurements and inverse scattering methods,” *IEEE European Microwave Week*, 2014 (under review).
- Okan Yurduseven and David Smith, “A Multi-Slot Planar Inverted-F Antenna Combined with a Polycrystalline Silicon Solar Cell,” *IEEE International Symposium on Antennas and Propagation (AP-S)*, 2014 (accepted).
- Okan Yurduseven and David Smith, “A Self-Complementary Slot Loaded Suspended Microstrip Patch Antenna Stacked with a Solar Cell for 2.4/5.2 GHz Band WLAN and 2.5/3,3/5.8 GHz Band WiMAX Networks,” *IEEE International Symposium on Antennas and Propagation (AP-S)*, 2014 (accepted).
- Michael Elsdon, Okan Yurduseven, and David Smith, “The Application of Indirect Microwave Holography in Early-Stage Breast Cancer Detection,” *IEEE International Symposium on Antennas and Propagation (APS)*, 2014 (accepted).
- David Smith, Okan Yurduseven, Bryan Livingstone, John Jackson, and Vladimir Schejbal, “Image Reconstruction from Intensity Only Measurements using

- Development in Fourier Transform Techniques,” *Mediterranean Microwave Symposium*, Lebanon, 2013 (invited paper).
- Okan Yurduseven, David Smith, and Nicola Pearsall, “Solar cell stacked modified Z-double L-slot Quad-band PIFA”, *European Conference on Antennas and Propagation (EuCAP)*, Gothenburg, Sweden, pp. 3721-3725, 2013.
  - Okan Yurduseven, David Smith, and Michael Elsdon, “Cross-coax fed wideband solar patch antenna”, *Microwave and Radio Electronics Week (MAREW)*, Pardubice, Czech Republic, pp. 25-30, 2013.
  - David Smith, Okan Yurduseven, and Bryan Livingstone, “The use of indirect holographic techniques for microwave imaging,” *Microwave and Radio Electronics Week (MAREW)*, Pardubice, Czech Republic, pp. 16-21, 2013 (invited paper).
  - Okan Yurduseven, David Smith, Bryan Livingstone, and Vladimir Schejbal, “Investigation of resolution limits for indirect microwave holographic imaging”, *Mediterranean Microwave Symposium (MMS)*, Istanbul, Turkey, 2012 – selected as best student paper (invited paper).
  - Okan Yurduseven, David Smith, Nicola Pearsall, Ian Forbes, and David Johnston, “A Meshed Multiband Solar Patch Array Antenna”, *Loughborough Antennas and Propagation Conference (LAPC)*, Loughborough, UK, pp. 1-5, 2012.
  - Okan Yurduseven, David Smith, Nicola Pearsall, and Ian Forbes, “A Triband Short-Circuited Suspended Solar Patch Antenna”, *International Symposium on Antennas, Propagation and EM Theory (ISAPE)*, Xi’an, China, pp. 294-297, 2012.
  - Okan Yurduseven, and David Smith, “Symmetric/Asymmetric H-Plane Horn Fed Offset Parabolic Reflector Antenna with Switchable Pencil/Fan-Beam Radiation Patterns”, *International Symposium on Antennas, Propagation and EM Theory (ISAPE)*, Xi’an, China, pp. 82-85, 2012.
  - Okan Yurduseven, David Smith, Nicola Pearsall, and Ian Forbes, “A Solar Parabolic Reflector Antenna Design for Digital Communication Systems”, *8<sup>th</sup> IEEE IET International Symposium on Communication Systems, Networks and Digital Signal Processing (CSNDSP)*, Poznan, Poland, pp. 1-3, 2012.
  - Freeborn Bobor-Oyibo, Stephen J. Foti, David Smith, and Okan Yurduseven, “Modelling and Analysis of a Smart Antenna System with Sub-Sector Dynamic Capacity Enhancement for Mobile Telecommunication Networks”, *8<sup>th</sup> IEEE IET International Symposium on Communication Systems, Networks and Digital Signal Processing (CSNDSP)*, Poznan, Poland, pp. 1-4, 2012.

- Okan Yurduseven, David Smith, Nicola Pearsall, and Ian Forbes, “Design of a Highly Efficient Wideband Suspended Solar Array Antenna”, *IEEE AP-S/URSI*, Chicago, USA, pp. 1-2, July 2012.
- Okan Yurduseven, David Smith, Freeborn Bobor-Oyibo, and Stephen J. Foti, “Design of a Highly Efficient Beam Scanning Asymmetric H-Plane Horn Antenna”, *IEEE International Workshop on Antenna Technology (IWAT)*, Tucson - Arizona, USA, pp. 108-111, March 2012.
- Freeborn Bobor-Oyibo, Stephen J. Foti, David Smith, and Okan Yurduseven, “A Smart Antenna System with Sub-Sector Capacity Enhancement for Mobile Telecommunication Networks”, *IEEE International Workshop on Antenna Technology (IWAT)*, Tucson – Arizona, USA, pp. 100-103, March 2012.
- Okan Yurduseven, David Smith, Nicola Pearsall, and Ian Forbes, “A Transparent Solar Patch Antenna for 2.4/2.5 GHz WLAN-WiMAX Applications”, *2<sup>nd</sup> International Symposium on Environment-Friendly Energies and Applications (EFEA)*, Newcastle upon Tyne, United Kingdom, pp. 614-617, 2012.
- Okan Yurduseven, David Smith, Nicola Pearsall, and Ian Forbes, “A suspended Solar Patch Array Fed Offset Reflector Antenna”, *URSI UK Radio Science Festival*, Durham, United Kingdom, 2012.
- Okan Yurduseven and Ozan Yurduseven, “Compact Parabolic Reflector Antenna Design with Cosecant-Squared Radiation Pattern”, *Microwaves, Radar and Remote Sensing Symposium (MRRS)*, Kiev, Ukraine, pp. 382-385, August 2011.
- Ozan Yurduseven and Okan Yurduseven, “Analysis of Back Wall Smoothing and Multisource Feeding Effects for H-Plane Horn Radiator”, *Microwaves, Radar and Remote Sensing Symposium (MRRS)*, Kiev, Ukraine, pp. 89-92, August 2011.

# Chapter 2 – Background on Antennas

## 2.1 Introduction

This chapter aims to provide an RF background on photovoltaically integrated microwave antennas. Section 2.2 explains the fundamental antenna parameters and provides a detailed theoretical background on microwave antennas whose photovoltaic integration is investigated in this research, i.e. microstrip patch antennas (including printed monopole antennas) and PIFAs. Section 2.3 demonstrates the challenges of the photovoltaic integration of microwave antennas from an RF perspective. These challenges will need to be considered in the examination of the RF antenna responses of the photovoltaic antennas studied in the subsequent chapters of this thesis.

## 2.2 Antennas

An antenna is a transitional structure which converts electric signals at its input to radiated electromagnetic waves in free space in transmitting mode and electromagnetic waves in free space to electric signals in receiving mode.

Antennas can be in different shapes and sizes depending upon the required radiation characteristics and the desired operational frequency band, and are one of the most critical components in wireless communication systems. Planar antennas, especially microstrip patch antennas, are widely used in mobile, WLAN and WiMAX communication systems as they are low-profile, easily conformable to planar/non-planar surfaces and have a simple low-cost manufacturing process [84-90].

### 2.2.1 Antenna Parameters

In this section, the fundamental antenna parameters, which will be required for the examination of the RF performance of the photovoltaic antennas studied in this thesis, are explained.

#### 2.2.1.1 Radiation Pattern

The radiation pattern of an antenna can be described as the spatial distribution or the mathematical function of the electromagnetic field radiated by an antenna in various directions and is mostly determined in the far-field region in a free space coordinate

system [85]. Although it is called radiation pattern, it should be noted here that due to the reciprocity, the radiation pattern of an antenna in transmission mode is equal to the reception pattern of the same antenna in reception mode. Therefore, determination of the radiation pattern of an antenna also reveals the reception pattern.

The radiation pattern of an antenna can be described in two ways:

- Field pattern: Describes the angular  $|\vec{E}|$  and  $|\vec{H}|$  distribution radiated by an antenna in the far-field region.
- Power pattern: Describes the angular distribution of  $|\vec{E}|^2$  and  $|\vec{H}|^2$  in the far-field region and is mostly given on a logarithmic scale. As demonstrated, there is a direct relationship between the field pattern and the power pattern of an antenna and therefore the power pattern of an antenna can easily be obtained from the field pattern. The power pattern can be considered as the most commonly used pattern form in the description of antenna radiation patterns.

In Fig. 2.1, the far-field radiation pattern of a directional antenna is demonstrated.

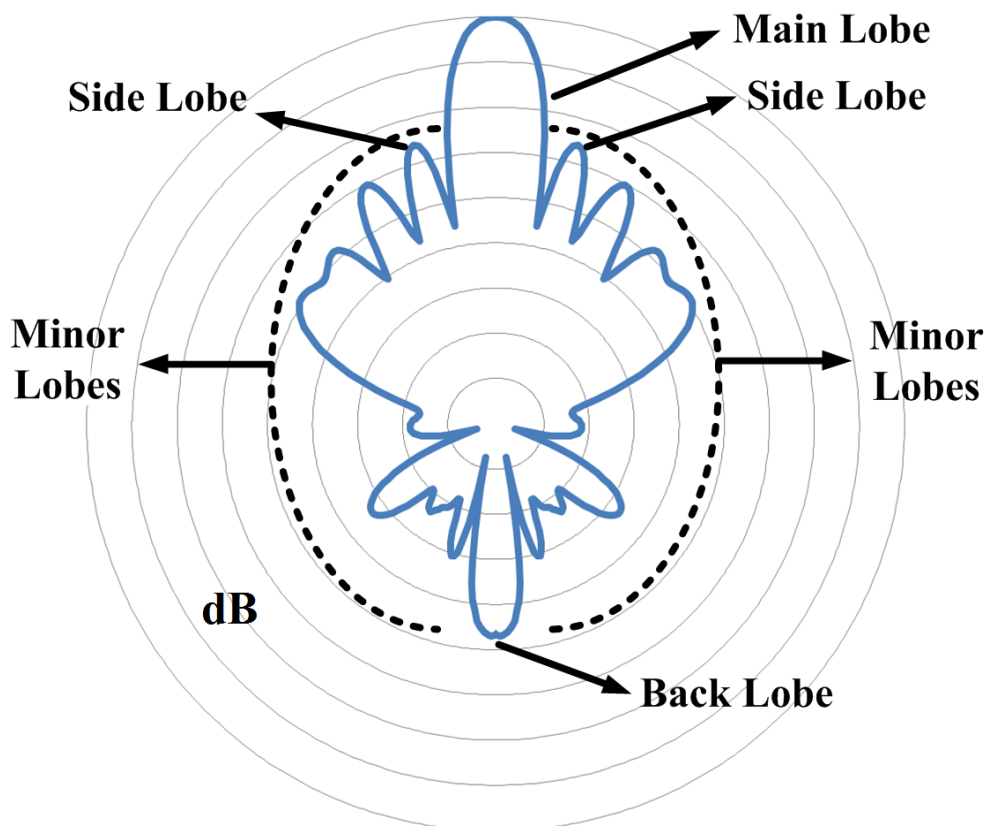


Fig. 2.1: Radiation pattern of an antenna.

Examination of Fig. 2.1 suggests that the far-field radiation pattern of an antenna consists of many lobes which can be classified as follows:

- Main lobe: This lobe describes the maximum radiation. Investigation of this lobe also reveals another antenna parameter, half-power beamwidth (HPBW) or usually simply beamwidth, which will be described in section 2.2.1.2 in detail. If the main lobe is parallel to the antenna plane, the antenna is said to have an end-fire radiation pattern whilst an antenna with a main lobe in the direction of the antenna axis perpendicular to the antenna plane is called a broadside antenna. Although most antennas have a single main lobe, some antennas may present multi-beam radiation characteristics. These types of antennas are generally used for multipath applications.
- Minor lobes: In Fig. 2.1, all lobes except for the main lobe can be classified as minor lobes. Within this scope, the radiation lobes different from the main lobe are called side lobes and are the first on the left and right of the main lobe in Fig. 2.1. As the minor lobes describe the radiation from an antenna in unwanted directions, typically, it is required that the sidelobe levels of an antenna to be as low as possible, i.e. -20 dB and below depending upon the application. Back lobe, on the other hand, represents the radiation in the direction which is  $180^\circ$  opposite to the direction of the main lobe as can be seen in Fig. 2.1.

### **2.2.1.2 Beamwidth**

In general, the definition of beamwidth of an antenna can be given as the angular range between two identical points in the radiation pattern both of which have a specific value in comparison to the radiation maximum as demonstrated in Fig. 2.2.

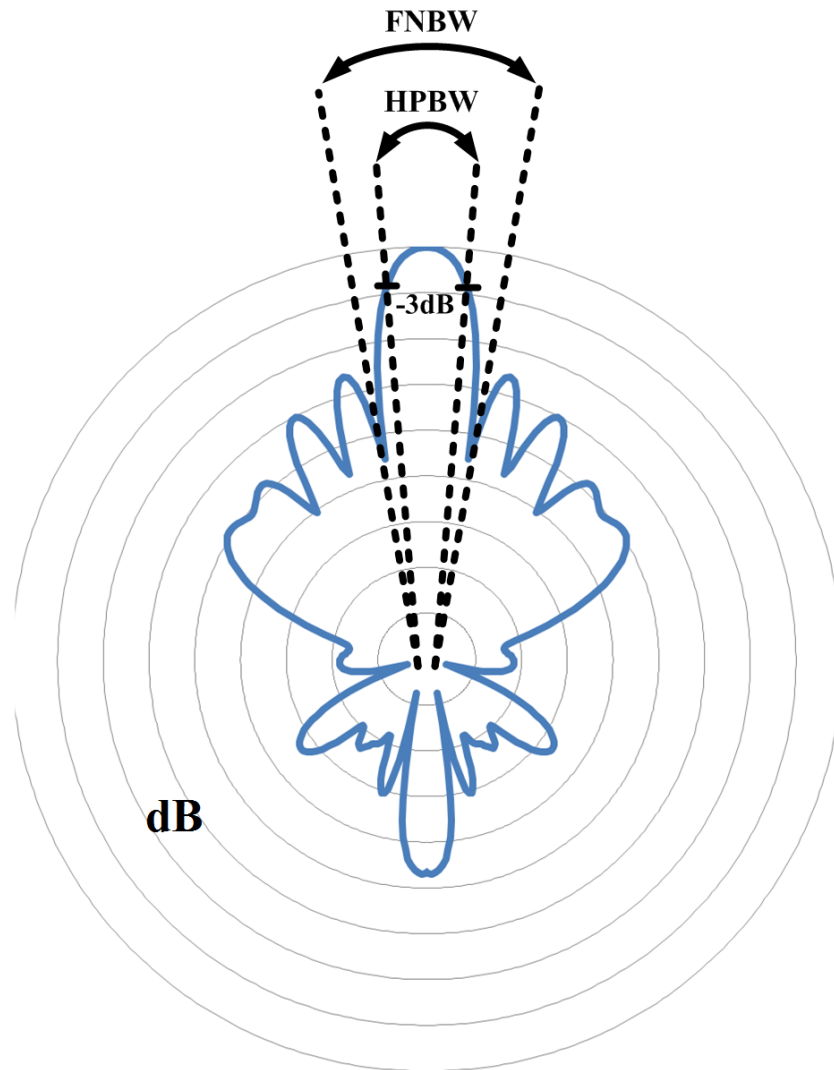


Fig. 2.2: FNBW and HPBW of an antenna.

As shown in Fig. 2.2, for a radiation pattern given on a logarithmic scale, if this value is selected to be  $-3$  dB, the beamwidth of the antenna is determined by the angular separation between the points which are 3 dB lower than the pattern maximum (on a linear scale, however, this is equivalent to one-half of the pattern maximum). This is known as  $-3$  dB beamwidth, which is called half-power beamwidth (HPBW). Other types of beamwidths can be given as first-null beamwidth (FNBW), which can be seen in Fig. 2.2, and  $-10$  dB beamwidth. Among these beamwidth types, HPBW is the most commonly used in antenna engineering and therefore the term beamwidth usually refers to HPBW if no other information is given [90].

In practical applications, antenna beamwidth is one of the most critical antenna parameters. Whilst antennas with narrow beam radiation patterns, such as pencil-beam, are widely used for microwave direction finding and high resolution scanning radar systems, wide beam

antennas offering relatively wide coverage in the azimuth plane are desired for broadcasting applications.

### 2.2.1.3 Directivity, Gain and Antenna Efficiency

Directivity of an antenna can be described as the ratio of the radiation intensity in a given direction to the average radiation intensity radiated in all directions. It can be accepted as an indicator of how well an antenna focuses the radiation in a certain direction and therefore is of a significant importance in the determination of the radiation performance of an antenna.

Directivity of an antenna can be investigated in two ways [91]:

- Angular directivity ( $D(\theta, \phi)$ ): Angular directivity of an antenna is the function of  $\theta$  and  $\phi$  in a spherical coordinate system, and can be obtained at any given angle. Mathematically,

$$D(\theta, \phi) = \frac{R(\theta, \phi)}{R_{av} = R_{Tot} / 4\pi} \quad (2.1)$$

Where,  $R(\theta, \phi)$  represents the radiation intensity at a given angle,  $R_{Tot}$  is the total radiation intensity and  $R_{av}$  is the average radiation intensity per unit solid angle.

- Maximum directivity ( $D_{max}$ ): Maximum directivity of an antenna is obtained in the maximum radiation direction and mathematically can be given as follows:

$$D_{max} = \frac{R_{max}}{R_{av}} \quad (2.2)$$

Where, maximum radiation intensity,  $R_{max}$ , is obtained in the direction of the maximum radiation.

In general, antenna efficiency can be considered as a combination of:

- Reflection (impedance mismatch) efficiency ( $e_r$ ): Determined by the impedance mismatch loss ( $1 - |r|^2$ ).
- Conductance efficiency ( $e_c$ ): Determined by the ohmic loss.

- Dielectric efficiency ( $e_d$ ): Determined by the dielectric loss.

In light of this, the total antenna efficiency ( $e_t$ ) is given as follows:

$$e_t = e_r e_c e_d \quad (2.3)$$

Due to the difficulty of measuring conductive and dielectric losses separately, they are combined together as a single term, which is called radiation efficiency ( $e_{cd}$ ) correlating directivity and gain as follows [5]:

$$G = e_{cd} D \quad (2.4)$$

As can be seen in equation (2.4), antenna gain is a combination of directivity and radiation efficiency and as indicated in IEEE standard definitions of terms for antennas [92], is not related to the impedance mismatching loss.

### 2.2.1.4 Bandwidth

The bandwidth of an antenna can be given as the operational frequency range across which the antenna offers satisfactory radiation characteristics in terms of the fundamental antenna parameters discussed in this chapter. As for different applications the antenna parameters of interest might change, it is not possible to give a unique definition of bandwidth of an antenna. Depending upon the applications that an antenna can be designed for, in general, two types of bandwidths are of great interest, which can be given as follows [5]:

- Pattern bandwidth: The definition of pattern bandwidth can include many parameters, such as sidelobe bandwidth, beamwidth bandwidth and axial ratio (AR) bandwidth. For example, if the design of a pencil-beam parabolic reflector antenna with a suppressed sidelobe level is required for an X-band radar (8-12 GHz), the beamwidth and sidelobe bandwidths of the antenna should be acceptable across the X-band. If the design of a circularly-polarised antenna is required, the 3 dB axial ratio bandwidth of the antenna will be of interest.
- Input impedance (or impedance) bandwidth: Impedance bandwidth of an antenna is one of the most critical factors of an antenna design process. It describes the frequency range across which an acceptable amount of the input power is successfully transferred to an antenna. It is not possible to define a unique ratio of the accepted input power by an antenna as this depends on the application that the

antenna is designed for. For example, while for radio-frequency identification (RFID) antennas -3 dB input impedance bandwidth can be acceptable, for most of other antennas -10 dB level is defined as a standard in the determination of the impedance bandwidth. It should also be noted here that an antenna with a -10 dB impedance bandwidth across a required operational frequency band refers to an antenna to which 90% of the input power is successfully transferred over this frequency band. For an antenna with a -3 dB impedance bandwidth, on the other hand, only 50% of the input power is successfully transferred to the antenna.

### 2.2.1.5 Input Impedance

The input impedance of an antenna is defined as the ratio of the voltage to the current at its input terminals and investigated in transmitting and receiving modes.

If an antenna operates in a transmitting mode, it needs to be connected to a signal generator feeding the antenna. This type of connection is illustrated in Fig 2.3 for a transmitting dipole antenna (other types of antennas can also be used) [5, 90].

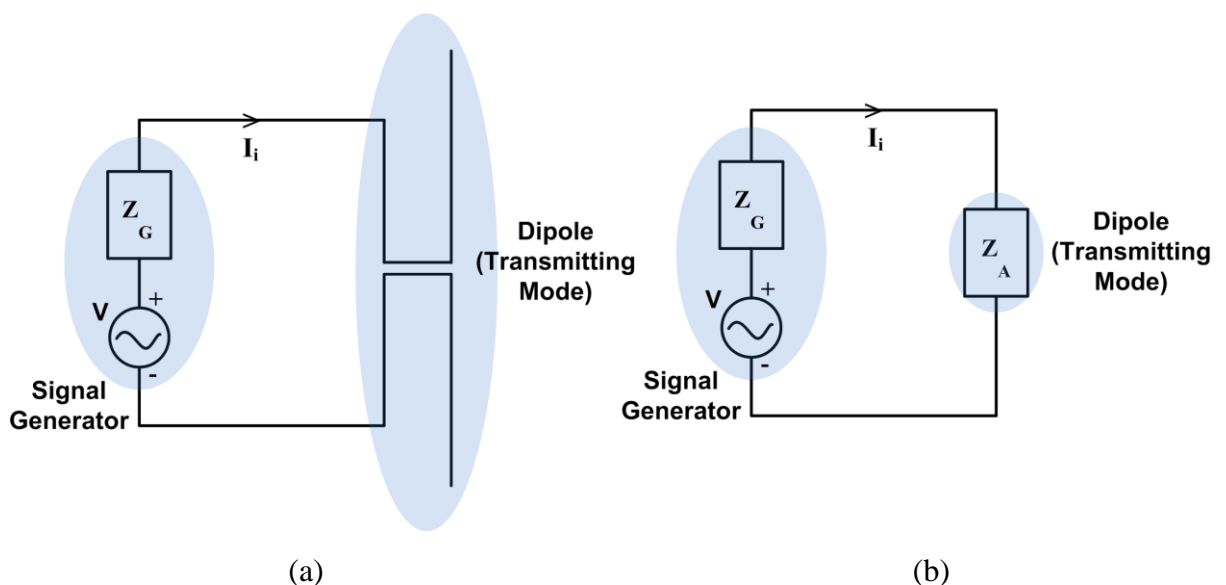


Fig. 2.3: A dipole antenna in transmitting mode (a) dipole connected to a signal generator (b) circuit equivalent.

In the connection in Fig 2.3, the transmitting dipole antenna acts as a load to the signal generator and radiates the power that is delivered to it from the generator. In this case, the input impedance of the antenna and the internal impedance of the signal generator can be given as follows:

$$Z_A = R_A + jX_A \quad (2.5)$$

$$Z_G = R_G + jX_G \quad (2.6)$$

Where,

$$R_A = R_R + R_L \quad (2.7)$$

In equation (2.7),  $R_R$  is the radiation resistance of the dipole while  $R_L$  is the loss resistance caused by the conductive loss of the antenna.

In this case, from the equivalent circuit model in Fig. 2.3(b), the current  $I_i$  flowing in the circuit can be calculated as:

$$I_i = \frac{V_G}{Z_G + Z_A} \quad (2.8)$$

As can be seen in Fig. 2.3(b), this current is also equal to the current at the input port of the dipole antenna. Following the determination of the circuit current,  $I_i$ , the total generated power and its distribution between the signal source and the antenna can be given as:

$$P_T = \frac{1}{2}|I_i|^2 R_A + \frac{1}{2}|I_i|^2 R_G \quad (2.9)$$

Equation (2.9) can also be given as:

$$P_T = P_A + P_G \quad (2.10)$$

Equations (2.9) and (2.10) demonstrate that the total generated power,  $P_T$ , is divided between the generator and the antenna due to the resistances  $R_G$  and  $R_A$ . In order to maximise the power delivered to the dipole antenna in Fig. 2.3, the input impedance of the antenna needs to be the conjugate of the internal impedance of the signal generator as follows:

$$Z_A = Z_G^* \quad (2.11)$$

Therefore,

$$R_A = R_G \quad (2.12)$$

$$X_A = -X_G \quad (2.13)$$

In this case, the power transmitted to the dipole antenna is maximum and can be calculated as:

$$P_{A_{\max}} = \frac{|V_g|^2}{4} \left[ \frac{1}{R_R + R_L} \right] \quad (2.14)$$

Although the maximum power can be transferred under the condition that the transmitting antenna has an input impedance which is the conjugate of the internal impedance of the signal generator, it is seen in equation (2.14) that only half of the generated power is transferred to the antenna while the rest half is dissipated as heat within the generator due to the internal resistance of the signal generator,  $R_G$ .

Examination of the real part of the antenna input impedance in equation (2.7) and the maximum power transferred to the antenna in equation (2.14) reveals that the power transferred to the transmitting antenna is further divided between the loss resistance and the radiation resistance, both of which determine the radiation efficiency of an antenna, which was earlier described as  $e_{cd}$  in section 2.2.1.3, and can also be given as follows:

$$e_{cd} = \frac{R_R}{R_R + R_L} \quad (2.15)$$

As can be seen in equation (2.15), increasing the radiation resistance of an antenna in comparison to the loss resistance improves the radiation efficiency.

In equation (2.15), while in ideal loss-free case ( $R_L = 0$ ), a maximum of half of the generated power is transmitted to the antenna with an input impedance conjugate of the internal impedance of the signal generator, in reality ( $R_L \neq 0$ ), the transferred power to the antenna is less than 50% of the power generated by the signal generator.

Moreover, in reality, the input impedance of a transmitting antenna is mostly not the conjugate of the internal impedance of a signal generator and therefore there is an impedance mismatch between them. For this case, the power received by the antenna can be given as:

$$P_A = P_{A_{\max}} (1 - |r_i|^2) \quad (2.16)$$

Where,  $r_i$  is the reflection coefficient of the antenna at the input. Similar to transmitting mode, for a receiving antenna whose circuit diagram is given in Fig. 2.4, half of the maximum power is delivered to the load if the antenna has a conjugate impedance matching.

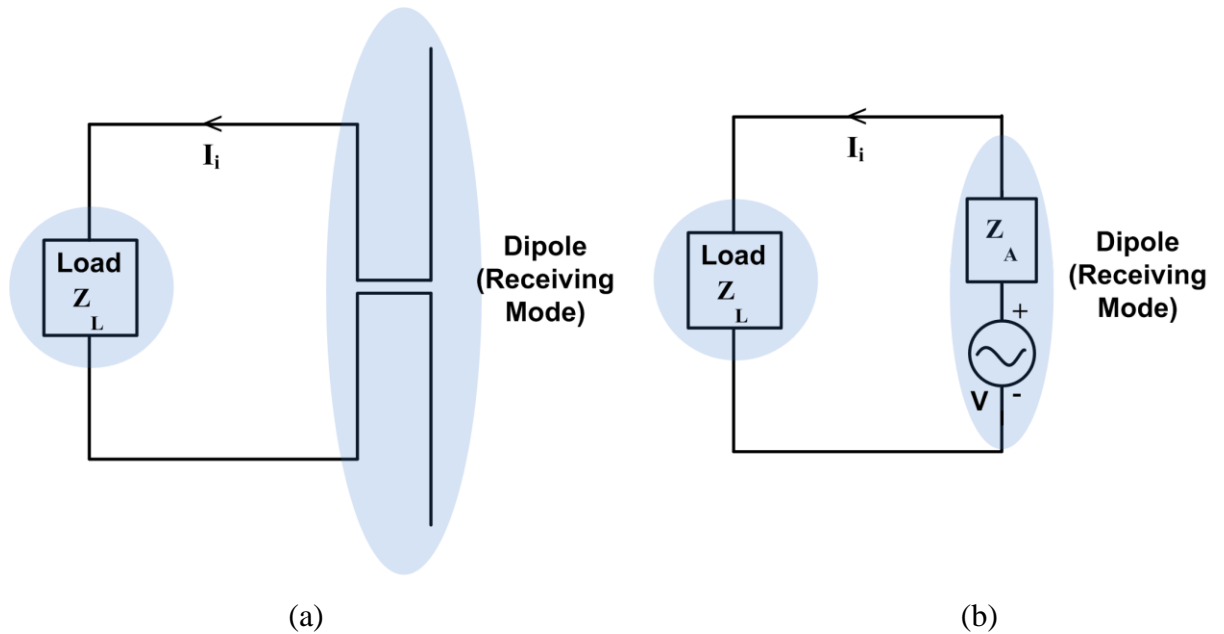


Fig. 2.4: A dipole in receiving mode (a) dipole connected to a load (b) circuit equivalent.

### 2.2.1.6 Polarisation

The polarisation of an antenna is defined as the orientation of the field vectors, mostly  $\vec{E}$  field, of the wave radiated by the antenna in the far-field region.

An antenna can have the polarisations given below:

- Linear polarisation: If the  $\vec{E}$  field vector radiated by an antenna (or  $\vec{H}$  field) have a linear orientation across a straight line at all times during the propagation as demonstrated in Fig. 2.5, the antenna is said to have linear polarisation.

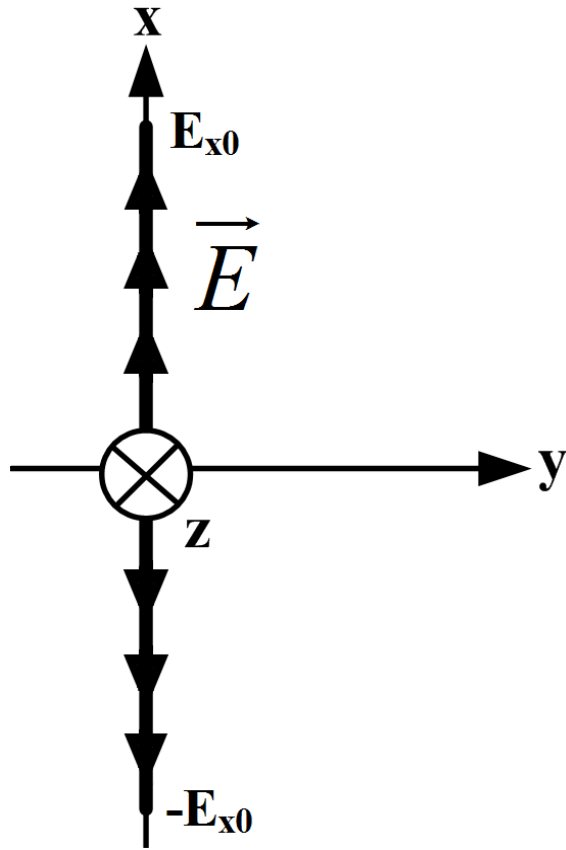


Fig. 2.5: Linear polarisation.

In order for an antenna to have linear polarisation:

- The radiated  $\vec{E}$  field should have a single component as given in equation (2.17),

$$E_x = E_{x0} \cos(\omega t - \beta_z) \quad (2.17)$$

Where,  $\beta_z$  is the phase shift of  $\vec{E}$  propagation in the direction of +z.

- Or, if the radiated  $\vec{E}$  has two components, the phase difference between these components,  $\delta$ , should be either  $0^\circ$  or  $180^\circ$  as given in equations (2.18) and (2.19) below.

$$E_x = E_{x0} \cos(\omega t - \beta_z) \quad (2.18)$$

$$E_y = E_{y0} \cos(\omega t - \beta_z + \delta) \quad (2.19)$$

Depending upon the orientation of  $\vec{E}$ , a further classification of linear polarisation can also be made as follows:

- If  $\vec{E}$  remains in the vertical axis at all times during the propagation, the antenna is said to have vertical linear polarisation.
- If  $\vec{E}$  remains in the horizontal axis at all times during the propagation, the antenna is said to have horizontal linear polarisation.
- If  $\vec{E}$  remains in the slant axis at all times during the propagation, the antenna is said to have slant linear polarisation.

This further classification of linear polarisation has a significant importance when it comes to practical applications. For example, it might seem that two identical linearly-polarised antennas can effectively communicate with each other as they both have linear polarisation. However, if these antennas are positioned at right angles with respect to each other as illustrated in Fig. 2.6, the fields radiated from these linearly-polarised antennas will also be perpendicular to each other, vertical linear polarisation and horizontal linear polarisation, which makes it impossible for them to communicate.

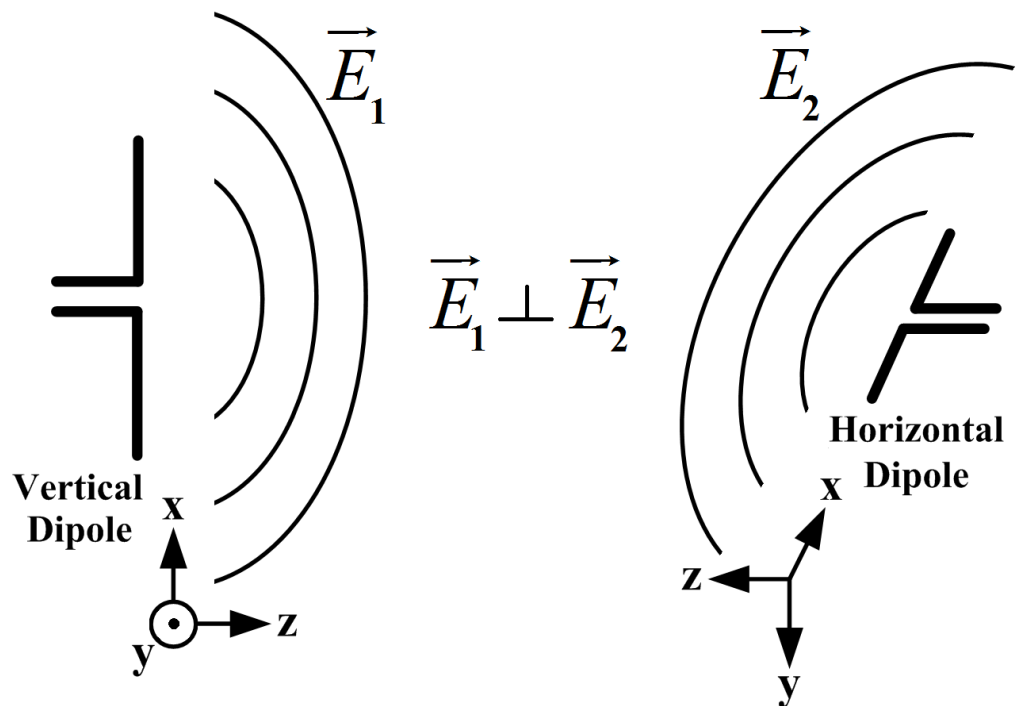


Fig. 2.6: Two linearly polarised dipole antennas oriented at right angle.

- Circular polarisation: An antenna is said to be a circularly-polarised antenna if the radiated  $\vec{E}$  field vector traces a circular figure in space during the propagation as can be seen in Fig. 2.7.

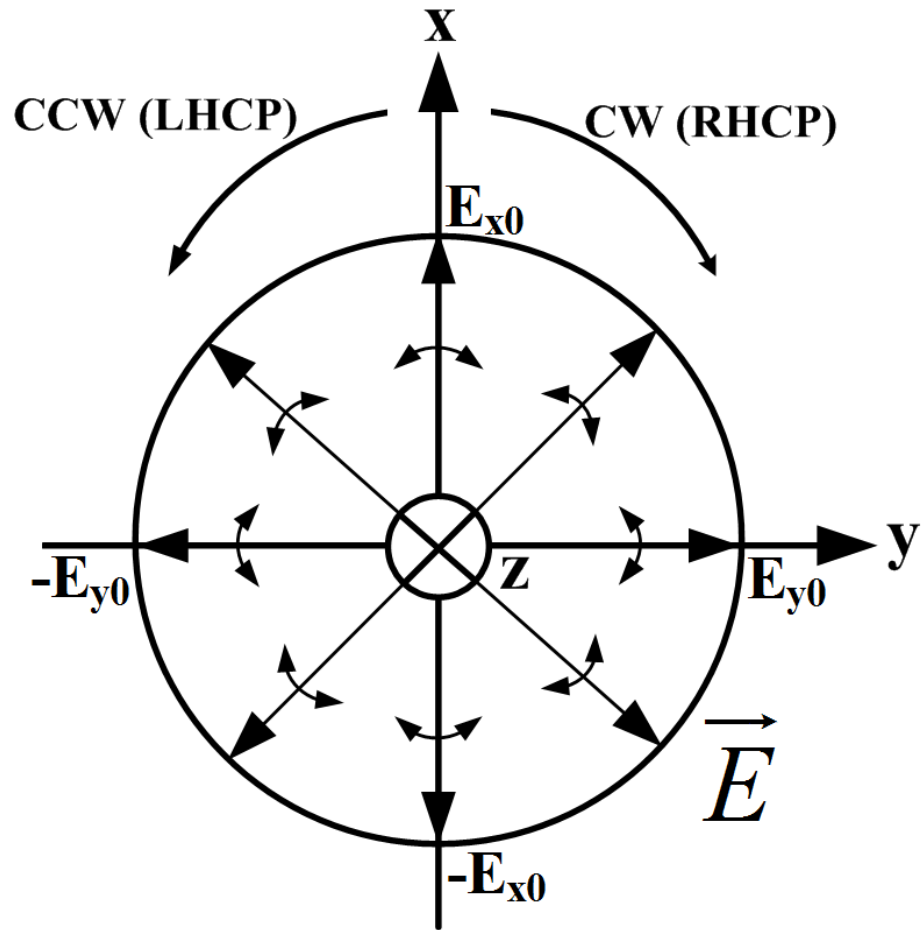


Fig. 2.7: Circular polarisation.

In order for an antenna to have circular polarisation,

- The radiated  $\vec{E}$  field should have two components, and
- These components should have the same amplitude, and
- The phase difference between these components ( $\delta$ ) should be  $\pm \frac{\pi}{2}$  as given in equations (2.20) and (2.21) below:

$$E_x = E_{x0} \cos(\omega t - \beta_z) \quad (2.20)$$

$$E_y = E_{y0} \cos(\omega t - \beta_z + \delta) \quad (2.21)$$

Where,

$$E_{x0} = E_{y0} \quad (2.22)$$

Further classification of circular polarisation can be made as follows:

- Right hand circular polarisation (RHCP): If the phase difference between the first component and the second component of the radiated  $\vec{E}$  field is  $+\frac{\pi}{2}$ , rotation in Fig. 2.7 is clockwise and the antenna is said to have right hand circular polarisation.
- Left hand circular polarisation (LHCP): If the phase difference between the first component and the second component of the radiated  $\vec{E}$  field is  $-\frac{\pi}{2}$ , rotation in Fig. 2.7 is counterclockwise and the antenna is said to have left hand circular polarisation.
- Elliptical polarisation: In general,  $\vec{E}$  radiated by an antenna traces an elliptical figure during the propagation in space as illustrated in Fig. 2.8 and therefore linear and circular polarisations can be seen as special cases of elliptical polarisation.

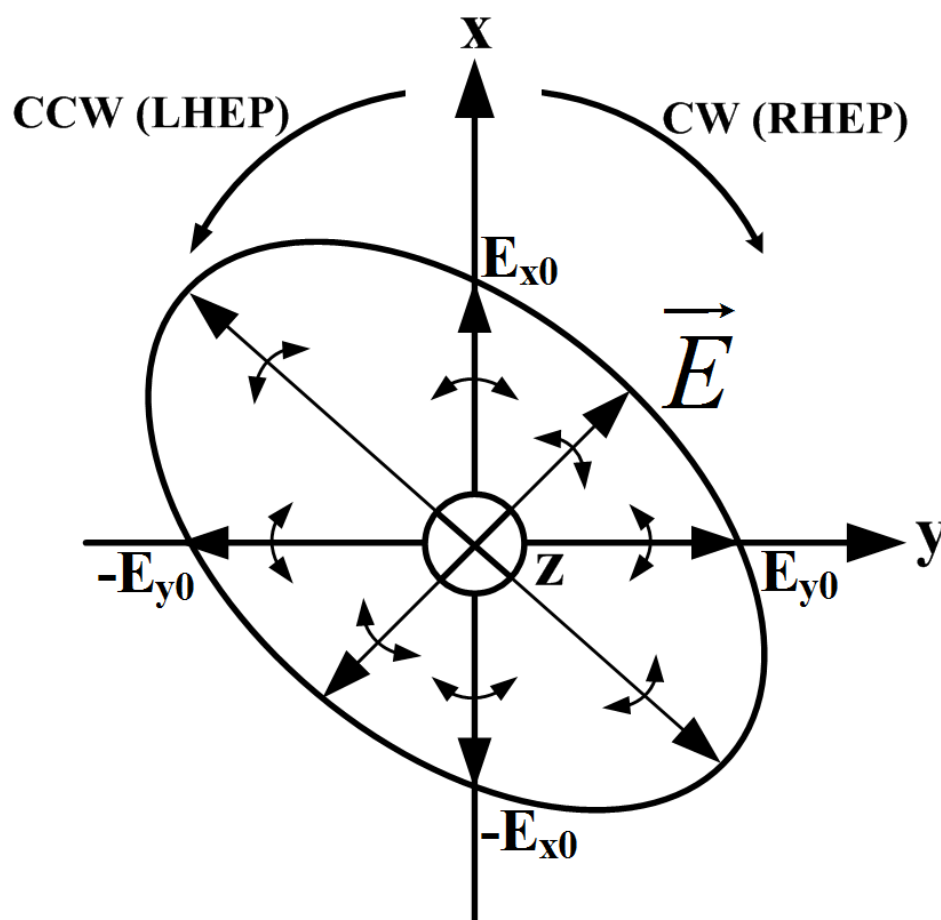


Fig. 2.8: Elliptical polarisation.

In order for an antenna to be elliptically polarised:

- The electric field vector should have two components, and
- These components should have different amplitudes, and
- The phase difference between these components ( $\delta$ ) should not be  $0^0$  or  $180^0$  as demonstrated in equations (2.23) and (2.24) below:

$$E_x = E_{x0} \cos(\omega t - \beta_z) \quad (2.23)$$

$$E_y = E_{y0} \cos(\omega t - \beta_z + \delta) \quad (2.24)$$

Where,

$$E_{x0} \neq E_{y0} \quad (2.25)$$

Similar to circular-polarisation, further classification of elliptical polarisation can be made as follows:

- Right hand elliptical polarisation (RHEP): If the phase difference between the first component and the second component of the radiated  $\vec{E}$  field is positive, rotation in Fig. 2.8 is clockwise and the antenna is said to have right hand elliptical polarisation.
- Left hand elliptical polarisation (LHEP): If the phase difference between the first component and the second component of the radiated  $\vec{E}$  field is negative, rotation in Fig. 2.8 is counterclockwise and the antenna is said to have left hand elliptical polarisation.

## 2.2.2 Photovoltaically Integrated Antennas

The photovoltaic integration of planar microwave antennas is the subject of the work performed in this thesis. This is due to the advantage of these antennas having planar and low-profile geometries, making them a suitable candidate to be employed in mobile, WLAN and WiMAX systems. In view of this, in this thesis, rigorous research is carried out on the integration of solar cells with the microwave antenna types given below:

- Microstrip patch antennas (also includes printed monopole antennas),
- Planar inverted-F antennas (PIFAs).

Printed monopole antennas shares the same background as microstrip patch antennas, which also form the basis of PIFAs. In view of this, a detailed examination of the theory of microstrip patch antennas and PIFAs is carried out in the following sections.

### **2.2.2.1 Microstrip Patch Antennas**

As indicated in section 1.1, the concept of microstrip patch antennas dates back to 1953 when G. A. Deshamps published a paper on an array of printed flared planar horns fed through a microstrip feed network [93] followed by a patent by H. Gutton and G. Baissinot in 1955 [94]. However, the practical application of microstrip patch antennas would need to wait until 1970s when R. E. Munson published two journal papers on microstrip phased array antennas [95, 96] followed by two conference papers [97, 98]. Since then, intensive research has been carried out on microstrip patch antennas due to their many advantages some of which can be given as follows [99-104]:

- Conformable to planar and non-planar surfaces,
- Low weight and low-profile structure making them a suitable candidate to be employed in commercial and military applications,
- Ease of fabrication and low fabrication cost due to modern printed circuit technology,
- Capability of being integrated with circuit elements in microwave integrated circuits (MIC),
- Capability of achieving various polarisations, such as linear polarisation, circular polarisation and dual-polarisation,
- Capability of achieving multiband and wideband (exceeding 100% reported in the literature [105]) resonance characteristics.

In its simplest form, a microstrip patch antenna consists of a radiating patch printed on a dielectric substrate with a ground plane on the backside as demonstrated in Fig. 2.9.

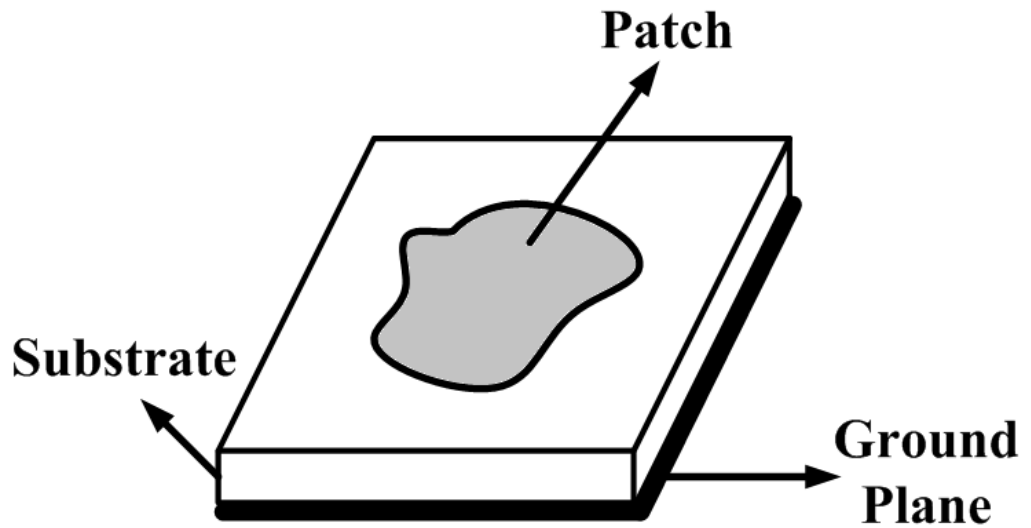


Fig. 2.9: A microstrip patch antenna with an arbitrary shaped radiating element.

In Fig. 2.9, the demonstrated microstrip radiating patch has an arbitrary shape. Although this is possible in principle, when it comes to practical applications, a microstrip patch in a certain shape, such as rectangular, square, dipole, circular, triangular, sectoral, circular ring and square ring, is used as demonstrated in Fig. 2.10.

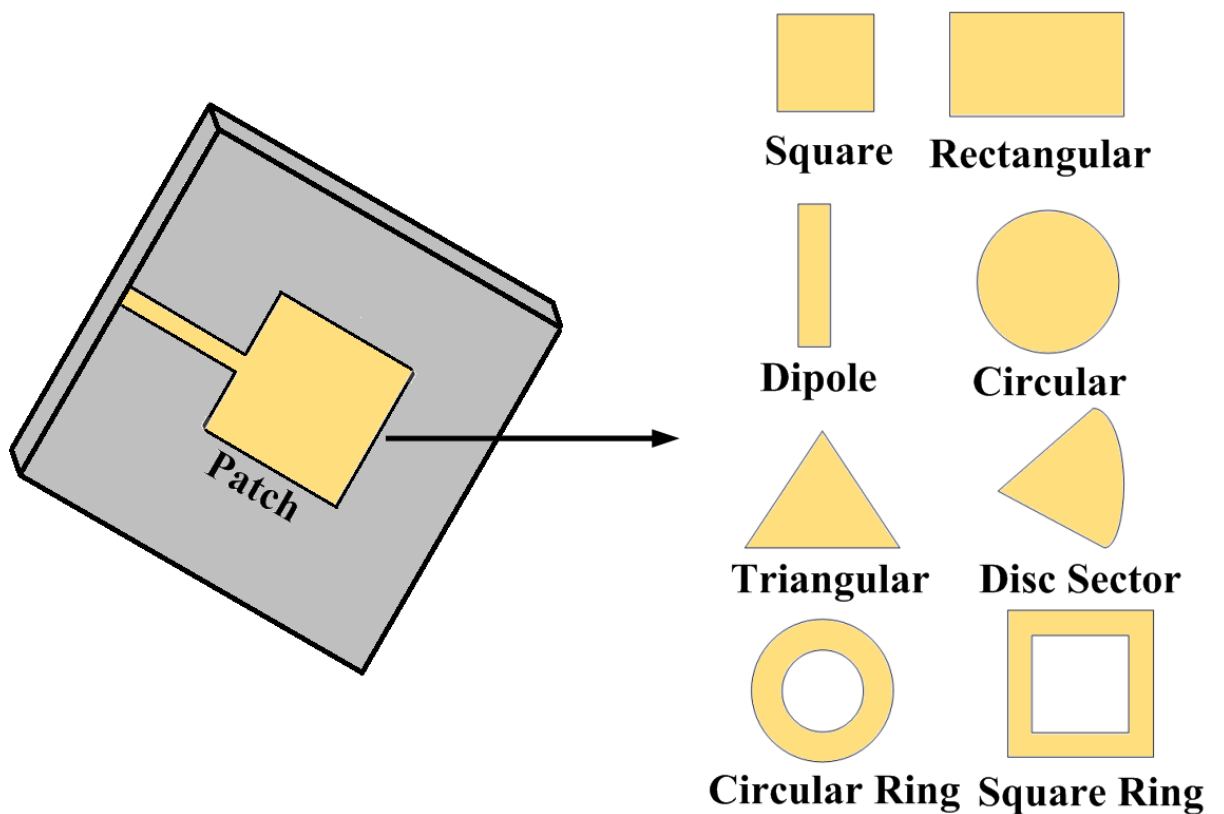


Fig. 2.10: Different shapes of microstrip radiating patch elements.

Among these patch shapes, square, rectangular and circular patches are the most commonly used types of patches due to their lower cross-polarisation levels and superior radiation characteristics in comparison to other types of patches [5]. The dielectric substrate has a typical thickness in the range of  $0.003\lambda_0 - 0.05\lambda_0$ , where  $\lambda_0$  is the wavelength in free space, and a dielectric constant in the range of 2.2 – 12. Although the microstrip patch antenna demonstrated in Fig. 2.10 has a microstrip line feed, it is not the only feed method used to feed microstrip patch antennas. In general, feed methods for microstrip patch antennas can be given as follows (detailed examination of these feed methods will be given in section 2.2.2.1.1):

- Microstrip line,
- Coaxial probe,
- Aperture-coupled,
- Proximity-coupled.

The drawbacks of microstrip patch antennas can be given as follows:

- Narrow impedance bandwidth, which is typically less than 5%. However, as mentioned earlier, this can be improved by using various impedance bandwidth widening techniques which have been the major thrust of the research conducted on microstrip patch antennas in the literature. These techniques include:
  - Increasing the thickness of the substrate [86, 87]. However, increasing the thickness of the substrate too much results in surface wave excitation which reduces the radiation efficiency of the patch antenna. This is due to the fact that the introduced surface waves propagating along the substrate surface extract power from the radiation and results in unwanted radiation at discontinuous points along the surface wave path, such as bends and corners.
  - Using capacitive elements and slot loading [59-83]. This technique is especially useful if a coaxial probe feed method is used. For this feed method, increasing the thickness of the substrate to widen the impedance bandwidth of a patch also increases the probe length and therefore increases the probe inductance. Loading the patch with capacitive elements and slots enables the increase in the probe inductance to be compensated.

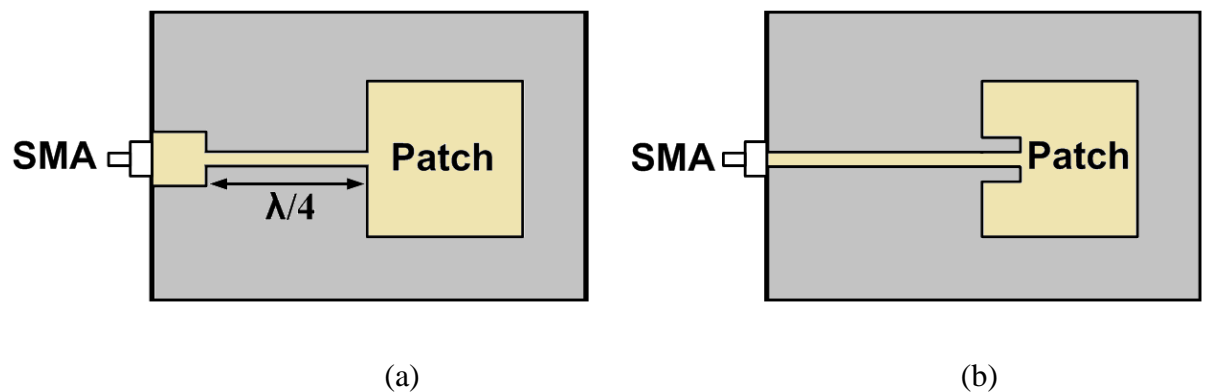
- Using suspended patch geometry [106-126]. In addition to increasing the thickness of the substrate, this technique decreases the effective substrate dielectric constant due to the presence of an air gap with a unity dielectric constant resulting in an increase in the impedance bandwidth. However, this technique results in an increased antenna size and therefore is not desirable for MIC integration where high dielectric constant and small substrate thickness is required.
- Using stacked elements [127-148].
- Capability of handling relatively low RF power due to the small thickness of the dielectric between the radiating patch and the ground plane.
- Ohmic losses and lower radiation efficiency in comparison to other types of antennas.

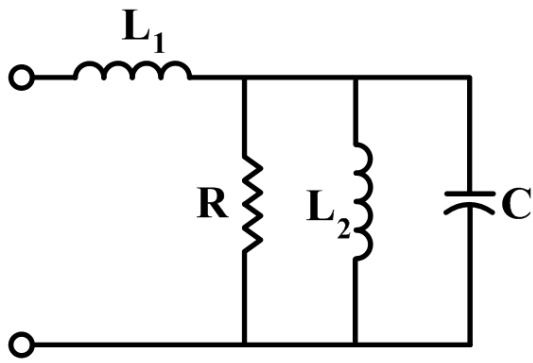
### 2.2.2.1.1 Feed Methods

#### 2.2.2.1.1.1 Microstrip Line Feed

A microstrip patch antenna fed through a microstrip line feed is demonstrated in Fig. 2.11(a) and Fig. 2.11(b) together with the equivalent circuit of the microstrip line feed given in Fig. 2.11(c). As illustrated in Fig. 2.11(a) and Fig. 2.11(b), two types of microstrip feed lines can be used for microstrip line feed method:

- Microstrip feed line consisting of a quarter-wavelength transmission line matching the impedance of the SMA port,  $50\Omega$ , to the input impedance of the microstrip patch at the edge.
- Inset microstrip feed line extended into the patch in order to find the feeding point with optimum input impedance.





(c)

Fig. 2.11: Microstrip line feed (a) patch fed by a feed line consisting of a  $\lambda/4$  line (b) patch fed by an inset feed line (c) Equivalent circuit of microstrip line feed [5].

The advantages and disadvantages of the microstrip line feed method are summarised in Table. 2.1.

Table 2.1: Advantages and disadvantages of the microstrip line feed method.

Advantages	Disadvantages
<ul style="list-style-type: none"> <li>• Ease of fabrication,</li> <li>• Simple to design and perform the impedance matching.</li> </ul>	<ul style="list-style-type: none"> <li>• High feed radiation especially for thick substrate,</li> <li>• Narrow bandwidth,</li> <li>• Introduced asymmetry in the overall patch design (increasing cross-polarisation).</li> </ul>

#### 2.2.2.1.1.2 Coaxial Probe Feed

A microstrip patch antenna fed through a coaxial probe feed is demonstrated in Fig. 2.12(a) and Fig. 2.12(b) together with the equivalent circuit of the coaxial probe feed given in Fig. 2.12(c).

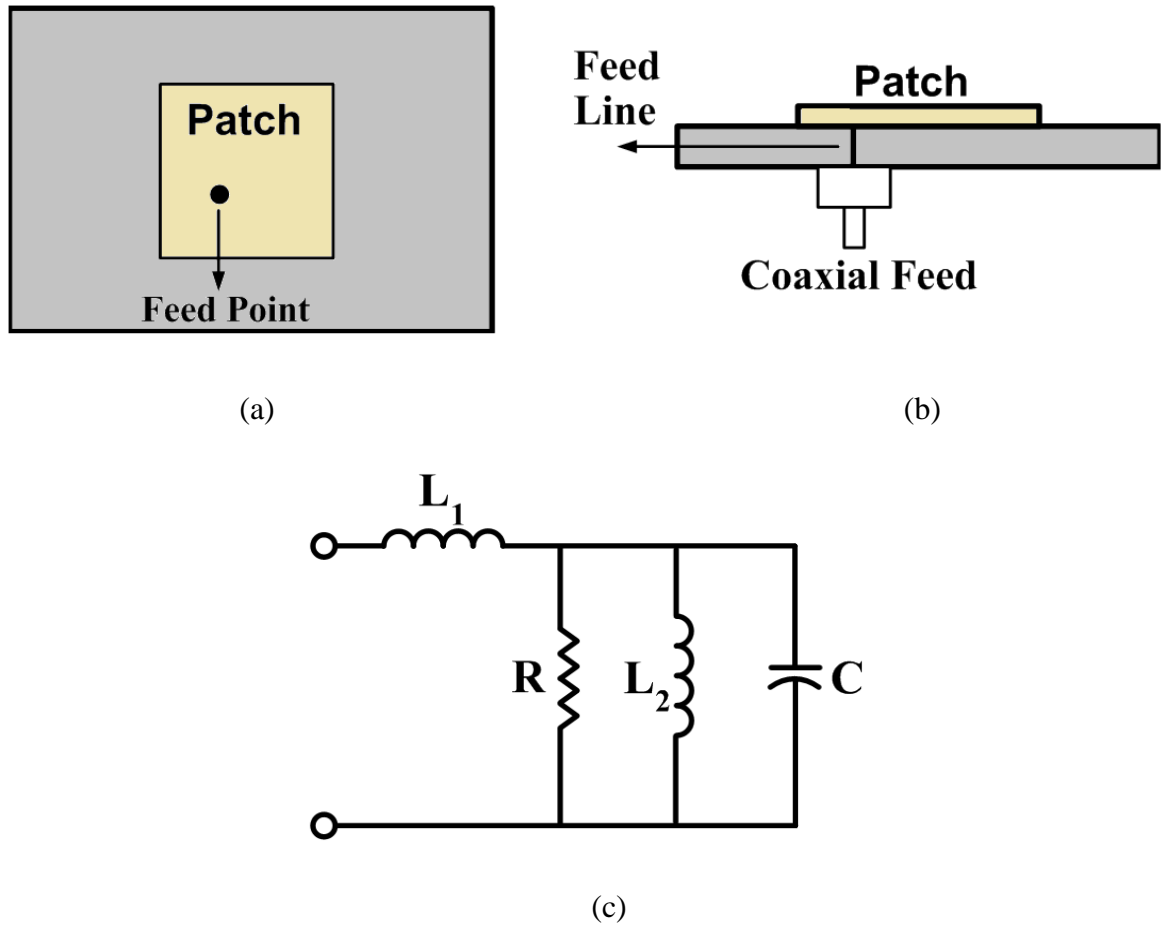


Fig. 2.12: Coaxial probe feed (a) top view (b) side view (c) equivalent circuit of coaxial probe feed [5].

As can be seen in Fig. 2.12(a) and Fig. 2.12(b), in this feed method, the antenna is fed through a coaxial feed line whose inner conductor is attached to the patch at the feeding point providing an optimum input patch impedance.

The advantages and disadvantages of the coaxial probe feed method are summarised in Table 2.2.

Table 2.2: Advantages and disadvantages of the coaxial probe feed method.

Advantages	Disadvantages
<ul style="list-style-type: none"> <li>• Ease of fabrication,</li> <li>• Simple to perform the impedance matching (simply by adjusting the position of the probe across the patch surface),</li> <li>• Low spurious radiation.</li> </ul>	<ul style="list-style-type: none"> <li>• Increased feed inductance especially for thick substrates,</li> <li>• Fabrication (soldering is required),</li> <li>• Narrow bandwidth,</li> <li>• Introduced asymmetry in the overall patch design (increasing cross-polarisation).</li> </ul>

### 2.2.2.1.1.3 Aperture-Coupled Feed

A microstrip patch antenna fed through an aperture-coupled feed is demonstrated in Fig. 2.13(a) and Fig. 2.13(b) together with the equivalent circuit of the aperture-coupled feed given in Fig. 2.13(c).

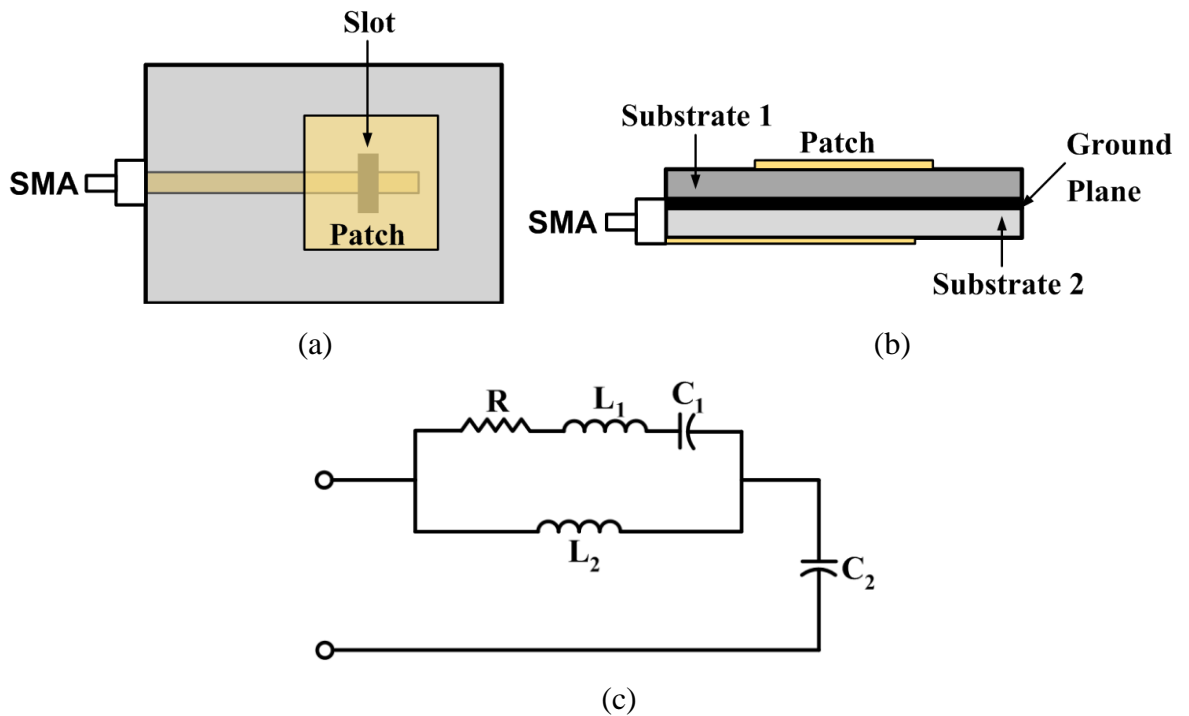


Fig. 2.13: Aperture-coupled feed (a) top view (b) side view (c) equivalent circuit of aperture-coupled feed [5].

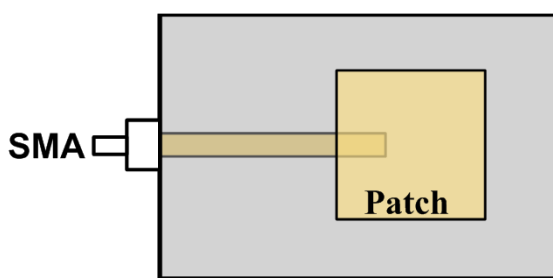
As can be seen in Fig. 2.13(b), the aperture-coupled feed method involves the use of two substrates separated by a ground plane in between. While a microstrip feed line is printed on the backside of the rear substrate, the patch is printed on the top surface of the front substrate. The rear microstrip feed line is aperture-coupled to the front microstrip patch through a slot cut in the ground plane. The advantages and disadvantages of the aperture-coupled feed method are summarised in Table 2.3.

Table 2.3: Advantages and disadvantages of the aperture-coupled feed method.

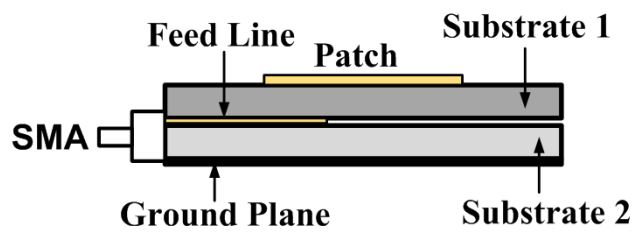
Advantages	Disadvantages
<ul style="list-style-type: none"> <li>• Low spurious radiation,</li> <li>• Lower cross-polarisation in principle planes in comparison to direct feed methods (microstrip line feed and coaxial probe feed methods).</li> </ul>	<ul style="list-style-type: none"> <li>• Registration and fabrication (multi-layer fabrication is required),</li> <li>• Narrow band,</li> <li>• Backlobe radiation,</li> <li>• Not as low profile as direct feed methods.</li> </ul>

#### 2.2.2.1.1.4 Proximity-Coupled Feed

A microstrip patch antenna fed through a proximity-coupled feed is demonstrated in Fig. 2.14(a) and Fig. 2.14(b) together with the equivalent circuit of the proximity-coupled feed given in Fig. 2.14(c).



(a)



(b)

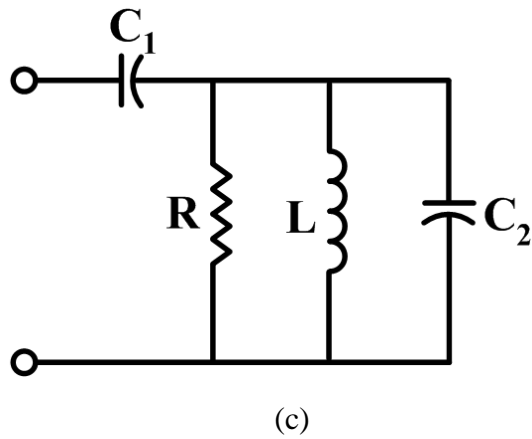


Fig. 2.14: Proximity-coupled feed (a) top view (b) side view (c) equivalent circuit of proximity-coupled feed [5].

Similar to the aperture-coupled feed method, proximity-coupled feed also consists of two substrates. Whilst the ground plane is printed on the backside of the rear substrate, the microstrip patch is printed on the top surface of the front substrate with the microstrip feed line on the backside. Therefore, as can be seen in Fig. 2.14(b), the microstrip feed line is between the front and rear substrates. The advantages and disadvantages of the proximity-coupled feed method are summarised in Table 2.4.

Table 2.4: Advantages and disadvantages of the proximity-coupled feed method.

Advantages	Disadvantages
<ul style="list-style-type: none"> <li>• Large bandwidth in comparison to direct feed methods</li> <li>• Low spurious radiation</li> <li>• Lower cross-polarisation in comparison to direct feed methods due to the symmetry</li> </ul>	<ul style="list-style-type: none"> <li>• Registration and fabrication (multi-layer fabrication is required)</li> <li>• Not as low profile as direct feed methods</li> </ul>

### 2.2.2.1.2 Analysis Methods

In general, two types of methods, analytical methods and numerical methods, can be used to analyse microstrip patch antennas.

Analytical methods can be given as follows:

- Transmission line model,
- Cavity model.

Numerical methods, on the other hand, can be given as:

- Method of moments (MoM),
- Finite difference time domain (FDTD),
- Finite element method (FEM).

Detailed information on these numerical methods can be found in [149-151].

### 2.2.2.1.2.1 Transmission Line Method

The transmission line method can be seen as the simplest method to analyse a microstrip patch antenna. It provides a physical insight on how microstrip patch antennas work and has a significant importance in determining the design parameters of these antennas. However, it provides less accurate results in comparison to the cavity method, which will be explained in section 2.2.2.1.2.2.

The transmission line method suggests that a microstrip patch antenna can be seen as an array of two radiating narrow slots separated by a low-characteristic impedance (selected to be  $Z_A$  in Fig. 2.15) transmission line in between as demonstrated in Fig. 2.15.

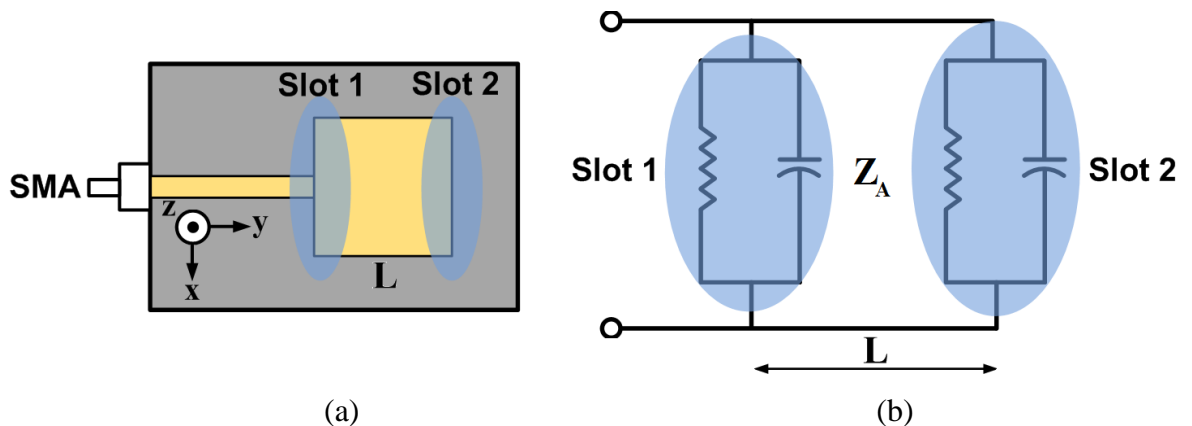


Fig. 2.15: Transmission line method (a) patch antenna with radiating slots (b) equivalent circuit model of the radiating slots.

As the radiating microstrip patch element is not infinite in size, the  $\vec{E}$  field fringes at the edges of the patch resulting in fringing fields which are responsible for the radiation as illustrated in Fig. 2.16.

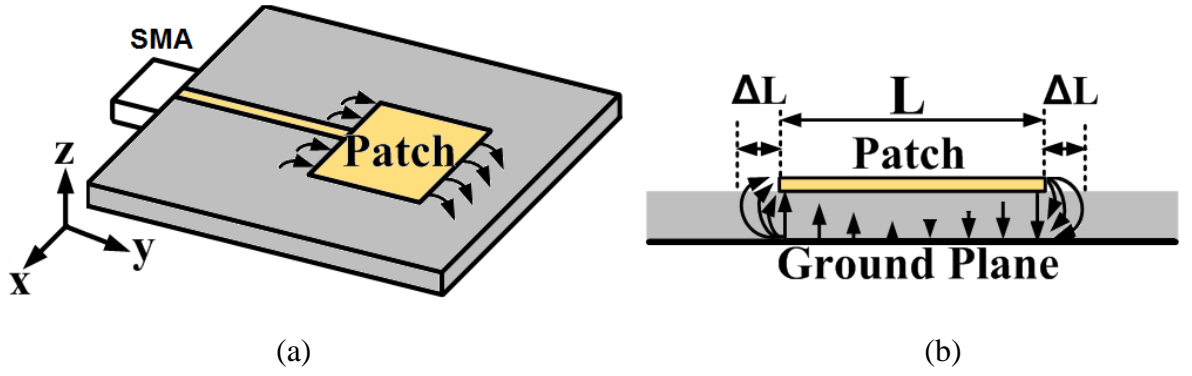


Fig. 2.16:  $\vec{E}$  field distribution along the length of the patch (a) patch antenna with radiating slots (b) cross-section along the patch length.

As can be seen in Fig. 2.16, at the radiating patch edges corresponding to the radiating slots given in Fig. 2.15, while the E-field components in the direction perpendicular to the patch plane (z-axis) are out of phase and therefore cancel each other, the E-field components in the axis parallel to the patch length (y-axis) are in phase and therefore contribute to the radiation from the antenna in the far-field.

An important factor that needs to be taken into consideration is the effect of the fringing fields on the antenna design procedure. To this end, if Fig. 2.16(b) is investigated in detail, it can be seen that due to the presence of the fringing fields at the patch edges, the electrical length of the patch is different from the physical length of the patch. This difference, which is given as  $2\Delta L$  in Fig. 2.16(b), needs to be calculated in order for a microstrip patch antenna required to operate at a desired frequency band to be correctly designed in a full-wave electromagnetic simulation program before the fabrication.

For this reason, the equation given below is used to calculate the length of a microstrip patch [5].

$$L = \frac{1}{2f_r \sqrt{\epsilon_{reff}} \sqrt{\mu_0 \epsilon_0}} - 2\Delta L \quad (2.26)$$

In equation (2.26), while  $f_r$  is the desired operational resonance frequency of a microstrip patch antenna,  $\epsilon_{reff}$  represents the effective dielectric constant and therefore is required to be obtained before calculating the effective length of a patch. Detailed examination of Fig. 2.17 given below reveals the reason why such a parameter called effective dielectric constant exists in addition to the dielectric constant of the substrate.

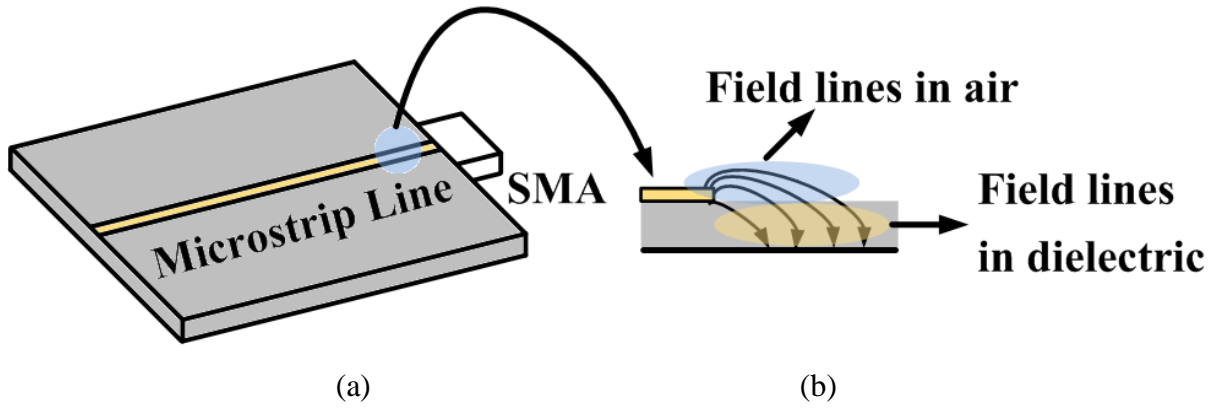


Fig. 2.17: Fringing fields from a microstrip line (a) microstrip line (b) fringing field lines in air and dielectric.

In Fig. 2.17, due to the fringing that the fields along the edges of the microstrip line undergo, they propagate through two separate mediums with two separate dielectric constants. These mediums are,

- Air with a unity dielectric constant,
- Dielectric substrate with a dielectric constant of  $\epsilon_r$ .

Therefore, an effective dielectric constant arises in addition to the dielectric constant of the dielectric substrate and can be given as:

$$\epsilon_{\text{reff}} = \frac{\epsilon_r + 1}{2} + \frac{\epsilon_r - 1}{2} \left[ 1 + 12 \frac{h}{W} \right]^{-1/2} \quad \text{for } W/h > 1 \quad (2.27)$$

In Equation (2.27),  $W$  is the width of the microstrip transmission line while  $h$  denotes the height of the dielectric substrate. Equation (2.27) gives accurate results for low frequencies whereas for higher frequencies the effective dielectric constant significantly approximates to the dielectric constant of the substrate due to the distribution of the field lines being mostly focused in the substrate rather than air. It can be concluded from equation (2.27) that the effective dielectric constant always remains in the range of:

$$1 < \epsilon_{\text{reff}} < \epsilon_r \quad (2.28)$$

Following the determination of  $L$  and  $\epsilon_{\text{reff}}$ , the last parameter in the design process of a microstrip patch antenna, the width of the radiating patch element,  $W$ , can be calculated as follows:

$$W = \frac{1}{2f_r \sqrt{\mu_0 \epsilon_0}} \sqrt{\frac{2}{\epsilon_r + 1}} = \frac{c}{2f_r} \sqrt{\frac{2}{\epsilon_r + 1}} \quad (2.29)$$

### 2.2.2.1.2.2 Cavity Method

The second analytical method to analyse a microstrip patch antenna is the cavity method, which provides more accurate results in comparison to the transmission line method described in the previous section but is more difficult to apply.

A careful examination of a conventional microstrip patch antenna geometry, such as the geometry given in Fig. 2.16, reveals that the patch structure can be treated as a dielectric-loaded electromagnetic resonator (cavity). An ideal conventional cavity consists of perfectly electric conducting (PEC) walls on front and rear surfaces together with PEC side walls as demonstrated in Fig. 2.18.

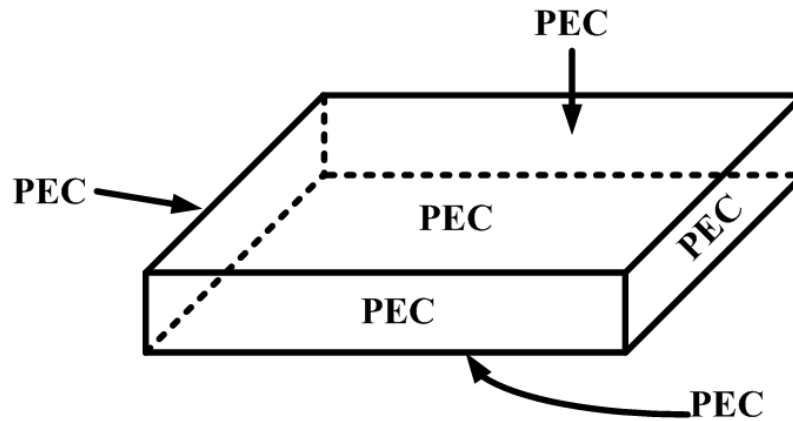


Fig. 2.18: PEC walls of a conventional cavity.

Therefore, the fields within the cavity can be obtained by applying Helmholtz's homogeneous wave equation under the boundary condition that the tangential component of the electric field on the PEC front, rear and side walls is equal to zero ( $E_t = 0$ ).

For a patch antenna, however, the conductive side walls do not exist whereas the electric conductive surfaces on top, which is the radiating patch element, and at the bottom, which is the ground plane, exist as demonstrated in Fig. 2.19.

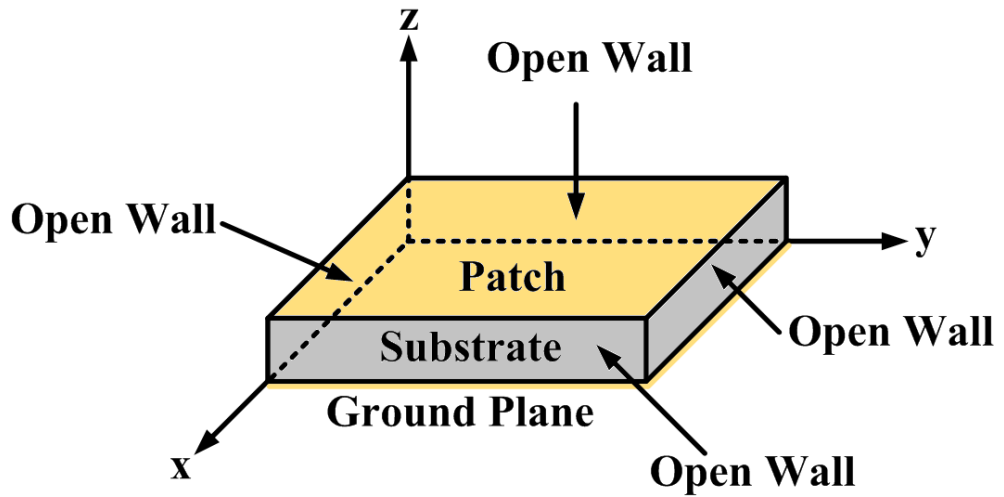


Fig. 2.19: Cavity description of a patch antenna.

As can be seen in Fig. 2.19, the side walls of the patch are open to space which leads to radiation into free space. In order to determine the radiated fields from the open side walls into free space, the fields within the cavity need to be obtained, which can be achieved by treating the patch as a special kind of cavity consisting of two PEC walls on front and rear surfaces representing the radiating patch element and the ground plane, respectively, and four perfectly magnetic conducting (PMC) walls surrounding the cavity as illustrated in Fig. 2.20. This assumption can be made given the fact that the substrate thickness is relatively small in comparison to the wavelength ( $h \ll \lambda$ ) resulting in the field distribution along the height of the cavity being almost constant.

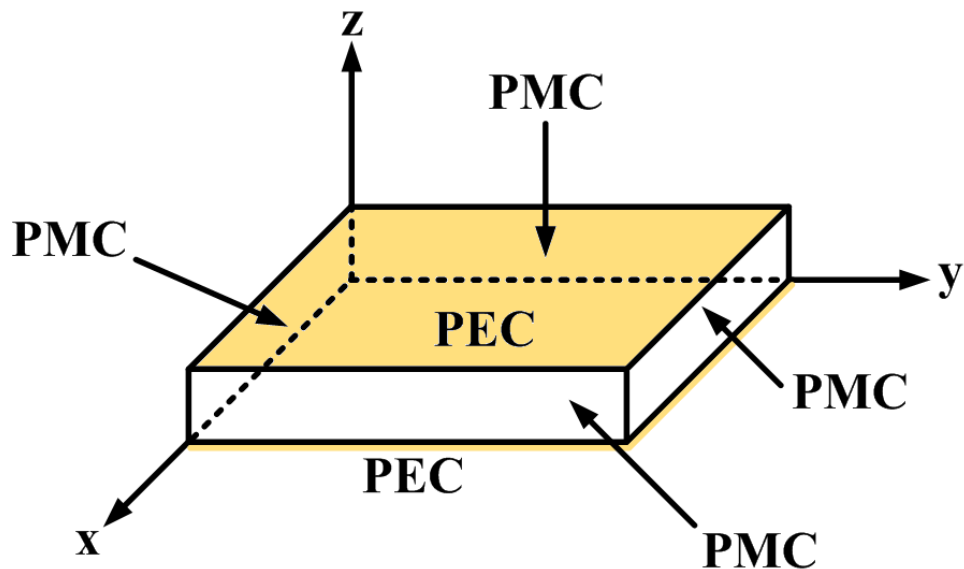


Fig. 2.20: Cavity description of a patch antenna with PEC and PMC walls.

In Fig. 2.20, while an electric current distribution, which will be represented as  $\vec{J}_s$  later, exists, the open side walls of the patch act as an open-circuit element with  $\vec{J}_s = 0$  making them possible to be modelled as PMC walls with magnetic current distribution  $\vec{J}_m$  (this is an assumption as in reality PMC walls do not exist from a physical point of view. However, this assumption makes the radiated field from a patch antenna in the far-field region simpler to analytically calculate due to the field equivalence principle as briefly mentioned at the end of this section. For more details about the principle, see [90]). In this case,

- Along PEC surfaces, tangential component of  $\vec{E}$  ( $E_t$ ) is equal to zero ( $E_t = 0$ ),
- Along PMC surfaces (side walls), tangential component of  $\vec{H}$  ( $H_t$ ) is equal to zero ( $H_t = 0$ ).

Due to the small thickness of the substrate, it is assumed that  $\vec{E}$  field in the direction of propagation inside the cavity (corresponding to TM propagation) can be accepted constant along the height of the substrate and therefore can be expressed as follows:

$$\vec{E} = E_z \vec{a}_z \quad (2.30)$$

Due to the 2D planar geometry of the patch antenna,  $\vec{E}$  inside the cavity should satisfy the 2D homogeneous wave equation within the cavity as illustrated in Fig. 2.21 and given in equation (2.31):

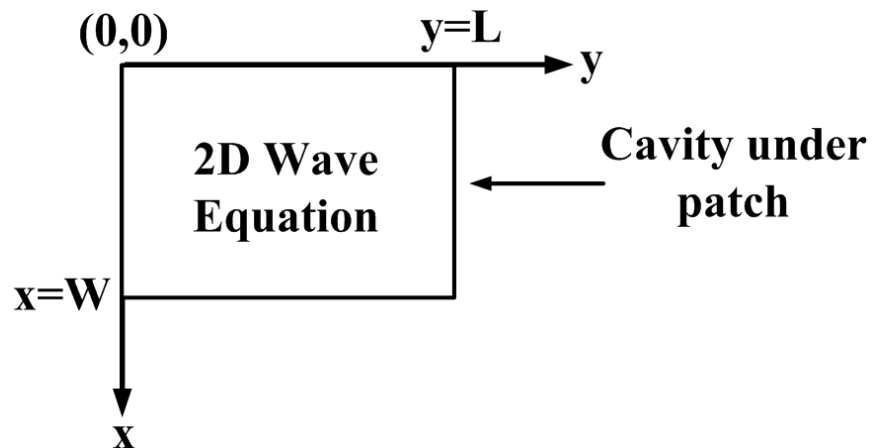


Fig. 2.21: Cavity under patch with boundaries for homogeneous 2D wave equation.

$$\nabla^2 \vec{E} + k_{m,n}^2 \vec{E} = 0 \quad (2.31)$$

From equation (2.31),

$$\frac{\partial^2 E_z}{\partial x^2} + \frac{\partial^2 E_z}{\partial y^2} + k_{m,n}^2 E_z = 0 \quad (2.32)$$

In equations (2.31) and (2.32),

$$k_{m,n}^2 = \left(\frac{m\pi}{L}\right)^2 + \left(\frac{n\pi}{W}\right)^2 \quad (2.33)$$

Along the PMC walls in Fig. 2.21:

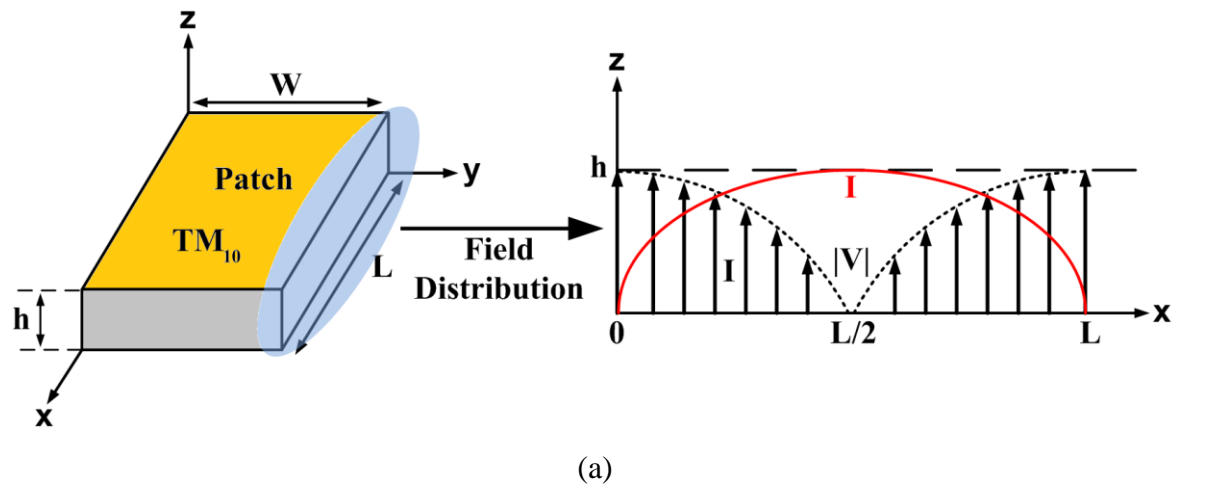
$$\frac{\partial E_z}{\partial x} = 0 \quad (2.34)$$

$$\frac{\partial E_z}{\partial y} = 0 \quad (2.35)$$

Solution of equation (2.32) under the boundary conditions given above leads to the Eigenfunctions given below:

$$\psi = k_{m,n} \cos\left(\frac{m\pi x}{L}\right) \cos\left(\frac{n\pi y}{W}\right), \quad m, n = 0, 1, 2, 3, \dots \quad (2.36)$$

From equation (2.36),  $TM_{m0}$  field distributions across the length of the patch (along the  $x$ -axis) can be obtained as illustrated in Fig. 2.22.



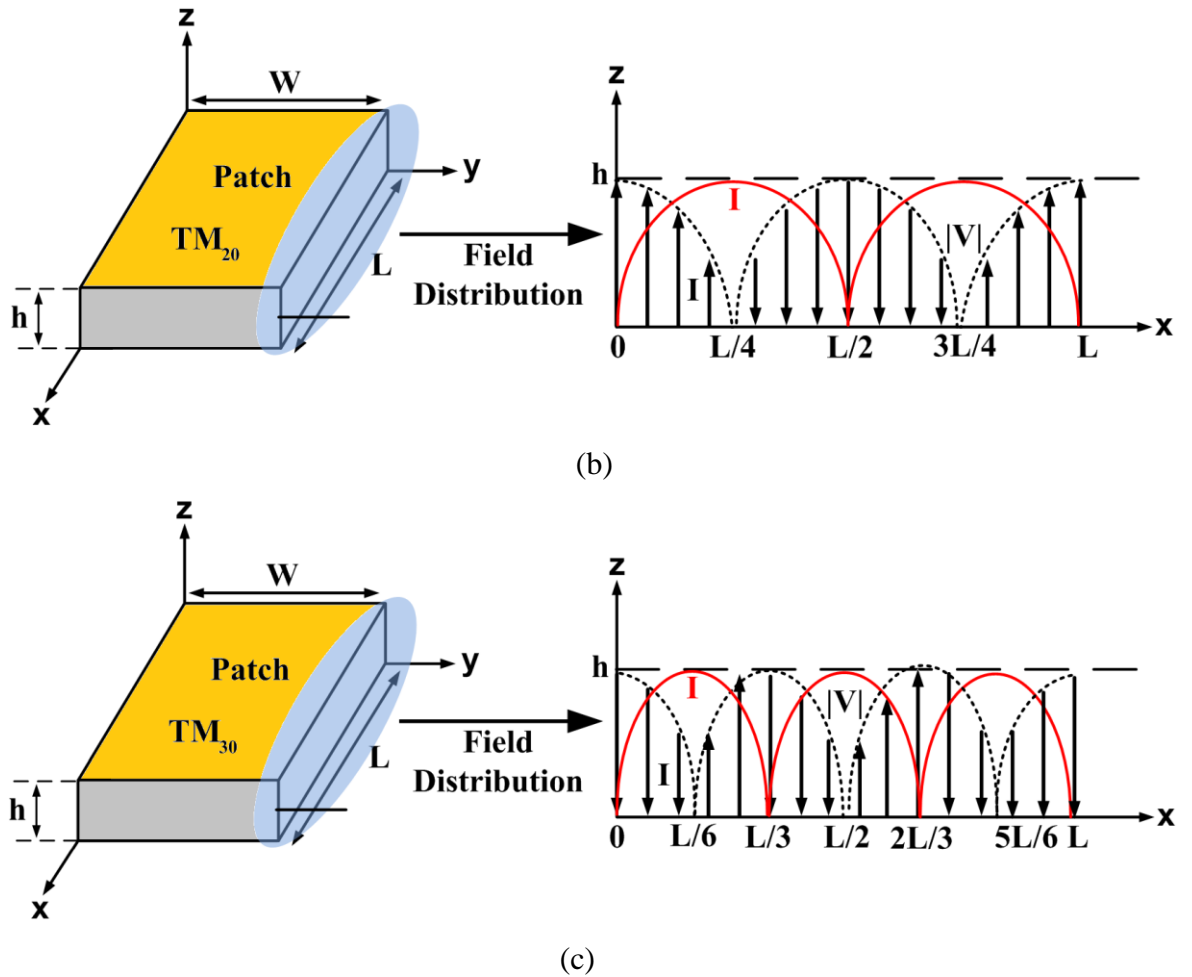


Fig. 2.22: Field, voltage and current distributions along the length of the patch (a)  $TM_{10}$  (b)  $TM_{20}$  (c)  $TM_{30}$ .

The field distributions demonstrated in Fig. 2.22 are for  $TM_{m0}$  ( $m=1,2,3$  and  $n=0$  in equation (2.36)) modes and the field distribution across the width of the patch (along the  $y$ -axis) remains constant and therefore is not illustrated. For  $TM_{0n}$  modes, however, the patch antenna should present the field distributions given in Fig. 2.22 along the width of the patch (in the  $x$ -axis in Fig. 2.22) whilst the field distribution along the length of the patch (in the  $y$ -axis) should remain constant.

The demonstrated field distributions in Fig. 2.22 also reveal some information regarding the input impedance behaviour of a microstrip patch antenna. For the fundamental propagation mode,  $TM_{10}$  or  $TM_{01}$ , the current distribution peaks in the centre of the patch and is equal to zero at the open-circuit edges. The voltage distribution, on the other hand, peaks at the edges of the patch and is equal to zero at the patch centre demonstrating a  $90^\circ$  phase difference in comparison to the current distribution as illustrated in Fig. 2.23.

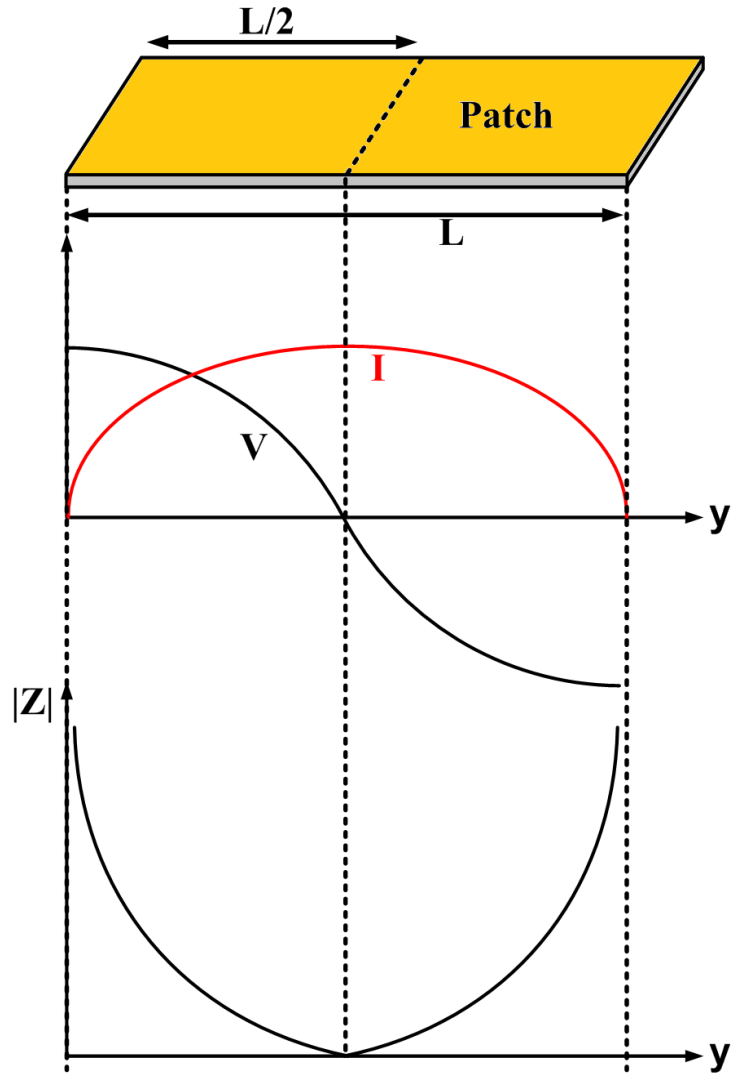


Fig. 2.23: Voltage and current distribution with the impedance curve along the patch for fundamental ( $TM_{10}$ ) mode.

The patch impedance at a selected point on the patch surface is:

$$Z = \frac{V}{I} \quad (2.37)$$

Therefore, From Fig. 2.23 and equation (2.37), it can be concluded that patch impedance is theoretically zero at the patch centre and open-circuit at the patch edges. Finding the feed point on the patch surface with an optimum input impedance is the main aim for some of the feeding methods described in section 2.2.2.1.1.

The electric ( $\vec{J}_s$ ) and magnetic ( $\vec{J}_m$ ) surface currents of a cavity consisting of PEC and PMC walls representing a microstrip patch with an ideal infinite ground plane are illustrated in Fig. 2.24.

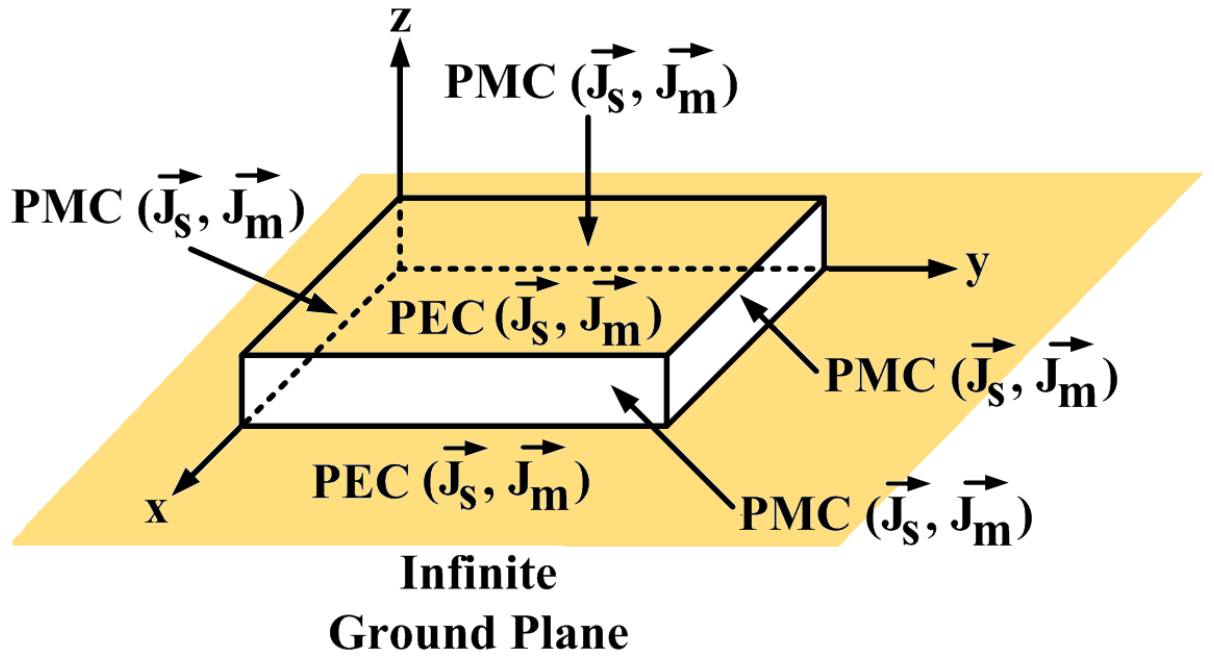


Fig. 2.24: Surface currents on PEC and PMC walls in the presence of an infinite ground plane.

In Fig. 2.24, due to the boundary conditions on PEC and PMC surfaces described earlier, the electric and magnetic surface currents can be given as follows:

- Surface currents along the PEC surface:

$$\circ J_s = \vec{n} \otimes \vec{H}_s \neq 0 \quad (2.38)$$

$$\circ J_m = -\vec{n} \otimes \vec{E}_s = 0 \quad (2.39)$$

- Surface current along the PMC walls:

$$\circ J_s = \vec{n} \otimes \vec{H}_s = 0 \quad (2.40)$$

$$\circ J_m = -\vec{n} \otimes \vec{E}_s \neq 0 \quad (2.41)$$

Due to the presence of an infinite ground plane, image theory applies and the patch without the ground plane can be modelled as illustrated in Fig. 2.25.

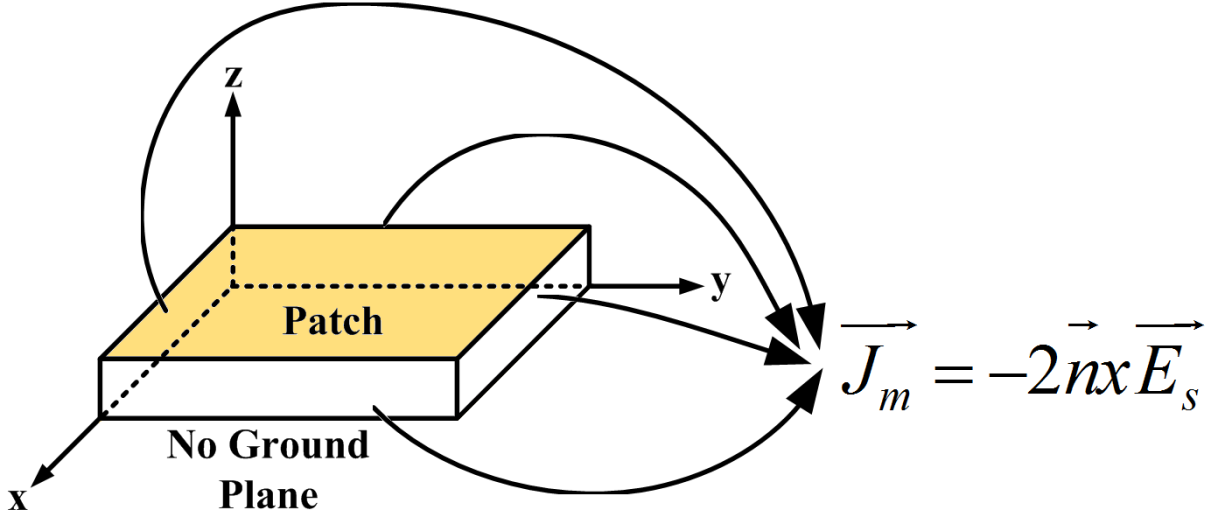


Fig. 2.25: Surface currents on the PMC walls in the absence of the ground plane (image theory).

Similar to the transmission line method, although four slots exist only two of them, which are along the length of the patch,  $L$ , contribute to the radiation whereas the fields radiated from the slots along the width of the patch are out of phase and therefore cancel each other in the far-field region.

Following the determination of the magnetic current distribution across the radiating PMC walls (or slots), the radiation in the far-field region can be calculated using the electric vector potential  $\vec{F}$  (equivalence principle [90]) obtained from the line integral along the patch perimeter as given below:

$$\vec{F} = \frac{\epsilon_0 h}{4\pi} \int \vec{J}(\vec{r}') \frac{e^{-jk_0|\vec{r}-\vec{r}'|}}{|\vec{r}-\vec{r}'|} dl \quad (2.42)$$

In equation (2.42),  $\vec{r}'$  represents the distance from the PMC walls of the patch cavity to a selected origin whereas  $\vec{r}$  is the distance from the observation point, which is in the far-field region, to the same origin and  $\vec{J}(\vec{r}')$  is the obtained magnetic current distribution across each PMC wall contributing to the radiation. Following the determination of the total  $\vec{F}$  from two radiating slots, the components of the total radiated  $\vec{E}$  and  $\vec{H}$  fields in the far-field region can be calculated as follows [152]:

$$H_r \approx 0 \quad (2.43)$$

$$H_\theta \approx -j\omega F_\phi \quad (2.44)$$

$$H_\phi \simeq -j\omega F_\theta \quad (2.45)$$

$$E_r \simeq 0 \quad (2.46)$$

$$E_\theta \simeq \eta_0 H_\phi \quad (2.47)$$

$$E_\phi \simeq -\eta_0 H_\theta \quad (2.48)$$

Where,

$\eta_0$  is the characteristics impedance in free space medium which can be given as:

$$\eta_0 = \sqrt{\frac{\mu_0}{\epsilon_0}} \quad (2.49)$$

### 2.2.2.2 Planar Inverted-F Antennas (PIFAs)

A conventional microstrip patch antenna described in the previous section operates at a half-wavelength mode and the length of the radiating patch element is given as [153, 154]:

$$L \approx \frac{\lambda}{2} \quad (2.50)$$

Although microstrip patch antennas are very suitable to be employed in low-profile systems, for some applications, such as mobile handsets, even a further reduction in the size of the antenna might be required. This can be addressed by using the symmetry in the surface current distribution of the radiating patch element of a microstrip patch antenna. In view of this, as shown in Fig. 2.26, a line perpendicular to the length of the patch can be introduced in the centre of the radiating patch element where the voltage is zero as demonstrated in Fig. 2.23.

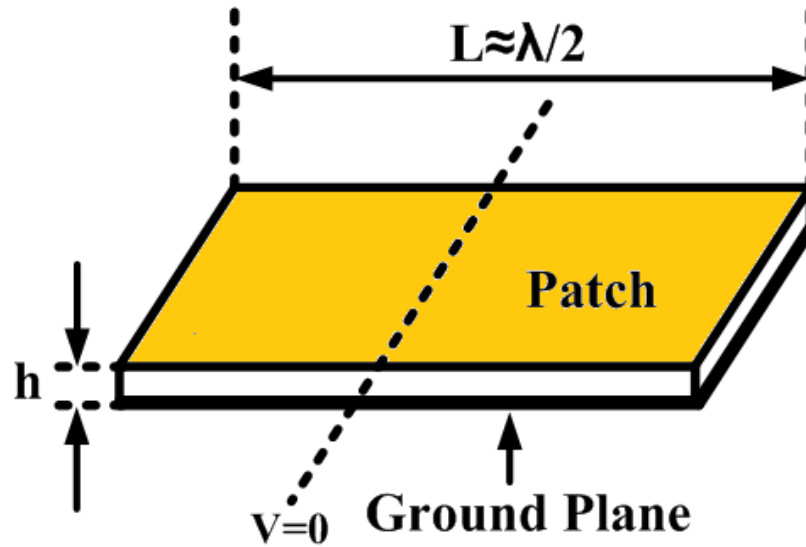


Fig. 2.26: A conventional microstrip patch operating at a half-wave mode.

Then, the patch can be divided up into two separate sub-patches and one half can be omitted and replaced with a wall short-circuiting the remained patch to the ground plane at the zero voltage edge as demonstrated in Fig. 2.27.

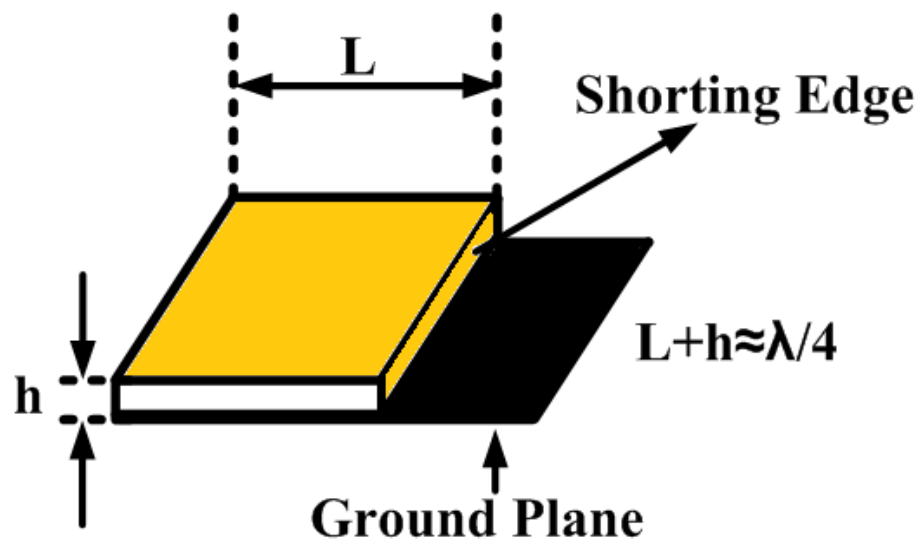


Fig. 2.27: Patch short-circuited to the ground plane through a shorting edge at the centre.

In Fig. 2.27, the resonance at the lowest mode is achieved when:

$$L+h \approx \frac{\lambda}{4} \tag{2.51}$$

In Fig. 2.27, the edge short-circuited to the ground plane does not contribute to the radiation in the far-field. For this reason, for practical applications, a shorting plate with a

smaller size is used in order to enhance the gain performance of the PIFA as can be seen in Fig. 2.28.

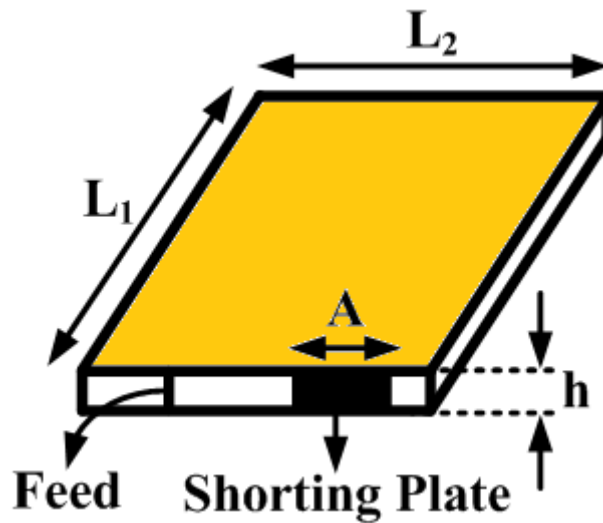


Fig. 2.28: Planar inverted-F antenna.

In Fig. 2.28, the resonance at the lowest mode is achieved when [86]:

$$L = L_1 + L_2 - A + h \approx \frac{\lambda}{4} \quad (2.52)$$

A significant advantage of the obtained antenna, which is called planar inverted-F antenna, is that it provides the same resonance characteristics as a microstrip patch antenna operating at a half-wavelength mode but with a size half of the conventional patch antenna due to the quarter-wavelength mode operation.

## 2.3 Integration Process and Challenges from an RF Point of View

Photovoltaic integration of microwave antennas brings considerable challenges from an RF perspective, which must be taken into account for the design of photovoltaic antennas.

The main challenges that need to be considered in the design process of a solar antenna can be given as follows:

- Encapsulation (if present): Encapsulation of a solar cell requires the cell to be placed between a protective optically transparent layer on top and a supportive dielectric layer at the bottom. From an RF point of view, the encapsulation of a

solar cell can be seen as a dielectric loading of the integrated solar cell, which has the potential to:

- Shift the operational resonance band. This is significantly important especially for antennas with a suspended radiating element. For these kinds of antennas, introducing an optically transparent protective layer on top of a solar cell operating as an RF ground plane (chapter 4), or a supporting dielectric layer underneath a solar cell operating as an RF radiating element (chapter 5), changes the effective substrate dielectric constant and therefore shifts the operational resonance band of the antenna. The amount of the shift in the operational frequency band of the antenna is directly dependent upon the dielectric constant of the encapsulation material.
- Increase the dielectric loss, which is a direct function of the loss tangent ( $\tan \delta$ ), and therefore decrease the radiation efficiency especially when the dielectric lamination material is placed upon a solar cell operating as an RF radiating element.
- Improve the input impedance response by widening the input impedance bandwidth and reducing the  $S_{11}$  level. However, this apparent improvement is due to the introduced dielectric losses and therefore more input power will be accepted into the antenna to be dissipated within the dielectric lamination material due to the introduced dielectric losses reducing the overall gain of the antenna.

For the photovoltaic antenna designs with encapsulation, typical encapsulation material used in this thesis is acrylic,  $\epsilon_r=3.6$  and  $\tan\delta=0.015$ , as an optically transparent protective material on top and FR4,  $\epsilon_r=4.3$  and  $\tan\delta=0.025$ , or RT/Duroid 5870,  $\epsilon_r=2.33$  and  $\tan\delta=0.0012$ , as a supporting dielectric material at the bottom.

- Cell structure: As described in chapter 3, a crystalline solar cell consists of two metal contacts, a front grid (negative DC terminal) and a solid rear (positive DC terminal), with a silicon layer in between. Whilst the metal rear contact, which is solid and homogeneous in structure, enables the cell to operate as an ideal metal plate from an RF point of view, other elements given below need to be considered in the examination of the RF operation:

- Silicon layer: Conventionally, the thickness of the silicon layer in a solar cell, which is 210  $\mu\text{m}$  for the solar cells used in this research, is much smaller in comparison to the operational wavelength for microwave antennas. However, in the microwave band, silicon is a high loss dielectric material,  $\tan\delta=0.015$ , and therefore its effect on the radiation response needs to be investigated.
- Front grid contact: The front grid DC contact of a solar cell, which consists of grid electrodes forming the negative DC terminal, is separated from the homogeneous bottom DC contact of the cell by the silicon layer in between. Although the separation is significantly small due to the small thickness of the silicon layer, 210  $\mu\text{m}$  in this thesis, due to the inducement of RF surface currents between the rear and front DC contacts, attention should also be given to the front grid contact of a solar cell in the examination of the RF operation.
- DC load connections: In order to withdraw the current produced by a solar cell to a DC load connected to its terminals, conductive DC connections between the cell terminals and the load are required. If no isolation is performed, these DC connections can have a significant effect on the radiation characteristics of a solar antenna when a solar cell is used as an RF radiating element (chapter 5) or as an RF stacked parasitic patch element (chapter 6).
- Trade-off between the antenna performance and solar performance: Although the amount of the short-circuit current produced by a solar cell is directly proportional to the size of the cell, i. e. the bigger the cell size the higher the short-circuit current and therefore the output power, the size of the cell is the main factor for the determination of the operational resonance frequency when the cell is used as an RF radiating element (chapter 5). Therefore the size of the integrated cell needs to be determined based upon the frequency at which a solar antenna is required to operate.
- Solar illumination intensity: Under practical conditions, the solar illumination intensity during a day is not constant and varies, which results in the number of freed electrons in a solar cell changing over time during the operation. This leads to a fluctuation in the amount of DC current produced by the cell whose possible

effect on the RF antenna performance should also be investigated. The investigation of this factor will be performed in chapter 5.

# Chapter 3 – Background on Photovoltaics and Solar Cells

## 3.1 Introduction

In this thesis, the integration of microwave antennas with crystalline silicon solar cells is investigated. This chapter aims to provide a background on photovoltaics and crystalline silicon solar cells. Section 3.1 presents the fundamentals of photovoltaics. Section 3.2 provides a background on crystalline silicon solar cells, covering the structure, I-V characteristics and efficiency/loss factors of these solar cells. Section 3.3 presents the module structure and explains the connection of individual crystalline silicon solar cells into a module. In section 3.4, challenges to be considered in the integration process from a photovoltaic perspective are given. Finally, section 3.5 presents the solar simulators used to measure the solar efficiency of the photovoltaic antennas studied in this research.

### 3.1.1 Photovoltaics

Photovoltaics can be described as the direct conversion of the solar energy into DC electrical power by using semiconductors illuminated by sunlight consisting of packets of energy, known as photons.

A photon is defined as a quantum of energy. The energy of a photon is dependent upon the wavelength of the photon within the solar spectrum which consists of high energy ultraviolet (UV), visible and low energy infrared (IR) wavelengths. The characteristic behaviour of electrons in a semiconductor material in the presence of light incident upon the semiconductor forms the basis of photovoltaics [155].

In order to understand the theoretical background behind this behaviour, electrons in a silicon semiconductor need to be investigated. In a silicon semiconductor, bonded electrons, which are in an energy band called the valence band, can be freed if enough amount of energy, bandgap energy,  $E_G$ , is provided [156, 157]. When a photon of sunlight with an energy level of greater than or equal to the bandgap energy is incident upon the semiconductor, the bond connecting the electron to the atom is broken and the freed electron jumps to another energy band known as conduction band, leaving behind a positively charged hole in the valence band as demonstrated in Fig. 3.1.

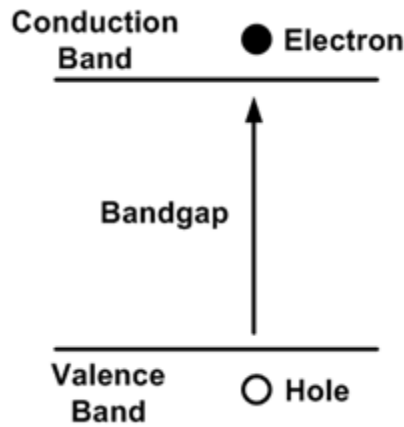


Fig. 3.1: Simplified energy band diagram.

The bandgap, which is also known as forbidden energy gap, between the conduction band and the valence band represents energy levels and cannot contain an electron. The freed electrons are separated from the holes and are collected by the top contact of a photovoltaic device, called solar cell, to be directed to flow through an external circuit consisting of a load. These electrons are then collected by the rear contact of the solar cell. During this movement through the load, the freed electrons deliver their energy to the load in the form of electrical power and return to the rear contact of the cell where they finally recombine with the holes, which is simply conservation of energy. This movement of electrons through an external circuit, as demonstrated in Fig. 3.2, produces an electric current and the process is known as photovoltaic effect [158-161].

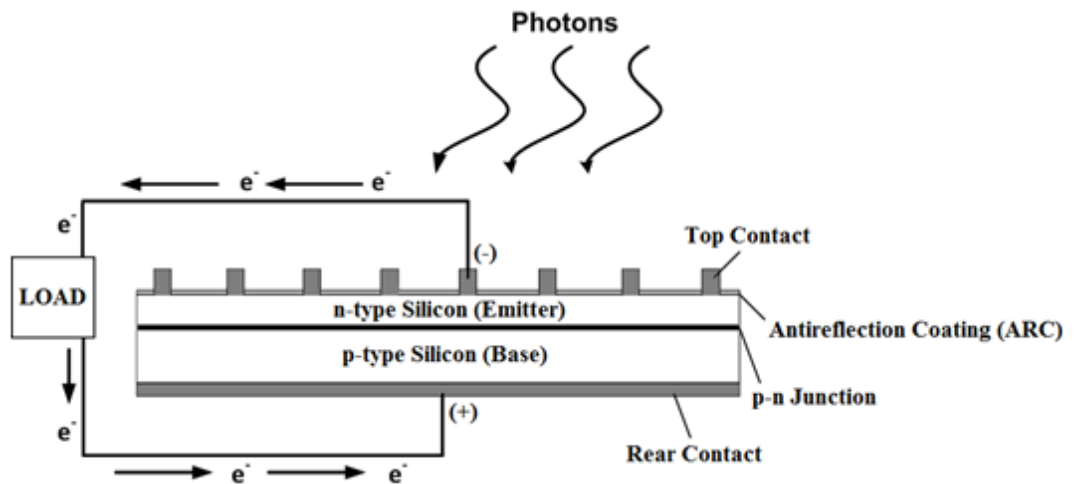


Fig. 3.2: Structure of a crystalline silicon solar cell and the movement of freed electrons.

## 3.2 Crystalline Silicon Solar cells

### 3.2.1 Structure of a crystalline silicon solar cell

In this thesis, the integration of microwave antennas with crystalline silicon solar cells is investigated. Crystalline silicon solar cells can be classified into the following types:

- Monocrystalline
- Polycrystalline

**Monocrystalline Silicon (Mono-Si):** The most widely used method in the production of monocrystalline silicon is the Czochralski method, which is based on the principle of using a seed of monocrystal to grow a monocrystal structure with a perfect lattice pattern. In order to accomplish this, first, pure molten silicon comes into contact with a seed of monocrystal. As the molten silicon in contact with the seed cools down, it grows into monocrystal structure with a perfect crystal lattice and the seed is slowly withdrawn. Then, the obtained monocrystal ingot is sliced into wafers.

Monocrystalline silicon solar cells offer typical efficiencies in the range of 13-22.5%, but are more time and energy consuming to produce due to the lattice perfection, which therefore makes them more expensive to manufacture compared to polycrystalline silicon solar cells [162].

**Polycrystalline Silicon (Poly-Si):** The method used to produce polycrystalline silicon is called casting process, which does not include the lattice perfection compared to Czochralski method. In this method, pure molten silicon is cooled down into ingots from which wafers with a multi-grain crystal lattice are sliced.

Polycrystalline silicon solar cells offer typical efficiencies in the range of 12-18%, less than monocrystalline cells offer, but are lower cost to manufacture and offer the advantage to have higher packing density for module applications due to their square or rectangular cell shapes compared to pseudo-square shape of monocrystalline silicon cells [163-165].

In a crystalline silicon, silicon atoms are in a regular periodic array forming a lattice structure and the valence electrons of these atoms are bonded to each other in a tetrahedral shape with an angle of  $109.5^\circ$  between the bonds forming the tetrahedral structure. Fig. 3.3 demonstrates the tetrahedral structure of silicon atoms in a crystal lattice.

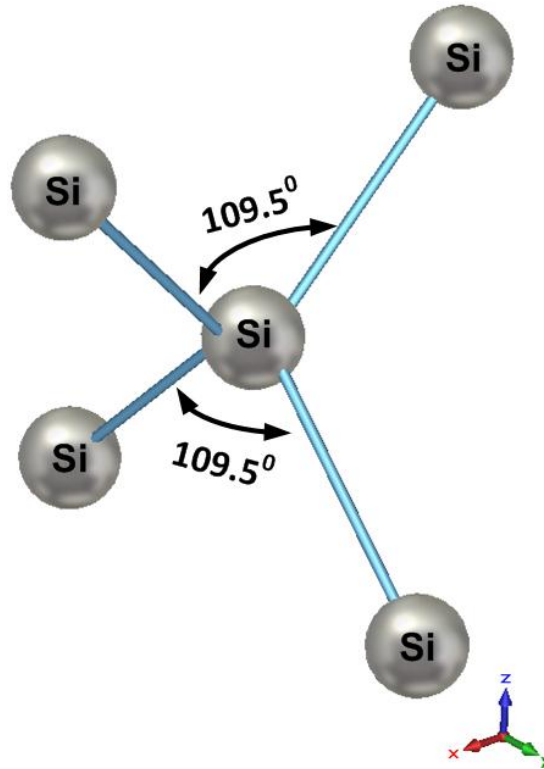


Fig. 3.3: Tetrahedral structure of silicon atoms in a crystal lattice.

When it comes to understanding the I-V characteristics, the equivalent circuit model of crystalline silicon solar cells needs to be investigated.

When there is no illumination, the cell operates as a semiconductor diode due to presence of a p-n junction as demonstrated in Fig. 3.2, letting a diode current,  $I_D$ , flow from the p-region to the n-region in the presence of an external voltage applied to its terminals. Under illumination, on the other hand, in addition to the diode current, a photogenerated current,  $I_{ph}$ , flows from the n-region to the p-region, which is opposite to the direction of the diode current. In light of this, the equivalent circuit model of an ideal crystalline silicon solar cell is demonstrated in Fig. 3.4.

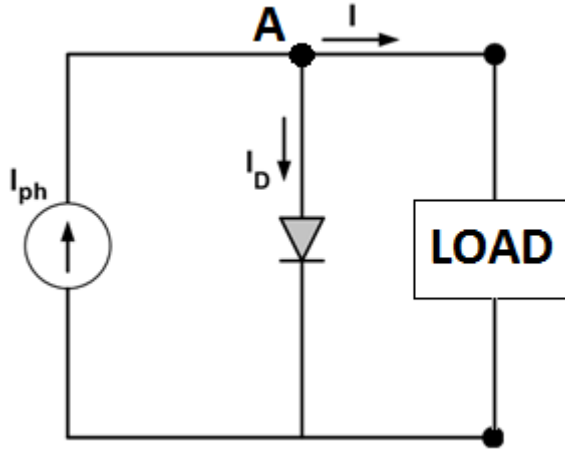


Fig. 3.4: Equivalent circuit model of an ideal cell.

As can be seen in Fig. 3.4, the equivalent circuit model consists of a current source representing the light generated photocurrent,  $I_{ph}$ , produced by the illuminated cell and a diode representing the barrier created by the electric field across the p-n junction, which forces the photocurrent to flow in a specific direction, from n-region to p-region through an external circuit.

From a circuit theory point of view, Kirchoff's current law needs to be applied to node A in order to analyse the given equivalent circuit model of an ideal cell in Fig. 3.4. At this point, the direction of the cell current  $I$  can be selected in two ways:

- Inside the cell from the load
- Outside the cell towards the load

For the analysis of the circuit model given Fig. 3.4, the direction of the cell current is selected outside the cell towards the load connected to the terminal. If Kirchoff's current law is applied to node A in Fig. 3.4, the cell current can be obtained as follows:

$$I = I_D - I_{ph} \quad (3.1)$$

where  $I_D$  is the diode current given in equation (3.2).

$$I_D = I_0 \left[ \exp\left(\frac{qV}{kT}\right) - 1 \right] \quad (3.2)$$

In equation (3.2),  $I_0$  is the amplitude of the saturation current of the diode whereas  $q$  is the electric charge of an electron. The Boltzmann's constant is given as  $k$  while  $T$  is the absolute temperature. The voltage applied across the terminals of the diode is given as  $V$ .

At this stage, the equivalent circuit model of an ideal cell given in Fig. 3.4 can be terminated in:

- A short-circuit load,
- An open circuit load.

### 3.2.1.1 Open-Circuit Termination

The equivalent circuit model of an ideal solar cell with an open-circuit termination is demonstrated in Fig. 3.5.

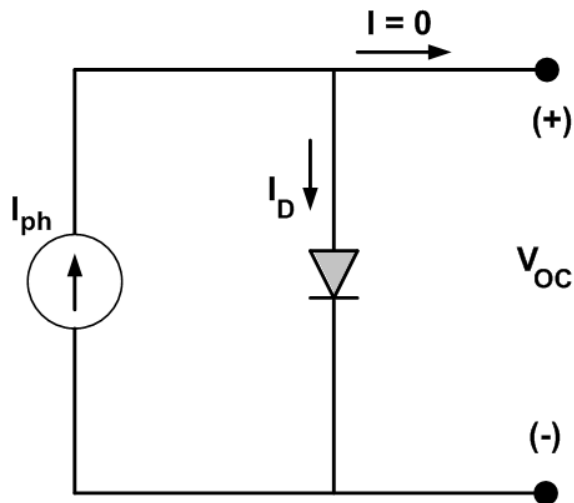


Fig. 3.5: Equivalent circuit model of an ideal cell with an open-circuit termination.

Under this circumstance, the cell current is equal to zero due to the open-circuit termination, which results in an open-circuit voltage,  $V_{OC}$ , with a generated DC power output equal to zero. In this case,  $I_{ph}$  is equal to the diode current as can be seen in Fig. 3.5. Substituting equation (3.2) in equation (3.1),

$$I = I_0 \left[ \exp\left(\frac{qV}{kT}\right) - 1 \right] - I_{ph} \quad (3.3)$$

In equation (3.3),

$$I_{ph} = qAG(L_h + L_e) \quad (3.4)$$

In equation (3.4),  $q$  is the electric charge,  $G$  is the generation rate,  $A$  is the cross-sectional area,  $L_h$  and  $L_e$  are the hole and electron diffusion lengths, respectively.

As the cell current is equal to zero due to the open-circuit termination,

$$I = \left\{ I_0 \left[ \exp\left(\frac{qV_{OC}}{kT}\right) - 1 \right] - I_{ph} \right\} = 0 \quad (3.5)$$

From equation (3.5), the open-circuit voltage can be obtained as follows:

$$V_{OC} = \frac{k_B T}{q} \ln \left[ \frac{I_{ph}}{I_s} + 1 \right] \cong \frac{k_B T}{q} \ln \left[ \frac{I_{ph}}{I_s} \right] \quad (3.6)$$

### 3.2.1.2 Short-Circuit Termination

The equivalent circuit model of an ideal solar cell with a short-circuit termination is illustrated in Fig. 3.6.

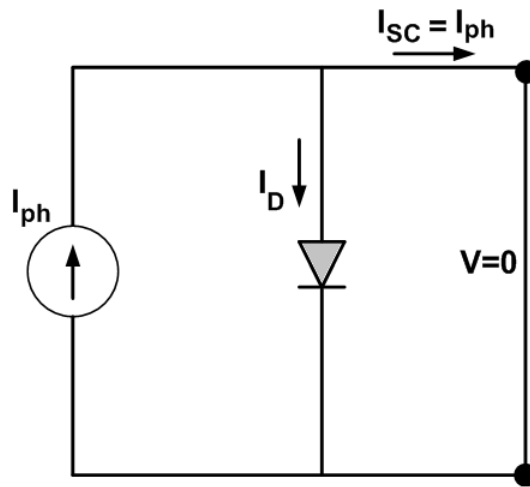


Fig. 3.6: Equivalent-circuit model of an ideal cell with a short-circuit termination.

In this case, as can be seen in Fig. 3.6, the voltage across the diode in the circuit model is equal to zero, which also means  $I_D=0$  in equation (3.7). From equation (3.8) it can be obtained that this also results in the cell current being equal to the photocurrent, delivering maximum current into the circuit,  $I_{SC}$ .

Using the equivalent circuit in Fig. 3.6, the short-circuit current can be determined as follows:

$$I_{SC} = \left\{ I_0 \left[ \exp\left(\frac{qV}{kT}\right) - 1 \right] - I_{ph} \right\}_{V=0} \quad (3.7)$$

Substituting  $V=0$  in equation (3.7), short-circuit current can be obtained as follows:

$$I_{SC} = I_{ph} = -qAG(L_h + L_e) \quad (3.8)$$

### 3.2.1.3 I-V Characteristics

Following the information provided on the equivalent circuit model of an ideal solar cell, I-V characteristics can now be investigated. The I-V characteristics of a crystalline silicon solar cell can be seen as a combination of the behaviour of the cell in the dark and under illumination.

As demonstrated in the equivalent circuit model of an ideal crystalline silicon solar cell in Fig. 3.4, there are two elements in the equivalent circuit model whose characteristics need to be investigated in the dark and under illumination in order to obtain the I-V characteristics of a crystalline silicon solar cell.

In the dark, when there is no illumination incident upon the cell, there is no generated photovoltaic current,  $I_{ph}=0$ . This means, the cell current is equal to the current of a diode,  $I=I_D$ , from equation (3.1) and thus the cell has the same I-V characteristics with a semiconductor diode. In this case, the crystalline silicon solar cell works as a passive element with I-V characteristics only in the first and third quadrants as demonstrated in Fig. 3.7.

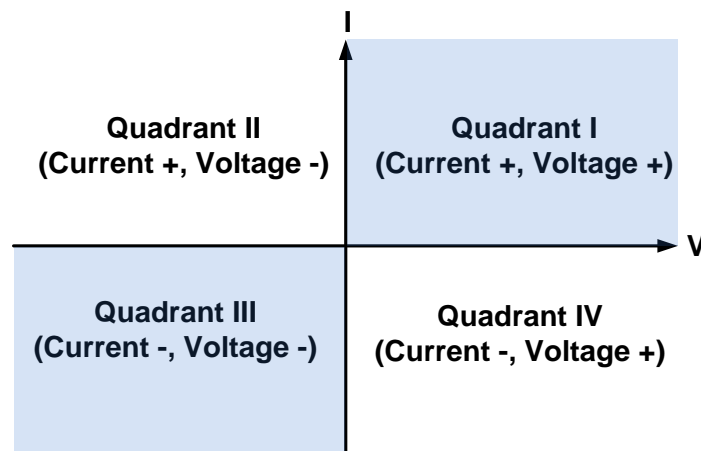


Fig. 3.7: Quadrants in the description of I-V characteristics.

Under illumination, on the other hand, the cell acts an active element generating a photovoltaic current,  $I_{ph}\neq 0$ . For this reason, when the cell is illuminated, the cell current is shifted to the fourth quadrant by an amount of the generated photovoltaic current as explained in equation (3.1) and shown in Fig. 3.8.

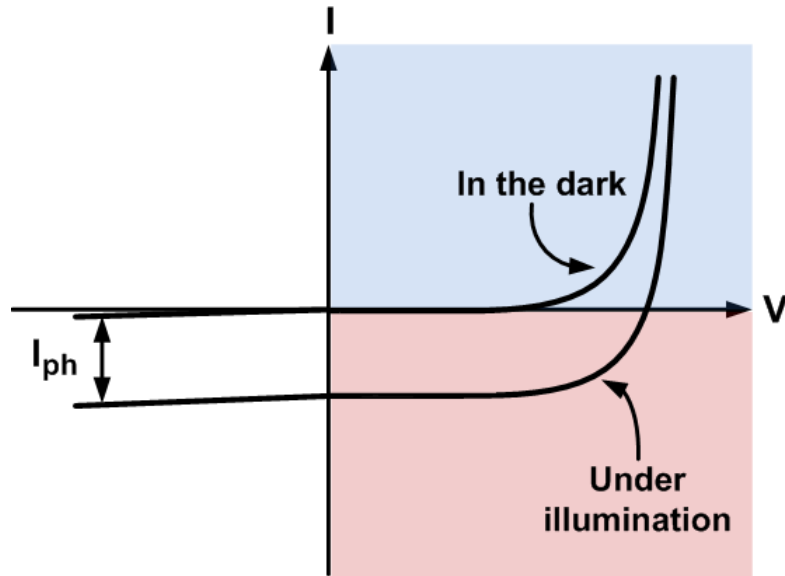


Fig. 3.8: I-V curve in the dark and under illumination.

This means, depending upon the amount of the generated photovoltaic current determining the position of the I-V curve of the cell in the fourth quadrant, the cell has negative current and positive voltage meaning that under illumination it works as an active element and generates power. For the sake of simplicity, although the I-V curve always remains in the fourth quadrant under illumination due to the fact that the photocurrent is in the reverse direction to the normal diode current, it is often shown with the current axis showing magnitude rather than direction [163, 166].

## 3.2.2 Efficiency and Loss

### 3.2.2.1 Efficiency

Efficiency ( $\eta$ ) is a key parameter in the determination of the performance of solar cells and can be defined as the ratio of the power generated by the solar cell to the total input power delivered to the cell. At this point, two important parameters need to be defined in order to understand the efficiency:

- Maximum power that can be obtained at the maximum power point ( $P_{MP}$ ) in the I-V curve of a solar cell,
- Fill factor (FF) determining the maximum power.

Fig. 3.9 shows the typical I-V curve of a crystalline silicon solar cell with a rectangle fitting under the I-V curve whose boundaries determined by the maximum power point.

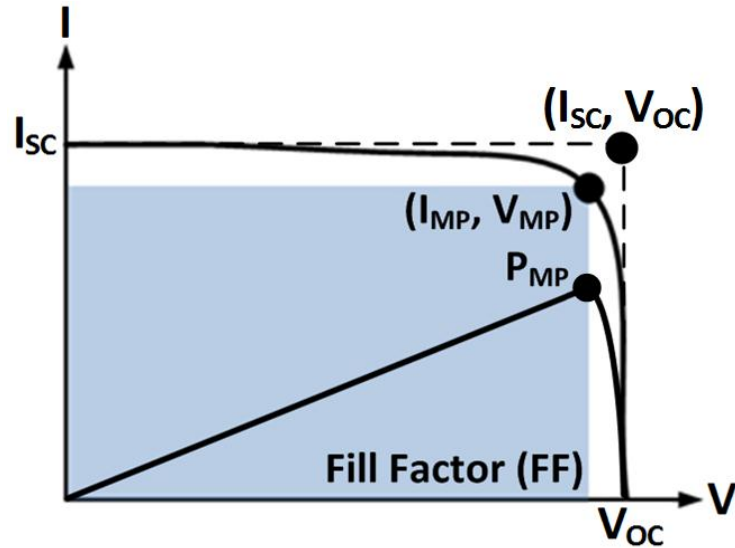


Fig. 3.9: I-V curve and Fill Factor (FF).

In this case, the fill factor can be given as:

$$FF = \frac{P_{MP}}{V_{OC} I_{SC}} \quad (3.9)$$

Although, it is known that when the solar cell is terminated in a short-circuit element,  $I=I_{SC}$ , or in an open-circuit element,  $V=V_{OC}$ , the actual generated power is equal to zero, the multiplication of these two parameters gives a theoretical absolute maximum power value, which is always greater than the practical maximum power,  $P_{MP}$ , in equation (3.9). The reason why the theoretical absolute maximum power is always greater than the practical maximum power can be given as follows:

- The theoretical absolute maximum power is obtained through the multiplication of the short-circuit current,  $I_{SC}$ , and the open-circuit voltage,  $V_{OC}$ , whereas the power at the maximum power point,  $P_{MP}$ , is calculated through the multiplication of current and voltage at the maximum power point,  $I_{MP}$  and  $V_{MP}$ , respectively.
- The open-circuit voltage,  $V_{OC}$ , is always greater than the voltage at the maximum power point,  $V_{MP}$ , as can be seen in Fig. 3.9.
- The short-circuit current,  $I_{SC}$ , is always greater than the current at the maximum power point,  $I_{MP}$ , as can be seen in Fig. 3.9.
- From equations (3.9) and (3.10), the power at the maximum power point,  $P_{MP}$ , is smaller than the theoretical absolute maximum power,  $P_{AM}$ , by a factor of fill factor (FF).

From equation (3.9), the maximum power at the maximum power point in Fig. 3.9,  $P_{MP}$ , which is originally equal to the multiplication of the voltage and current values at the maximum power point,  $V_{MP} \times I_{MP}$ , can be obtained in terms of fill factor as follows:

$$P_{MP} = V_{OC} I_{SC} FF \quad (3.10)$$

By definition, the efficiency of a solar cell can then be given as:

$$\eta = \frac{V_{OC} I_{SC} FF}{P_{in}} \quad (3.11)$$

In (3.11),  $P_{in}$  is the total input solar power and is given as:

$$P_{in} = P_{il} A \quad (3.12)$$

In (3.12),  $P_{il}$  is the total solar illumination intensity used for testing photovoltaic cells,  $1000 \text{ W/m}^2$ , whilst  $A$  is the surface area of the solar cell. Substituting (3.10) in (3.11), the simplified version of  $\eta$  independent of FF can be obtained as follows:

$$\eta = \frac{P_{MP}}{P_{in}} \quad (3.13)$$

Table 3.1 illustrates the recorded maximum efficiencies obtained for different types of solar cells [169].

Table 3.1: Recorded maximum solar cell efficiencies ( $1000 \text{ W/m}^2$ ,  $25^\circ\text{C}$ ) [167].

<b>Classification</b>	<b>Efficiency (%)</b>	<b>Area (<math>\text{cm}^2</math>)</b>
Si (crystalline)	25.0±0.5	4.00
Si (multicrystalline)	20.4±0.5	1.002
Si (thin film transfer)	19.1±0.4	3.983
Si (thin film submodule)	10.5±0.3	94.0
GaAs (thin film)	28.8±0.9	0.9927
GaAs (multicrystalline)	18.4±0.5	4.011
Si (amorphous)	10.1±0.3	1.036
Si (nanocrystalline)	10.1±0.2	1.199

### 3.2.2.2 Losses

The main loss factors determining the maximum energy conversion efficiency of crystalline silicon solar cells can be given as follows:

- Losses due to quantization of energy in photons
- Optical losses
  - Shading by the top contact
  - Reflection from the top surface
  - Reflection from the rear surface
- Recombination Losses
- Resistance losses

#### 3.2.2.2.1 Losses due to Quantization of Energy in Photons

The photons of light with different wavelengths in the solar spectrum have different energy levels. Only the photons with an energy level equal to or greater than the bandgap are used to create electron-hole pairs whilst the extra energy is dissipated as heat within the cell. This quantum factor alone reduces the theoretical efficiency for crystalline silicon solar cells significantly.

#### 3.2.2.2.2 Optical Losses

In a crystalline silicon solar cell, the factors causing optical losses can be given as:

- **Shading by the front contact:** The typical front contact pattern of a solar cell is demonstrated in Fig. 3.10.

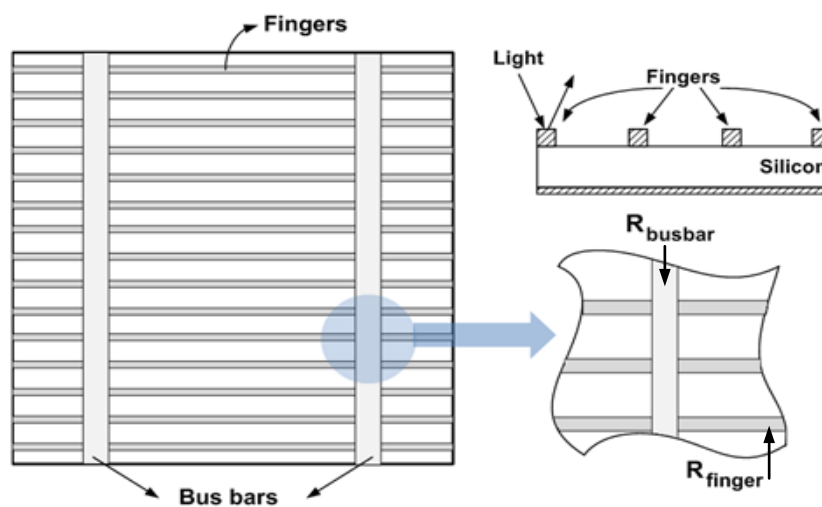


Fig. 3.10: Grid structure of the front contact of a solar cell.

As can be seen in Fig. 3.10, the front contact consists of metal fingers connected together with bus bars. The optical reflection from the top contact can be decreased by widening the separation between the fingers and narrowing the width of the bus bars along with metal fingers at the cost of increasing the electrical resistance.

- **Reflection from the front surface:** Reflection from the front surface of a crystalline silicon solar cell can be reduced by applying a quarter-wavelength dielectric antireflection coating (ARC) on the front surface of silicon as demonstrated in Fig. 3.11.

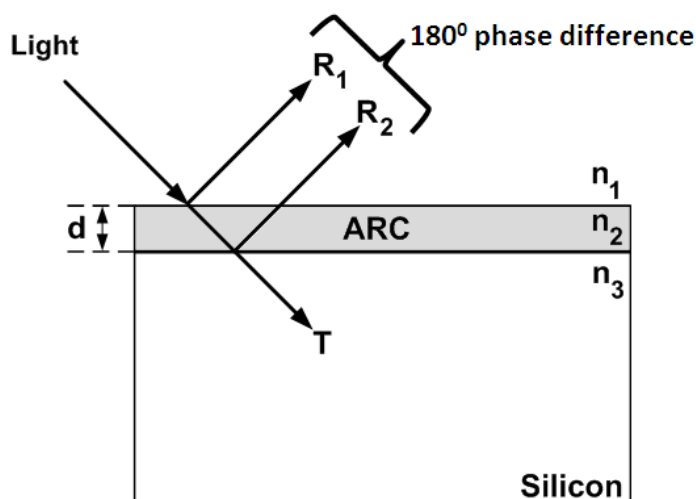


Fig. 3.11: Antireflection coating.

In Fig. 3.11, the reflections from the front surface and the rear surface of the antireflection layer have a phase difference of  $180^\circ$ , which cancels out the total reflection. The thickness of the antireflection coating layer is given as:

$$d = \frac{\lambda}{4n} \tag{3.14}$$

where,  $d$  is the thickness of the ARC,  $\lambda$  is the wavelength and  $n$  is the refractive index of the material.

Another method used to minimise the reflection from the front surface of the cell is to texturize the silicon surface to direct the reflected light in such a way that it would be incident upon the textured surface for a second time after rather than being reflected back from a flat silicon surface. A texturized cell surface in comparison to the silicon layer with a flat surface is illustrated in Fig. 3.12.

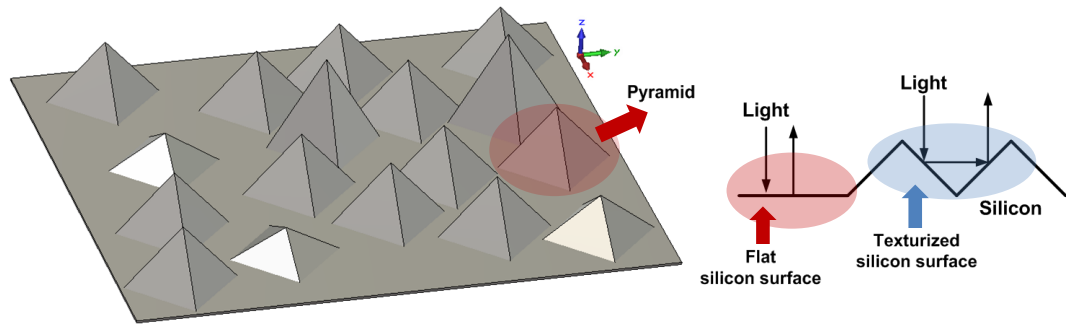


Fig. 3.12: Texturization of the cell surface (a) texturized silicon surface (b) reflection from texturized silicon surface in comparison to flat silicon surface.

As can be seen in Fig. 3.12, the reflection from the silicon with a flat surface happens in the opposite direction with the incident light. However, the textured silicon surface consisting of pyramidal structures directs the reflected light in such a way that it is re-reflected back to the cell from the surface of the neighbouring pyramidal structures as a result of different surface normal angles [168, 169].

- Reflection from the rear surface:** Crystalline silicon is an indirect bandgap material offering poor absorption characteristics for photons with long wavelengths in the IR regions, which travel long distances in the cell to be absorbed. Increasing the random reflection from the rear surface enables the light to be reflected back into the cell in random directions resulting in possible absorptions as demonstrated in Fig. 3.13.

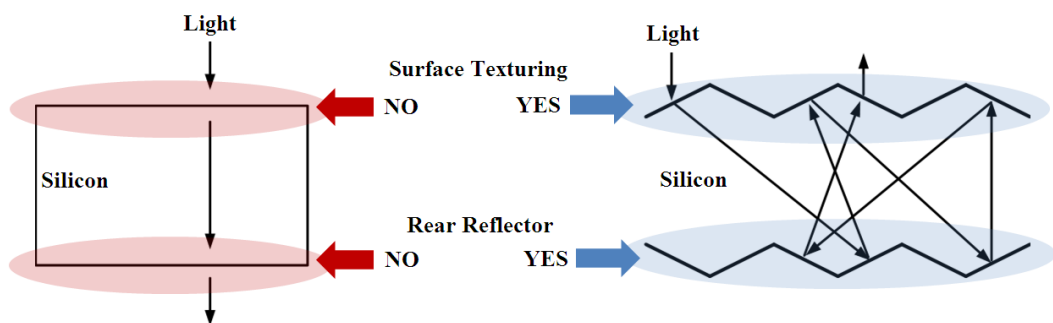


Fig. 3.13: Light trapping in a cell.

This technique is called light trapping and has a significant importance in the enhancement of the absorption performance for crystalline silicon solar cells.

### 3.2.2.2.3 Recombination Losses

The combination of electrons in the conduction band and the holes in the valence band before the electrons move through an external circuit to contribute to electricity, which tends to happen at interfaces and defect sites, affects the efficiency of a crystalline silicon solar cell.

Although the photons in the visible spectrum are absorbed close to the junction where they are separated by an electric field instantaneously without travelling great distances within the cell, high energy UV photons and low energy IR photons are absorbed far away from the p-n junction. Whereas high energy UV photons are absorbed close to the front surface of the cell, low energy IR photons with energy levels greater than the bandgap are absorbed close to the rear contact of the cell depending upon the cell thickness. This makes electrons and holes wander within the cell subject to possible recombinations with other electrons and holes at any time before they contribute to the generation of electricity. This kind of recombination is called bulk recombination. The second type of recombination within the cell occurs due to the impurities and defects in the semiconductor structure and the areas close to the edges, surface and contacts.

### 3.2.2.2.4 Resistance Losses

The ideal equivalent circuit model of a crystalline silicon solar cell is investigated in section 3.2.1. However, the actual full equivalent circuit model of crystalline silicon solar cells consists of two more elements whose effects on the I-V characteristics need to be investigated in order to provide a better understanding about the loss mechanisms in crystalline silicon solar cells. These elements are:

- Series resistance ( $R_{sr}$ ): This resistance is introduced by the contacts and the bulk of the silicon. It can be seen as a resistance connected in series to the output terminal. A crystalline silicon solar cell has a typical series resistance of  $2\Omega/\text{cm}^2$ .
- Shunt resistance ( $R_{sh}$ ): This resistance is introduced by the impurities in and around the p-n junction and at the edges of the cell forming ohmic conduction paths. Typical shunt resistance of a crystalline silicon solar cell can be given as  $500\Omega/\text{cm}^2$ .

The equivalent circuit model including these resistances is shown in Fig. 3.14.

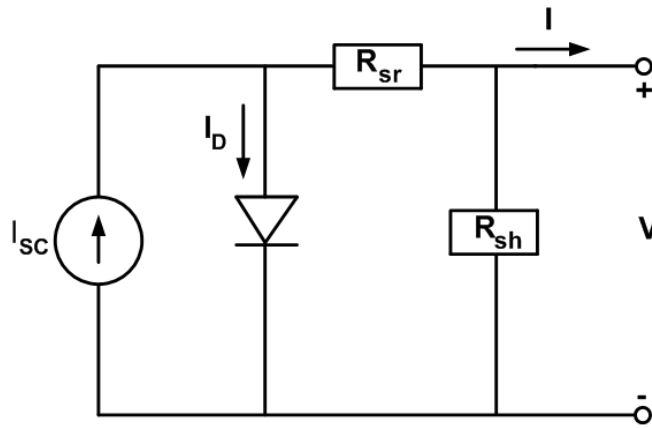


Fig. 3.14: The equivalent circuit model with series and shunt resistances.

From a circuit theory point of view, it is required for the series resistance to be as small as possible while for the shunt resistance to be as big as possible in order to deliver maximum power to the load.

In order to investigate the effect of these resistances on the I-V characteristics, the equivalent circuit model is thought to have these resistances separately for the sake of simplicity.

Fig. 3.15(a) illustrates the equivalent circuit model of a crystalline silicon solar cell with a series resistance connected in series to the output.

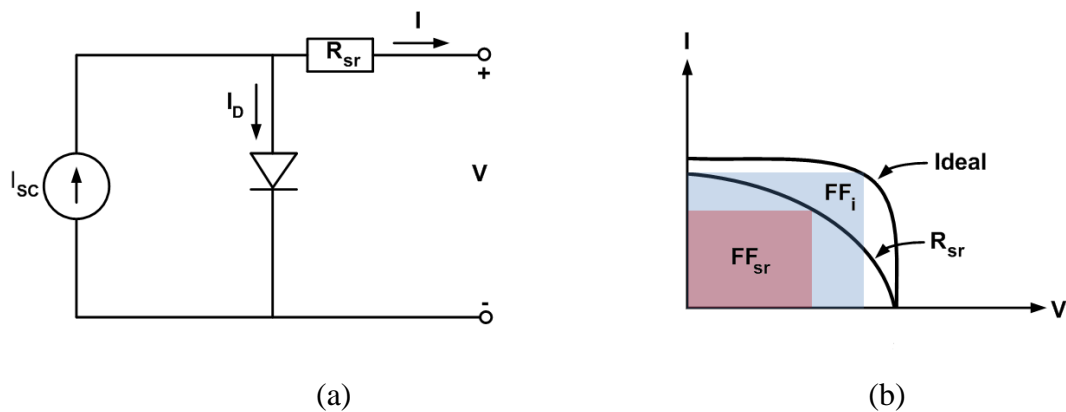


Fig. 3.15: Equivalent circuit model with series resistance (a) circuit-diagram (b) I-V curve.

With an open-circuit termination, the power across the series resistance is equal to zero as the cell current,  $I$ , flowing through the resistance is equal to zero. For this reason, the series resistance does not change the open-circuit voltage but affects the short-circuit current with finite load impedances and thus causes a considerable decrease in the fill factor as can be seen in Fig. 3.15(b).

Fig. 3.16(a) demonstrates the equivalent circuit model with a shunt resistance connected in parallel to the current source representing the photogenerated current.

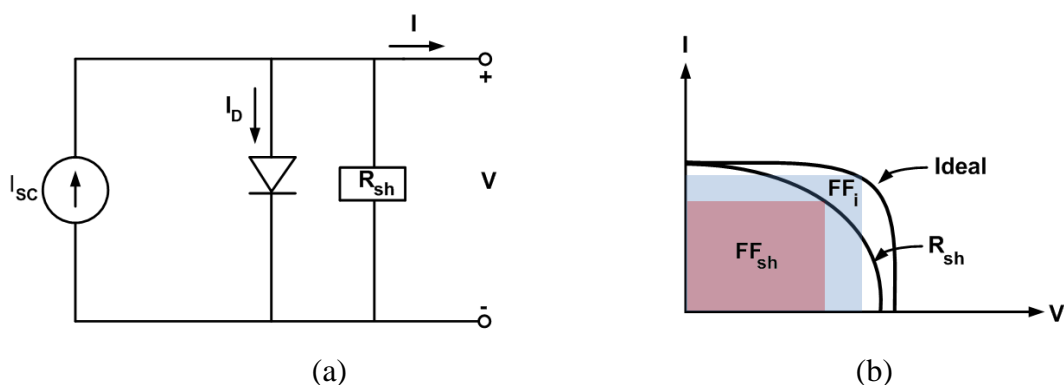


Fig. 3.16: Equivalent circuit model with shunt resistance in parallel (a) circuit-diagram (b) I-V curve.

With a short-circuit termination, the voltage across the shunt resistance is equal to zero, which means that in this case there is no current flowing through the shunt resistance, and for this reason, the cell current does not change and is equal to short-circuit current,  $I_{SC}$ . However, termination in a finite load impedance affects the open-circuit voltage and the FF as illustrated in Fig. 3.32(b) [162, 164, 170, 171].

## 3.3 Crystalline Silicon Solar Modules

### 3.3.1 Connection of Solar Cells

For applications requiring higher voltages or currents than those that can be provided by a single solar cell, modules, which consist of series or parallel connected solar cells, are used. Modules with 36 series connected crystalline solar cells providing a voltage output in the range of 15-20 V under maximum power operating conditions are widely used for commercial applications, especially for 12V battery charging [172]. In addition, larger modules are becoming common for large installations since they reduce the number of connections required.

Crystalline silicon solar cells in modules can be connected in two ways:

- Series connection
- Parallel connection

### 3.3.1.1 Series Connection

In commercial modules, crystalline silicon solar cells within the module are generally connected in series. In this case, the characteristics of each individual cell forming the module determine the operation characteristics of the module.

Fig. 3.17 shows a model of  $N$  identical crystalline silicon solar cells connected in series in a module.

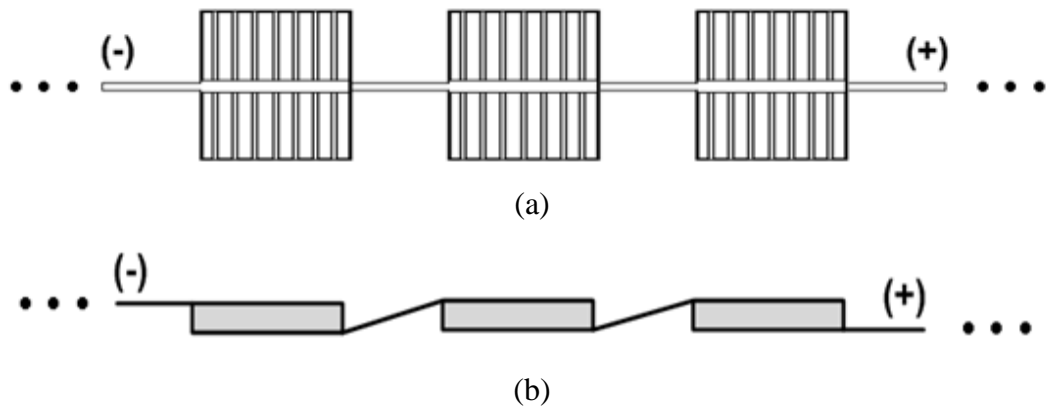


Fig. 3.17: Series connection of solar cells in a module (a) top view (b) front view.

Considering that the cells are identical and are exposed to the same solar illumination intensity, it would be expected that the open-circuit voltage of the module,  $V_{MOC}$ , would be  $N$  times of the open-circuit voltage of a single crystalline silicon solar cell given in equation (3.6).

$$V_{MOC} = N.V_{OC} \quad (3.15)$$

Whereas the short-circuit current would be the same as the short-circuit current of an individual crystalline silicon solar cell within the module given in equation (3.8).

In this case the I-V curve of the module is demonstrated in Fig. 3.18.

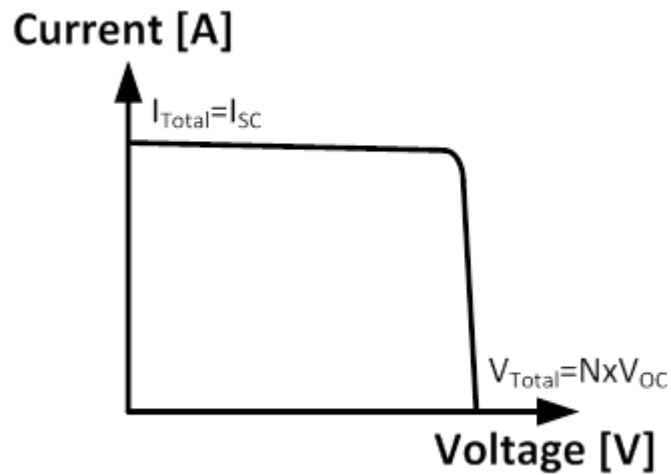


Fig. 3.18: Total I-V curve of the module consisting of  $N$  series connected solar cells.

### 3.3.1.2 Parallel Connection

Fig. 3.19 demonstrates  $M$  crystalline silicon solar cells connected in parallel in a module.

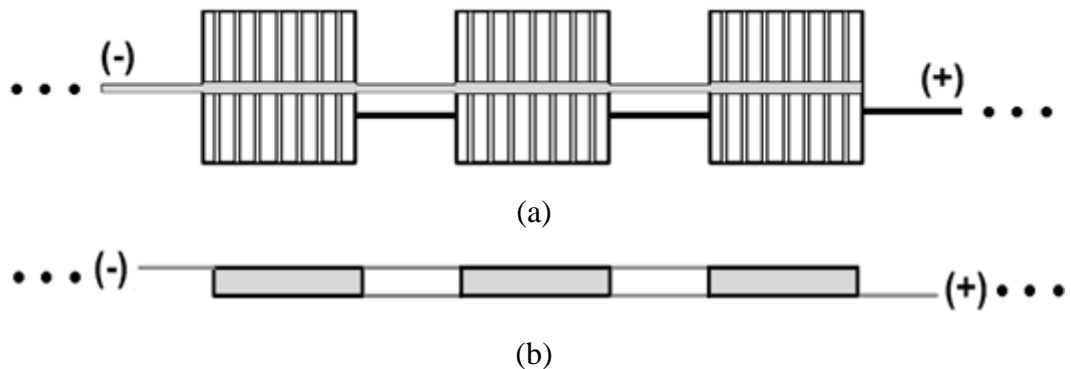


Fig. 3.19: Parallel connection of solar cells in a module (a) top-view (b) front-view.

Assuming that the cells are identical and are exposed to uniform illumination intensity, the module short-circuit current,  $I_{MSC}$ , can be given as follows:

$$I_{MSC} = M \cdot I_{SC} \quad (3.16)$$

The open-circuit voltage of the module, on the other hand, is the same with the open-circuit voltage of a single cell within the module given in equation (3.6).

In this case, the I-V curve of the module is illustrated in Fig. 3.20.

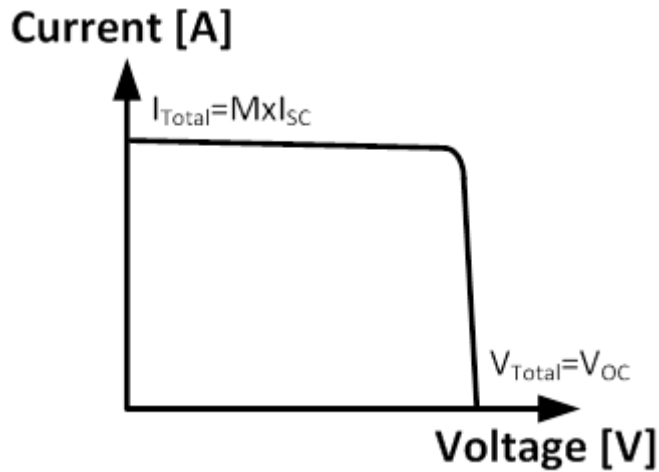


Fig. 3.20: Total I-V curve of the module consisting of  $M$  parallel connected solar cells.

### 3.4 Integration Process and Challenges from a Photovoltaic Point of View

In Chapter 2, the factors and challenges that need to be considered in the photovoltaic integration process were discussed from an RF perspective. In this section, the challenges of the integration process from a photovoltaic point of view are investigated.

From a photovoltaic perspective, main challenges that need to be considered in the design process of a solar antenna can be given as follows:

- Shading: For solar antennas in which the solar cell is used as an RF ground plane (chapter 4), the radiating element, which is conventionally an opaque copper plate, is required to be placed upon/above the ground plane, i.e. the solar cell. This arrangement blocks the solar illumination incident upon the solar antenna and therefore shades the solar cell. This has the potential to significantly reduce the solar efficiency of a solar antenna as investigated and addressed in chapter 4.
- Homogeneity of a solar cell: As explained in chapter 2, conventional microstrip patch antennas offer relatively narrow impedance bandwidths limiting the usability of these antennas when it comes to multiband and wideband applications. In the literature, this has been overcome by applying additional techniques requiring the modification of the radiating element, such as capacitive slot-loading [59-83], to achieve the excitation of multiple  $TM_{mn}$  propagation modes. However, from a photovoltaic point of view, this would require the surface of the integrated solar cell to be modified when the solar cell is used as an RF radiating element in a solar

antenna (chapter 5). However, the homogeneity of the cell is of vital importance to achieve optimum solar operation performance. This is investigated in chapter 5 and a solution to this problem is offered in chapter 6.

- Trade-off between the solar performance and the antenna performance: While it is required for a solar cell to be oriented in the direction of the Sun to achieve optimum solar performance, the target to be communicated with might be located at a different position. In this case, rotating the solar antenna physically to the direction of the communication target would deteriorate the solar performance of the antenna and therefore an alternative solution needs to be adopted to overcome this challenge. This is addressed in a solar array antenna design demonstrated in chapter 6, which is capable of electronically steering the main lobe while maintaining the physical orientation of the solar antenna.

### 3.5 Solar Simulators

In this thesis, two types of solar simulators were used for the examination of the solar performance of the studied photovoltaic antennas:

- Metal halide solar simulator: The solar performance measurements of most of the photovoltaic antennas studied in this research were carried out using a metal halide solar simulator, which can be seen in Fig. 3.21.

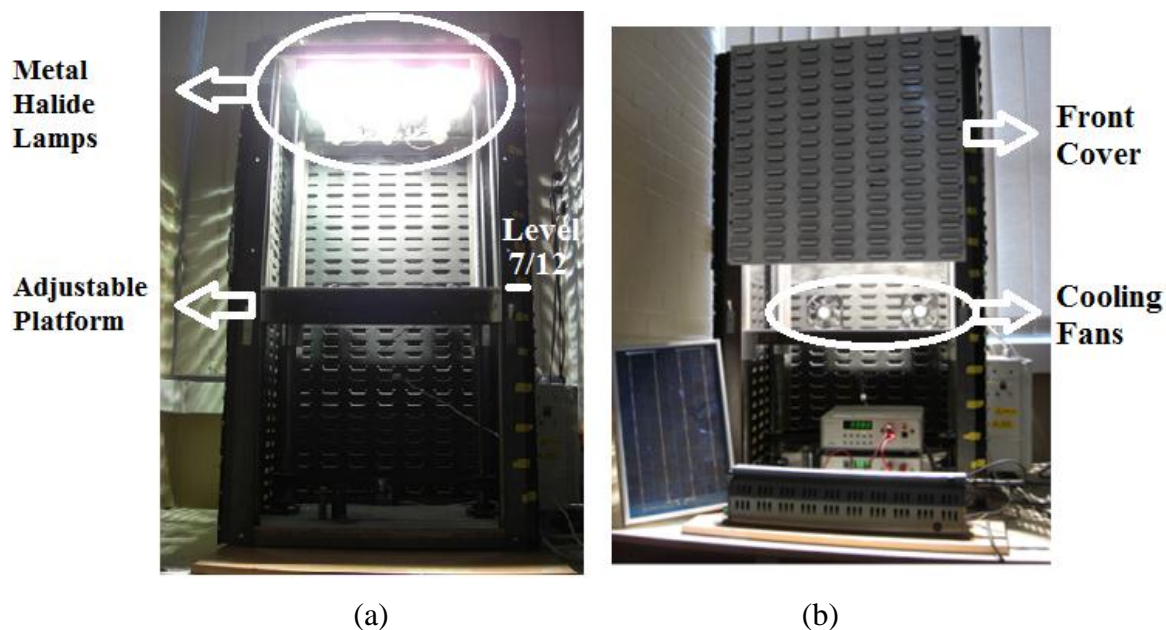


Fig. 3.21: Metal halide solar simulator (a) without front cover (b) with front cover.

As can be seen in Fig. 3.21, the solar simulator consists of three metal halide lamps (Osram Powerstar HQI-BT400W/D [173]), one of which is illustrated in Fig. 3.22, and an adjustable platform, on which solar antenna under test is placed. The metal halide lamps have a colour temperature of 5200K. The height of the platform can be adjusted to achieve the required illumination intensity,  $1000 \text{ W/m}^2$ , upon the photovoltaic antenna under test.



Fig. 3.22: Metal halide lamp (Osram Powerstar HQI-BT400W/D).

The spectral power distribution of the metal halide lamps in the wavelength range of 380-780 nm is demonstrated in Fig. 3.23 [173].

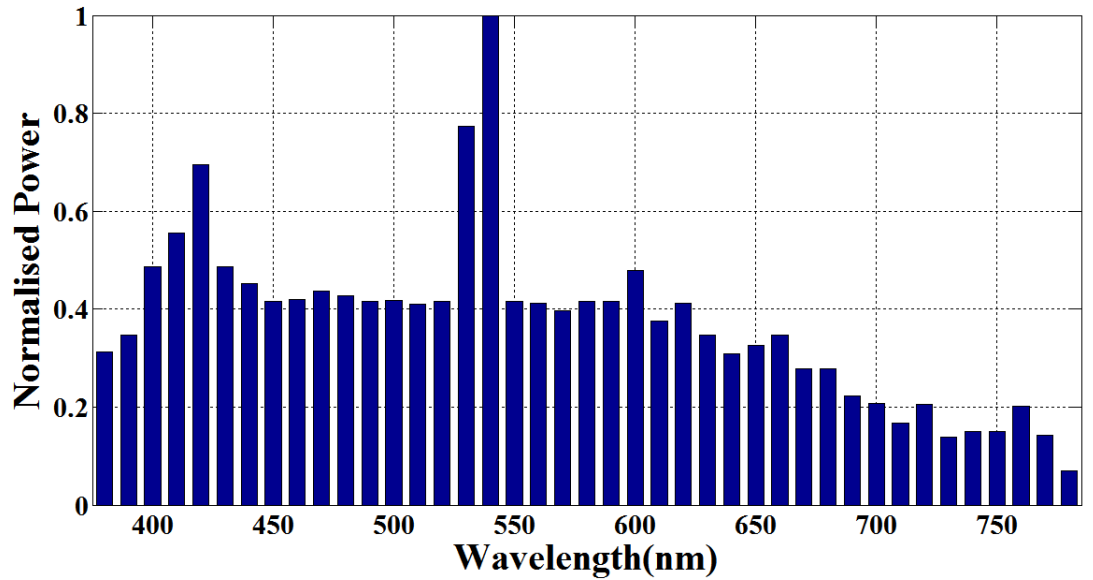


Fig. 3.23: Spectral power distribution of the Osram Powerstar HQI-BT400W/D metal halide solar lamps [173].

As can be seen in Fig. 3.23, the metal halide lamps within the solar simulator have their spectral power distribution peak close to 550nm.

Following the demonstration of the spectral power distribution, the measurements given below were performed in order to determine the illumination characteristics of the solar simulator:

- Illumination homogeneity measurement: A proper solar measurement of a photovoltaic antenna requires the illumination incident upon the antenna within the simulator to be homogeneous. In view of this, in order to obtain the illumination distribution across the adjustable platform of the simulator, an illumination map consisting of equally spaced measurement points was created as demonstrated in Fig. 3.24.

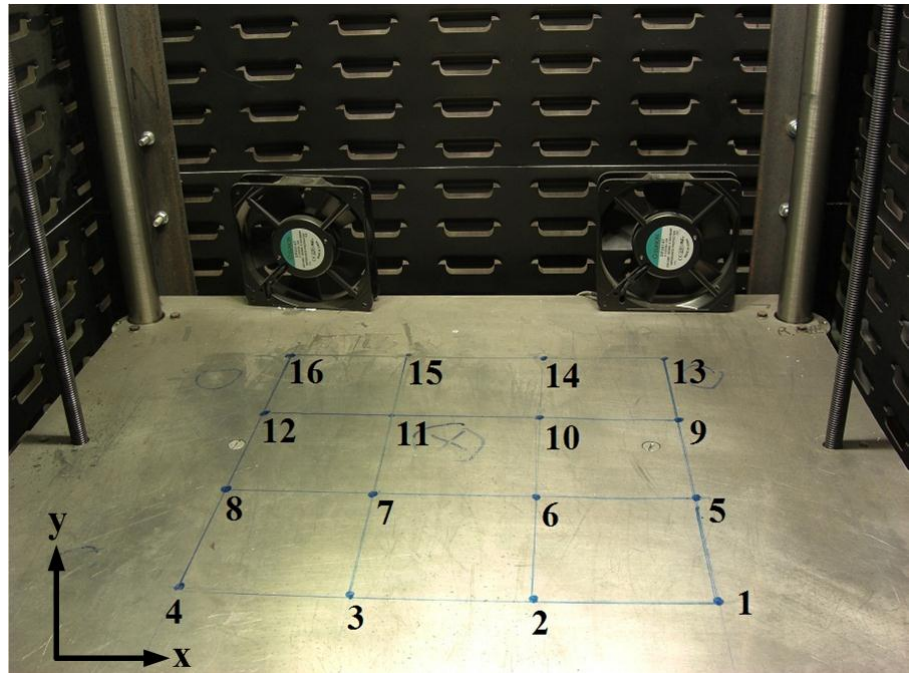


Fig. 3.24: Adjustable platform and the illumination map.

At each measurement point, a light meter was used in order to measure the illumination intensity and the obtained data was transferred to MATLAB in order to create the illumination distribution map across the platform of the solar simulator. The obtained illumination distribution is demonstrated in Fig. 3.25.

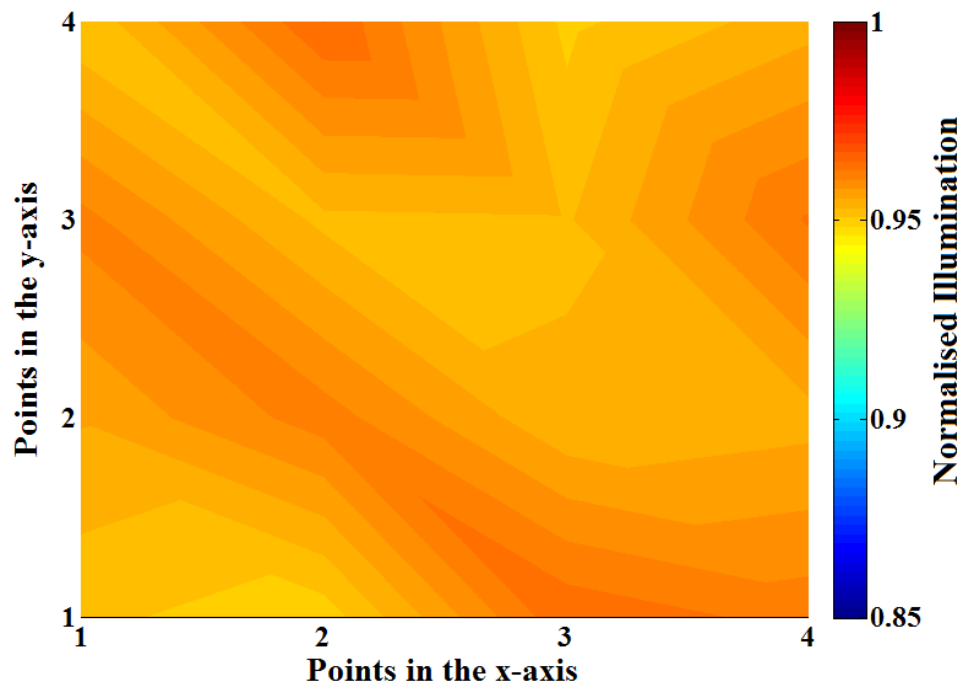


Fig. 3.25: Normalised illumination distribution scanning result in MATLAB.

As can be seen in Fig. 3.25, the obtained illumination distribution is considerably homogeneous enabling the solar performance of the studied solar antennas to be measured properly.

- Illumination intensity measurements: In order to determine the optimum position of the platform for an illumination intensity of  $1000 \text{ W/m}^2$ , the light meter mentioned above was used. The standard illumination intensity was obtained as  $1000 \text{ W/m}^2$  when the platform of the solar simulator was set to the level of 7/12 as demonstrated in Fig. 3.21(a).

The advantages and disadvantages of the metal halide solar simulator are given in Table 3.2.

Table 3.2: Advantages and disadvantages of the metal halide solar simulator.

<b>Advantages</b>	<b>Disadvantages</b>
<ul style="list-style-type: none"> <li>• Temperature control consisting of two cooling fans: Solar measurements were taken at a cell temperature in the range of <math>17.6 \text{ }^\circ\text{C} - 19.4 \text{ }^\circ\text{C}</math>,</li> <li>• Low-cost,</li> <li>• Possible to measure large solar antennas (up to <math>500 \text{ mm} \times 500 \text{ mm}</math>).</li> </ul>	<ul style="list-style-type: none"> <li>• Manual resistance change,</li> <li>• Large amount of measurement time due to the manual resistance change.</li> </ul>

- Abet Sun 2000 Solar simulator: This commercial solar simulator illustrated in Fig. 3.26 was used for the determination of the solar performance of a single solar antenna, which is demonstrated in section 6.5 in chapter 6.



Fig. 3.26: Abet Sun 2000 solar simulator.

Detailed information about this solar simulator can be found in [174]. Although this simulator is more professional in comparison to the metal halide solar simulator, it is not as suitable as the metal halide simulator when it comes to the size of the solar antenna to be measured (it can measure solar antennas with a maximum size up to 100 mm x 100 mm) and does not have a temperature control.

# Chapter 4 – RF Ground Plane Solar Integration

## 4.1 Introduction

As mentioned in chapter 1, existing solar antenna integration topologies can be given as follows:

- The use of solar cells as an RF ground plane or as an additional element attached to an existing RF ground plane [35-47],
- The use of solar cells as an RF radiating element or as an additional element attached to an existing RF radiating element [48-57].

In this chapter, the concept of using solar cells as an RF ground plane is investigated in detail. A major disadvantage of using solar cells as an RF ground plane is the shading problem which is caused by the traditionally opaque RF radiating element located above the ground plane, i.e. the integrated solar cell. This has the potential of significantly reducing the solar efficiency and therefore must be addressed in order to achieve optimum solar performance from photovoltaic antennas using RF ground plane solar antenna integration topology. In view of this, meshing the RF radiating element to achieve optical transparency is investigated in this chapter. It is demonstrated that by correctly meshing the RF radiating element, significant enhancement in the solar efficiency can be achieved whilst maintaining similar RF antenna response in comparison to the use of conventional opaque RF radiating elements.

## 4.2 The Integration Topology

In order to understand the integration topology of using solar cells as an RF ground plane in a photovoltaic antenna design, firstly, the structure of a poly-Si solar cell needs to be investigated from an RF perspective.

The RF ground plane integration topology together with the structure of the integrated solar cell is illustrated in Fig. 4.1.

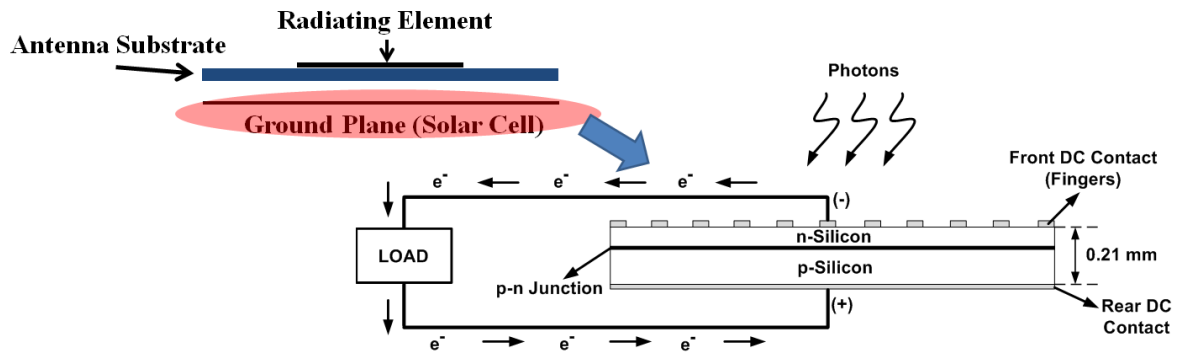


Fig. 4.1: RF ground plane solar antenna integration topology.

In Fig. 4.1, if attention is given to the rear DC metal contact of the cell, it can be seen that it is homogeneous in structure and therefore has the potential to replace the RF ground plane of a planar antenna. The solar antennas demonstrated in this chapter are designed based upon this principle. However, in the case of using the rear contact of a solar cell as an RF ground plane, the RF radiating element, which is opaque in structure, is conventionally required to be placed upon/above the solar cell. This results in the cell being shaded by the RF radiating element, which reduces the solar efficiency. Work carried out in the literature to address this problem involves the use of transparency techniques, which can be given as:

- Meshing the RF radiating element [40, 175]
- Making the RF radiating element out of an optically transparent conductive material, such as AgHT-4 [41].

Although it was successfully demonstrated in [175] that by correctly meshing the radiating element of a microstrip patch antenna, similar radiation characteristics in comparison to a non-meshed conventional counterpart can be achieved, none of the designs proposed in [40, 175] was investigated from a photovoltaic perspective. Therefore, the enhancing effect of the meshing technique on the solar performance has not been studied in the literature. Whilst in [40] a single band meshed solar patch antenna was proposed, the solar measurements of the antenna were not carried out. The meshed microstrip patch antenna demonstrated in [175], which was placed upon a window of a vehicle using the window as a dielectric substrate, on the other hand, was not photovoltaically integrated. For the transparent microstrip patch antenna design in [41], the use of a transparent conductive material is required, which significantly increases the cost of the antenna.

In this chapter, meshed solar antennas integrated with solar cells operating as an RF ground plane are investigated from both RF and photovoltaic perspectives. In addition to the demonstration of the RF antenna results, this enables the demonstration of the enhancement effect of meshing the RF radiating element on the solar performance of photovoltaic antennas using this integration topology. In order to widen the impedance bandwidth, the meshed photovoltaic patch antennas demonstrated in this chapter have a suspended geometry. In addition to the demonstration of the meshing technique for photovoltaic patch antennas, the meshing technique is also applied to a printed monopole antenna for the first time in this thesis for UWB applications.

## **4.3 Transparent Solar Patch Antenna for 2.4 GHz band WLAN and 2.3/2.5 GHz band WiMAX Applications**

Meshing the RF radiating element and making the RF radiating element out of a transparent conductive material have successfully been studied in the literature to address the shading problem [40, 41, 175]. However, in addition to the absence of photovoltaic measurements, a significant disadvantage associated with these designs is the single narrow band -10 dB impedance response, which was reported as 4.3% [40], below 2.5% [41] and below 1.6% [175], respectively, preventing these antennas from being employed in wideband applications.

In order to widen the impedance response whilst providing optical transparency, a suspended meshed microstrip patch antenna integrated with a poly-Si solar cell operating as an RF ground plane is demonstrated in this section. The proposed design provides full coverage for 2.4 GHz band WLAN (2.4-2.484 GHz) and 2.3 GHz band WiMAX (2.3-2.4 GHz) networks whilst covering 2.5 GHz band WiMAX (2.5-2.7 GHz) network partly.

### **4.3.1 Meshed Solar Patch Antenna**

The RF modelling of the proposed suspended meshed solar patch antenna was performed in CST Microwave Studio. The non-optimised initial design of the antenna has a meshed patch element consisting of initially selected vertical (along the patch length) and horizontal (along the patch width) meshing line numbers of 20 with a meshing line width of 0.5 mm as illustrated in Fig. 4.2.

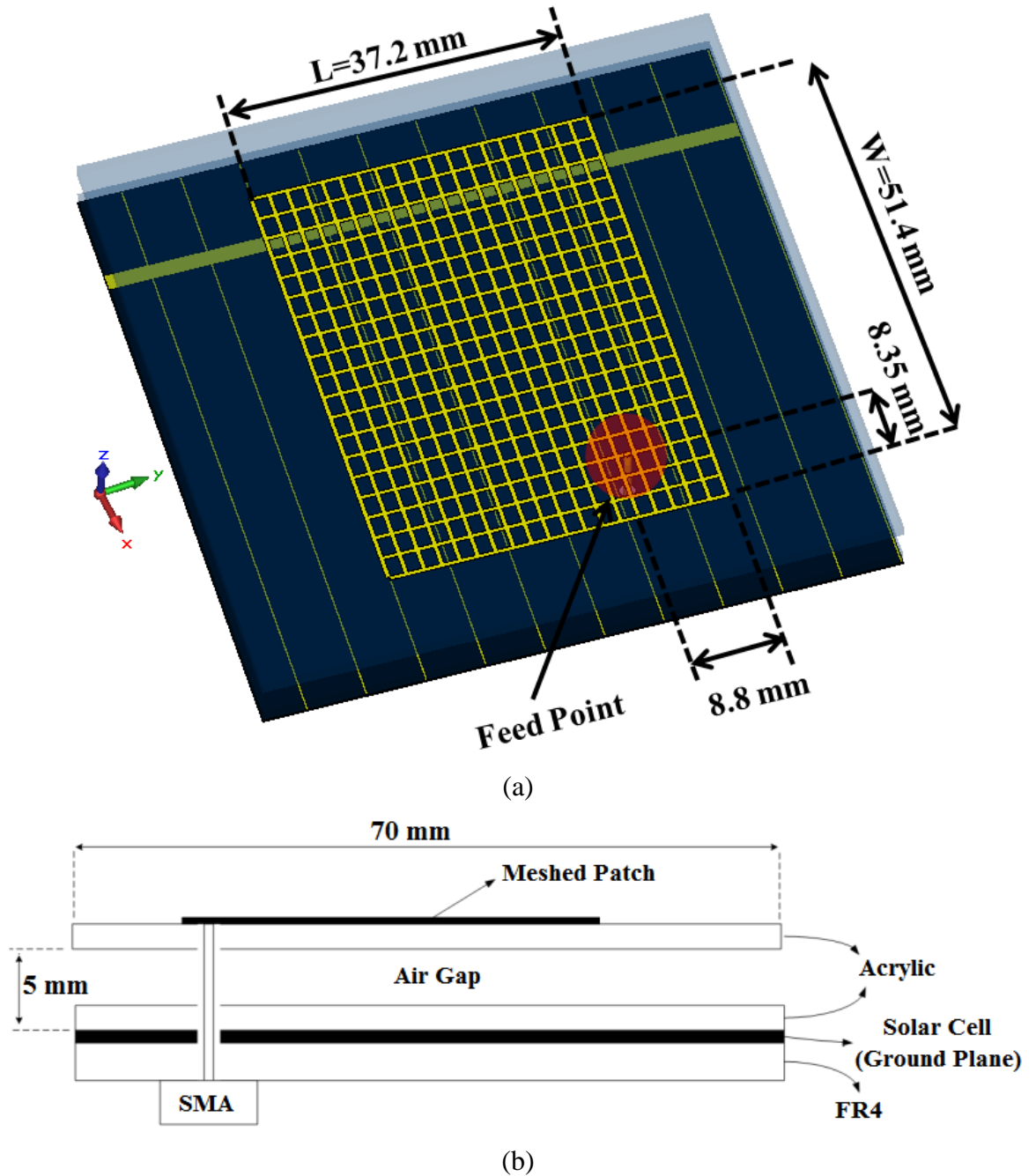


Fig. 4.2: Suspended meshed solar patch antenna with non-optimised initially selected meshing parameters (a) overall view in CST Microwave Studio (b) side view (x-z plane).

As can be seen in Fig. 4.2, the antenna consists of a meshed radiating patch element printed upon a transparent acrylic substrate,  $\epsilon_r=3.6$  and  $\tan\delta=0.015$ , suspended at 5 mm above the integrated poly-Si solar cell operating as an RF ground plane. The poly-Si solar cell is encapsulated between a transparent acrylic layer on top and an FR4 dielectric layer,  $\epsilon_r = 4.3$  and  $\tan \delta = 0.025$ , at the bottom. The suspended geometry results in an effective substrate dielectric constant of  $\epsilon_{reff}=1.97$ . This design is based upon the solid version of the

antenna, which traditionally consists of an opaque non-meshed copper patch radiating element. Therefore, equations (2.26) and (2.29) were used to calculate the patch design parameters,  $L=37.2$  mm and  $W=51.4$  mm in Fig. 4.2(a), at the resonance frequency of 2.45 GHz. In order to determine the position of the coaxial feeding point with a patch input impedance of  $50\Omega$ , which is equal to the impedance at the coaxial SMA port, CST Microwave Studio was used. The position of the optimised feeding point of the antenna is illustrated in Fig. 4.2(a).

A significant challenge that needs to be addressed in this integration topology is the requirement of minimising the shading upon the solar cell caused by the RF radiating element. The use of a conventional solid radiating element, which is optically opaque, is not suitable to achieve optimum solar performance and therefore, transparency techniques need to be applied in order to address this challenge. In this work, meshing the RF radiating patch element is proposed as a solution to this problem [40, 175].

$$Transparency = \frac{Meshed\ Patch\ Surface\ Area}{Solid\ Patch\ Surface\ Area} \quad (4.1)$$

For the meshing process, as given in equation (4.1), whilst it is desired that the number and the width of the meshing lines forming the radiating patch element to be selected as small as possible in order to increase the optical transparency by decreasing the footprint of the radiating patch, the factors given below must also be considered:

- The input impedance versus changing the number of the vertical meshing lines,
- The input impedance versus changing the number of the horizontal meshing lines,
- The input impedance versus changing the width of the vertical and horizontal meshing lines.

Therefore, the first stage in the design process of the proposed meshed solar patch antenna can be given as the determination of the meshing parameters given above, which requires parametric analyses to be carried out in CST Microwave Studio.

### **4.3.2 Solar Patch Antenna with Transparent Meshed Rectangular Radiating Patch Element**

The parametric analyses in CST Microwave Studio were performed in the following order:

- Determination of the optimum width of the horizontal and vertical meshing lines:

During the parametric analysis for the determination of the optimum meshing line width, the line width parameter was varied in the range of 0.2 mm – 1 mm while the other two parameters, the number of vertical and horizontal meshing lines, were initially selected as 20 and remained constant. The meshed microstrip solar patch antennas with varying meshing line widths and the transparency values calculated using equation (4.1) for each configuration are demonstrated in Fig. 4.3.

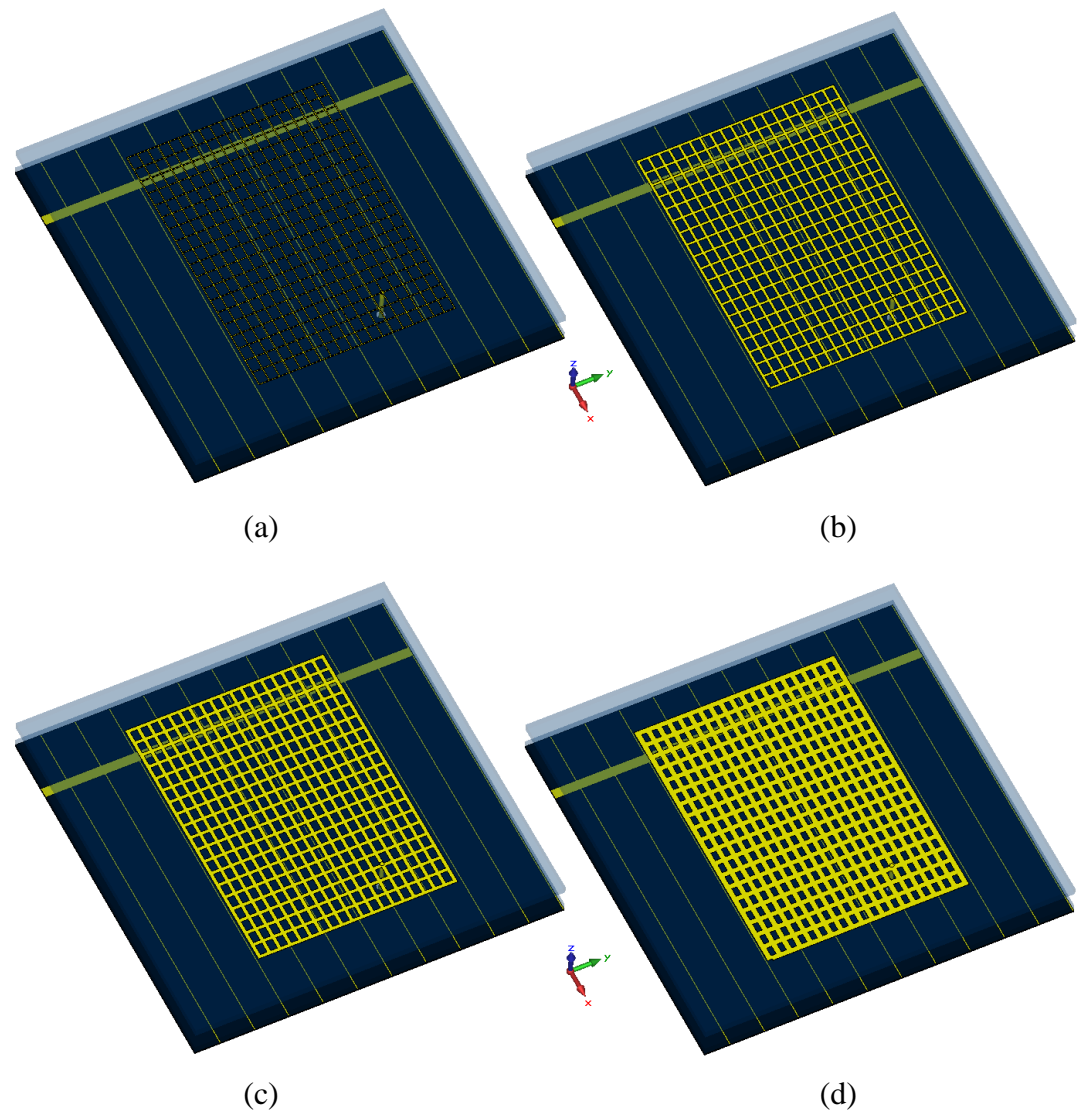
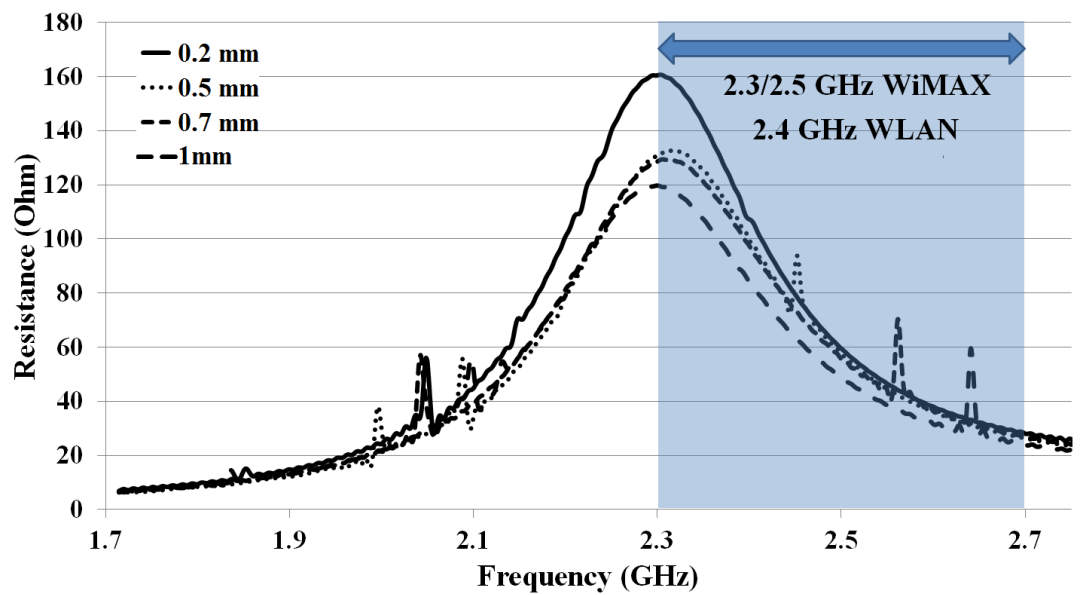
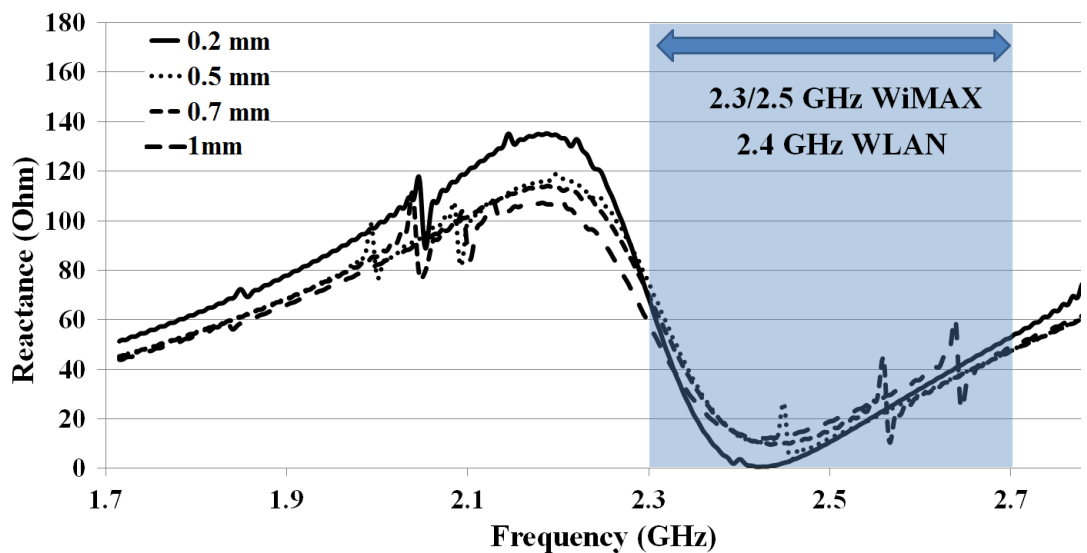


Fig. 4.3: Meshed solar patch antenna with varying meshing line widths (a) line width of 0.2 mm (optical transparency = 81.46%) (b) line width of 0.5 mm (optical transparency = 53.66%) (c) line width of 0.7 mm (optical transparency = 35.13%) (d) line width of 1 mm (optical transparency = 7.32%).

The obtained impedance responses of the antenna versus varying meshing line widths in the range of 0.2 mm-1 mm are demonstrated in Fig. 4.4.



(a)



(b)

Fig. 4.4: Impedance response of the meshed solar patch antenna versus varying line widths (a) resistance (b) reactance.

If attention is given to Fig. 4.4(a), it can be seen that for all investigated meshing line widths the meshed solar patch antenna offers similar resistance curves. As explained earlier, in order to increase the optical transparency of the radiating meshed patch element, the smallest meshing line width, which is 0.2 mm in Fig. 4.4, should be selected. This selection offers an optical transparency of 81.46% calculated using equation (4.1).

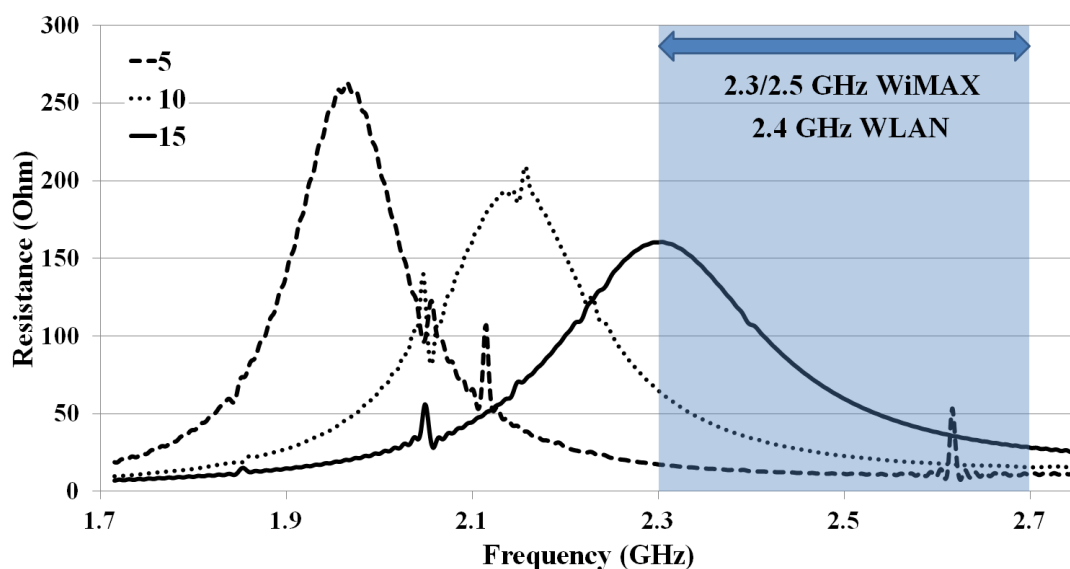
If attention is given to Fig. 4.4(b), similarly, it can be seen that for all investigated meshing line widths the meshed solar patch antenna offers similar reactance responses. Although it can be seen in Fig. 4.4(b) that 0.2 mm meshing line width slightly increases the fluctuation in the reactance response of the antenna, in the frequency range for 2.4 GHz band WLAN and 2.3/2.5 GHz band WiMAX networks, the reactance response with a meshing line width of 0.2 mm is almost identical to the reactance responses with greater meshing line widths, 0.5 mm, 0.7 mm and 1 mm.

In light of the observed resistance and reactance responses, the optimum meshing line width was selected as 0.2 mm.

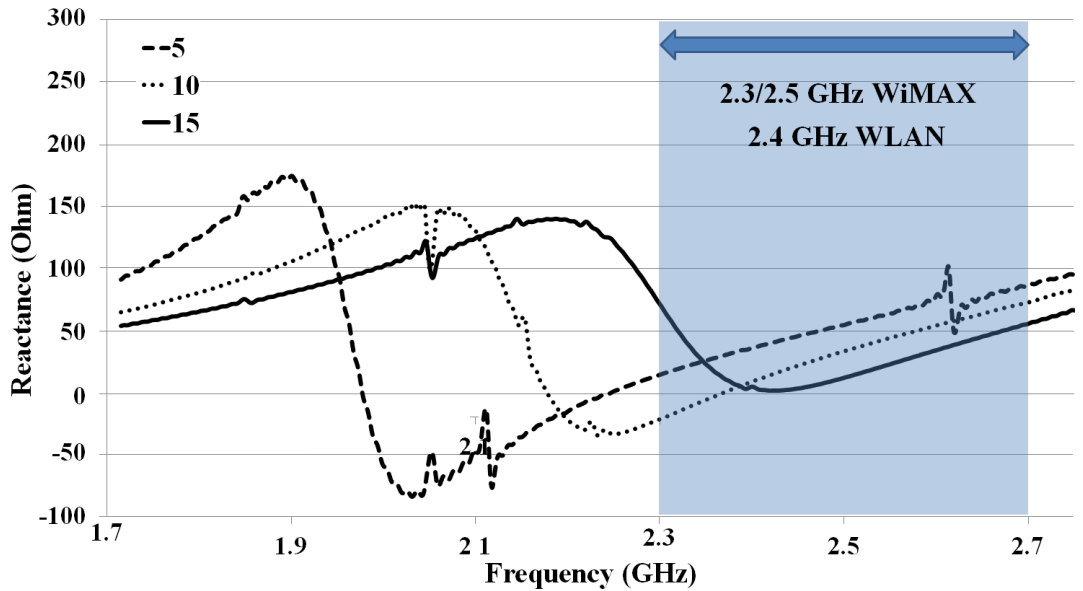
- Determination of the optimum number of vertical meshing lines:

Following the determination of the optimum meshing line width as 0.2 mm, a second parametric analysis was carried out in order to determine the optimum number of the vertical meshing lines. During this analysis, the number of the vertical meshing lines was varied in the range of 5-15 while the meshing line width, which was optimised as 0.2 mm above, and the number of the horizontal meshing lines were fixed at 0.2 mm and 20, respectively.

The input impedance responses of the antenna obtained versus varying number of vertical meshing lines are demonstrated in Fig. 4.5.



(a)



(b)

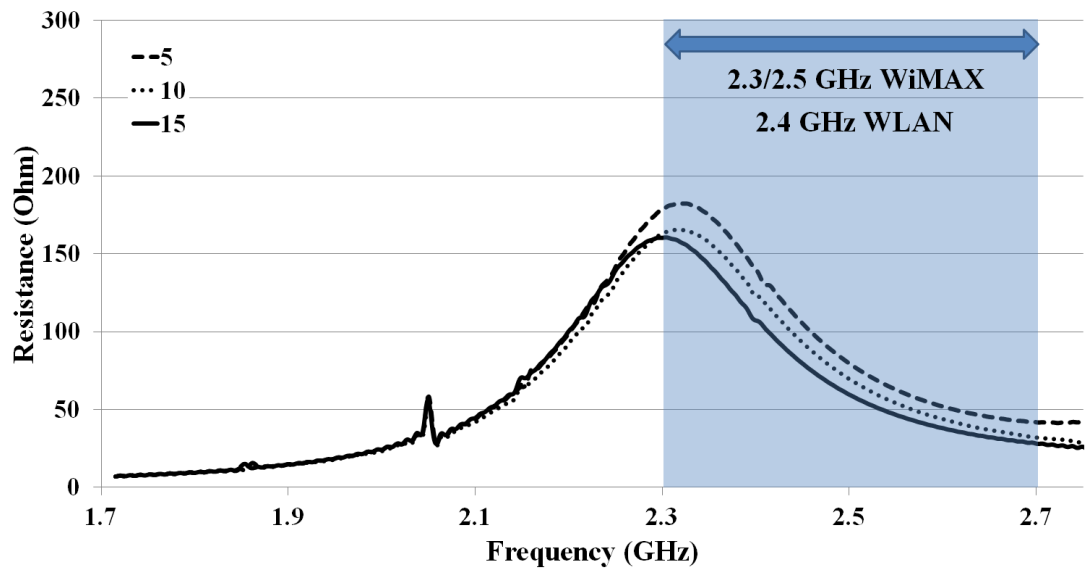
Fig. 4.5: Impedance response of the meshed solar patch antenna versus varying number of vertical meshing lines (a) resistance (b) reactance.

As can be seen in Fig. 4.5(a), varying the number of the vertical meshing lines has a significant effect on the resistance response of the antenna. In Fig. 4.5(a) and Fig. 4.5(b), it can be seen that decreasing the number of the vertical meshing lines shifts the resistance curve of the solar patch antenna to a lower band and increases the fluctuation in the reactance response. Although it is desirable from a photovoltaic perspective that the number of the vertical meshing lines is selected as small as possible to increase the optical transparency of the radiating patch element, due to the requirement of providing coverage at the frequency bands required for 2.4 GHz band WLAN and 2.3/2.5 GHz band WiMAX networks, 15 vertical meshing lines were used in the optimised final design of the meshed solar patch antenna.

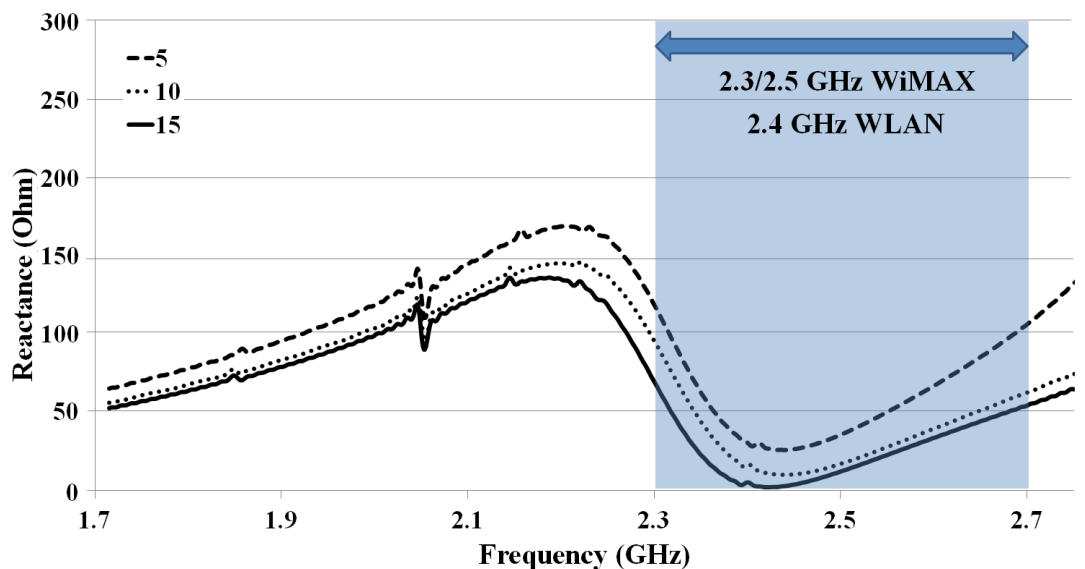
If attention is given to Fig. 4.5(b), it can be seen that similar to the resistance response, decreasing the number of the vertical meshing lines shifts the reactance curve of the antenna to a lower frequency band and increases the fluctuation in the reactance response. For the selected optimum vertical meshing line number of 15, the meshed solar patch antenna has a reactance close to zero in the frequency range of 2.4 GHz band WLAN network, 2.4-2.484 GHz.

- Determination of the optimum number of horizontal meshing lines:

Following the determination of the optimum number of the vertical meshing lines, parametric analysis to determine the optimum number of the horizontal meshing lines was carried out. During the analysis, whilst the number of the horizontal meshing lines was varied in the range of 5-15, the optimised minimum line width and the number of the vertical meshing lines were fixed at 0.2 mm and 15, respectively. The obtained input impedance responses of the antenna versus varying number of horizontal meshing lines are demonstrated in Fig. 4.6.



(a)



(b)

Fig. 4.6: Impedance response of the meshed solar patch antenna versus varying number of horizontal meshing lines (a) resistance (b) reactance.

As can be seen in Fig. 4.6(a), decreasing the number of the horizontal meshing lines slightly increases the fluctuation in the impedance response of the antenna. As this increase becomes more dominant when the number of the horizontal meshing line is selected as 5, especially in the reactance curve given in Fig. 4.6(b), the optimum horizontal meshing line number was determined as 10 in the optimised final design of the meshed solar patch antenna.

If a comparison needs to be made between Fig. 4.5 and Fig. 4.6, it can be seen that the number of the vertical meshing lines has a dominant effect on the input impedance response of the antenna in comparison to the number of the horizontal meshing lines. This is due to the fact that in its fundamental propagation mode,  $TM_{01}$ , the surface current of the antenna mainly flows through the vertical meshing lines along the length of the patch (y-axis in Fig. 4.7) as demonstrated in Fig. 4.7. Therefore, changing the number of the vertical meshing lines brings a dramatic change in the surface current distribution, significantly affecting the impedance response of the antenna as demonstrated in Fig. 4.5 whilst the effect of the number of the horizontal meshing lines remains almost negligible. This outcome provides excellent agreement with the investigation performed in [175].

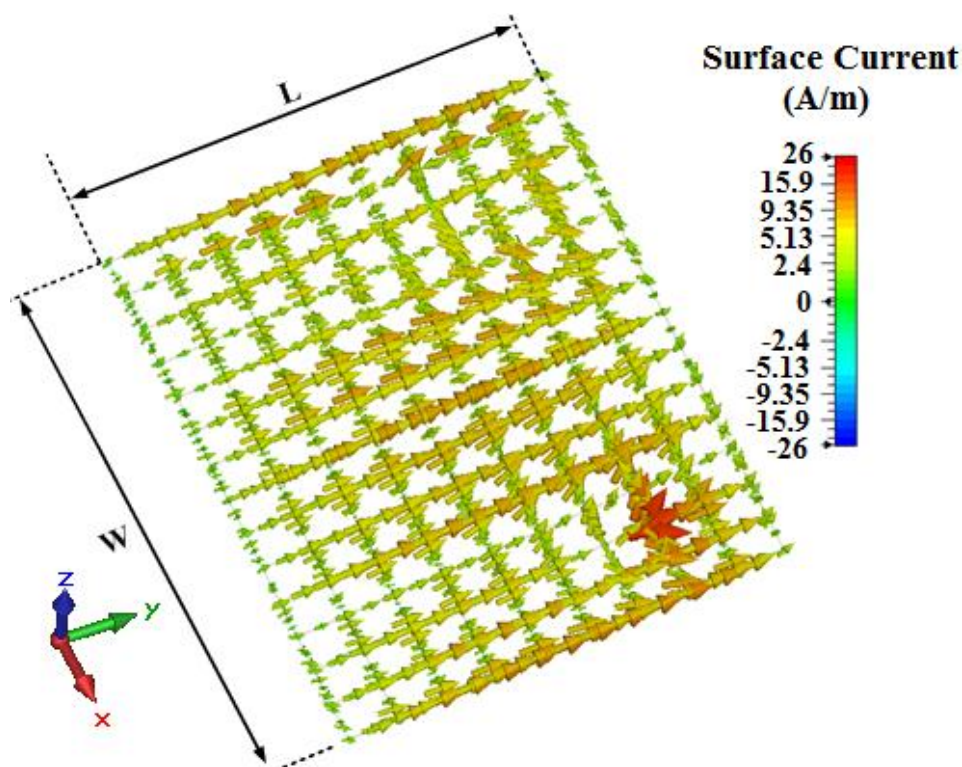


Fig. 4.7: Simulated current distribution across the optimised meshed radiating patch element.

Following the determination of the optimum meshing parameters as:

- Meshing line width=0.2 mm,
- Vertical meshing line number=15,
- Horizontal meshing line number=10,

The optical transparency of the optimised radiating meshed patch was calculated as 88.78% using equation (4.1). The optimised meshed solar patch antenna designed in CST Microwave Studio is demonstrated in Fig. 4.8.

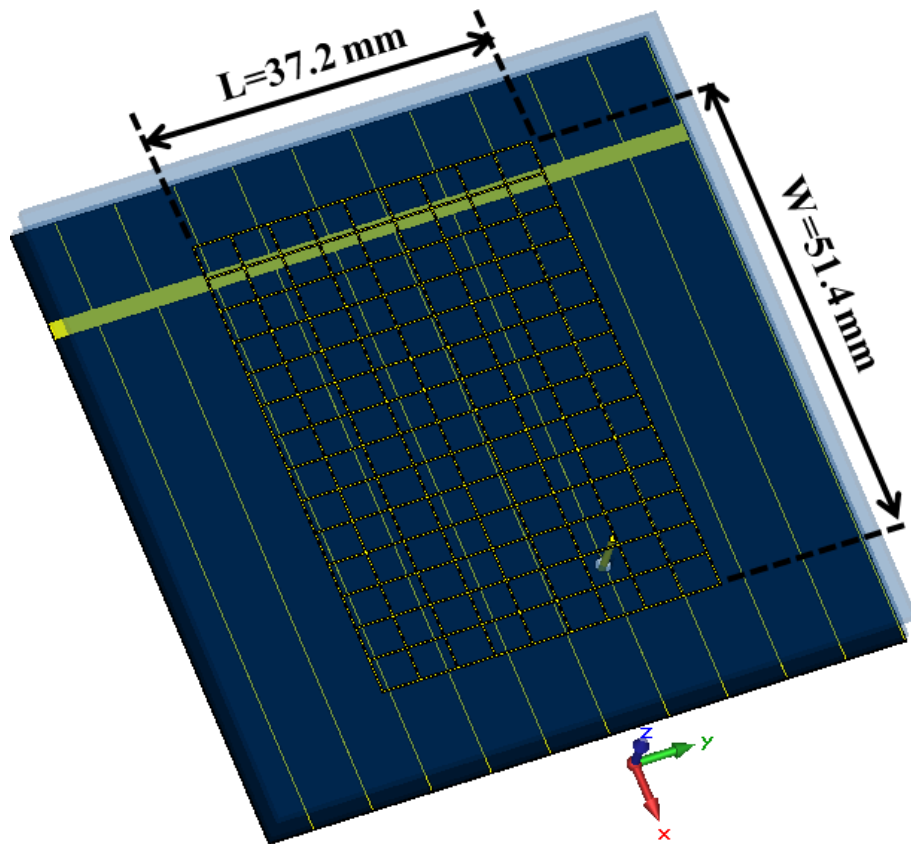


Fig. 4.8: Optimised meshed solar patch antenna in CST Microwave Studio.

The simulated  $S_{11}$  pattern of the proposed meshed solar patch antenna is illustrated in Fig. 4.9.

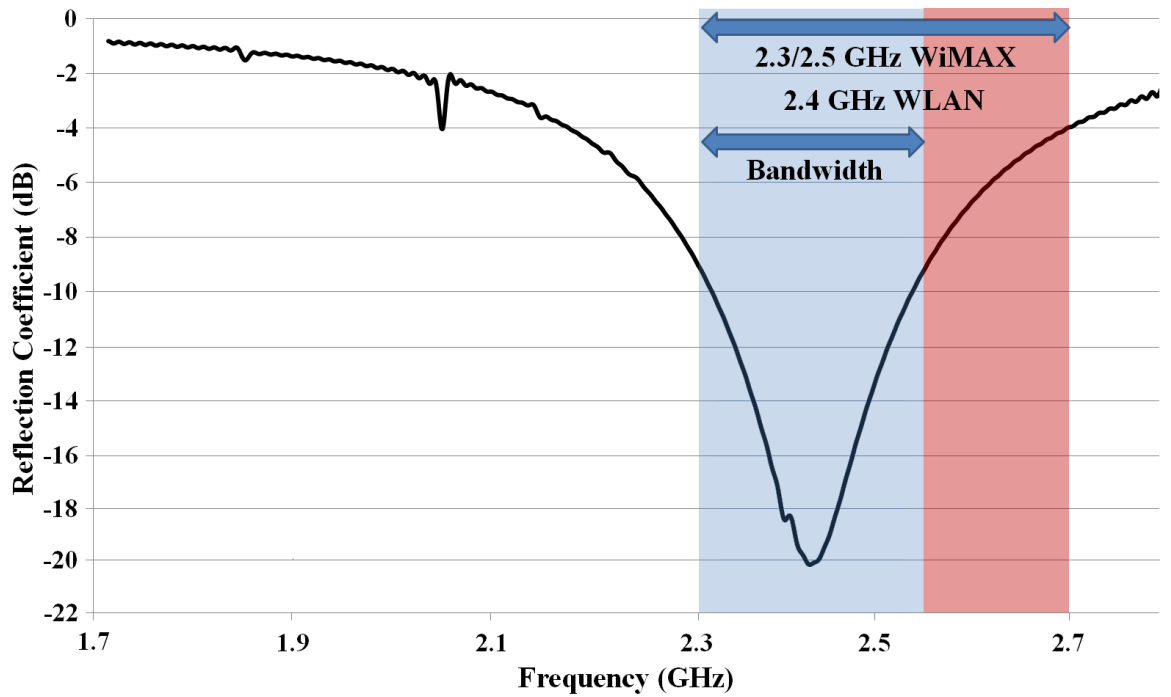
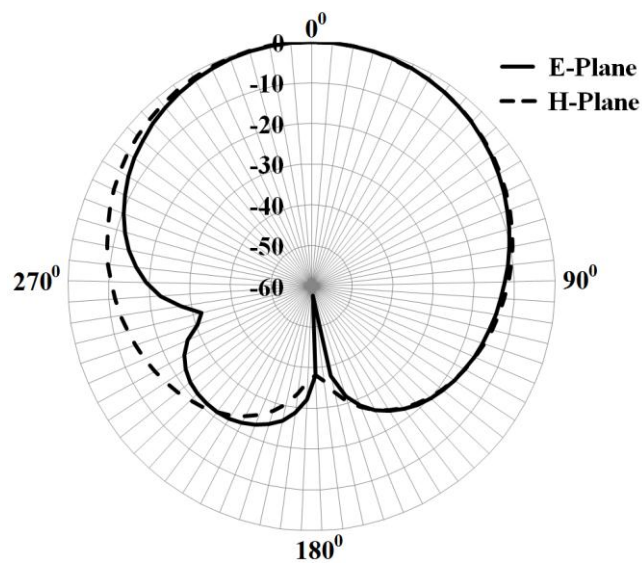


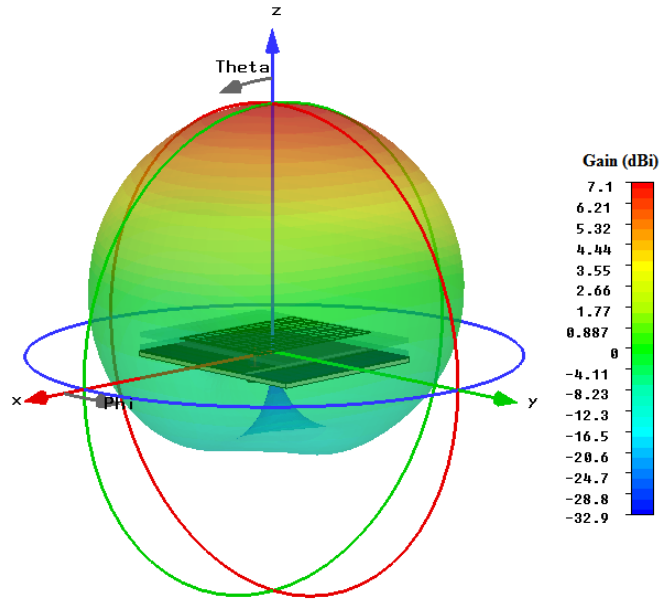
Fig. 4.9: Simulated  $S_{11}$  response of the meshed solar patch antenna.

As can be seen in Fig. 4.9, the antenna resonates at the centre frequency of 2.45 GHz with a -10 dB operational frequency band of 2.3-2.55 GHz, covering 2.4 GHz band WLAN (2.4-2.484 GHz) and 2.3 GHz band WiMAX (2.3-2.4 GHz) networks in full and 2.5 GHz band WiMAX network (2.5-2.7 GHz) partly.

The far-field radiation pattern simulations of the optimised meshed solar patch antenna were performed at 2.45 GHz in CST Microwave Studio. The obtained E-plane (y-z) and H-plane (x-z) patterns are demonstrated in Fig. 4.10(a) whilst the 3D radiation pattern illustrated in Fig 4.10(b).



(a)  
105



(b)

Fig. 4.10: Simulated far-field radiation patterns of the meshed solar patch antenna (a) E-plane and H-plane far-field radiation patterns (b) 3D far-field radiation pattern.

As can be seen in Fig. 4.10, the meshed solar patch antenna has a broadside radiation pattern in the E-plane and H-plane. The  $-3$  dB beamwidths were recorded as  $71.6^\circ$  and  $83.3^\circ$  in the E-plane and in the H-plane, respectively, with a maximum gain of 7.1 dBi observed in both planes.

Following the demonstration of the meshing technique, the solar patch antenna with a conventional solid rectangular patch radiating element was also designed in order to provide a comparison between the antenna characteristics of the proposed solar patch antenna with the transparent meshed and the conventional solid radiating patches, respectively. The solar patch antenna with the conventional solid radiating patch element is demonstrated in Fig. 4.11.

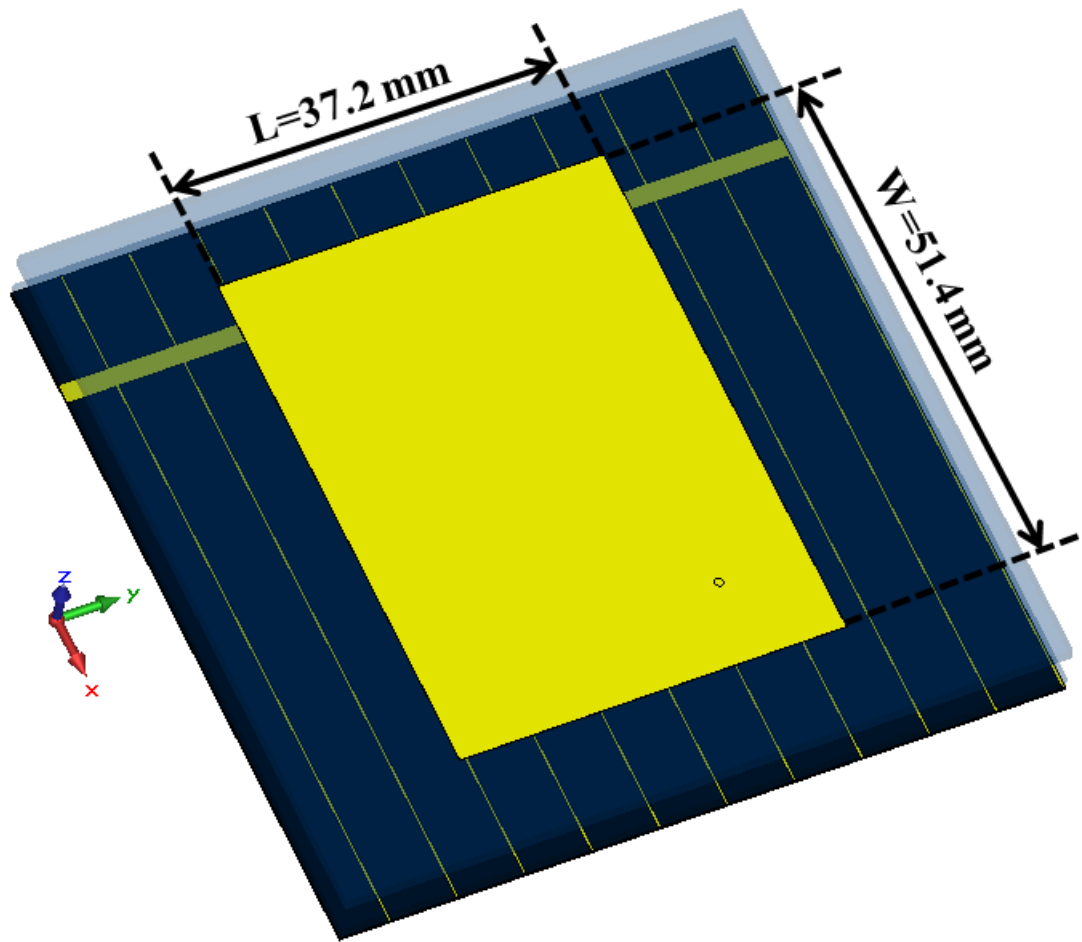
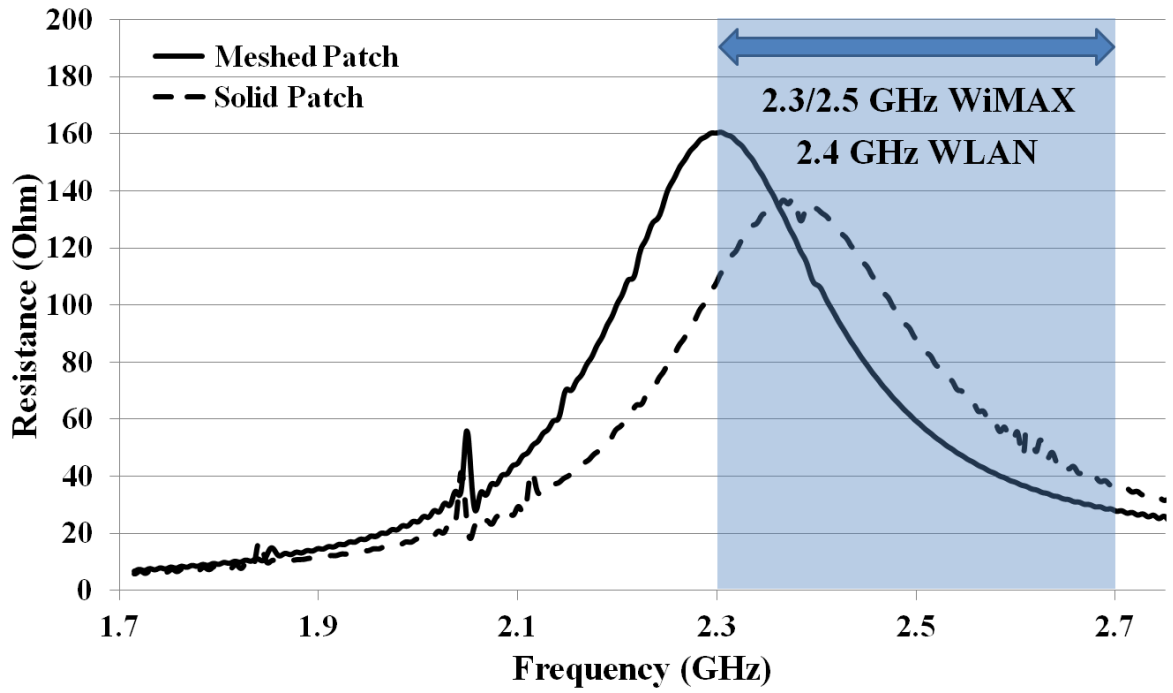
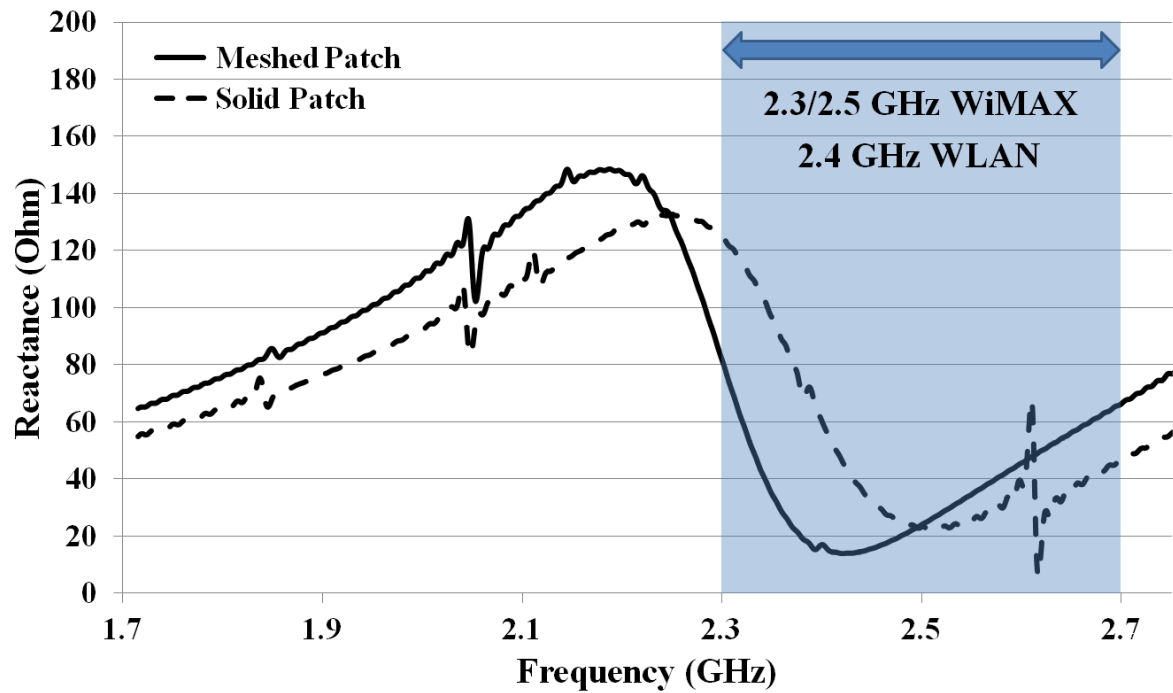


Fig. 4.11: Solar patch antenna with a conventional solid radiating patch element.

The simulated input impedance response of the antenna with the conventional solid patch is illustrated in Fig. 4.12(a) in comparison to the input impedance response of the optimised meshed solar patch antenna.



(a)



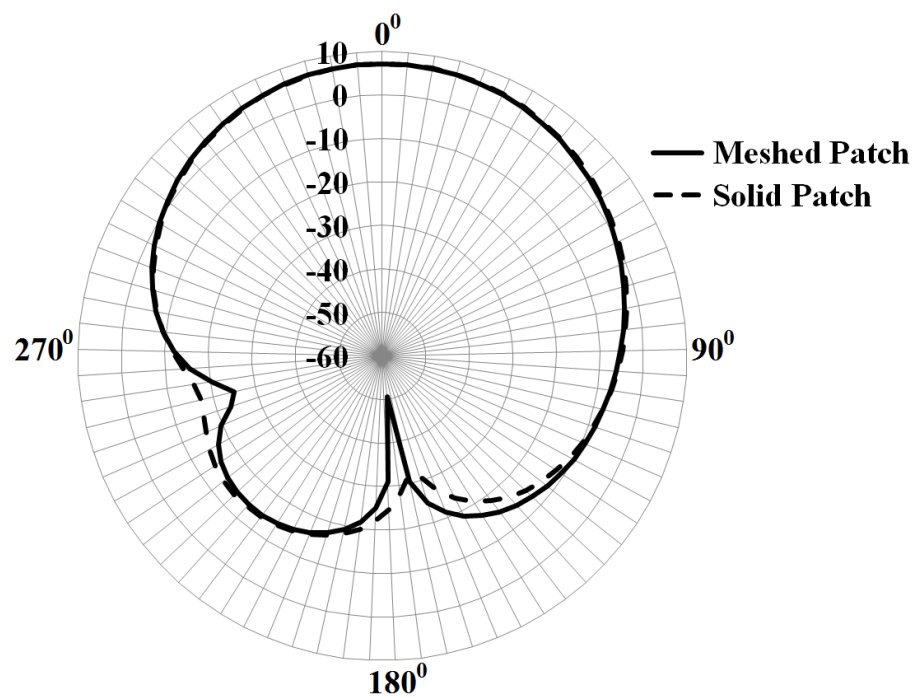
(b)

Fig. 4.12: Impedance response of the solar patch antenna with the proposed meshed radiating patch element and the conventional solid radiating patch element, respectively (a) resistance (b) reactance.

The obtained resistance and reactance curves illustrated in Fig. 4.12 provide good agreement with the results illustrated in Fig. 4.4. In Fig. 4.4, it was shown that decreasing the meshing line width slightly increases the fluctuation in the resistance and the reactance

responses of the antenna. As can be seen in Fig. 4.12, the optimised meshed solar patch antenna, which consists of 15 vertical and 10 horizontal meshing lines, has a slight increase of 11.2% and 7.4% in the fluctuation of its resistance and reactance responses in comparison to the conventional solid counterpart. In addition to this, the proposed meshed solar patch antenna offers a frequency shift of 65 MHz in the impedance response as illustrated in Fig. 4.12.

In order to demonstrate the effect of meshing the RF radiating element on the far-field radiation patterns, E-plane and H-plane radiation pattern simulations of the solar antenna with the proposed meshed and conventional non-meshed patches were carried out, respectively. The obtained patterns are demonstrated in Fig. 4.13.



(a)

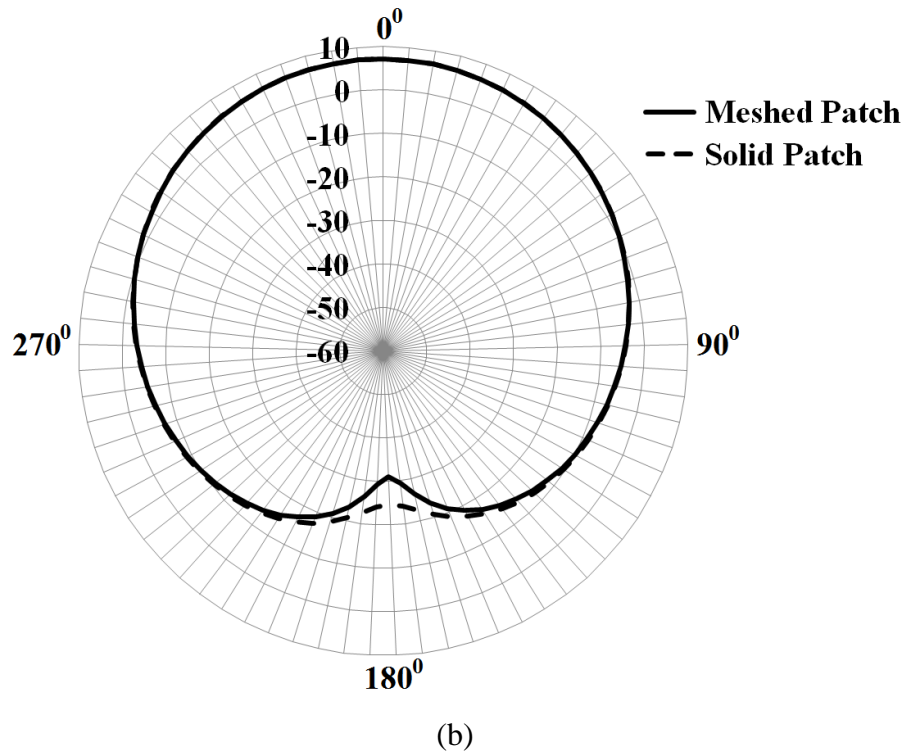


Fig. 4.13: Far-field radiation patterns of the solar patch antenna with meshed and conventional solid patches, respectively (a) E-plane (b) H-plane.

As can be seen in Fig. 4.13, correctly meshing the RF radiating patch element has a negligible effect on the E-plane and H-plane far-field radiation patterns of the proposed solar patch antenna.

### 4.3.3 Effect of Photovoltaic Integration on the Resonance Characteristics of the Antenna

In order to investigate the effect of the photovoltaic integration of the proposed meshed solar patch antenna on the  $S_{11}$  response, two prototypes of the antenna, with and without the poly-Si silicon solar cell, were designed in CST Microwave Studio as illustrated in Fig. 4.14.

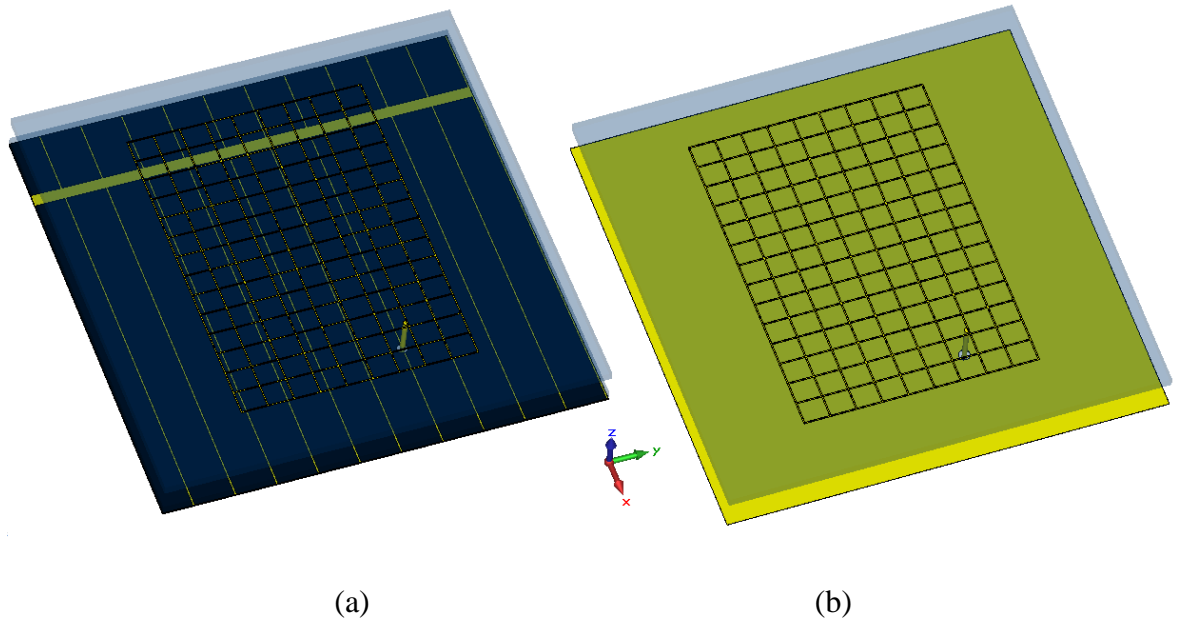


Fig. 4.14: Meshed solar patch antenna (a) with solar cell (b) without solar cell (conventional copper ground plane).

In Fig. 4.15, a comparison is made between the  $S_{11}$  patterns of the proposed meshed solar patch antenna with and without the integrated solar cell.

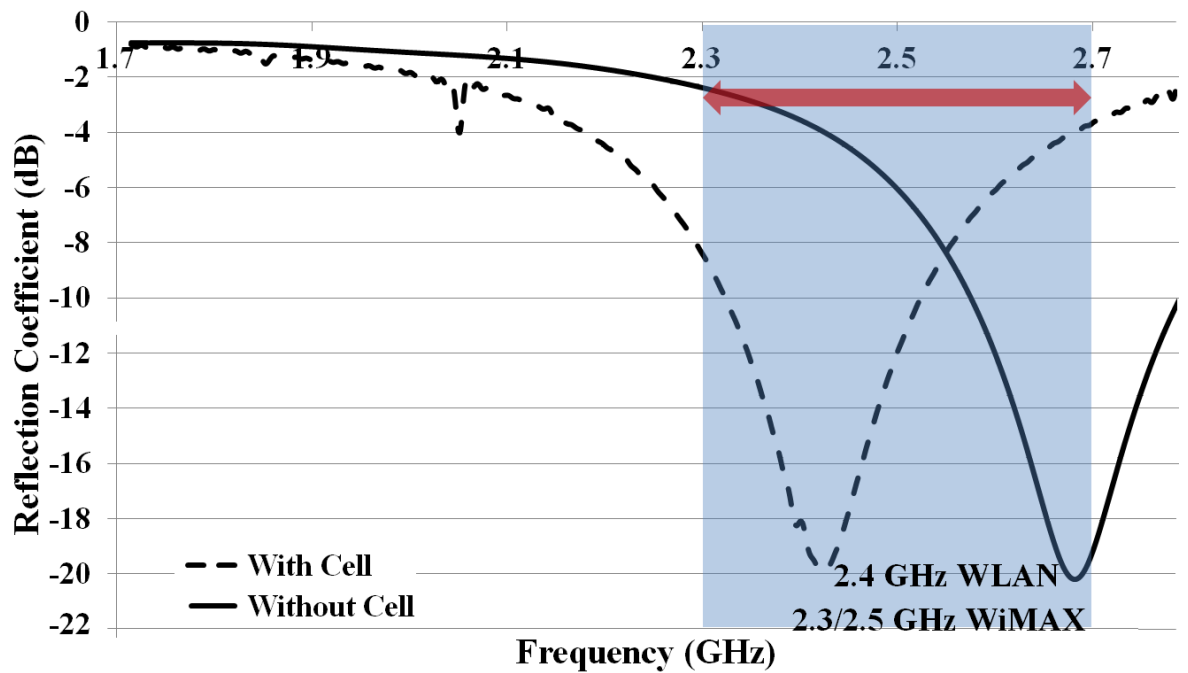


Fig. 4.15: Simulated  $S_{11}$  patterns of the proposed meshed solar patch antenna with and without the encapsulated poly-Si solar cell operating as an RF ground plane.

As can be seen in Fig. 4.15, the integration of the meshed patch antenna with the encapsulated poly-Si solar cell shifts resonance frequency. While the transparent patch

antenna without the encapsulated silicon solar cell, i.e. consisting of a traditional copper ground plane replacing the encapsulated silicon solar cell, resonates at the centre frequency of 2.68 GHz, the photovoltaic version of the antenna resonates at the frequency of 2.43 GHz, corresponding to a frequency shift by 250 MHz, 9.3%. Moreover, the meshed solar patch antenna with the conventional ground plane operates across the frequency band of 2.57-2.78 GHz with a -10 dB impedance bandwidth 210 MHz, which is 40 MHz narrower in comparison to the proposed meshed solar patch antenna using the encapsulated silicon solar cell as an RF ground plane.

Following the observation of the shift in the resonance frequency of the antenna as a result of the photovoltaic integration, further investigations were performed in order to find out the reason behind the frequency shift. To this end, simulations into the effect of the solar cell encapsulation elements, i.e. acrylic layer on top and FR4 dielectric layer at the bottom, on the  $S_{11}$  performance of the antenna were carried out. Fig. 4.16 illustrates the  $S_{11}$  patterns of the proposed meshed solar patch antenna obtained,

- with encapsulation,
- without encapsulation,
- with only acrylic layer upon the cell,
- with only FR4 dielectric layer under the cell.

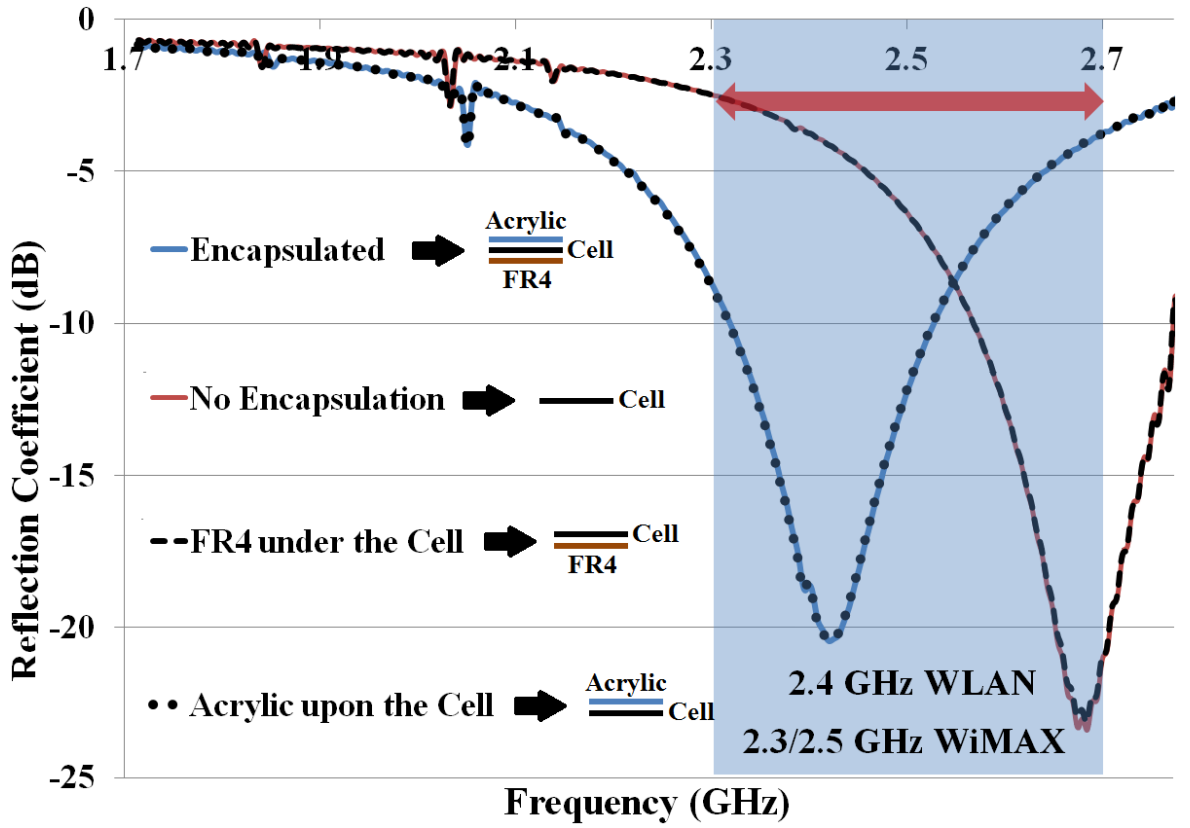


Fig. 4.16: The effect of the encapsulation elements on the  $S_{11}$  performance of the meshed solar patch antenna.

As can be seen in Fig. 4.16, the main factor shifting the resonance frequency of the proposed meshed solar patch antenna is the presence of the acrylic layer placed upon the solar cell operating as an RF ground plane since. This is due to the fact that the frequency shift is observed only when the acrylic layer is included and excluded whilst all other prototypes in Fig. 4.16 include the silicon solar cell integrated with the antenna. The presence of the acrylic layer with a dielectric constant of  $\epsilon_r=3.6$  between the suspended radiating meshed patch element and the ground plane, changes the effective substrate dielectric constant to  $\epsilon_{reff}=1.97$  and reduces the wavelength within the effective substrate, which is now a combination of air and acrylic layer in comparison to pure air, as follows:

$$\lambda_{eff} = \frac{\lambda}{\sqrt{\epsilon_{reff}}} \quad (4.2)$$

Whilst the physical length of the meshed radiating patch element remains the same, due to the decreased wavelength, the electrical length of the meshed patch is now larger shifting the operational frequency band of the antenna to a lower frequency band as demonstrated in Fig. 4.16.

If a comparison is made between Fig. 4.15 and Fig. 4.16, it can clearly be seen that the resonance frequency remains the same for the prototypes given below:

- Antenna without the solar cell,
- Antenna with the solar cell including only the FR4 dielectric layer under the cell,
- Antenna with non-encapsulated solar cell.

Therefore, it can be concluded that the use of the poly-Si solar cell as an RF ground plane without the acrylic layer on top has a negligible effect on the  $S_{11}$  response of the antenna.

### 4.3.4 Effect of Meshing the Radiating Patch Element on the Photovoltaic Performance

In order to demonstrate the effect of meshing the suspended radiating patch element to create a transparent solar path upon the solar cell on the solar efficiency, the photovoltaic measurements of the prototypes given below were performed.

- A fabricated prototype of the parametrically optimised meshed transparent radiating patch element printed on an acrylic substrate placed upon a solar panel as demonstrated in Fig. 4.17. The patch was cut out of a copper sheet and placed upon the acrylic substrate. The meshing of the patch was carried out using a Stanley utility knife.



Fig. 4.17: Proposed transparent meshed patch element placed upon a poly-Si solar panel for solar measurements in a solar chamber.

- A traditional non-meshed solid radiating patch printed on an acrylic substrate placed upon the solar panel as demonstrated in Fig. 4.18,



Fig. 4.18: Solid patch element placed upon a poly-Si solar panel for solar measurements in a solar chamber.

- Solar panel on its own without any elements placed upon as demonstrated in Fig. 4.19,



Fig. 4.19: A poly-Si solar panel without any elements placed upon for solar measurements in a solar chamber.

The solar panel used in these measurements consists of 18 series-connected poly-Si solar cells. The open-circuit voltage,  $V_{OC}$ , and short-circuit current,  $I_{SC}$ , readings of the solar panel in the prototypes given above were measured in the metal halide solar simulator, which was described in chapter 3, providing an illumination density of  $1000\text{W}/\text{m}^2$ . The observed open-circuit voltage and short-circuit current values for the configurations given

above were then compared to the original performance data of the solar panel. i.e. the solar panel on its own, as demonstrated in Table 4.1.

Table 4.1: Solar performance readings.

<b>Configuration</b>	<b>V<sub>OC</sub> (V)</b>	<b>I<sub>SC</sub> (mA)</b>
Panel (with no element placed above)	10.86	219.7
Panel (with transparent patch) – Optical transparency: 88.78%	10.61	213.4
Panel (with opaque patch) – Optical Transparency: 0%.	10.41	167.3

As can be seen in Table 4.1, for the solar panel with no element placed above, the open-circuit voltage and short-circuit current were measured as 10.86 V and 219.7 mA, respectively. When the proposed parametrically optimised meshed patch printed on a transparent acrylic substrate was placed upon the panel, the open-circuit voltage and short-circuit current readings were recorded as 10.61 V and 213.4 mA, corresponding to a slight decrease of 2.3% in the open-circuit voltage and 2.87% in the short-circuit current. However, when a conventional non-meshed solid copper patch was used, the open-circuit voltage and short-circuit current dropped to 10.41 V and 167.3 mA, respectively. Whilst the drop in the open-circuit voltage, 4.1%, can be considered small, a decrease of 23.6% in the short-circuit current demonstrates the vital importance of meshing the radiating element in order to maintain a high solar efficiency.

## **4.4 A Meshed Multiband Solar Patch Array**

### **Antenna**

A significant disadvantage associated to the reported research on photovoltaic antennas in the literature is the single band resonance response, which prevents these antennas from covering the frequency bands required for multiband applications. Although it was demonstrated in the previous section that by using a suspended geometry it is possible to achieve a photovoltaic antenna resonance response to cover multi applications, i.e. 2.4 GHz band WLAN and 2.3/2.5 GHz band WiMAX, single band resonance still remains as a

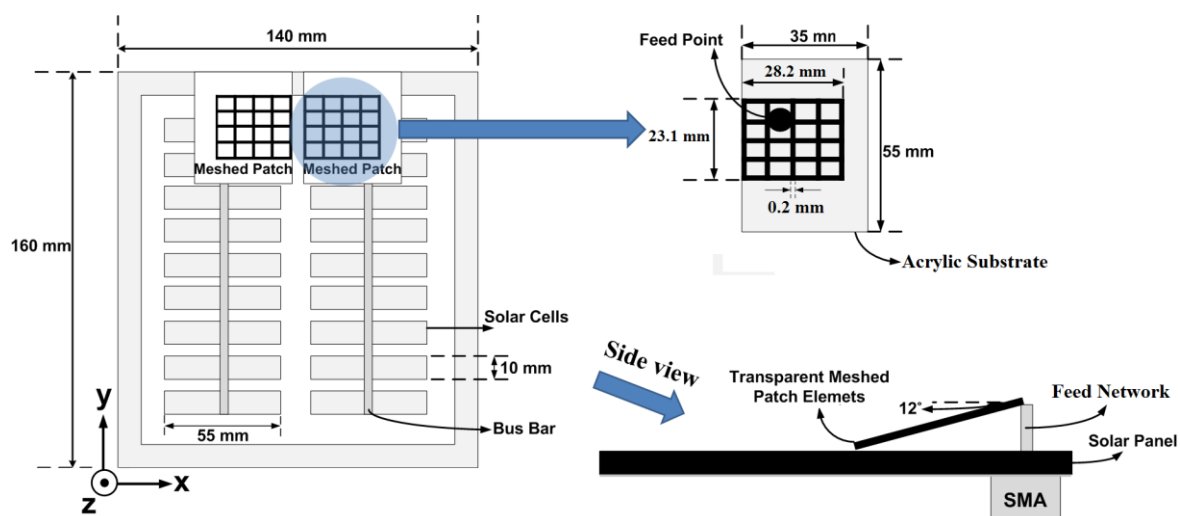
challenge to be addressed for multiband applications. To this end, in this section, a new meshed solar patch array antenna resonating at multiple frequency bands required for GSM/UMTS 1800 (1.71-1.88 GHz), GSM/UMTS 1900 (1.85-1.99 GHz), 3.5 GHz band WiMAX (3.4-3.6 GHz) and C-band applications is demonstrated. While the coupling between the radiating array element and the ground plane is used to achieve the multiband response, the array geometry is used to enhance the gain performance of the antenna for long-range applications.

#### 4.4.1 Design and Fabrication of the Meshed Solar Patch Array Antenna

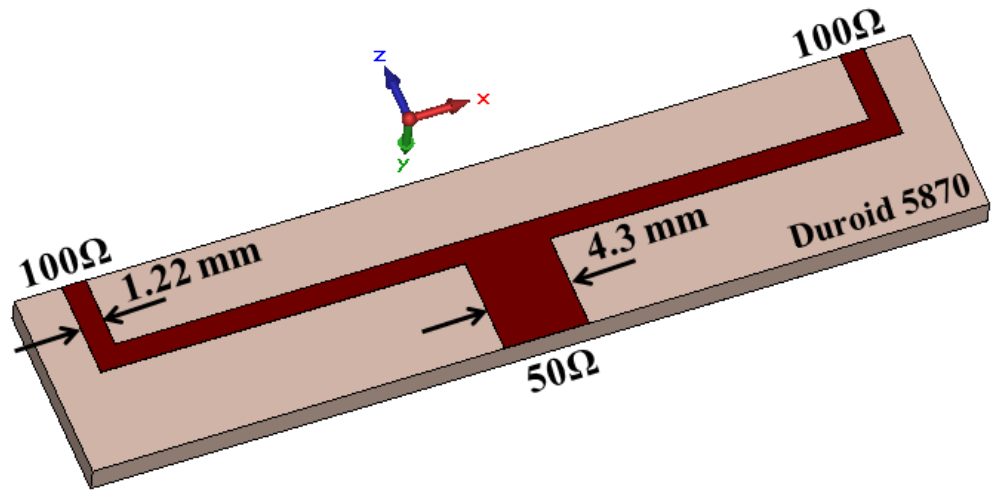
The fabricated meshed solar patch array antenna is shown in Fig. 4.20 whilst the designed version in CST Microwave Studio illustrated in Fig. 4.21.



(a)



(b)



(c)

Fig. 4.20: Meshed solar patch array antenna (a) fabricated antenna (b) antenna geometry (c) feeding network.

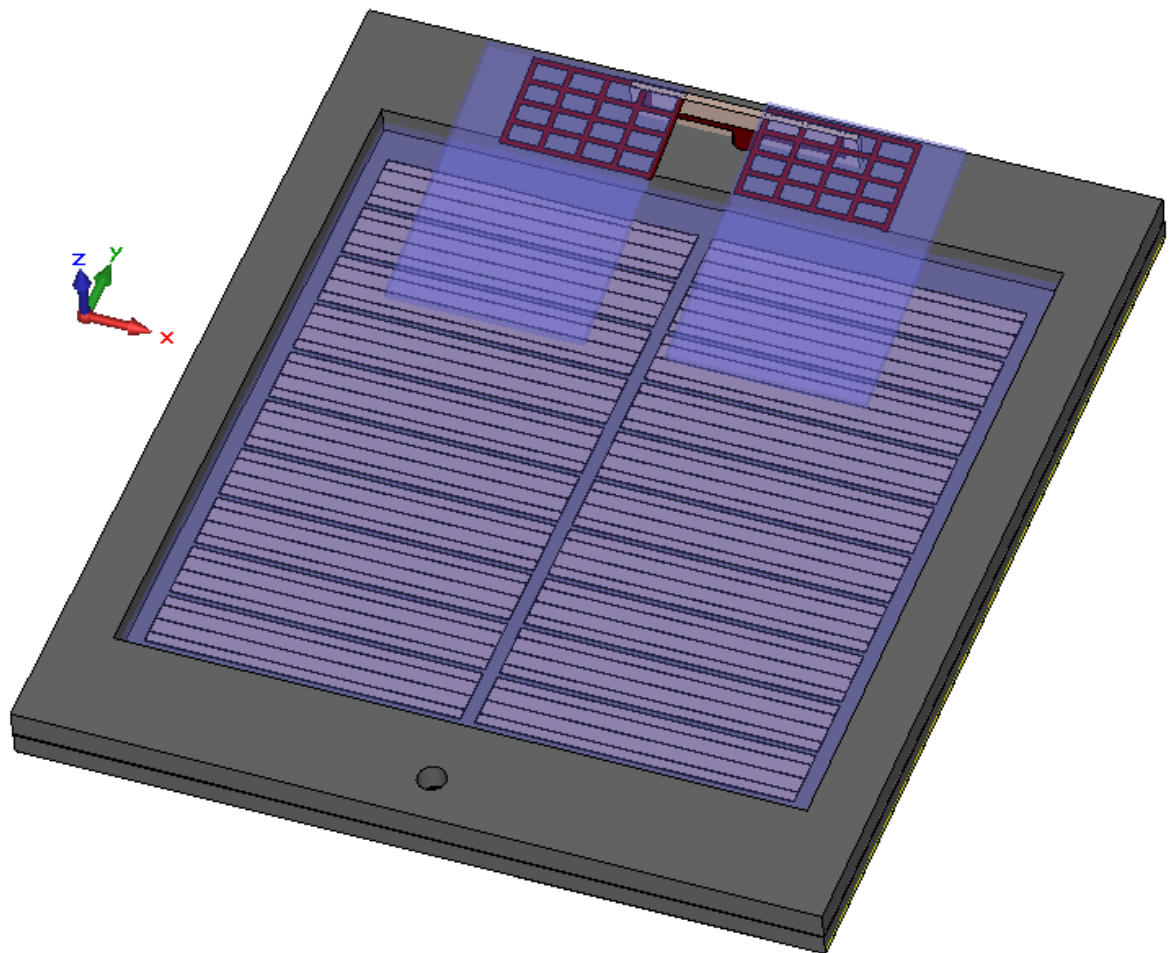


Fig. 4.21: The meshed microstrip patch array antenna designed in CST Microwave Studio.

As can be seen in Fig. 4.20 and Fig. 4.21, the proposed meshed solar patch array antenna consists of an array of two meshed copper patch elements each printed on a 2 mm thick

transparent acrylic substrate,  $\epsilon_r=3.6$  and  $\tan\delta=0.015$ . Fig. 4.20(b) provides a closer look at the structure of a single radiating meshed patch element within the proposed array configuration. Under the radiating meshed patch elements, a commercial poly-Si solar panel was introduced to be used as an RF ground plane element as illustrated in Fig. 4.20. The solar panel consists of 18 series connected poly-Si solar cells, each has dimensions of 55 mm x 10 mm as can be seen in Fig. 4.20(b). The rear contacts of these poly-Si solar cells within the panel form the ground plane of the proposed antenna. Placed upon the solar cells, the poly-Si solar panel has a 2 mm thick acrylic encapsulation material. The meshed patch array was suspended at 6 mm above the ground plane, resulting in an effective substrate dielectric constant of  $\epsilon_{reff}=2.3$ .

For the design of the meshed radiating patch elements in the proposed array, first, the design of the conventional solid version of the patches was carried out. Using equations (2.26) and (2.29), the width and the length of the patches were calculated as  $W=28.2$  mm and  $L=23.1$  mm at the frequency of 3.5 GHz. Following the design of the solid patches, the same meshing optimisation procedure as adopted in the previous section was applied in CST Microwave Studio in order to determine the optimum meshing parameters. As a result of the optimisation process performed for each radiating patch element within the array, the meshing parameters were obtained as follows:

- The meshing line width was determined as 0.2 mm,
- The number of the vertical meshing lines was determined as 5,
- The number of the horizontal meshing lines was determined as 5.

Following the determination of the meshing parameters in CST Microwave Studio, the transparency of each meshed radiating patch element within the array was calculated as 93.3% using equation (4.1).

As can be seen in Fig. 4.20(c), the meshed patch array is fed through a microstrip feeding network consisting of 50 $\Omega$  and 100 $\Omega$  microstrip transmission lines printed upon a low-loss 1.5 mm thick RT/Duroid 5870 substrate,  $\epsilon_r=2.33$  and  $\tan\delta=0.0012$ . The microstrip transmission line with a characteristic impedance of 50 $\Omega$  has a width of 4.3 mm and is divided into two microstrip sub-transmission lines, each has a width of 1.22 mm and a characteristic impedance of 100 $\Omega$ . These 100 $\Omega$  microstrip transmission lines are connected to the meshed patch array elements at the feeding point demonstrated in Fig. 4.20(b),

where the meshed patch input impedance was obtained as  $100\Omega$  in CST Microwave Studio.

Investigation into the effect of meshing a conventional solid copper microstrip patch radiating element on the impedance response and the radiation characteristics of an antenna was carried out in the previous section and in [175], and it was demonstrated that correctly meshing the radiating patch element itself does not have a significant effect on the radiation characteristics of microstrip patch antennas. However, different from the previous section, another factor to be considered in the design process of this meshed solar patch array antenna is the separation between the radiating patch elements forming the array due to the coupling. In order to minimise the coupling between the radiating patch elements, parametric analysis was carried out in CST Microwave Studio and the obtained  $S_{11}$  responses of the antenna versus varying separation distances between the radiating meshed patch elements are demonstrated in Fig. 4.22.

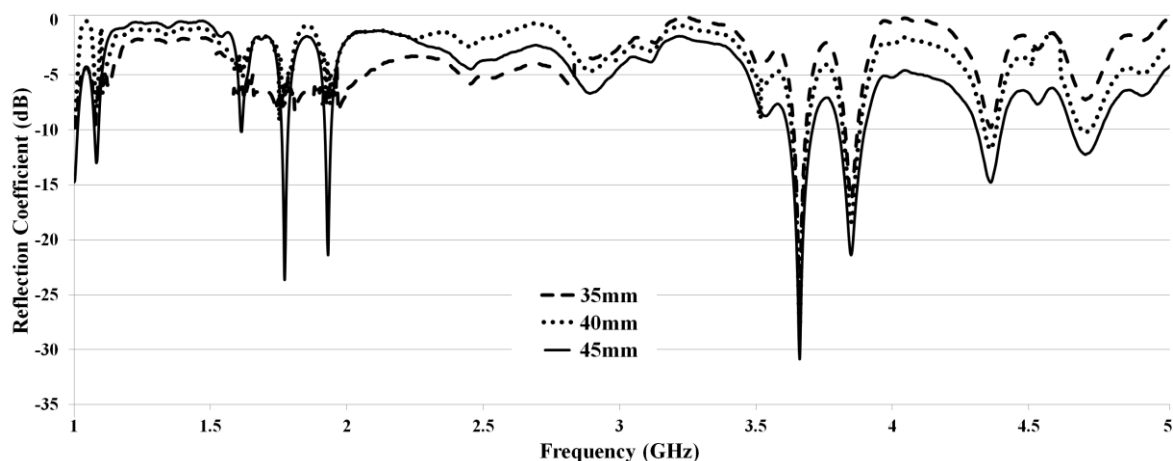


Fig. 4.22: Simulated  $S_{11}$  responses of the antenna versus varying distances between the meshed radiating patch elements within the array.

As can be seen in Fig. 4.22, the distance between the meshed radiating patch elements of the array has a serious effect on the  $S_{11}$  response of the antenna and therefore needs to be determined carefully. It can be seen in Fig. 4.22 that a separation distance of less than 45 mm significantly deteriorates the multiband resonance characteristics of the proposed solar array antenna and therefore the optimum distance between the meshed radiating meshed patch elements was selected as 45 mm, which is larger than the quarter-wavelength at the frequency of 1.92 GHz, 39.06mm, in order to minimise the coupling.

As illustrated in Fig. 4.20(b), a patch tilt angle of  $12^\circ$  was introduced in the suspended geometry of the meshed patch array antenna in the y-z plane, resulting in an enhancement in the multiband  $S_{11}$  response as a result of the coupling between the radiating meshed patches and the ground plane. Due to the difficulty of performing an analytical modelling of the coupling between these two elements, parametric analysis was carried out in CST Microwave Studio in order to optimise the introduced patch tilt angle. The simulated  $S_{11}$  responses of the meshed solar patch array antenna versus varying tilt angles in the range of  $0^\circ$ - $18^\circ$  are demonstrated in Fig. 4.23.

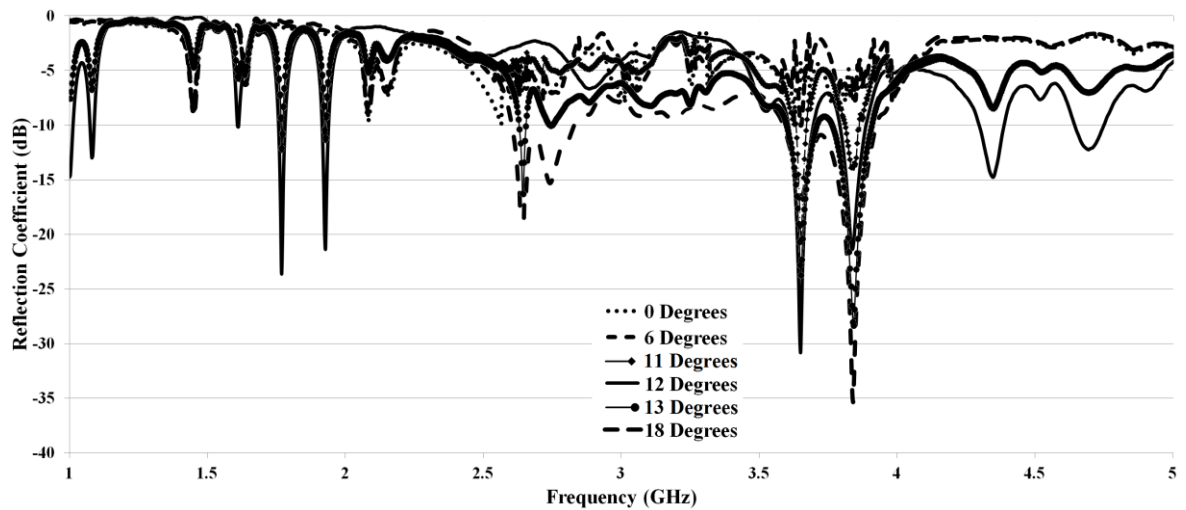


Fig. 4.23: Simulated  $S_{11}$  responses of the antenna versus varying patch tilt angle.

As can be seen in Fig. 4.23, the proposed meshed solar patch array antenna with a patch tilt angle of  $12^\circ$  offers optimum multiband resonance characteristics enabling the proposed solar antenna to be employed in mobile, UMTS and WiMAX band applications. Selecting a patch tilt angle smaller than  $12^\circ$  significantly affects the coupling between the radiating patch elements and the ground plane, and seriously degrades the  $S_{11}$  response of the antenna across the entire investigated frequency band. Similarly, introducing a tilt angle of greater than  $12^\circ$  deteriorates the resonance response of the antenna in the low and high bands while offering superior resonance characteristics in the mid-band in comparison to the proposed meshed solar patch array antenna with a tilt angle of  $12^\circ$ .

## 4.4.2 Measurement Results and Discussion

### 4.4.2.1 Antenna Measurements

The  $S_{11}$  simulations of the meshed solar patch array antenna were performed in CST Microwave Studio whilst the measurements were carried out using a vector network analyser (VNA), Agilent E8634B. The simulated and measured  $S_{11}$  patterns of the fabricated meshed solar patch array antenna at the frequency band of 900 MHz - 6 GHz are shown in Fig. 4.24.

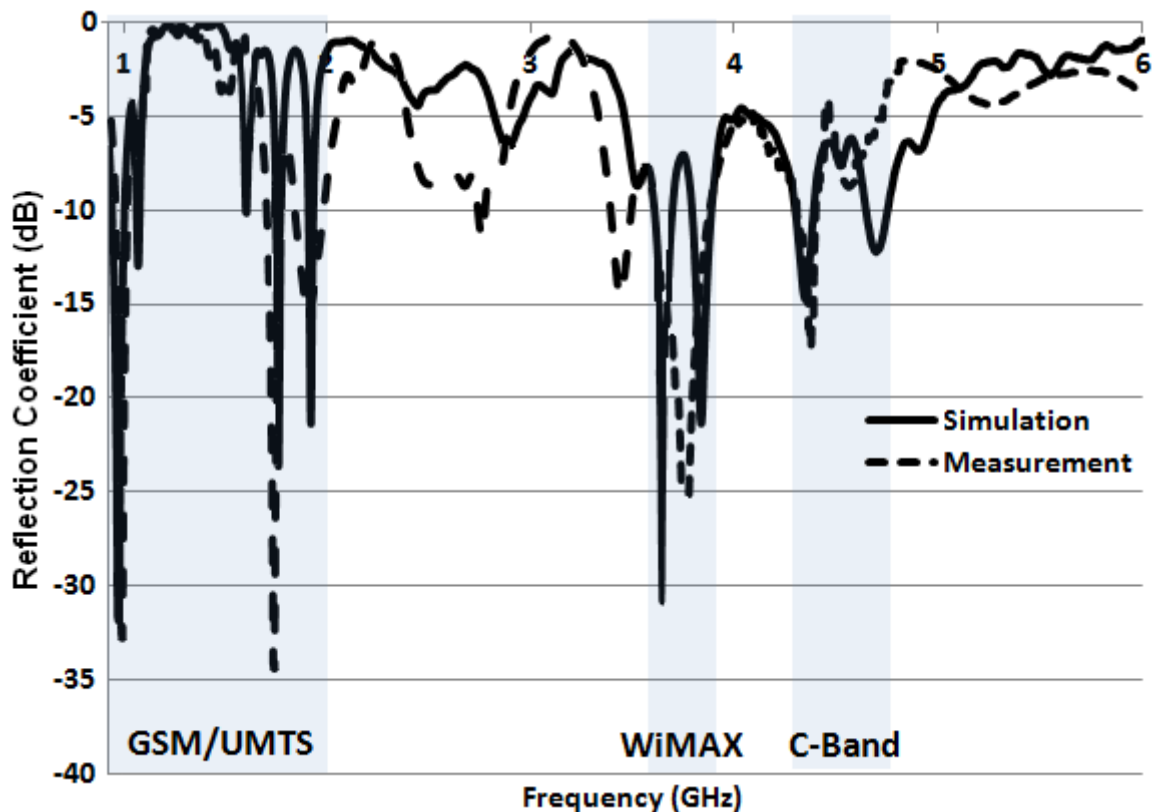


Fig. 4.24: Simulated and measured  $S_{11}$  patterns of the proposed meshed solar patch array antenna.

As can be seen in Fig. 4.24, there is good agreement between the simulation and measurement results. The slight difference between these results can be attributed to the imperfections caused by the attachment of the SMA to the bottom of the solar panel frame, which has a plastic surface making the SMA unsuitable to be soldered. The proposed solar antenna resonates at multiple frequency bands, enabling the operation at GSM/UMTS 1800 (1.71-1.88 GHz), GSM/UMTS 1900 (1.85-1.99 GHz), 3.5 GHz band WiMAX (3.4-3.6 GHz) and C-band networks. However, as can be seen in Fig. 4.24, although multiband

resonance response was obtained, the proposed meshed solar patch array antenna offers narrow impedance bandwidths at the resonance bands as given in Table 4.2.

Table 4.2: -10 dB impedance bandwidth performance of the meshed solar patch array antenna.

<b>Resonance Frequency (GHz)</b>	<b>Operational Frequency Band (GHz)</b>	<b>- 10 dB Impedance Bandwidth (%)</b>
1	0.98-1.015	3.5
1.08	1.07-1.09	1.85
1.61	1.6-1.63	1.86
1.76	1.75-1.79	2.27
1.92	1.91-1.94	1.6
3.62	3.52-3.7	4.97
3.83	3.78-3.89	2.87
4.33	4.29-4.39	2.3
4.7	4.64-4.76	2.55

The E-plane and H-plane far-field radiation pattern measurements of the fabricated meshed solar patch array antenna were performed in an anechoic chamber with a signal generator power level of  $P_G=14$  dBm. A conical spiral antenna with a constant gain of  $G_T=4$  dBi at the frequency range of 1-10 GHz was used as a reference antenna in order to determine the gain performance of the Antenna Under Test (AUT), i.e. the fabricated meshed solar patch array antenna. In the determination of the E-plane and H-plane gain values of the solar antenna, Friis equation given below was used:

$$G_R = \frac{P_R (4\pi R)^2}{P_0 G_T \lambda^2} \quad (4.3)$$

In equation (4.3),  $G_R$  is the gain of the meshed solar patch array antenna, AUT, to be measured,  $G_T$  is the gain of the reference conical spiral antenna, 4 dBi,  $P_R$  is the power received by the AUT,  $R$  is the distance between the AUT and the reference conical spiral antenna, and  $P_0$  is the input power fed to the reference conical spiral antenna taking cable losses into account given as follows:

$$P_0 (dBm) = P_G (dBm) - L_{Cable} (dB) \quad (4.4)$$

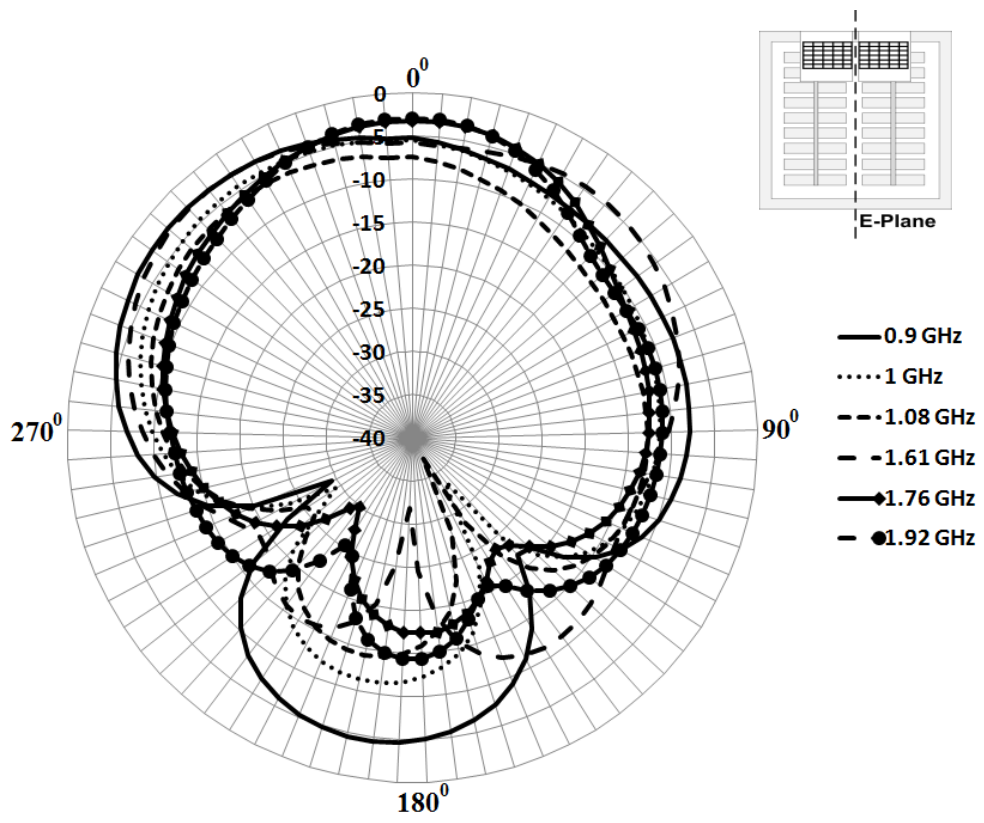
In equation (4.4),  $P_G$  is the power generated by the signal generator,  $P_G=14$  dBm, and  $L_{Cable}$  is the cable loss. The uncertainty values for the far-field radiation pattern measurements were in the range of  $\pm 0.6$  dB.

The E-plane and H-plane far-field radiation pattern measurements were performed over  $360^\circ$  with a sampling angle of  $5^\circ$ . The distance between the antennas was set to  $R=3$ m satisfying the far-field condition. The received power level,  $P_R$ , was recorded at each sampling angle and the maximum E-plane and H-plane gain values of the solar antenna were calculated using equation (4.3) by taking the cable losses into account as given in equation (4.4). The measured maximum E-plane and H-plane gain values of the proposed meshed solar patch array antenna at the resonance frequencies of 1, 1.08, 1.61, 1.76, 1.92, 3.64, 3.83, 4.3 and 4.7 GHz are demonstrated in Table 4.3.

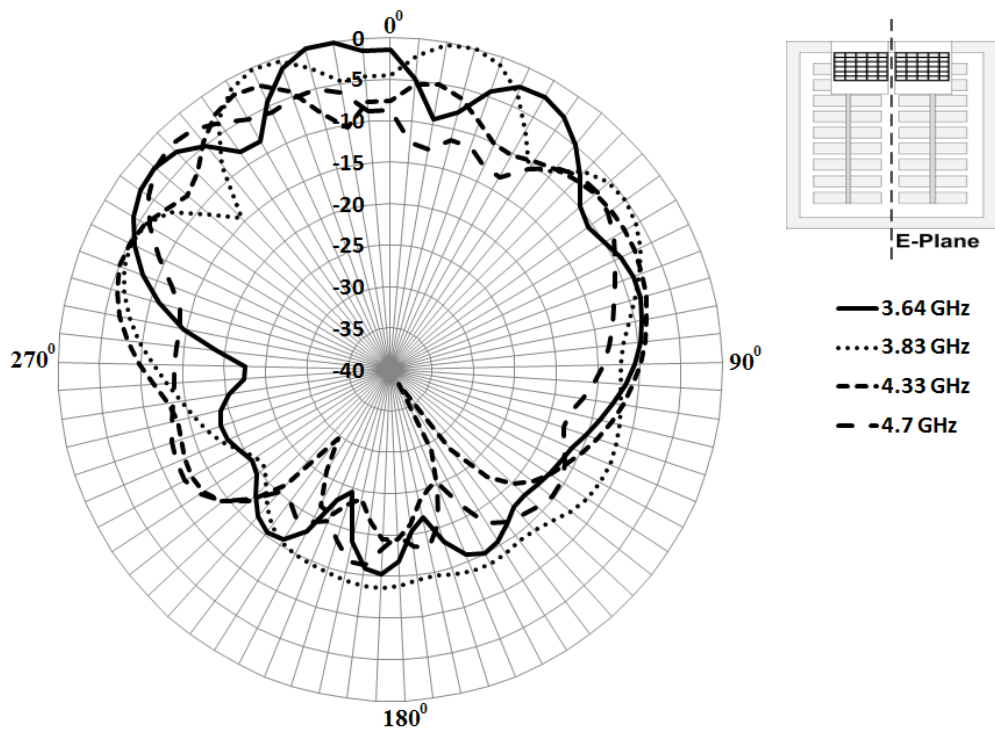
Table 4.3: Measured maximum E-plane and H-plane gain values across multiple resonance frequency bands.

Frequency (GHz)	$P_R$ (dBm)		$P_G$ (dBm)	$L_{Cable}$ (dB)	$G_R$ (dBi)	
	E-Plane (y-z)	H-Plane (y-z)			E-Plane (y-z)	H-Plane (y-z)
1	-25.01	-26.01	14	4.52	3.5	2.5
1.08	-27.36	-28.76	14	4.71	2	1.1
1.61	-28.78	-31.68	14	5.85	5.2	2.3
1.76	-30.19	-31.79	14	6.10	4.8	3.2
1.92	-30.93	-31.73	14	6.38	5.1	4.3
3.64	-34.98	-41.08	14	9.18	9.4	3.3
3.83	-35.57	-38.87	14	9.43	9.5	6.2
4.33	-40.7	-44.78	14	10.09	6.1	2
4.7	-42.18	-43.48	14	10.56	5.8	4.5

The measured E-plane and H-plane far-field radiation patterns are demonstrated in Fig. 4.25. In order to improve the readability, both E-plane and H-plane far-field radiation patterns were separated into two graphs; the first graphs illustrate the E-plane and H-plane patterns measured at the frequencies for GSM/UMTS bands while the second graphs are for the E-plane and H-plane patterns obtained at the frequencies for WiMAX and C-band networks. All E-plane and H-plane far-field radiation patterns were normalised to maximum E-Plane and H-plane gain values of 9.5 dBi and 6.2 dBi respectively, which were obtained at 3.83 GHz as can be seen in Table 4.3.



(a)



(b)

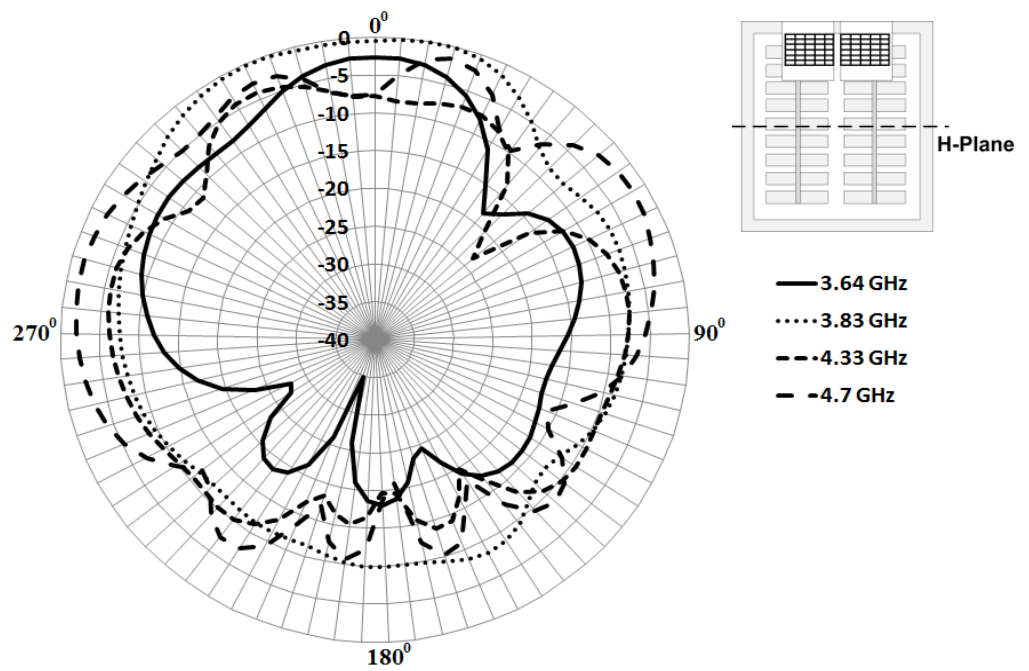
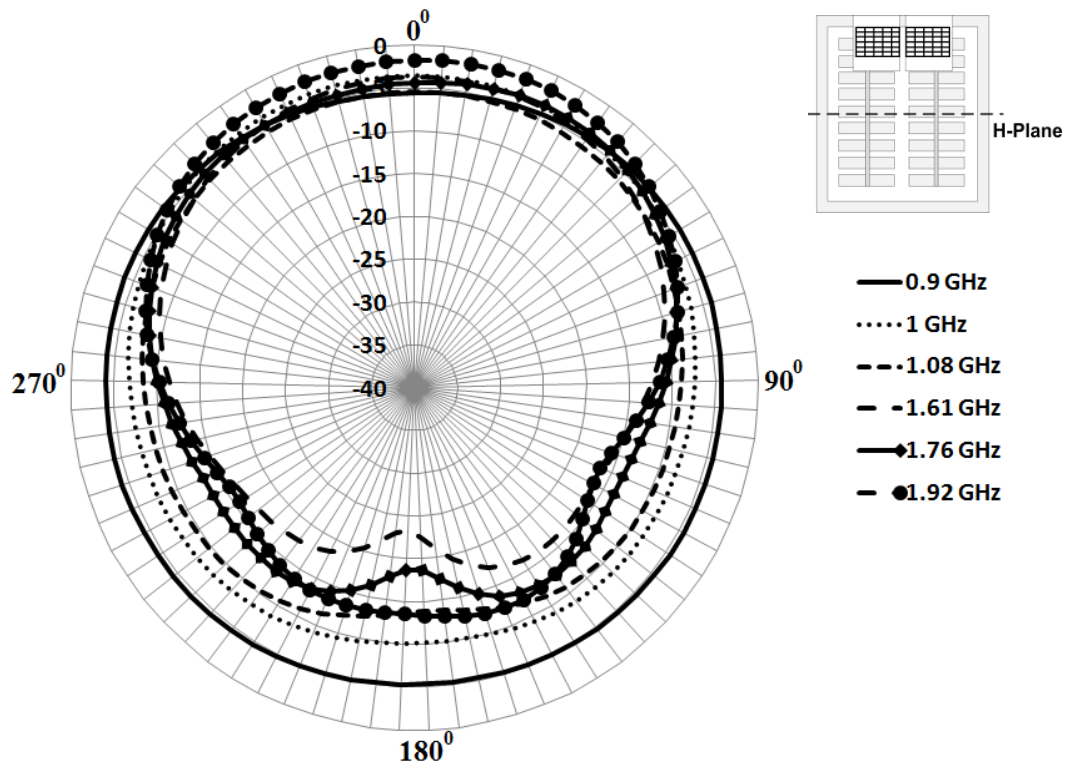


Fig. 4.25: Measured E-plane (normalized to maximum gain of 9.5 dBi) and H-plane (normalized to maximum gain of 6.2 dBi) far-field radiation patterns (a) E-Plane for GSM/UMTS bands (b) E-Plane for WiMAX and C-band (c) H-plane for GSM/UMTS bands (d) H-plane for WiMAX and C-band.

As can be seen in Fig. 4.25(a), below 1.92 GHz the antenna has a broadside hemispherical E-plane far-field radiation patterns with a slight asymmetry caused by the introduction of the patch tilt angle. Also, it can be noticed in Fig. 4.25(a) that the antenna has a back-lobe radiation, which remains below -10 dB above 900 MHz. This is due to the structure of the solar panel, which consists of poly-Si solar cells each separated by 2 mm from each other in the x and y-axes. Therefore, from an RF perspective, the solar panel is not homogeneous and consists of slots between the solar cells resulting in a back-lobe radiation. This is especially evident at 900 MHz where a back-lobe radiation in the range of -5 dBi was measured as can be seen in Fig. 4.25(a).

At the high frequency band above 3.64 GHz, however, these slots become smaller in comparison to the wavelength and the back-lobe radiation drops below -15 dBi. However, due to the increased frequency, the effect of the introduced patch tilt angle on the radiation response of the antenna becomes more significant. At this frequency band, the main lobe of the antenna shows multipath characteristics and shifts from the broadside direction as the frequency increases.

As can be seen in Fig. 4.25(c), at 900 MHz, the antenna has a monopole-like omnidirectional radiation pattern in the H-plane. As the frequency increases, the radiation from the antenna in the H-plane becomes more directional. However, the back-lobe radiation is still present due to the non-homogeneous structure of the panel consisting of slots between the individual solar cells.

As can be seen in Fig. 4.25(d), similar to the E-plane, at the high frequency band above 3.64 GHz, the back-lobe radiation level in the H-plane considerably decreases below -10 dB with multipath radiation patterns shifting from the broadside direction due to the effect of the patch tilt angle, which becomes more dominant as the frequency increases.

#### **4.4.2.2 Solar Measurements**

A significant factor to be considered in this design is the effect of the suspended meshed radiating patch elements placed above the solar panel on the photovoltaic performance. Although the transparency of both meshed patch elements was calculated as 93.3%, the meshed pattern of the patch array elements still results in a slight non-uniformity in the illumination intensity incident upon the surface of the panel. This has the potential to become a serious challenge for the total DC output current level generated by the solar panel as the total current output is limited by the current of a single poly-Si solar cell within the panel. Therefore, a decrease in the DC current output level of a single solar cell

would also reduce the total DC current output level of the panel. The reason behind the selection of acrylic as a substrate material and the use of the meshing technique on the copper patch elements printed on the acrylic substrates is to minimise the non-uniformity by increasing the patch transparency to avoid such a decrease in the total DC current output of the solar panel.

The solar measurements of the proposed meshed solar patch array antenna were performed in the metal halide solar simulator, which was demonstrated in chapter 3. The measurement set-up is illustrated in Fig. 4.26.

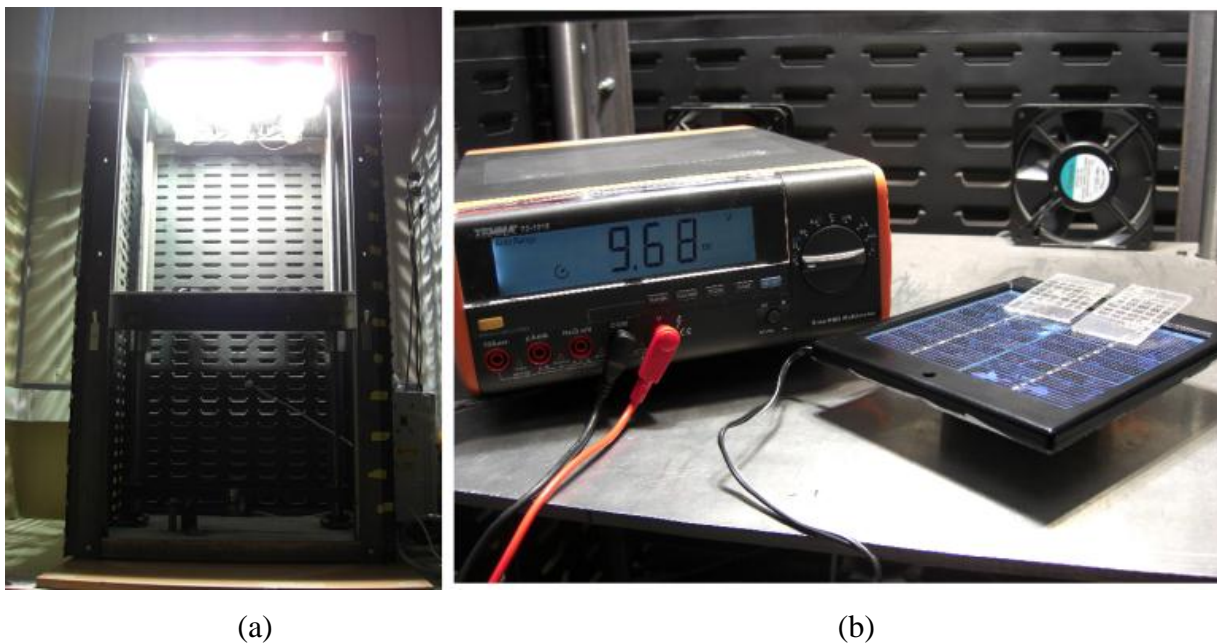


Fig. 4.26: Solar measurement of the meshed solar patch array antenna (a) solar simulator (b) measurement setup within the chamber.

In this design, meshing the RF radiating patch elements and printing them on transparent acrylic substrates was studied as a solution to minimise the shading and therefore decrease the non-uniformity in the illumination intensity upon the solar panel in comparison to the use of conventional non-transparent copper patch elements. In order to demonstrate the enhancing effect of the proposed meshing technique on the solar performance of the antenna, solar measurements were taken in the metal halide solar simulator under three circumstances given below:

- Without any elements placed above the solar panel,
- With the proposed transparent meshed radiating patch array above the solar panel,
- With non-transparent conventional solid patch array above the solar panel.

For the photovoltaic measurements of the antenna, a group of resistors, from  $100\Omega$  to  $2.7k\Omega$ , were connected to the terminals of the solar panel as a load, and the voltage and current readings were measured for each configuration given above in order to obtain the I/V curves and the solar efficiencies. In Fig. 4.27, the obtained I/V curves are illustrated.

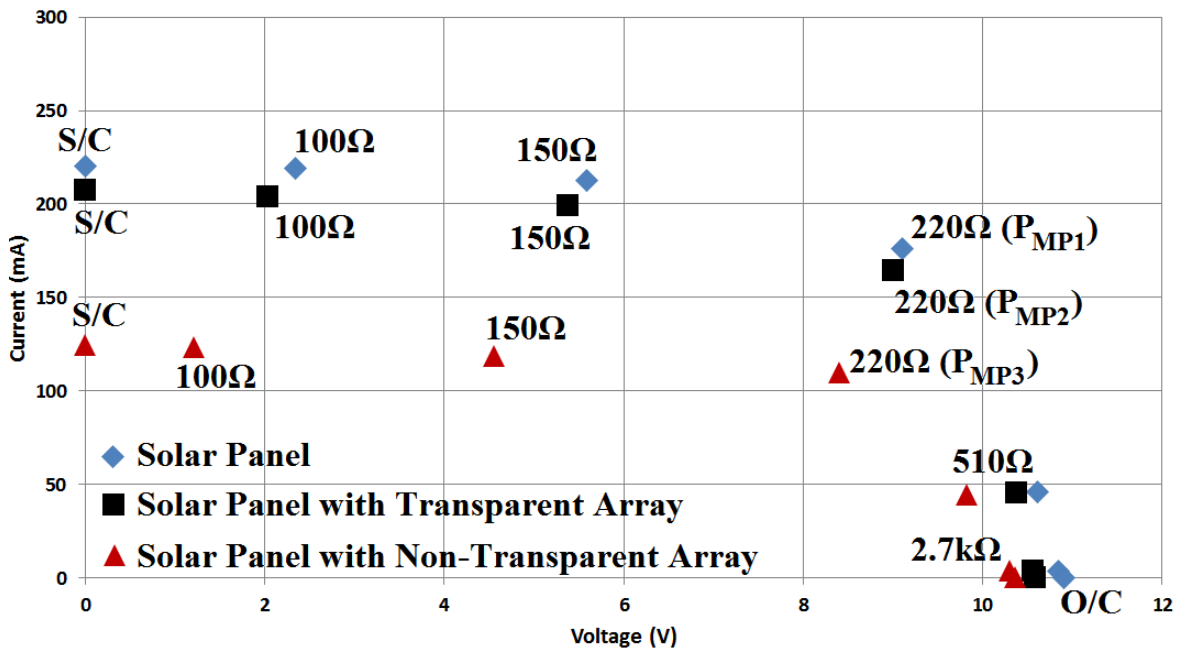


Fig. 4.27: Measured I/V curves of the antenna.

The measurement results can be given as follows:

- The solar panel without any elements placed above generates a measured open circuit voltage of  $V_{OC}=10.9$  V with a short circuit current of  $I_{SC}=220.3$  mA. At the maximum power point of the solar panel without any radiating elements placed above,  $P_{MP1}$  in Fig. 4.27, where the DC power output is maximum, the measured voltage and current readings were recorded as  $V_{MP}=9.1$  V and  $I_{MP}=176.4$  mA, together providing a maximum DC power output of  $P_{MP1}=1.6$  W.
- When the proposed transparent radiating patch array is placed above the solar panel, the open circuit voltage drops by 2.84%, from 10.9 V to 10.59 V, and the short circuit current decreases by 5.85%, from 220.3 mA to 207.4 mA. At the maximum power point,  $P_{MP2}$  in Fig. 4.27, the measured voltage and current readings were recorded as  $V_{MP}=9$  V and  $I_{MP}=164.5$  mA, respectively, equivalent to a maximum DC power output of  $P_{MP2}=1.48$  W.

- The use of the non-transparent solid patch array, which is in the same dimensions as the transparent meshed patch array, on the other hand, degrades the solar performance significantly by resulting in a sharp decrease of 43.6% in the measured short-circuit current, from 220.3 mA to 124.3 mA, with a drop of 4.86% in the open-circuit voltage, from 10.9 V to 10.37 V. At the maximum power point,  $P_{MP3}$  in Fig. 4.27, the measured voltage and current values were observed as  $V_{MP}=8.41$  V and  $I_{MP}=109.7$  mA, providing a maximum DC power output of  $P_{MP3}=0.92$  W.

Table 4.4 summarises the solar performance readings obtained for the solar panel combined with the proposed transparent meshed radiating patch array and the non-transparent solid patch array, respectively.

Table 4.4: Measured DC solar performance characteristics.

<b>Configuration</b>	<b>V<sub>OC</sub></b> <b>(V)</b>	<b>I<sub>SC</sub></b> <b>(mA)</b>	<b>V<sub>MP</sub></b> <b>(V)</b>	<b>I<sub>MP</sub></b> <b>(mA)</b>	<b>P<sub>MP</sub></b> <b>(W)</b>	<b>Panel</b> <b>Efficiency</b> <b>(<math>\eta</math>) (%)</b>
Panel	10.9	220.3	9.1	176.4	1.6	7.14
Panel with transparent array	10.59	207.4	9	164.5	1.48	6.6
Panel non- transparent array	10.37	124.3	8.41	109.7	0.92	4.1

Considering the solar illumination intensity of  $1000 \text{ W/m}^2$  within the solar simulator, and the total surface area of the solar panel, i.e. the outer frame of the panel as illustrated in Fig. 4.20(b), which has dimensions of 160 mm x 140 mm resulting in a total surface area of  $0.0224 \text{ m}^2$ , the total incident power upon the solar antenna within the solar simulator can be calculated as  $P_{in}=22.4$  W. Following the determination of  $P_{MP}$  and  $P_{in}$  values for the configurations given in Table 4.4, equation (3.13) was used to calculate the solar panel efficiencies as given in Table 4.4.

While the solar efficiency of the solar panel without any elements placed above was calculated as 7.14%, the introduction of the proposed transparent patch array resulted in a slight decrease of 7.5% in the solar efficiency of the solar panel, from 7.14% to 6.6%. The non-transparent solid patch array element, on the other hand, decreased the solar efficiency by a significant factor of 42.5%, from 7.14% to 4.1%. The obtained results clearly demonstrate that for the solar antenna integration topology in which solar cells are used as an RF ground plane in addition to their photovoltaic function, meshing the radiating element upon the solar cells provide a significant enhancement in the solar efficiency.

## **4.5 UWB Meshed Solar Monopole Antenna**

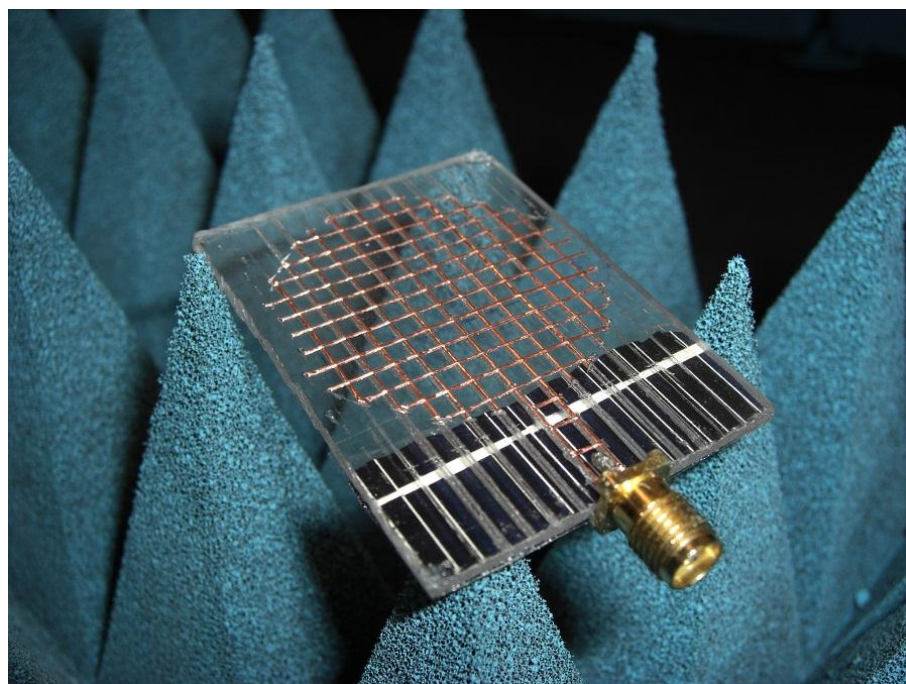
In the field of wideband communications, the introduction of UWB by FCC in 2002 marked the beginning of a new era in modern communication systems. Since then, the design and analysis of antennas covering UWB has been of great interest. In section 4.3 and section 4.4, the meshing technique was successfully applied to and demonstrated for photovoltaically integrated microstrip patch antennas. Although it was demonstrated that correctly meshing the radiating patch element significantly enhances the solar performance whilst maintaining similar antenna characteristics in comparison to the use of a conventional solid radiating patch element, the obtained narrow impedance bandwidth performance limits the usability of these antennas for wideband applications. While the meshed solar patch antenna demonstrated in section 4.3 offers a single band operation, the meshed solar patch array antenna demonstrated in section 4.4 has a multiband resonance response with narrow impedance bandwidths at the resonance bands. This frequency response for these antennas suggests that they cannot be used for UWB applications and a new design is required.

In view of this, in this section, a novel low-profile printed meshed circular disc monopole antenna combined with a poly-Si solar cell operating as an RF ground plane covering the frequency band of 2.33-10.8 GHz with an average broadband gain of 4.1 dBi is proposed for UWB applications.

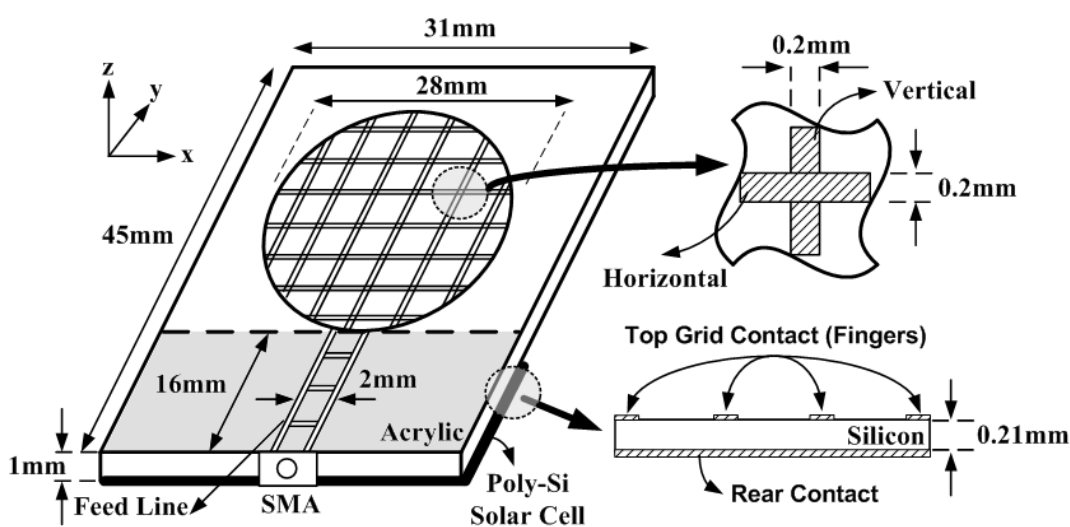
### **4.5.1 Meshed Solar Monopole Antenna Design**

The fabricated meshed solar monopole antenna is demonstrated in Fig. 4.28. Similar to the design of the suspended meshed solar patch antenna demonstrated in section 4.3, the meshed solar monopole antenna design is based upon its conventional solid counterpart

whose design parameters given in Fig. 4.28(b) were optimised in CST Microwave Studio to achieve a UWB resonance response.



(a)



(b)

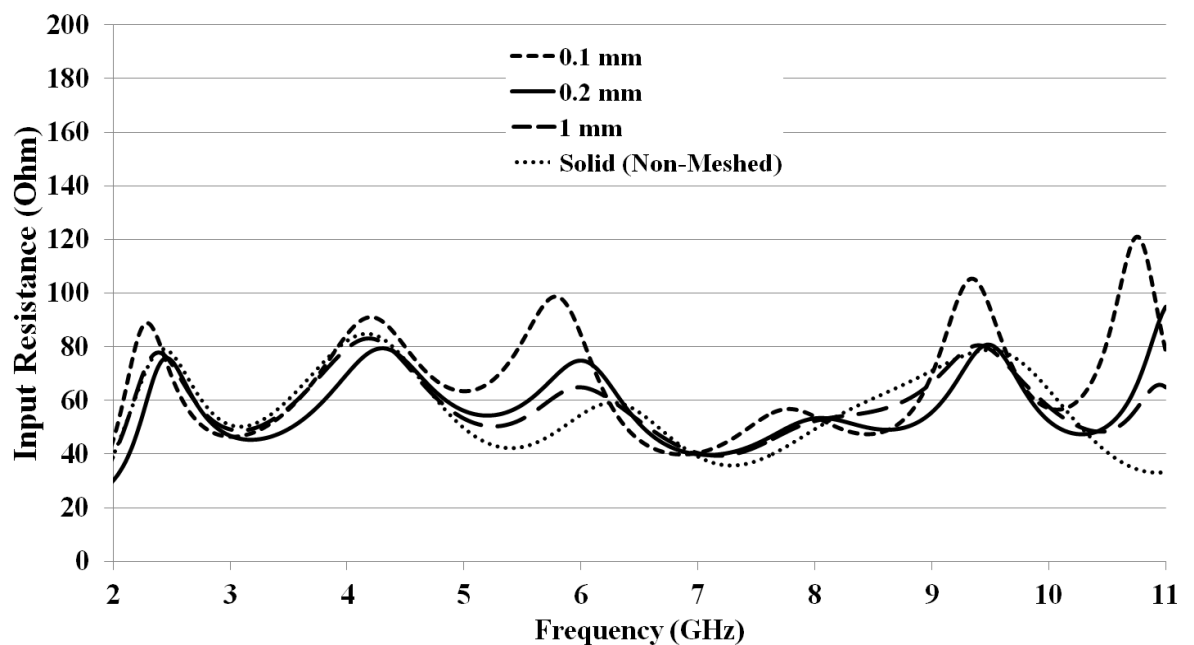
Fig. 4.28: Meshed solar monopole antenna (a) fabricated antenna (b) technical overall view.

The fabrication of the proposed meshed solar monopole antenna was done by hand using a Stanley utility knife to achieve the meshed monopole pattern. As illustrated in Fig. 4.28, the proposed design consists of a circular monopole printed on a transparent acrylic substrate,  $\epsilon_r=3.6$  and  $\tan\delta=0.015$ , with a poly-Si solar cell on the backside operating as an RF ground plane. The circular monopole with the feed line was meshed in order to

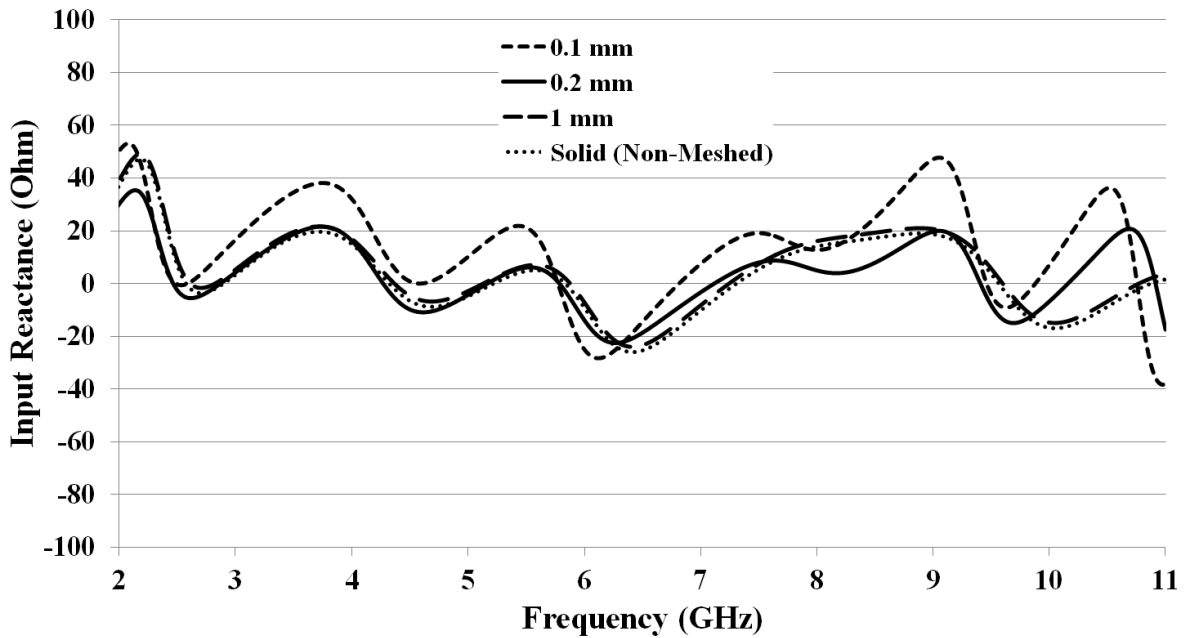
increase the optical transparency of the monopole to minimise the shading upon the solar cell to achieve optimum solar performance. Similar to the photovoltaic meshed patch antennas demonstrated in the previous sections, for the meshing of the printed monopole, parametric analysis was performed in CST Microwave Studio in order to determine the optimum meshing parameters given below:

- Optimum meshing line width,
- Optimum number of the vertical meshing lines, which are parallel to the direction of the surface current of the meshed monopole (y-axis) in Fig. 4.28,
- Optimum number of the horizontal meshing lines, which are perpendicular to the direction of the surface current of the meshed monopole (x-axis) in Fig. 4.28.

An important factor to be considered here is the requirement of achieving a high optical transparency by selecting the parameters above as small as possible whilst maintaining the input impedance response suitable for UWB (3.1-10.6 GHz) operation. To this end, first, parametric analysis of the width of the meshing lines was performed with an initially selected non-optimised number of 20 vertical and horizontal lines in CST Microwave Studio. In view of this, meshing line widths in the range of 0.1 mm-1 mm were investigated and the obtained input resistance and reactance curves of the meshed solar monopole antenna in comparison with the solid non-meshed version are demonstrated in Fig. 4.29.



(a)

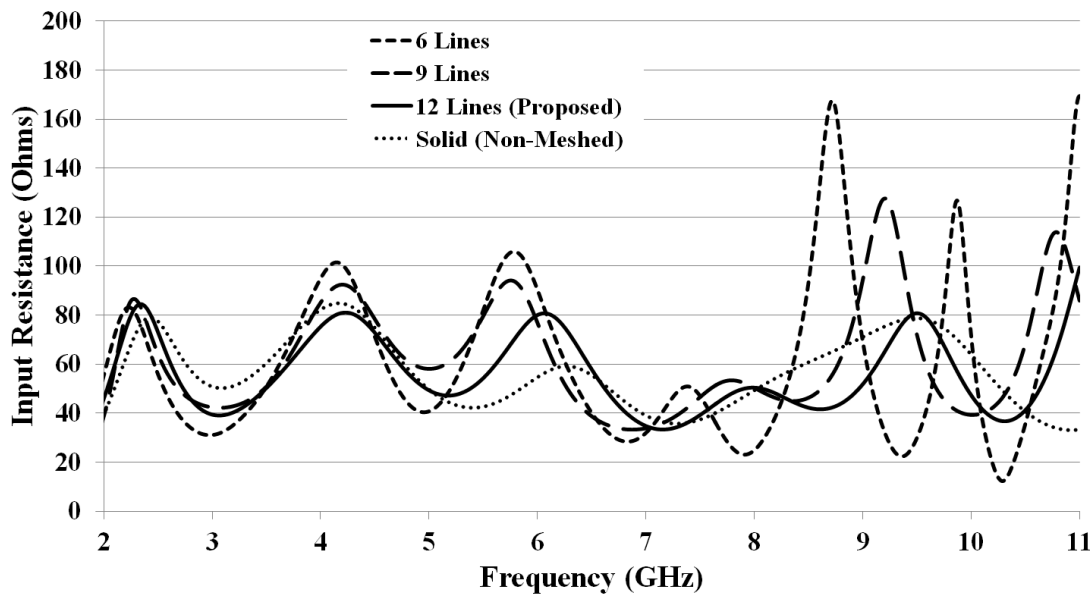


(b)

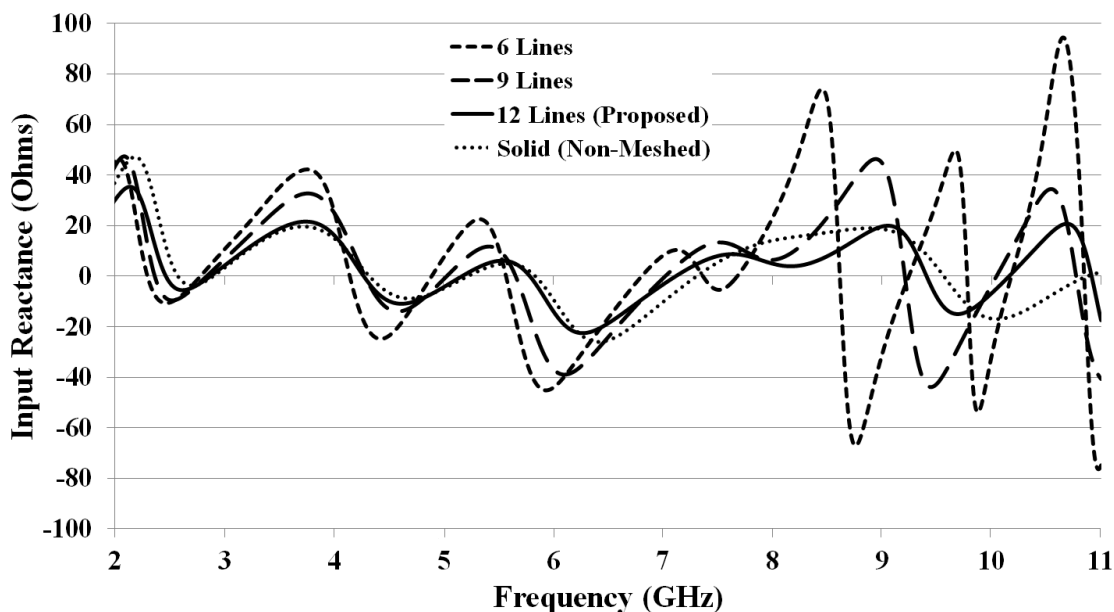
Fig. 4.29: Input impedance response of the monopole antenna versus varying meshing line widths (a) resistance response (b) reactance response.

If attention is given to Fig. 4.29(a), it can be seen that the width of the meshing lines has a considerable effect on the resistance response of the solar monopole antenna. Although it is desirable from a solar point of view that the meshing line width to be determined as small as possible, i.e. 0.1 mm in Fig. 4.29(a), to decrease the footprint of the meshed monopole, the increase in the fluctuation of the resistance curve when the meshing line width is selected as 0.1 mm can clearly be seen in Fig. 4.29(a). A meshing line with of greater than 0.2 mm, on the other hand, results in a similar resistance response in comparison to the solid non-meshed monopole but at the expense of a decreased optical transparency. Therefore, in order to address the trade-off between the optimum antenna performance and solar performance, the minimum optimum meshing line width was determined as 0.2 mm, which offers a relatively flattened resistance curve in comparison to the meshing line width of 0.1 mm and a greater optical transparency in comparison to the meshing line widths larger than 0.2 mm. If consideration is given to Fig. 4.29(b), similarly, the meshed solar monopole antenna with a meshing line width of 0.1 mm has a considerable increase in the fluctuation of the reactance response especially above 5 GHz, which with the resistance curve illustrated in Fig. 4.29(a), makes it significantly difficult to perform a smooth impedance matching across UWB. For the meshing line width of 1 mm, although considerably similar reactance response in comparison with the solid non-meshed version was achieved, due to the decreased optical transparency of the printed monopole,

0.2 mm meshing line width, which was determined as the optimum meshing line width in Fig. 4.29(a), remains as the optimum choice. Following the determination of the optimum meshing line width as 0.2 mm, parametric analysis to determine the optimum number of the vertical monopole meshing lines was carried out. To this end, the number of the vertical meshing lines was varied in the range of 6-12 and the obtained input resistance and reactance curves are demonstrated in Fig. 4.30. It should be noted here that during this analysis, the number of the horizontal meshing lines was fixed at an initially selected meshing line number of 20.



(a)

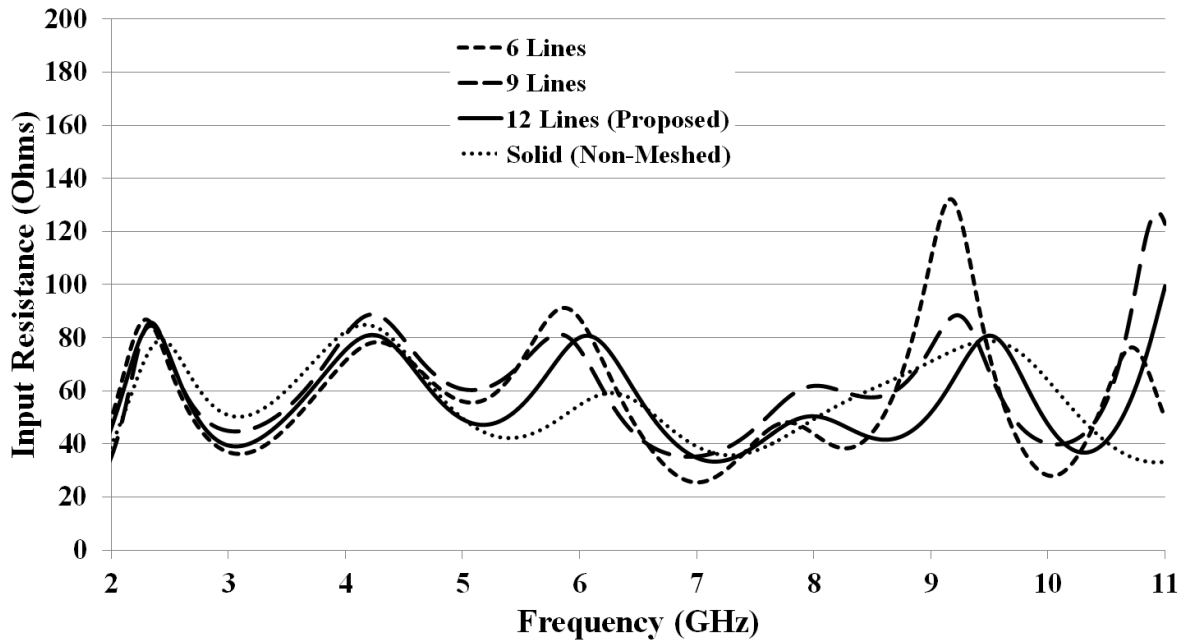


(b)

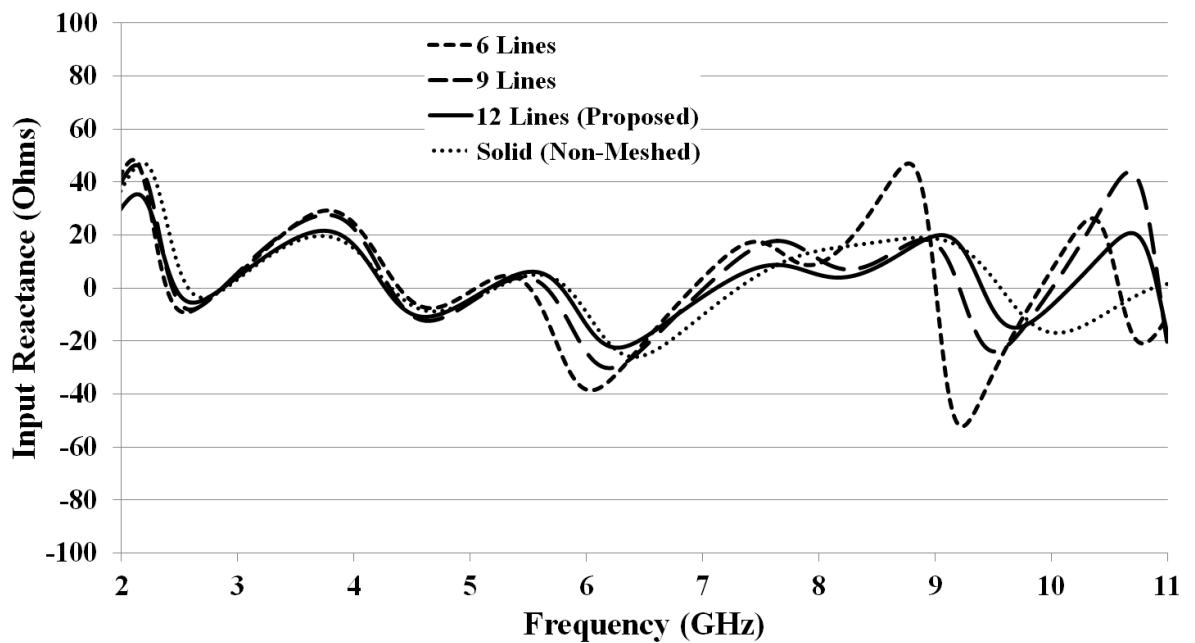
Fig. 4.30: Input impedance response of the monopole antenna versus varying number of vertical meshing lines (a) resistance response (b) reactance response.

In Fig 4.30(a), it can be seen that decreasing the number of the vertical meshing lines increases the fluctuation in the resistance and reactance curves of the meshed monopole. In Fig. 4.30(a), the meshed monopole with a vertical meshing line number of 6 has a considerable fluctuation in the resistance response in comparison to the meshed monopole with greater numbers of vertical meshing lines, especially above 8 GHz, which makes this selection not suitable for UWB applications. As the number of the vertical meshing lines increases to 9, the resistance response of the meshed solar monopole becomes more flattened, however, the high fluctuation in the resistance curve is still present above 9 GHz. The meshed monopole with a vertical meshing line number of 12, on the other hand, offers a considerably flattened resistance response, which is almost identical to the resistance response of the solid non-meshed monopole. Similarly, in Fig. 4.30(b), it can be seen that decreasing the number of the vertical meshing lines increases the fluctuation of the reactance curve of the meshed solar monopole antenna. Although a vertical meshing line number of 6 might seem as an optimum choice to achieve the highest optical transparency by reducing the footprint of the meshed monopole, due to the fluctuation present above 8 GHz in Fig. 4.30(b), it is not the optimum choice for UWB operation. Despite the decreased fluctuation in the reactance curve of the monopole when the vertical meshing line number is selected as 9, performing a smooth impedance matching still remains as a difficult task to achieve. For this reason, in the optimum final design of the meshed solar monopole antenna, the optimum minimum number of the vertical meshing lines was selected as 12, which offers an almost identical flattened impedance response in comparison to the non-meshed solar monopole.

Following the determination of the optimum number of the vertical meshing lines as 12, parametric analysis to determine the optimum minimum number of the horizontal meshing lines was performed. Whilst the meshing line width and the number of the vertical meshing lines were fixed at 0.2 mm and 12, respectively, the number of the horizontal meshing lines was varied in the range of 6-12 and the obtained input impedance curves are shown in Fig. 4.31.



(a)



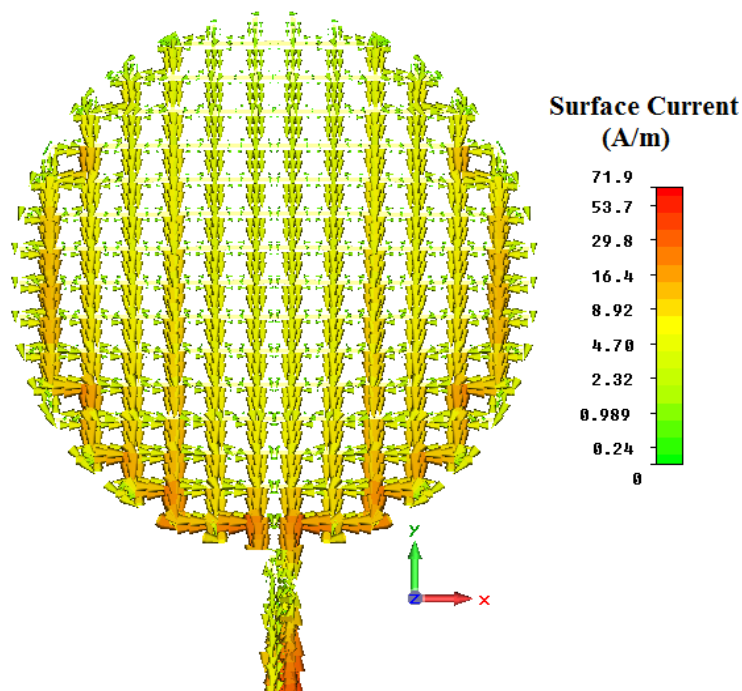
(b)

Fig. 4.31: Input impedance response of the monopole antenna versus varying number of horizontal meshing lines (a) resistance response (b) reactance response.

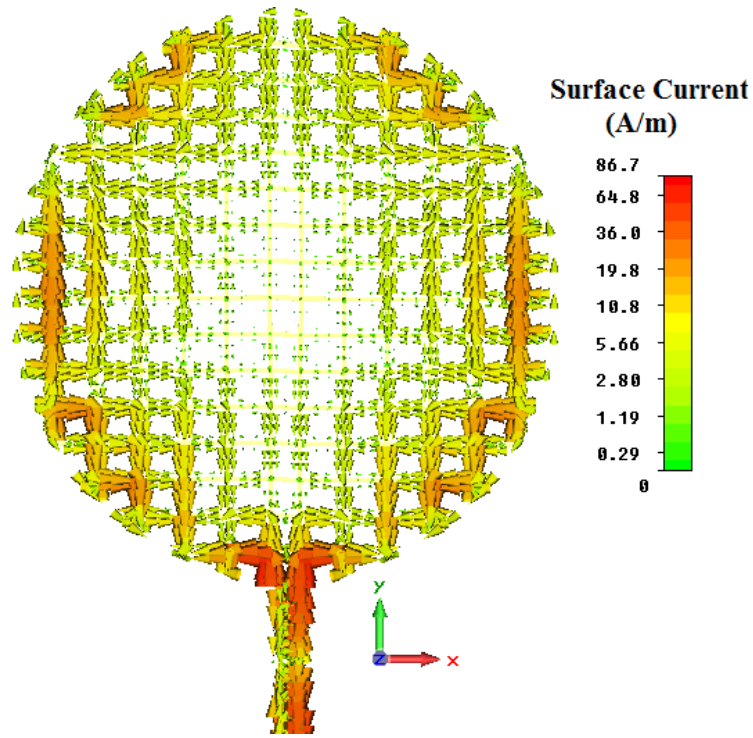
It can be seen in Fig. 4.31 that decreasing the number of the horizontal meshing lines has a negligible effect on the impedance response of the meshed solar monopole antenna below 8 GHz and slightly increases the impedance fluctuation above 8 GHz. If attention is given to Fig. 4.31(a), it can be seen that decreasing the number of the horizontal meshing lines below 9 increases the fluctuation in the resistance response of the meshed solar monopole antenna above 8 GHz. This increase is especially evident when the number of the

horizontal meshing lines is selected as 6. Similarly, as illustrated in Fig. 4.31(b), the change in the reactance response of the meshed monopole antenna as a result of the variation of the number of the horizontal meshing lines is negligible below 8 GHz and is evident above 8 GHz when the number of the horizontal meshing lines is selected as 6 and 9, respectively. Due to the increase in the fluctuation of the input impedance response of the meshed monopole above 8 GHz, the optimum number of the horizontal meshing lines was selected as 12, which offers almost identical flattened impedance response in comparison to the solid non-meshed monopole across the entire investigated frequency band, enabling the proposed meshed solar monopole antenna to cover UWB applications.

In general, as can be seen in Fig. 4.31, the effect of varying the number of the horizontal meshing lines on the impedance response of the meshed monopole antenna is less crucial in comparison to the effect of the variation in the number of the vertical meshing lines as illustrated in Fig. 4.30. As explained in section 4.3 for the meshed solar patch antenna, this is due to the surface current of the printed monopole to mainly flow through the vertical meshing lines in the y-axis perpendicular to the direction of the horizontal meshing lines in the x-axis as demonstrated in Fig. 4.32.



(a)



(b)

Fig. 4.32: Simulated surface current distribution (a) 3.1 GHz (b) 10.6 GHz.

Following the determination of the optimum meshing parameters:

- Optimum meshing line width as 0.2 mm,
- Optimum vertical meshing line number as 12,
- Optimum horizontal meshing line number as 12,

The transparency of the meshed monopole was calculated as 85.4% using equation (4.1).

The  $S_{11}$  response of the proposed meshed solar monopole antenna was simulated and measured. Simulations were carried out in CST Microwave Studio while the measurements were performed using a VNA, Agilent E8364B. The obtained results are demonstrated in Fig. 4.33.

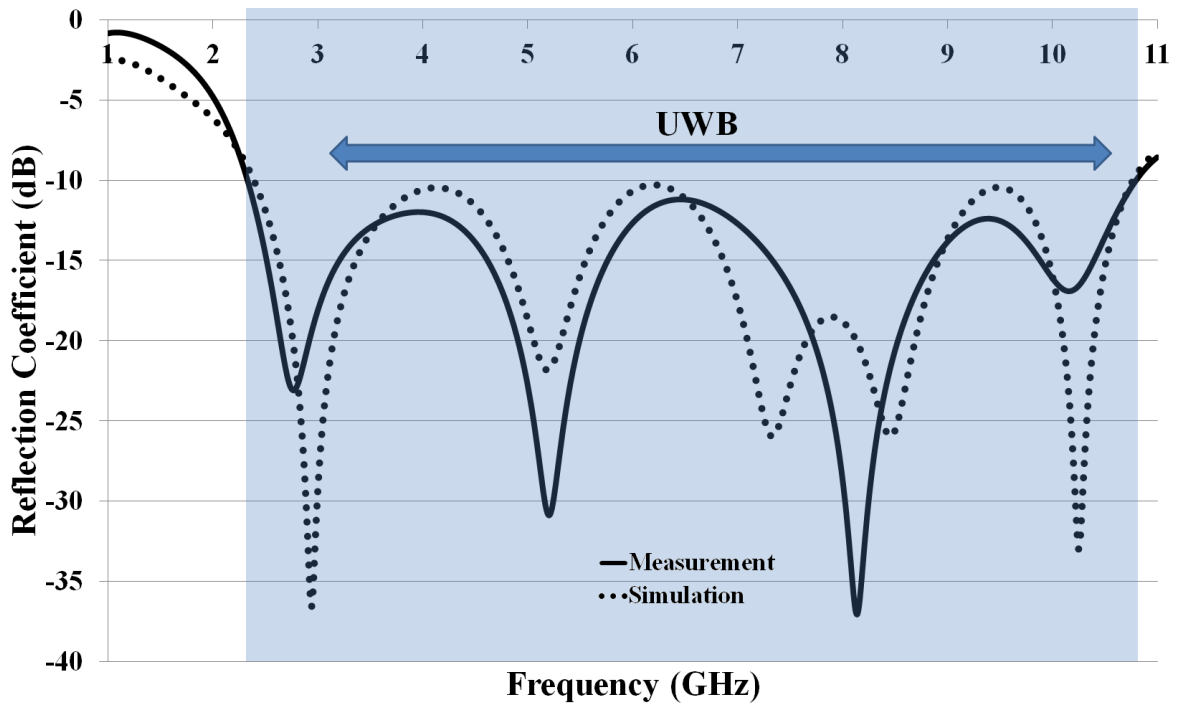
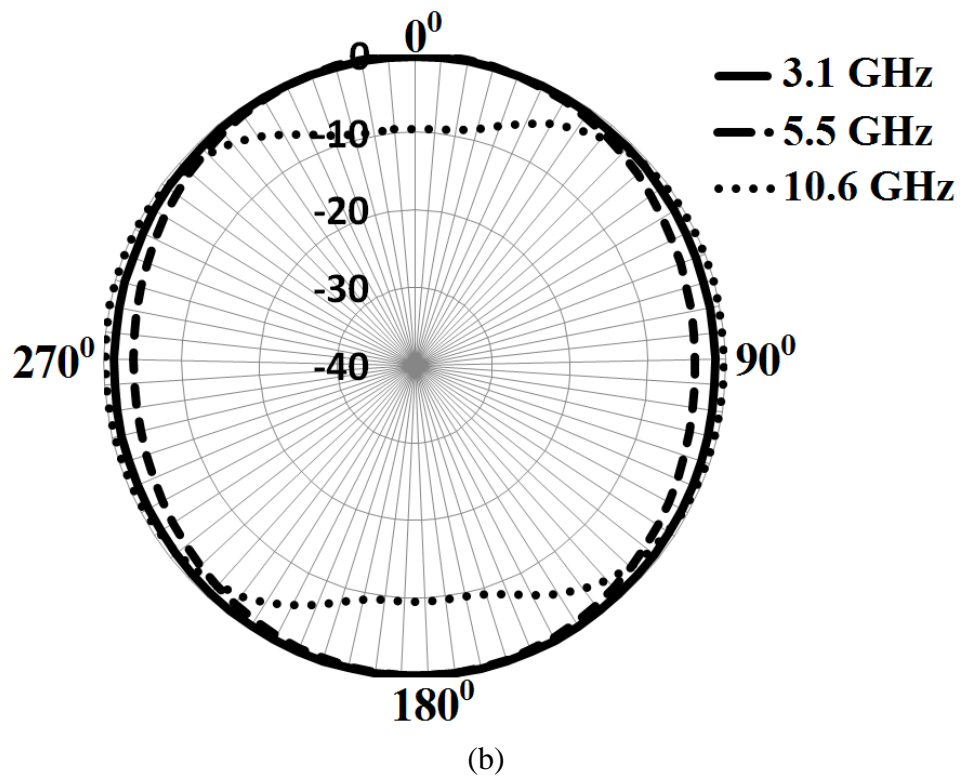
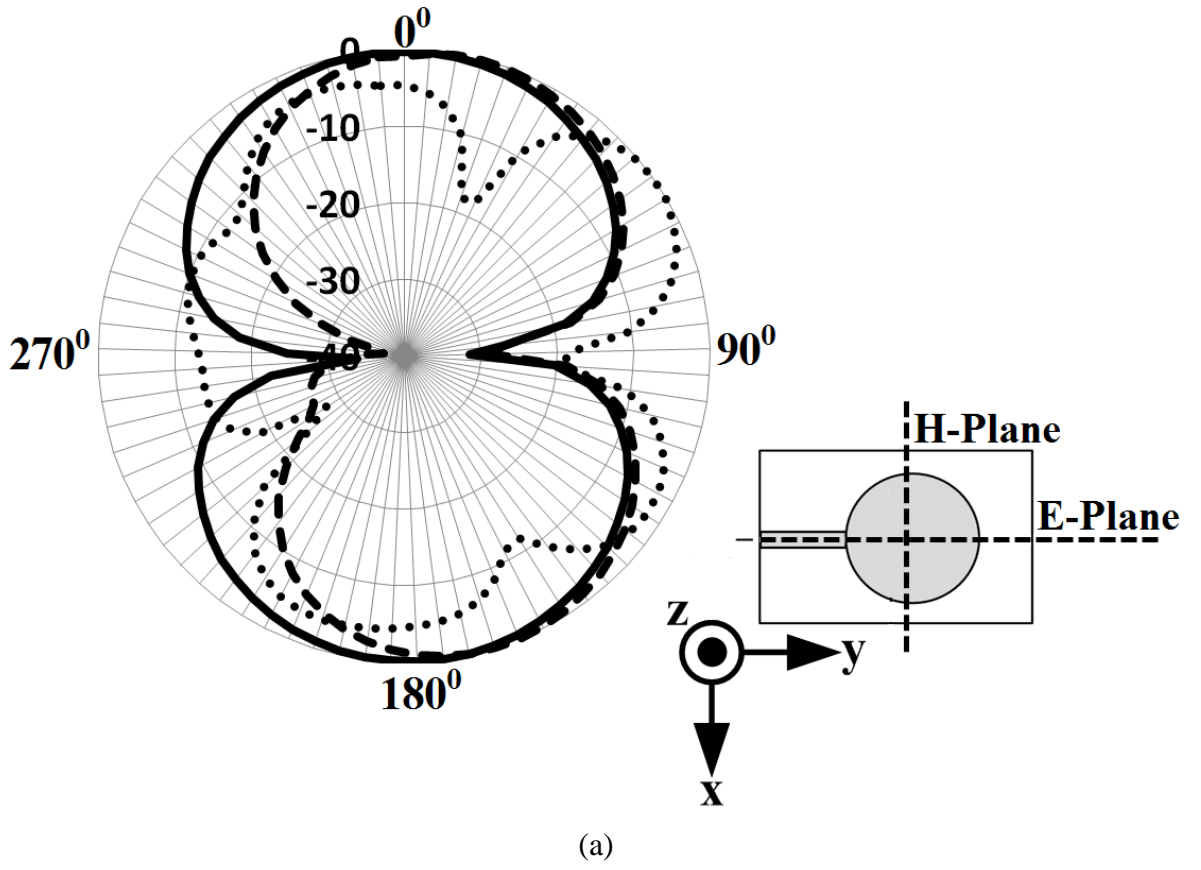
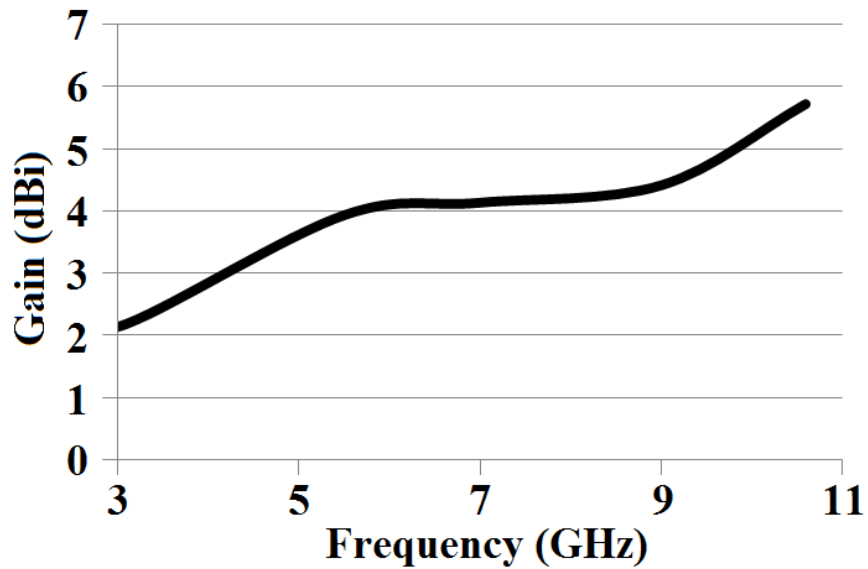


Fig. 4.33: Simulated and measured  $S_{11}$  patterns of the meshed solar monopole antenna.

As illustrated in Fig. 4.33, there is good agreement between the simulated and measured  $S_{11}$  responses. The proposed meshed solar patch antenna operates across a measured frequency band of 2.33-10.8 GHz, fully covering UWB applications.

The E-plane (y-z) and H-plane (x-z) far-field radiation patterns of the antenna were measured in an anechoic chamber. For the measurements, the meshed solar monopole, AUT, was placed at a distance of  $R=3$  m from the reference conical spiral antenna with a gain of  $G_T=4$  dBi. The received power level by the AUT,  $P_R$ , was measured over  $360^\circ$  with a sampling interval of  $5^\circ$  in the E-plane and H-plane. Gain values at each sampling interval were calculated using Friis equation given in equation (4.3) by taking the cable losses into account as given in equation (4.4). The normalised E-plane and H-plane far field radiation patterns are illustrated in Fig. 4.34(a) and Fig. 4.34(b) together with the calculated maximum gain values across UWB demonstrated in Fig. 4.34(c).





(c)

Fig. 4.34: Measured far-field radiation patterns of the meshed solar monopole antenna (a) E-plane (y-z) (b) H-plane (x-z) (c) maximum gain values across 3.1-10.6 GHz.

At the lower frequencies, 3.1 GHz and 5.5 GHz, traditional monopole far-field radiation patterns were observed in the E-plane as can be seen in Fig. 4.34(a). As the frequency increases to 10.6 GHz, the pattern becomes near end-fire directed with multiple nulls occurring in different directions, enabling the proposed meshed solar monopole antenna to be employed in multipath applications. The far-field H-plane radiation patterns illustrated in Fig. 4.34(b), on the other hand, are omnidirectional at the frequencies of 3.1 GHz and 5.5 GHz and present near omnidirectional characteristics as the frequency increases to 10.6 GHz.

Table 4.5: Measured maximum E-plane and H-plane gain values.

Frequency (GHz)	$P_R$ (dBm)	$L_{Cable}$ (dB)	Measured Maximum Gain (dBi)	Simulated Maximum Gain (dBi)
3.1	-39.94	8.39	2.26	2.6
5.5	-46.16	11.46	4.1	4.7
10.6	-55.14	16.5	5.85	6.1

Solar measurements of the meshed solar monopole antenna were carried out in a metal halide solar simulator providing a homogeneous illumination intensity of  $1000 \text{ W/m}^2$ . Similar to the solar measurements of the meshed solar patch antennas demonstrated in the previous sections, a group of resistors from  $10\Omega$  to  $2.7\text{k}\Omega$  were connected to the terminals of the poly-Si solar cell and the voltage and current readings were measured for each resistor in order to obtain the I-V curve of the solar monopole antenna, which is demonstrated in Fig. 4.35.

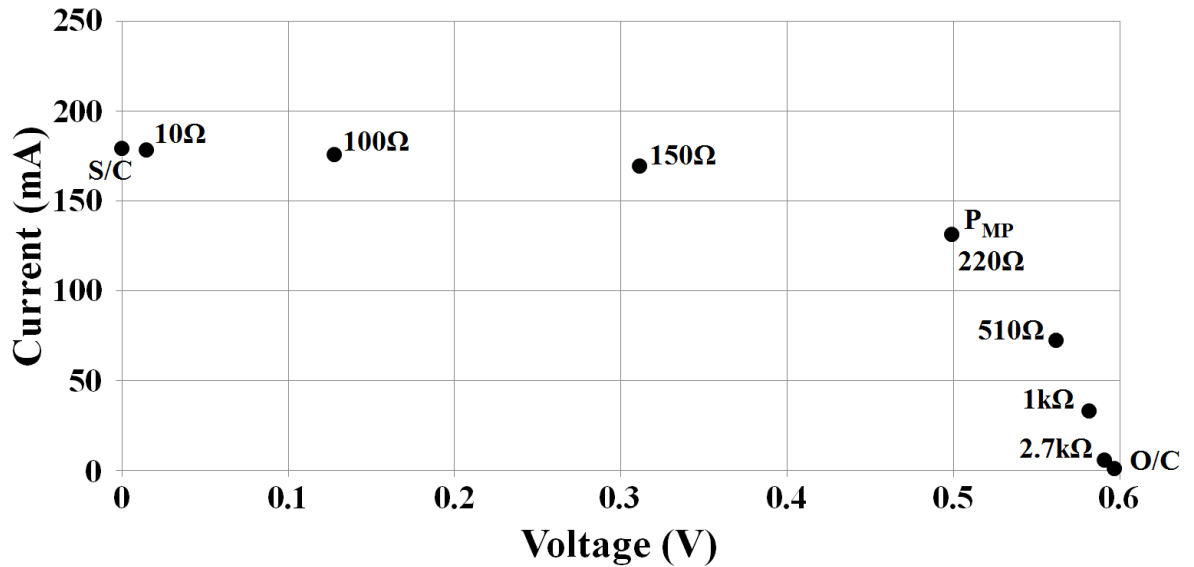


Fig. 4.35: Measured I/V curve of the meshed solar monopole antenna.

The open-circuit voltage and short-circuit current readings were measured as  $V_{OC}=0.592 \text{ V}$  and  $I_{SC}=179 \text{ mA}$ , respectively. The current and voltage at the maximum power point in the I/V curve given in Fig. 4.35 were measured as  $I_{MP}=131.1 \text{ mA}$  and  $V_{MP}=0.5 \text{ V}$ , respectively, resulting in a maximum generated DC power output of  $P_{MP}=65.5 \text{ mW}$ . In order to calculate the solar efficiency of the meshed solar monopole antenna, equation (3.13) was used. In equation (3.13), whilst  $P_{MP}$  is the generated power at the maximum power point calculated as 65.5 mW above,  $P_{in}$  is the total illumination power incident upon the solar monopole antenna within the solar simulator, which is determined by the dimensions of the integrated poly-Si solar cell, 16 mm x 31 mm. Considering the illumination intensity within the solar simulator,  $1000 \text{ W/m}^2$ ,  $P_{in}$  can be obtained as 0.496 W resulting in a calculated solar efficiency of 13.1% from equation (3.13).

## 4.6 Summary

In this chapter, RF ground plane solar antenna integration topology, which involves the use of solar cells as an RF ground plane in addition to their photovoltaic function, was investigated.

It was demonstrated that:

- Using solar cells as an RF ground plane brings the shading problem. This is due to the fact that the RF radiating element of a planar antenna, such as microstrip patch antennas and printed monopole antennas, is traditionally opaque in structure and placed upon the ground plane. This results in the radiating element blocking the solar illumination incident upon the photovoltaic antenna, significantly reducing the solar efficiency, which was reported by a factor of up to 42.5% in this chapter.
- Meshing the RF radiating element has a significant potential in order to address this challenge. It was demonstrated in this chapter that by meshing the RF radiating element and printing it upon an optically transparent substrate, such as acrylic, a radiating element transparency of as high as 93.3% can be achieved.
- Correctly meshing the RF radiating element has a negligible effect on the input impedance and the radiation characteristics of a planar antenna,
- If a solar cell operating as an RF ground plane is encapsulated, the effect of the dielectric encapsulation material is a frequency shift, which must be taken into account in the design process. This is due to the presence of the transparent protective layer on top of the cell, which is in between the radiating element on top and the ground plane, i.e. the solar cell, at the bottom. The presence of an encapsulation element between the radiating element and the ground plane changes the effective dielectric constant of the antenna substrate, which results in a frequency shift in the resonance band.
- Although it was successfully demonstrated that meshing the RF radiating element addresses the shading problem, it increases the cost and complexity of the antenna fabrication process. This is due to the fact that, in order to achieve a meshing line width of as narrow as 0.2 mm demonstrated in this chapter, special cutting equipment needs to be used.

# Chapter 5 – RF Radiating Element Solar Integration

## 5.1 Introduction

In chapter 4, the use of solar cells as an RF ground plane element replacing the conventional ground plane of planar antennas was discussed. It was shown that this solar antenna integration topology has a disadvantage from a photovoltaic perspective that the RF radiating element shades the solar cell, which significantly reduces the solar efficiency. Although this challenge was successfully addressed by meshing the RF radiating element, this technique requires the use of special printing equipment, which increases the fabrication cost and complexity of the antennas.

In this chapter, the second solar antenna integration topology, which is the use of solar cells as an RF radiating element, is investigated in order to address the shading problem from a photovoltaic perspective.

## 5.2 The Integration Topology

The solar antennas presented in this chapter are designed based upon the fact that, as illustrated in Fig. 5.1, the metal rear contact of a silicon solar cell can be seen as a homogeneous metal plate from an RF perspective and therefore has the potential to replace the conventional radiating copper patch element of a planar antenna.

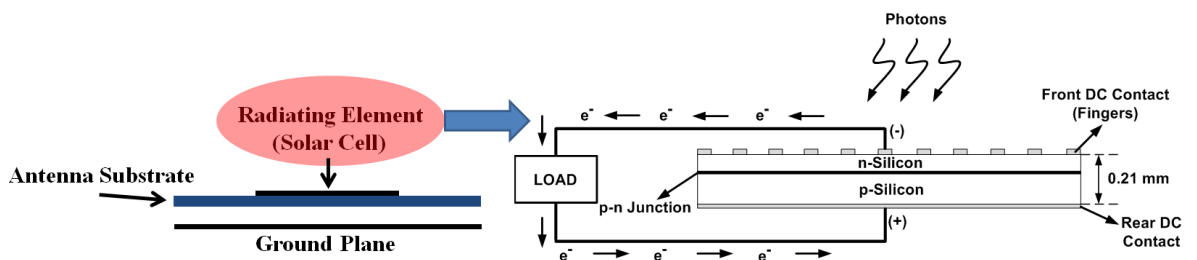


Fig. 5.1: RF radiating element solar antenna integration topology.

As mentioned earlier in chapter 1, this type of integration topology has the advantage of ensuring optimum operation characteristics from a photovoltaic perspective. This is due to the alignment of the solar cells operating as an RF radiating element above the other RF components. This successfully prevents the solar cells from being shaded by any RF

elements of the antenna. However, due to the requirement for a solar cell to be homogenous in structure to achieve optimum solar performance, techniques requiring the modification of the radiating element to excite multiple  $TM_{mn}$  propagation modes to achieve multiband and wideband resonance characteristics, such as loading the radiating element with capacitive slots [59-83], cannot be applied in this integration topology. Therefore, the solar patch antennas presented in this chapter have a suspended structure enabling them to have wider impedance bandwidths in comparison to the conventional microstrip patch antennas combined with solar cells operating as an RF radiating element studied in the literature [52-55].

## **5.3 Suspended Solar Patch Antenna for 2.4 GHz Band WLAN and 2.5 GHz band WiMAX**

### **Applications**

In this section, a suspended microstrip patch antenna integrated with a poly-Si solar cell operating as an RF radiating patch element is demonstrated for 2.4 GHz band WLAN (2.4-2.484 GHz) and 2.5 GHz band WiMAX (2.5-2.7 GHz) applications. It is demonstrated that whilst the use of the solar cell as an RF radiating element replacing the conventional microstrip patch enables the solar cells to operate without being shaded by any RF components of the antenna, the use of a suspended geometry results in an enhanced -10 dB impedance bandwidth enabling the antenna to provide a simultaneous coverage for 2.4 GHz band WLAN and 2.5 GHz band WiMAX applications.

#### **5.3.1 Solar Patch Antenna Design**

The design of the proposed suspended solar patch antenna was carried out in CST Microwave Studio. The proposed solar antenna in CST Microwave Studio is illustrated in Fig. 5.2.

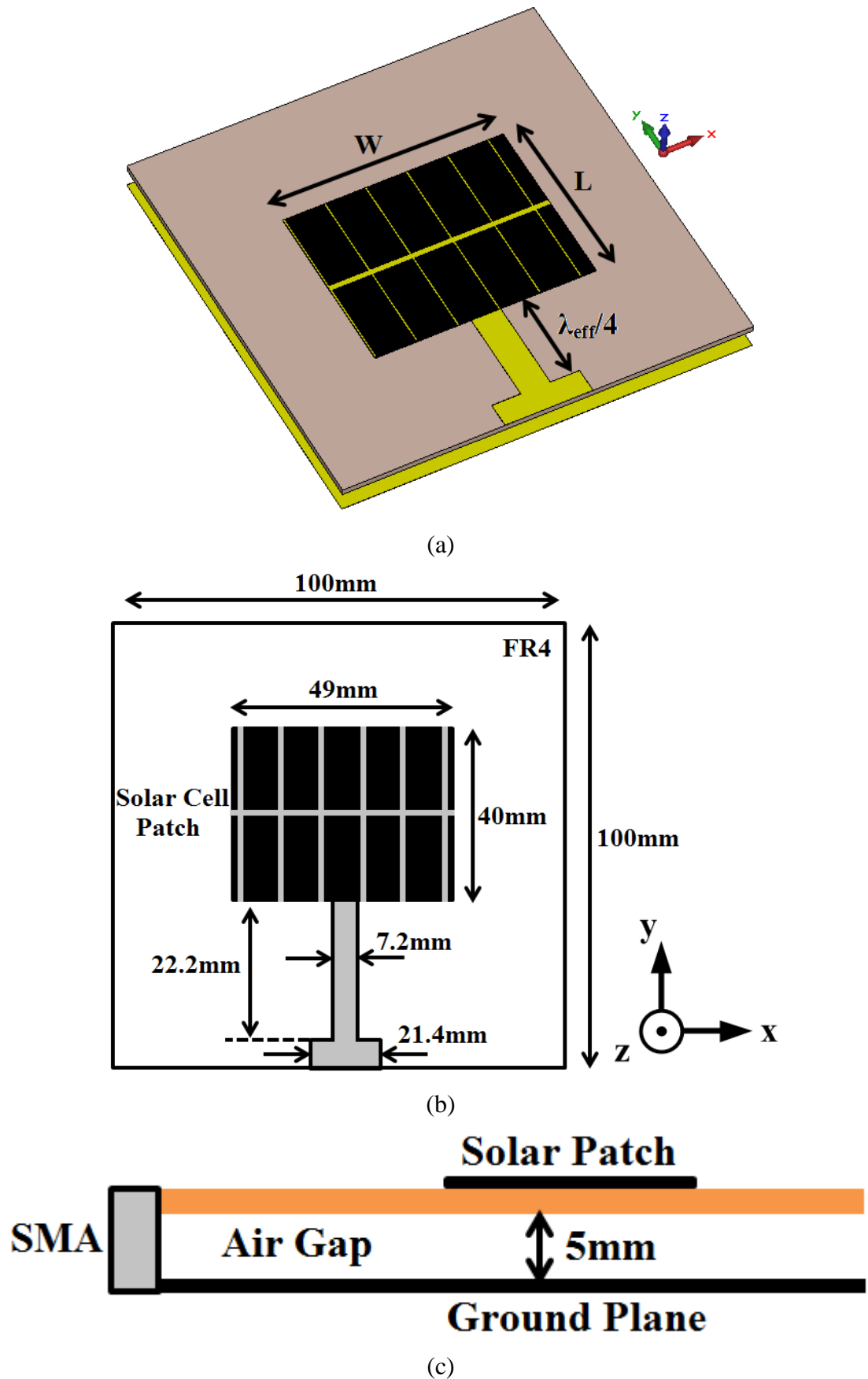


Fig. 5.2: Suspended solar patch antenna (a) design in CST Microwave Studio (b) top view (x-y plane) (c) side view (y-z plane).

As illustrated in Fig. 5.2, the photovoltaic patch antenna consists of an FR4 substrate,  $\epsilon_r=4.3$  and  $\tan\delta=0.025$ , suspended at 5 mm above the ground plane, resulting in  $\epsilon_{eff}=1.82$ . The first stage of the design process was the calculation of the design parameters for the conventional version of the proposed suspended solar patch, which are given as  $W$ ,  $L$  and  $\lambda_{eff}/4$  in Fig. 5.2(a), at the centre frequency of 2.5 GHz. Using equations (2.26) and (2.29), the design parameters were calculated as  $W=49$  mm,  $L=40$  mm and  $\lambda_{eff}/4=22.2$  mm. Following the design of the conventional version, the photovoltaic integration of the suspended patch antenna was performed. As can be seen in Fig. 5.2, placed upon the suspended FR4 substrate, following elements are present:

- 1) Radiating poly-Si solar cell replacing the conventional copper patch element: The antenna consists of a poly-Si solar cell replacing the conventional microstrip patch element. As illustrated in Fig. 5.1, the poly-Si solar cell has two metal contacts, a front grid and a rear solid, together with a silicon layer in between. If consideration is given to the rear metal contact of the cell, it can be seen that from an RF perspective, it is homogeneous in structure and therefore can replace the conventional microstrip patch element.
- 2) Microstrip feeding line: The microstrip feeding line was printed upon the suspended FR4 substrate,  $\epsilon_{reff}=1.82$ , and matches the impedance at the input of the solar patch, which was obtained in CST Microwave Studio as  $181.6\Omega$ , to the impedance at the SMA feeding port,  $50\Omega$ . This was achieved using a quarter-wavelength microstrip transmission line with a characteristic impedance of  $Z = \sqrt{181.6 \times 50} = 95.3\Omega$  as demonstrated in Fig. 5.2. Considering the effective substrate dielectric constant of  $\epsilon_{reff}=1.82$  due to the suspended geometry, the widths of the microstrip transmission lines with characteristics impedances of  $50\Omega$  and  $95.3\Omega$  were calculated as 21.4 mm and 7.2 mm, respectively.

### 5.3.2 Simulation and Measurement Results

The  $S_{11}$  simulations of the suspended solar patch antenna were performed in CST Microwave Studio while the measurements were carried out using a VNA, Agilent E8364B. The simulated and measured  $S_{11}$  patterns are demonstrated in Fig. 5.3.

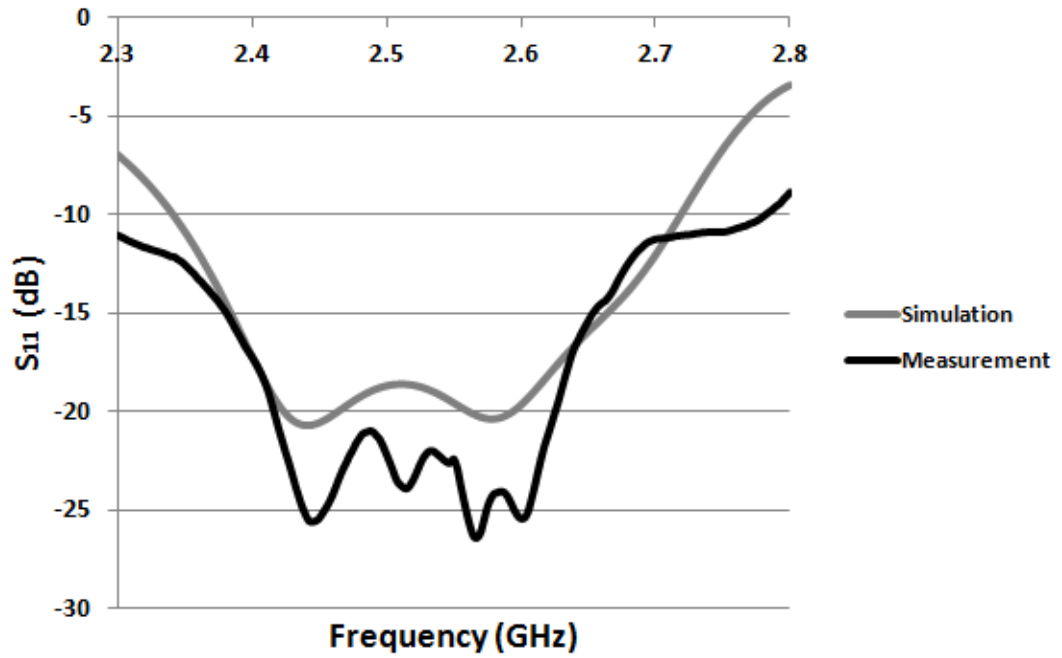


Fig. 5.3: Simulated and measured  $S_{11}$  patterns.

As can be seen in Fig. 5.3, there is good agreement between the simulated and measured  $S_{11}$  patterns of the suspended microstrip solar patch antenna confirming the accuracy of the modelling of the poly-Si solar cells in CST Microwave Studio illustrated in Fig. 5.4.

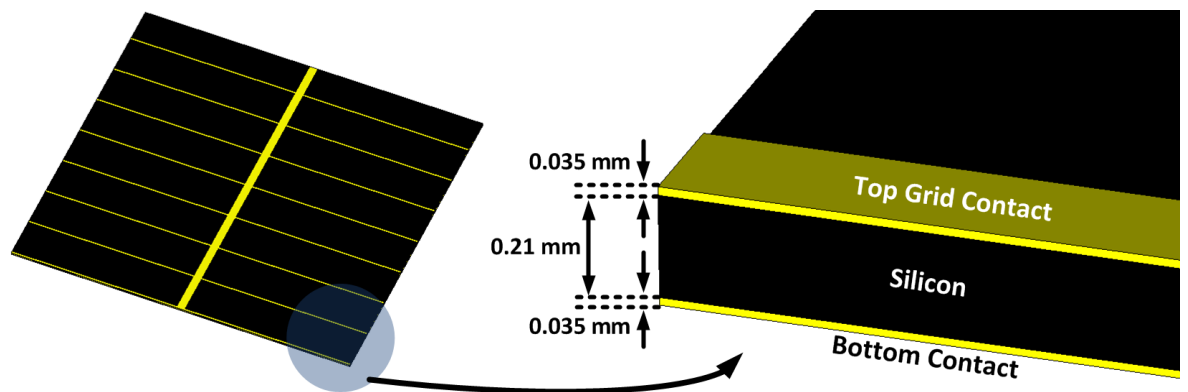


Fig. 5.4: Silicon solar cell modelled in CST Microwave Studio.

Due to the suspended geometry, the proposed solar patch antenna offers a widened -10 dB impedance bandwidth, which was measured as 490 MHz, 19.2%, operating at the frequency band of 2.3-2.79 GHz. The obtained -10 dB impedance bandwidth enables the proposed suspended solar patch antenna to be employed in 2.4 GHz band WLAN (2.4-2.484 GHz) and 2.5 GHz band WiMAX (2.5-2.7 GHz) networks.

The E-plane ( $y$ - $z$  plane) and H-plane ( $x$ - $z$  plane) far-field radiation pattern measurements of the proposed solar patch antenna, AUT, were taken in an anechoic chamber. Similar to

the far-field radiation pattern measurements of the photovoltaic antennas demonstrated in the previous chapter, the conical spiral antenna with a gain of  $G_T=4$  dBi was used as a reference antenna placed at a distance of  $R=3$  m from the AUT as illustrated in Fig. 5.5.

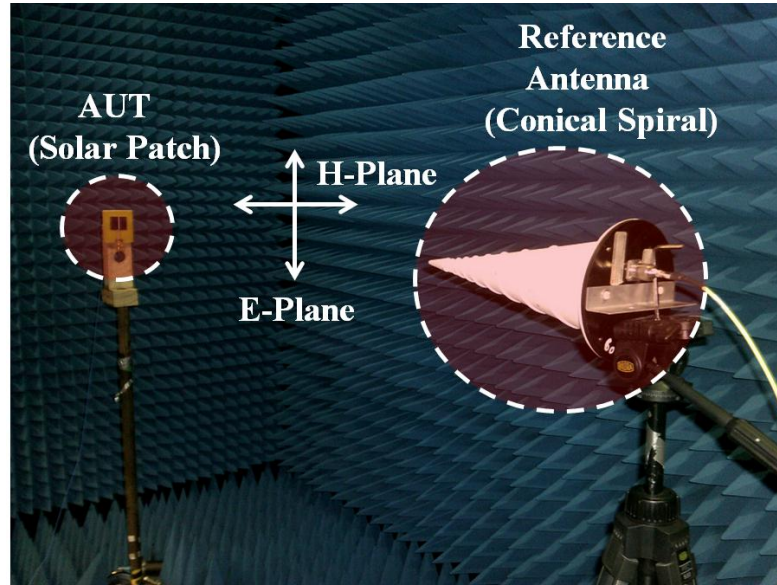


Fig. 5.5: E-plane and H-plane far-field radiation pattern measurement set-up in anechoic chamber.

The solar microstrip patch antenna was rotated by  $360^\circ$  in the E-plane and H-plane with a sampling angle of  $5^\circ$ . At each sampling angle, the received power by the AUT,  $P_R$ , was measured and Friis equation given in equation (4.3) was used to calculate the gain by taking the cable losses into account as given in equation (4.4). The normalised simulated and measured E-plane and H-plane far-field radiation patterns are illustrated in Fig. 5.6 whilst the maximum gain values are given in Table 5.1.

Table 5.1: Measured maximum E-plane and H-plane gain values.

Frequency (GHz)	$P_R$ (dBm)	$L_{\text{Cable}}$ (dB)	Measured Maximum Gain (dBi)	Simulated Maximum Gain (dBi)
2.4	-32.24	7.32	6.6	6.2
2.5	-32.63	7.49	6.8	6.3
2.6	-32.83	7.65	7.1	6.9
2.7	-33.02	7.81	7.4	7

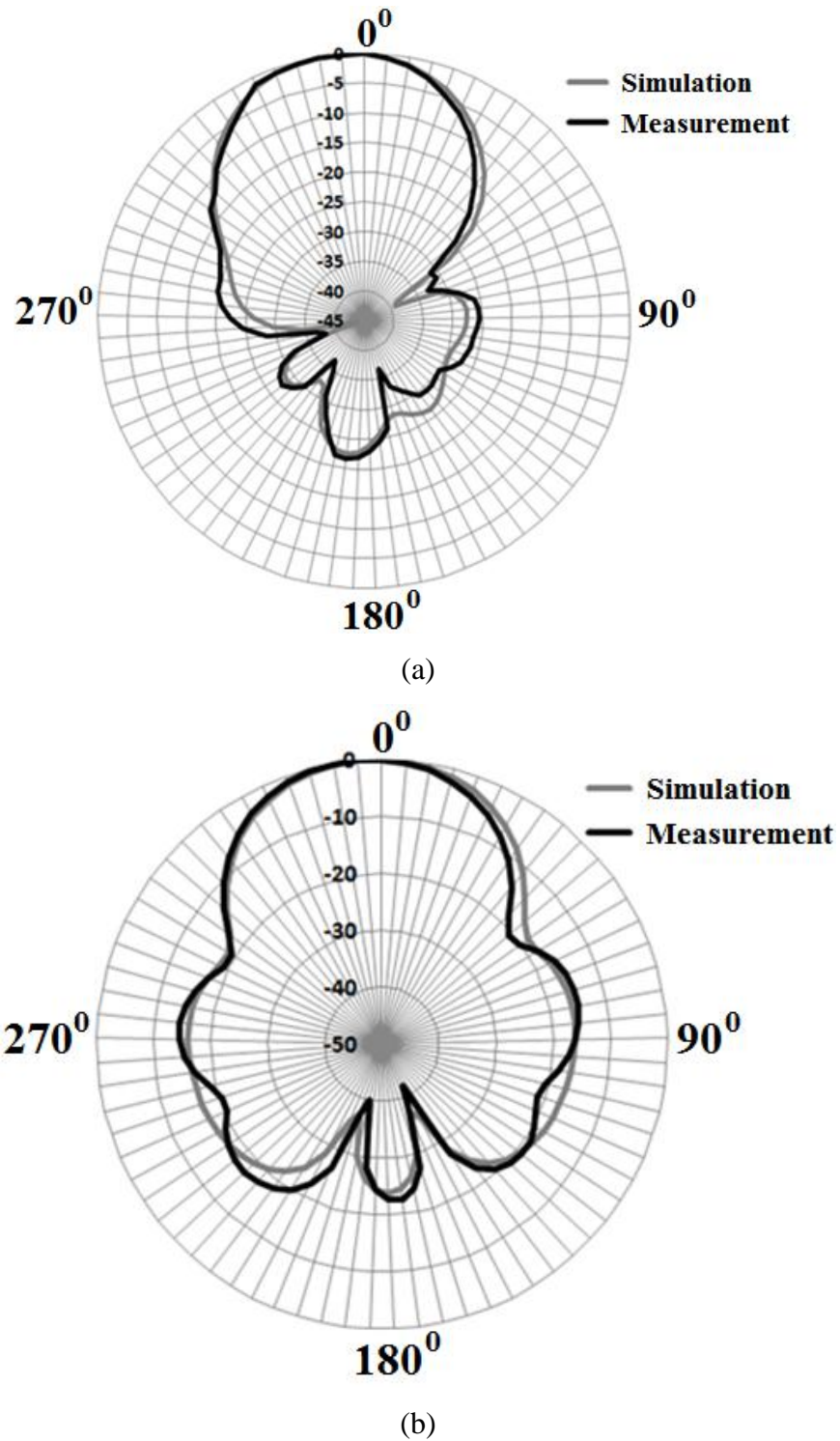


Fig. 5.6: Far-field radiation patterns (a) E-plane (b) H-plane.

As demonstrated in Fig. 5.6, the suspended microstrip solar patch antenna has its maximum radiation in the broadside direction and there is good agreement between the simulated and measured far-field radiation patterns.

### 5.3.3 Effect of Solar Integration on the Antenna

#### Performance

In addition to providing narrow-band resonance characteristics, the RF radiating element solar antenna integration topology demonstrated in the literature does not provide an investigation into the effect of the photovoltaic integration on the RF antenna response. For RF radiating element solar antenna integration topology, this investigation is of significant importance due to the fact that solar cells work as an RF radiating element and therefore determine the radiation characteristics of the integrated antennas. In order to study the effect of the photovoltaic integration of the proposed suspended microstrip patch antenna on the antenna performance, two prototypes of the antenna were designed and fabricated:

- The suspended microstrip patch antenna consisting of an poly-Si solar cell radiating patch element as illustrated in Fig. 5.2,
- The suspended microstrip patch antenna consisting of a conventional printed copper patch radiating element as illustrated in Fig. 5.7.

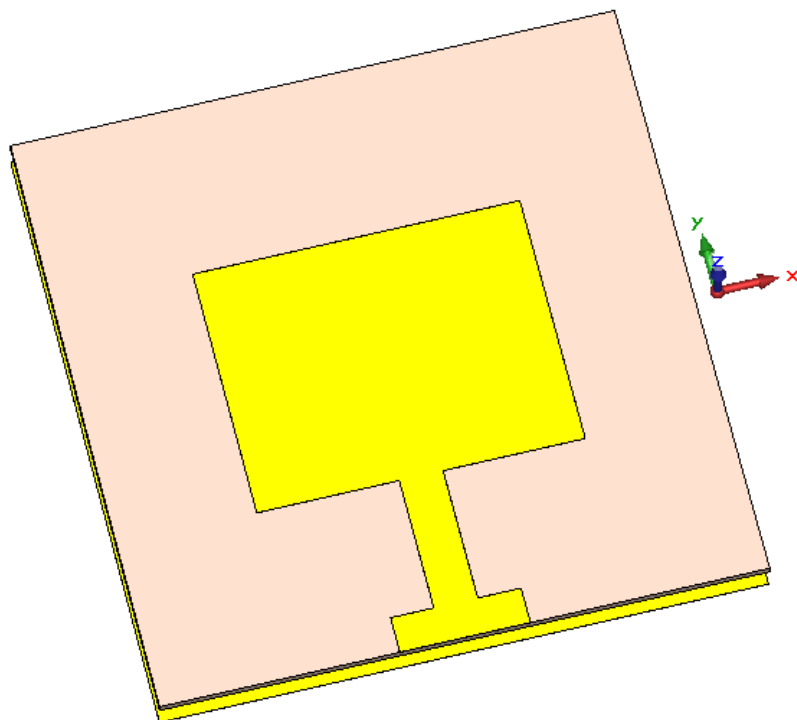


Fig. 5.7: Suspended microstrip patch antenna consisting of conventional printed copper patch radiating element.

The  $S_{11}$  and E-plane and H-plane far-field radiation pattern measurements of solar and non-solar versions of the suspended microstrip patch antenna were performed and a comparison between the obtained results is provided in Table 5.2. The far-field radiation pattern measurements were carried out at the resonance frequency of 2.5 GHz.

Table 5.2: Comparison between the resonance characteristics of solar and conventional non-solar versions of the antenna.

	Copper Patch		Solar Patch	
	Simulation	Measurement	Simulation	Measurement
<b>-10 dB Impedance Bandwidth (MHz)</b>	424	410	485	490
<b>E-plane Sidelobe (dB)</b>	-15.9	-16.5	-14.8	-15.1
<b>E-plane - 3 dB Beamwidth (Degrees)</b>	62.5	62.1	62.6	62.2
<b>Maximum Gain (dBi)</b>	7	7.2	6.3	6.8
<b>H-plane Sidelobe (dB)</b>	-14.3	-15.2	-14.2	-14.6
<b>H-plane - 3 dB Beamwidth (Degrees)</b>	63.6	62.3	63.8	62.3

As can be seen in Table 5.2, the use of the solar cell as an RF radiating element within the antenna replacing the conventional copper radiating patch element:

- Increases the -10 dB impedance bandwidth of the antenna. As can be seen in Table 5.2, while the non-solar version of the antenna has a measured -10 dB impedance bandwidth of 410 MHz, the proposed solar version of the antenna has a -10 dB impedance bandwidth of 490 MHz equating to an increase in the measured bandwidth by 80 MHz, 19.51%. This can be attributed to the loss introduced by the silicon layer of the cell.

- Increases the sidelobe level of the antenna. As given in Table 5.2, in the E-plane, while the suspended solar patch antenna has a measured sidelobe level of -15.1 dB, the non-solar version of the antenna offers a sidelobe level of -16.5 dB corresponding to an increase in the sidelobe level of the solar version by 1.4 dB. Similarly, in the H-plane, while the solar version has a sidelobe level of -14.6 dB, the non-solar version has a sidelobe level of -15.2 dB corresponding to an increase in the sidelobe level of the solar patch by 0.6 dB,
- Has a negligible effect on -3 dB beamwidth. In the E-plane, the solar and non-solar versions of the suspended microstrip patch antenna have -3 dB beamwidths of 62.2° and 62.1°, respectively. Similarly, in the H-plane, -3 dB beamwidths were measured as 62.3° for both solar and non-solar versions of the antenna,
- Decreases the maximum gain. Whilst the conventional non-solar version of the antenna has a measured maximum gain of 7.2 dBi, the proposed suspended solar patch antenna has a maximum gain of 6.8 dBi, corresponding to a decrease in the measured maximum gain by 0.4 dB. This decrease in the maximum gain is due to the presence of the silicon layer, which acts as a lossy dielectric element stacked upon the rear contact of the solar cell operating as an RF radiating element.

### **5.3.3.1 Effect of DC Termination on the RF Antenna Response**

From a photovoltaic perspective, the integrated solar cell is required to be terminated in a DC load to be powered, which was selected as a conventional 220Ω resistor in this design. Different from the previous chapter in which the use of solar cells as an RF ground plane was investigated, the use of solar cells as an RF radiating element brings an additional challenge that the effect of the DC connections between the solar cell and the DC load terminals must be taken into account. This is due to the potential of these DC connections to significantly affect the RF surface current distribution across the radiating element, which is the rear contact of the integrated solar cell. Therefore, in order to minimise the effect of the DC terminal connections on the RF characteristics of the antenna, two methods were studied in this section:

- The first method is connecting the DC load to the terminals of the solar cell at the non-radiating edges as demonstrated in Fig. 5.8,
- The second method is the use of a DC/RF isolation circuit.

The introduction of the DC load at the non-radiating edge of the solar patch is demonstrated in Fig. 5.8.

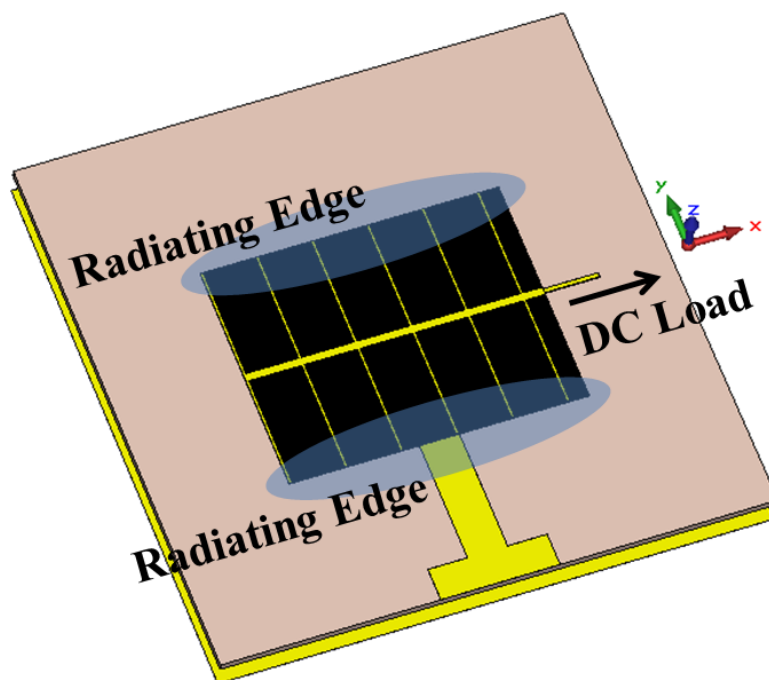


Fig. 5.8: DC load connection introduced at the non-radiating edge.

The simulated surface current distribution across the rear metal contact of the solar cell when the DC load, which is a  $220\Omega$  resistor, is connected at the non-radiating edge is demonstrated in Fig. 5.9.

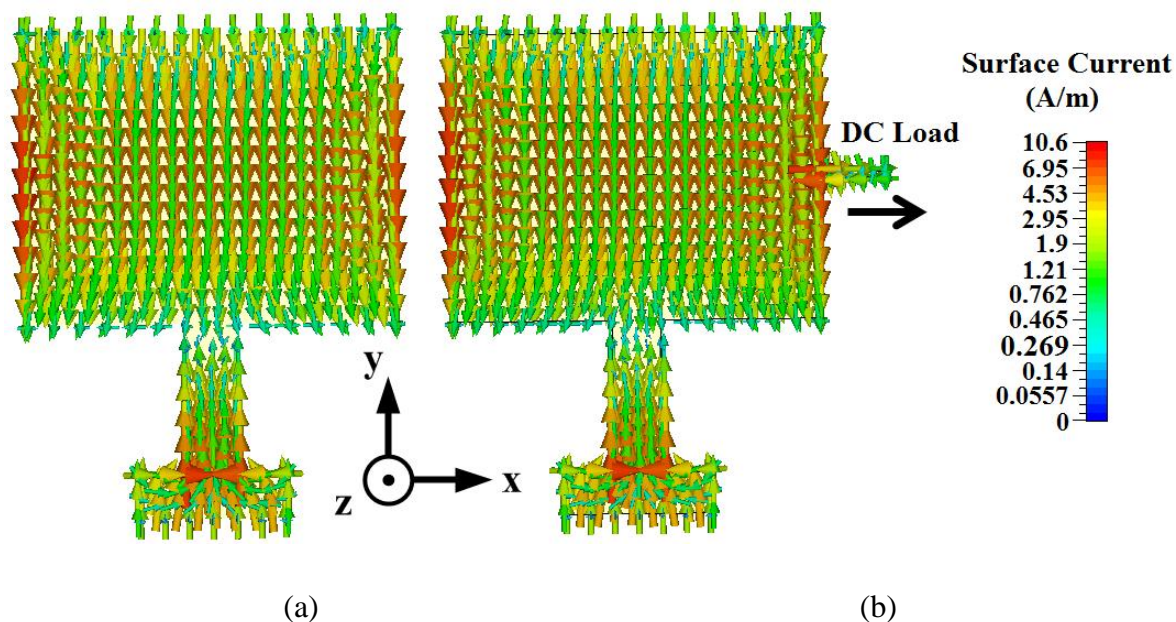


Fig. 5.9: Surface current distribution at 2.5 GHz (a) solar patch without the DC load (b) solar patch with the DC load attached at the non-radiating edge.

As can be seen in Fig. 5.9(a), the suspended solar patch antenna operates in  $TM_{10}$  fundamental propagation mode with the surface current flowing along the length of the patch in the y-axis. Whilst the edges on top and at the bottom in the y-axis are responsible for the radiation, the patch edges on the left and right in the x-axis do not contribute to the RF radiation in the far-field. Therefore, it is expected that connecting a DC load to the cell terminals at the non-radiating edges, i.e. perpendicular to the direction of the surface current, should bring a negligible effect on the RF response of the antenna. If consideration is given to the demonstrated current distribution in Fig. 5.9(b), it can be seen that the current distribution across the rear contact of the cell, i.e. the patch, connected to the DC load at the non-radiating edge is almost identical to the surface current distribution of the solar patch without the DC load illustrated in Fig. 5.9(a). This suggests that both solar patches present identical input impedance responses regardless of the presence of the DC load connection and therefore it can be concluded that the introduction of the copper wires at the non-radiating edges does not affect the RF response of the antenna ensuring stable RF characteristics in the presence of a DC load connected to the cell terminals.

In Fig. 5.10, however, the DC connection is provided at the radiating edge and the simulated current distributions are illustrated in Fig. 5.11.

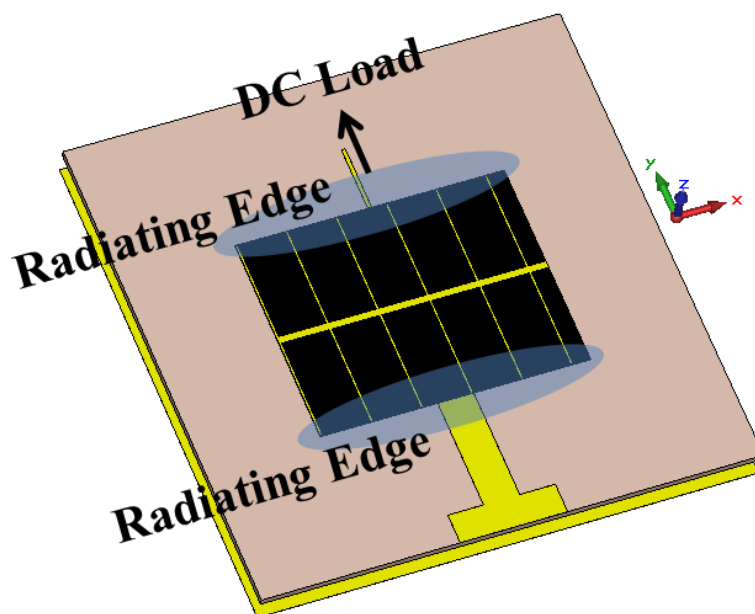


Fig. 5.10: DC load connection introduced at the radiating edge.

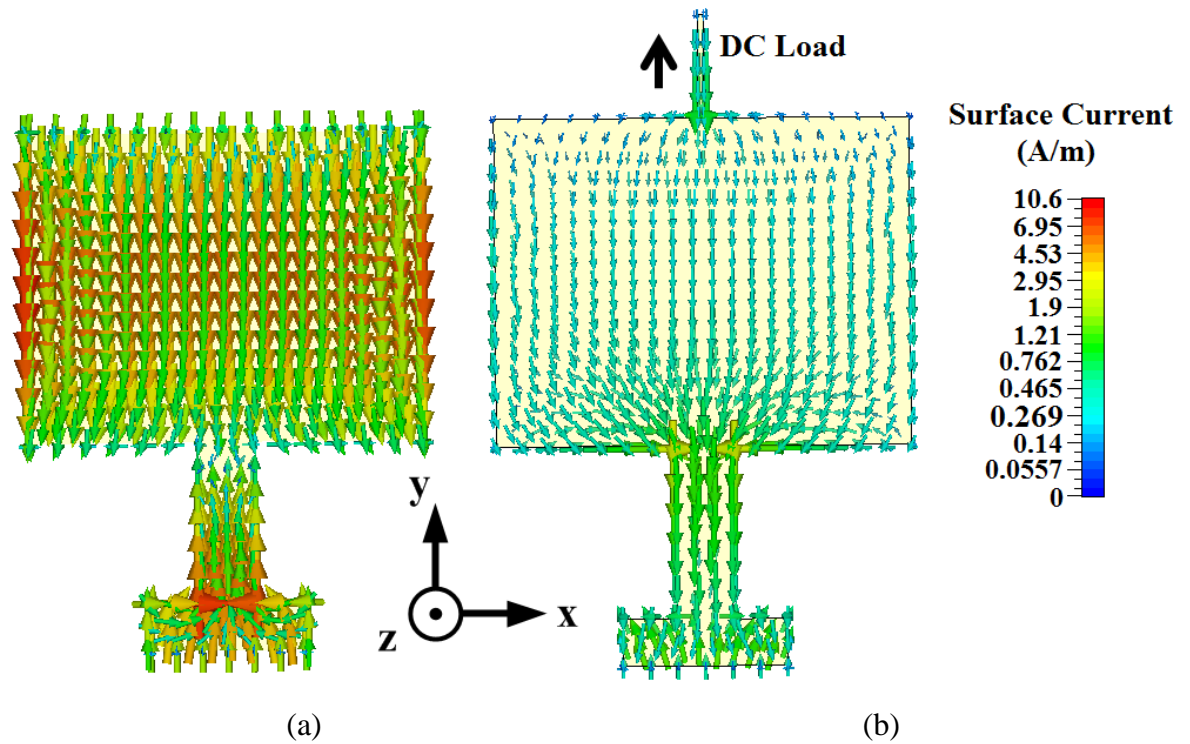


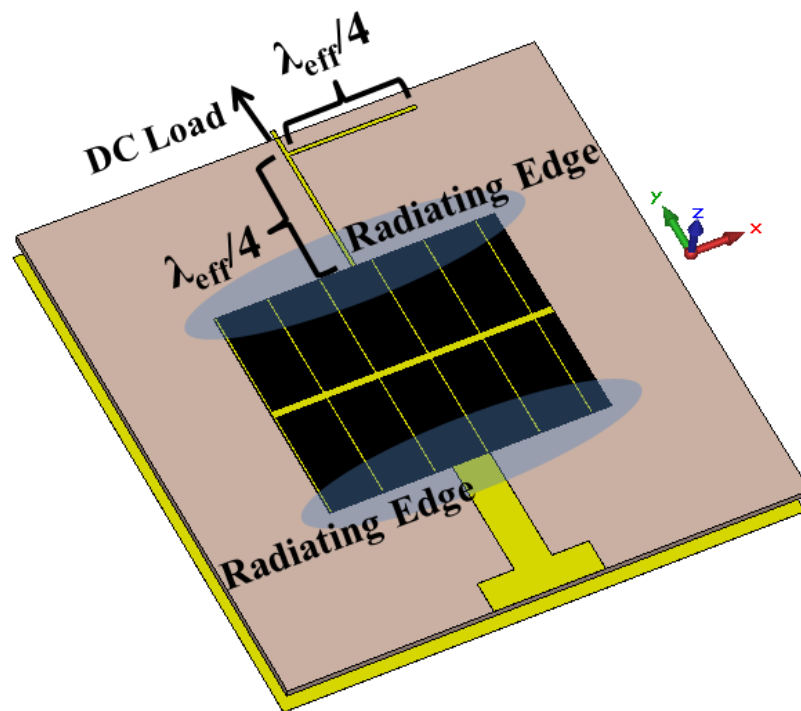
Fig. 5.11: Surface current distribution at 2.5 GHz (a) solar patch without the DC load (b) solar patch with the DC load connected at the radiating edge.

As can be seen in Fig. 5.11, introducing the DC load at the radiating edge seriously affects the surface current distribution, which also changes the input impedance of the solar patch. This is due to the fact that the surface current of the solar patch continues to flow through the DC connection at the radiating edge, which now operates as a part of the RF radiation, significantly affecting the RF response of the antenna.

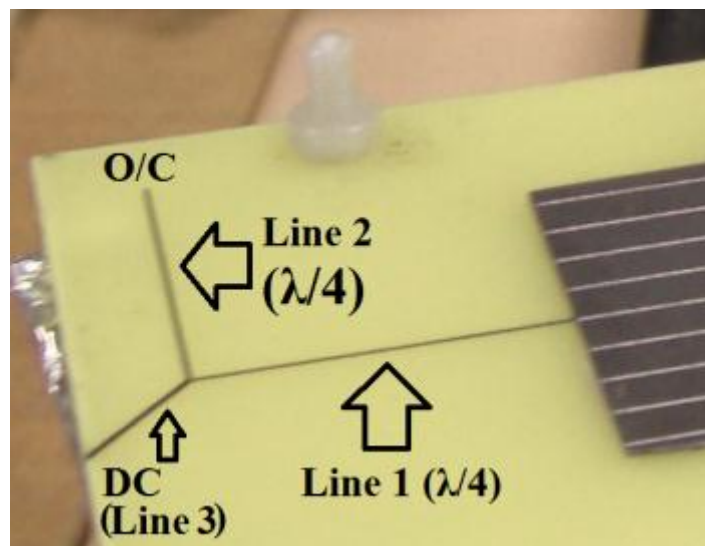
### 5.3.3.2 DC/RF Isolation for DC Load Connection at the Radiating Edge

As demonstrated in the previous section, although using the non-radiating edges for the DC load terminal connection is an optimum solution for linearly-polarised microstrip solar patch antennas, this observation brings a new challenge for photovoltaic antennas in which all edges contribute to the RF radiation, such as dual-polarised solar patch antennas described in chapter 6. For these antennas, both fundamental propagation modes  $TM_{01}$  and  $TM_{10}$  are present and therefore the antenna has two radiating edges for  $TM_{01}$  and the other two for  $TM_{10}$ . For this reason, all edges contribute to the RF radiation in the far-field and therefore a DC/RF isolation circuit must be provided to ensure the RF stability. Although this type of solar antenna will be one of the subjects of the next chapter, in which a new solar antenna integration topology will be introduced, the DC/RF isolation circuit is

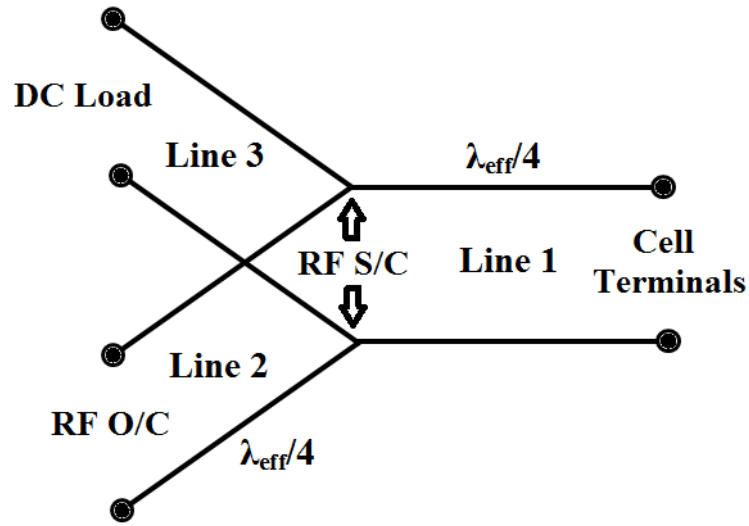
presented in this chapter as a second method to minimise the effect of the DC terminal connections on the RF response of the proposed solar patch antenna. In Fig. 5.12, the solar patch antenna consists of a DC load connected through the DC/RF isolation circuit at the radiating edge.



(a)



(b)



(c)

Fig. 5.12: DC/RF isolation circuit introduced at the radiating edge (a) design in CST Microwave Studio (b) fabricated prototype (c) equivalent circuit model of the proposed DC/RF isolation circuit.

As illustrated in Fig. 5.12, the proposed DC/RF isolation circuit consists of two quarter-wavelength ( $\lambda_{eff}/4$ ) microstrip transmission lines, labelled as line 1 and line 2, and a DC line, labelled as line 3 in Fig. 5.12(b). The quarter-wavelength of the transmission lines 1 and 2 was determined by the effective dielectric constant ( $\epsilon_{reff}$ ) due to the suspended geometry, which was calculated as  $\epsilon_{reff}=1.82$ . The surface current distribution across the rear contact of the solar patch in the presence of the proposed DC/RF isolation circuit is demonstrated in Fig. 5.13.

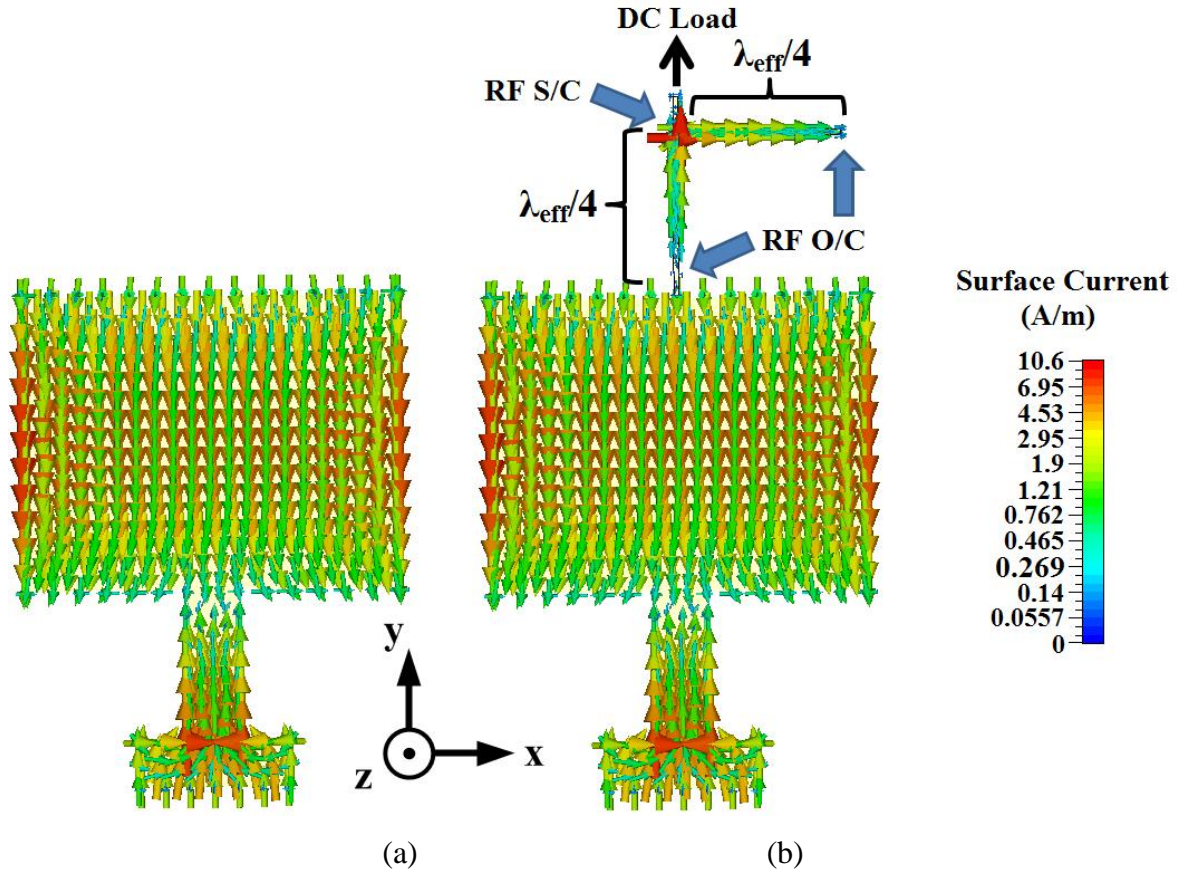


Fig. 5.13: Surface current distribution at 2.5 GHz (a) solar patch without the DC load (b) solar patch with the DC load connected at the radiating edge through the proposed DC/RF isolation circuit.

As can be seen in Fig. 5.13, the quarter-wavelength ( $\lambda_{eff}/4$ ) microstrip transmission lines, which are labelled as line 1 and line 2 in Fig. 5.12, are to create a high RF impedance to the cell whilst transmission line 3 is to withdraw the DC solar cell current to the load through transmission line 1. As can be seen in Fig. 5.12(c) and Fig. 5.13(b), the impedance at the input of the microstrip transmission line 2 in the x-axis is very high, ideally an RF open-circuit, and it results in a very low impedance, ideally an RF short-circuit, at the input of the microstrip transmission line 1 in the x-axis due to the quarter-wavelength impedance transformation. At the input of the transmission line 1 in the x-axis, which is indicated as RF S/C in Fig. 5.13(b), the amplitude of the RF surface current peaks due to the low RF impedance. Due to the quarter-wavelength impedance transformation, at the output of transmission line 1 in the y-axis, i.e. the cell terminal, a high RF impedance, ideally an RF open-circuit, is obtained. Therefore, as demonstrated in Fig. 5.13(b), the RF current is choked at the DC terminals of the solar patch whilst from a photovoltaic perspective, the

short-circuit cell generated DC current path, which is the combination of line 1 and line 3 in Fig. 5.12, is maintained.

In order to demonstrate the isolation achieved through the proposed DC/RF isolation circuit, the  $S_{11}$  patterns of the of the suspended solar patch array antenna were measured under two circumstances given below:

- In the absence of the DC load,  $220\Omega$ , and the DC/RF isolation circuit (solar cell is in isolation),
- Solar cell connected to the DC load,  $220\Omega$ , through the proposed DC/RF isolation circuit.

A comparison between the obtained  $S_{11}$  patterns is provided in Fig. 5.14.

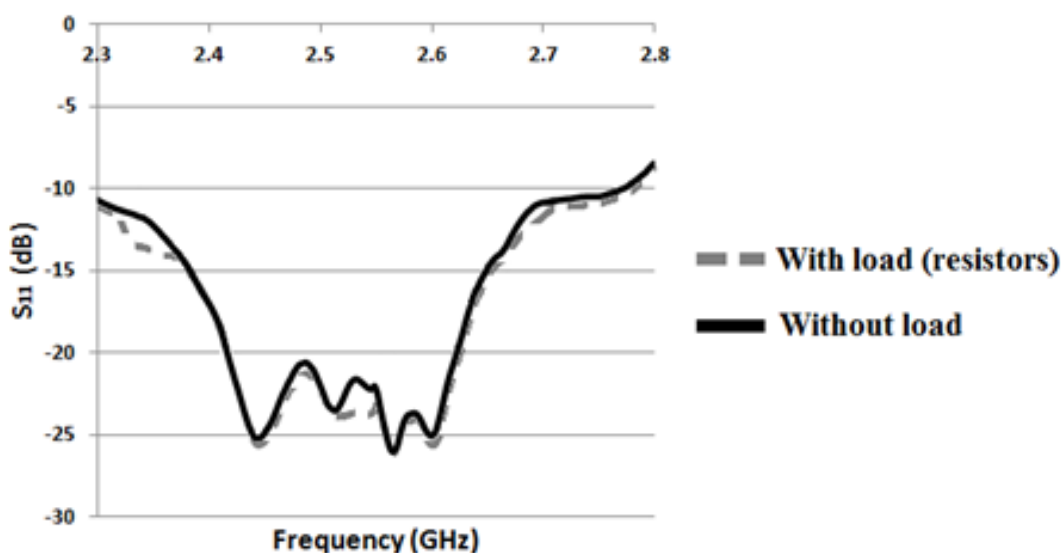


Fig. 5.14: Measured  $S_{11}$  patterns with and without DC load.

As can be seen in Fig. 5.14,  $S_{11}$  response of the antenna remains almost identical regardless the presence of the DC load,  $220\Omega$ , connected to the solar patch at the radiating edge. Negligible difference between the  $S_{11}$  patterns with and without the DC load can be attributed to the fact that the quarter-wavelength of transmission lines 1 and 2 in the DC/RF isolation circuit was designed for the centre frequency of 2.5 GHz, resulting in a slight difference below and above 2.5 GHz. In comparison to attaching the DC load at the radiating edge of the solar patch without using a DC/RF isolation circuit demonstrated earlier, the surface current distribution in Fig. 5.13 and the  $S_{11}$  patterns in Fig. 5.14 illustrate how effectively the proposed DC/RF isolation circuit isolates the DC load connections from the RF response of the antenna when the DC connection is required to be

provided at the radiating edge. This will be crucial to achieve stable RF characteristics from dual-polarised solar patch antennas, which will be discussed in Chapter 6.

## **5.4 Cross-Coaxial Fed Wideband Solar Patch**

### **Antenna**

As mentioned earlier, due to the narrow impedance bandwidth response of conventional microstrip patch antennas, existing photovoltaic patch antennas using solar cells as an RF radiating element offer narrow impedance bandwidths making these antennas unsuitable for multiband and wideband applications. Therefore, the RF radiating element solar antenna integration topology brings the challenge that modifying the RF radiating element, i.e. the solar cell, such as capacitive slot loading [59-83], in order to excite multiple  $TM_{mn}$  propagation modes to achieve multiband/wideband resonance response is not possible. This is due to the requirement for the integrated solar cells to be homogeneous in structure to achieve an optimum solar performance. To this end, in order to achieve a wideband resonance response, a suspended patch antenna integrated with a poly-Si solar cell operating as an RF radiating element offering a -10 dB impedance bandwidth of 490 MHz, 19.2%, was successfully demonstrated in the previous section. However, the proposed solar antenna in the previous section does not cover the frequency band required for 2.3 GHz band WiMAX applications. In this section, a further -10 dB impedance bandwidth widening is achieved using a new feeding structure, called cross-coaxial feed, in a suspended short-circuited solar patch antenna. This design offers a -10 dB impedance bandwidth of 840 MHz, 35%, and is proposed for 2.4 GHz band WLAN (2.4-2.484 GHz) and 2.3/2.5 GHz band WiMAX (2.3-2.4 GHz / 2.5-2.7 GHz) networks. This represents a bandwidth improvement of 82.3% compared to the previous design. The fabricated solar patch antenna consists of an encapsulated poly-Si solar cell operating as a suspended RF radiating element replacing traditional copper patch.

### **5.4.1 Solar Patch Antenna Design**

As demonstrated in Fig. 5.1, the integrated poly-Si solar cell consists of front and rear metal contacts with a silicon layer in between. From an RF perspective, the rear DC contact of the cell allows the cell to be used as a homogeneous metal plate replacing the RF radiating element of a planar antenna. In the proposed design, the rear contact of the

cell operates as an RF radiating element replacing the conventional microstrip patch. The geometry of the short-circuited suspended solar patch antenna is illustrated in Fig. 5.15.

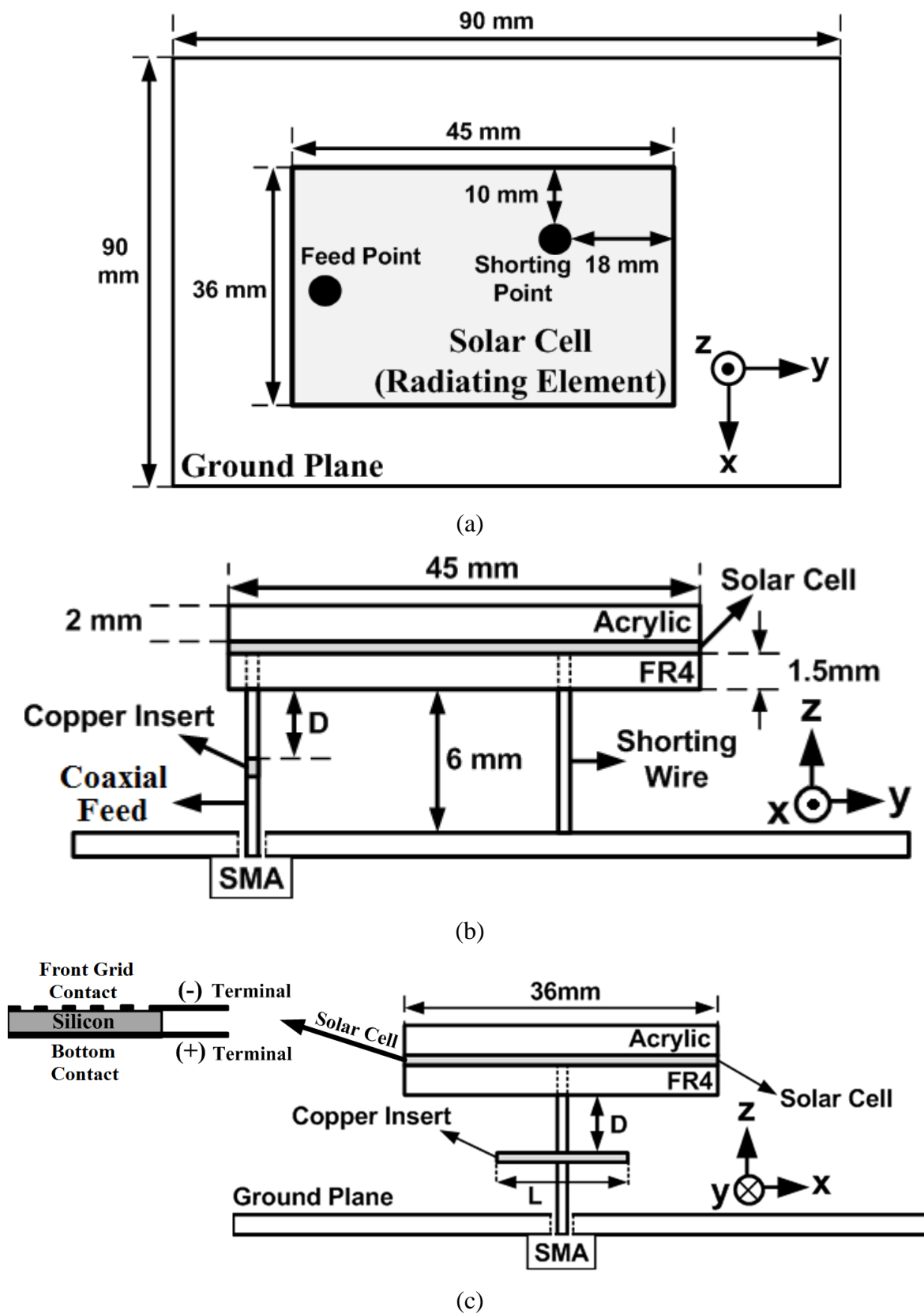


Fig. 5.15: Cross-coaxial fed suspended solar patch antenna (a) top view (b) front view (c) back view.

As can be seen in Fig. 5.15, the proposed solar patch antenna consists of an encapsulated poly-Si solar cell suspended at 6 mm above the ground plane. The cell is encapsulated between an acrylic layer,  $\epsilon_r=3.6$  and  $\tan\delta=0.015$ , on top and an FR4 supporting layer,  $\epsilon_r=4.3$  and  $\tan\delta=0.025$ , at the bottom. The conventional coaxial feed line is loaded with a copper insert attached at right angle to the inner conductor of the coaxial feeding line forming the proposed cross-coaxial feeding structure. The cross-coaxial feed together with its equivalent circuit model is illustrated in Fig. 5.16.

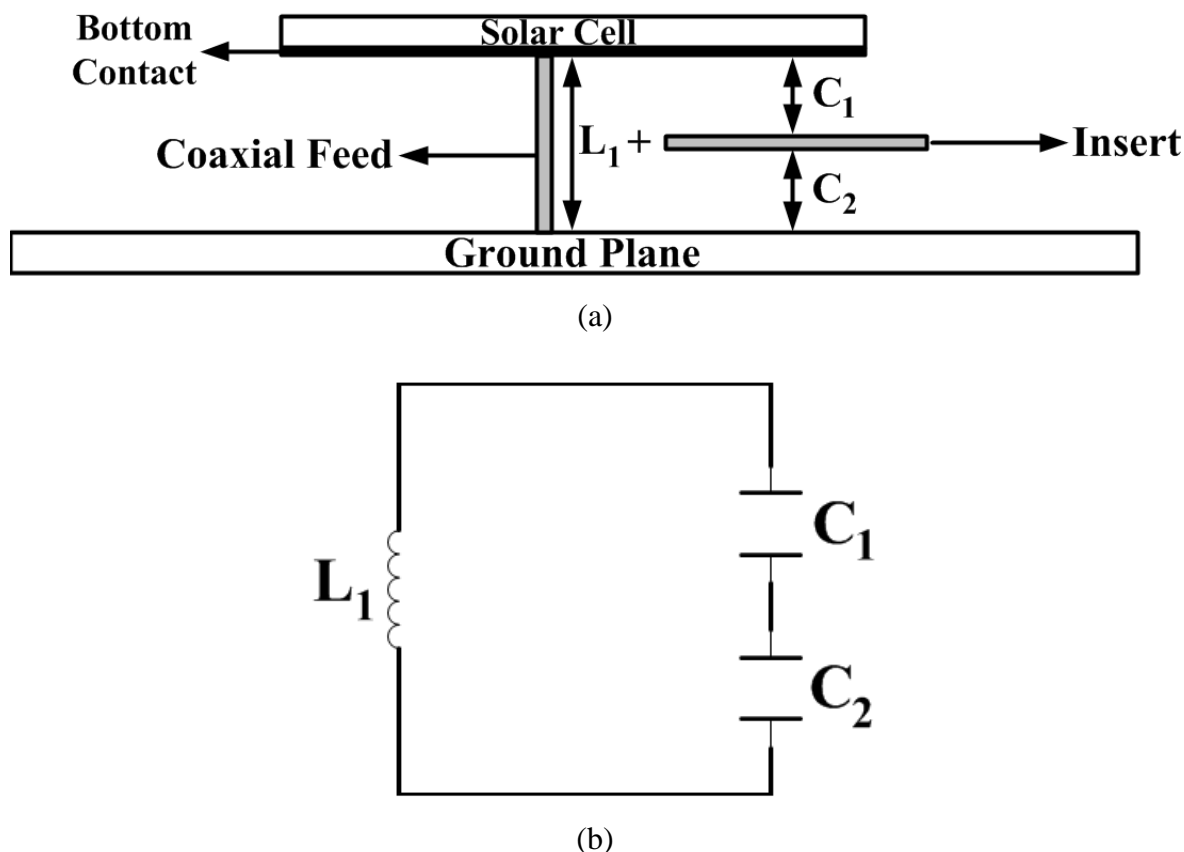


Fig. 5.16: Equivalent circuit model of the proposed cross-coaxial feed (a) circuit element representation of the cross-coaxial feeding elements (b) equivalent circuit model.

As illustrated in Fig. 5.16, due to the suspended geometry, the length of the inner conductor of the coaxial feed line in the air gap between the cell and the ground plane introduces an inductance represented by  $L_1$  in Fig. 5.16. The copper insert, on the other hand, acts as a capacitance between the solar cell and the insert, which is  $C_1$ , and the insert and the ground plane, which is  $C_2$ , respectively, as demonstrated in Fig. 5.16. The increased inductance due to the suspended geometry is balanced by the introduced capacitance from the copper insert making the proposed cross-coaxial feed to provide a superior impedance matching performance.

As illustrated in Fig. 5.15 and 5.16, the rear contact of the cell, operating as an RF radiating element, is connected to the cross-coaxial feed line at the feed point optimised in CST Microwave Studio. A second connection, which provides an RF short-circuit between the radiating element and the ground plane, is introduced at the shorting point as demonstrated in Fig. 5.15(a). It should be noted here that the length of the metal insert,  $L$ , in Fig. 5.15(c), and its distance from the suspended poly-Si cell,  $D$ , were the subject of parametric analyses performed in CST Microwave Studio in order to obtain the optimum  $S_{11}$  response as demonstrated in section 5.4.2.

## 5.4.2 Simulation and Measurement Results

### 5.4.2.1 Antenna Performance

The  $S_{11}$  measurements of the fabricated solar patch antenna were taken with and without the proposed copper insert and are illustrated in Fig. 5.17.

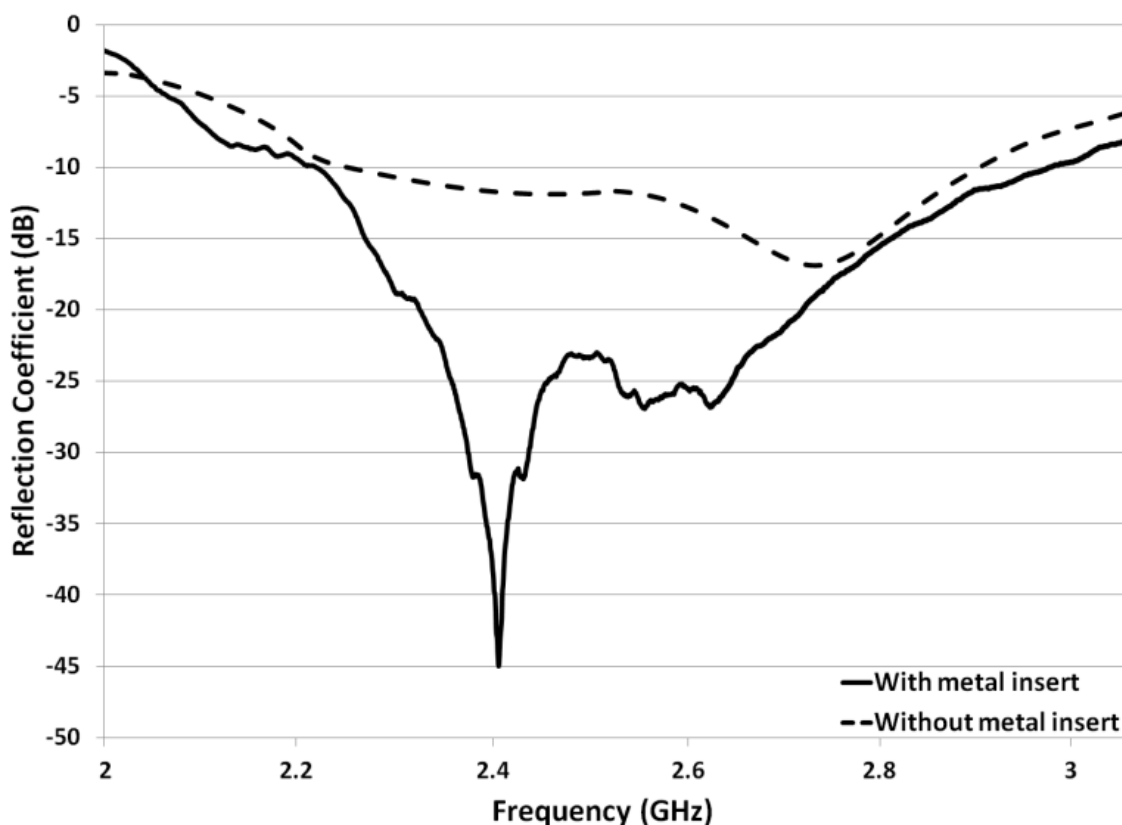


Fig. 5.17: Measured  $S_{11}$  patterns with and without the copper insert forming the cross-coaxial feed structure.

As can be seen in Fig. 5.17, the proposed metal insert brings a considerable enhancement in the  $S_{11}$  performance of the proposed solar patch antenna. Whilst the solar patch fed

through the conventional coaxial feed operates across -10 dB impedance band of 2.27-2.9 GHz, the proposed cross-coaxial fed solar patch covers the frequency band of 2.24-3.08 GHz widening the impedance bandwidth of the antenna by a factor of 33%. In addition, as can be seen in Fig. 5.17, across the frequency band of 2.33-2.72 GHz, the  $S_{11}$  response of the cross-coaxial fed solar antenna is below -20 dB demonstrating a considerable enhancement in the impedance matching performance as a result of using the proposed cross-coaxial feed structure. The fabricated cross-coaxial fed solar patch provides a simultaneous coverage for 2.4 GHz band WLAN (2.4-2.484 GHz) and 2.3/2.5 GHz band WiMAX (2.3-2.4 GHz / 2.5-2.7 GHz) networks.

At this stage, there are two design parameters of the proposed cross-coaxial feed structure whose effect on the  $S_{11}$  performance of the solar patch antenna needs to be investigated. The first parameter is the length of the copper insert,  $L$ , and the second parameter is the distance of the insert from the suspended solar cell,  $D$ , as demonstrated in Fig. 5.15(c).

In view of this, first, parametric analysis was performed in CST Microwave Studio in order to determine the optimum length of the copper insert to achieve optimum  $S_{11}$  performance. For the parametric analysis, the insert was attached to the coaxial feed line at a fixed distance from the cell,  $D=3$  mm, which is the centre of the coaxial feed line in the z-axis representing a initially selected non-optimised distance from the solar cell. The simulated  $S_{11}$  patterns of the cross-coaxial fed suspended solar patch antenna versus varying insert lengths are illustrated in Fig. 5.18.

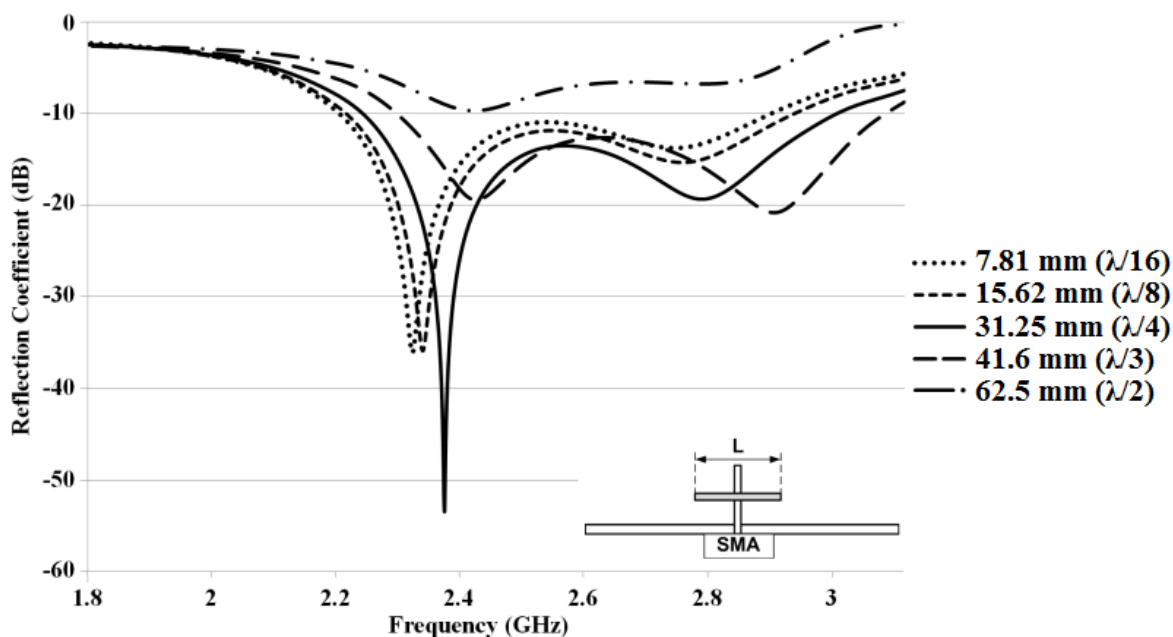


Fig. 5.18: Simulated  $S_{11}$  patterns versus varying insert lengths.

As can be seen in Fig. 5.18, the length of the insert has a significant effect on the  $S_{11}$  response of the antenna. Increasing the length of the insert shifts the operational frequency band of the solar patch antenna to a higher frequency. Also, the length of the insert seriously affects the impedance bandwidth. It can be seen in Fig. 5.18 that the optimum bandwidth was obtained when the insert length was selected as 31.25 mm. This corresponds to a quarter-wavelength at the frequency of 2.4 GHz. However, beyond 31.25 mm, deterioration in the  $S_{11}$  level and the bandwidth can clearly be seen in Fig. 5.18. This is especially evident when the insert length is selected as 62.5 mm, corresponding to a half-wavelength at 2.5 GHz, where the antenna demonstrates poor  $S_{11}$  performance staying above the level of -10 dB across the entire investigated frequency band. From Fig. 5.18, the optimum insert length was determined as 31.25 mm.

Following the determination of the optimum length of the insert as  $L=31.25$  mm, a second parametric analysis was performed in order to obtain the optimum distance of the insert from the suspended solar cell patch. In Fig. 5.19, the effect of increasing the distance between the suspended cell and the insert,  $D$ , on the  $S_{11}$  response is illustrated. For this analysis, the length of the insert was kept constant at  $L=31.25$  mm, corresponding to a quarter-wavelength at 2.4 GHz, which was determined as the optimum insert length.

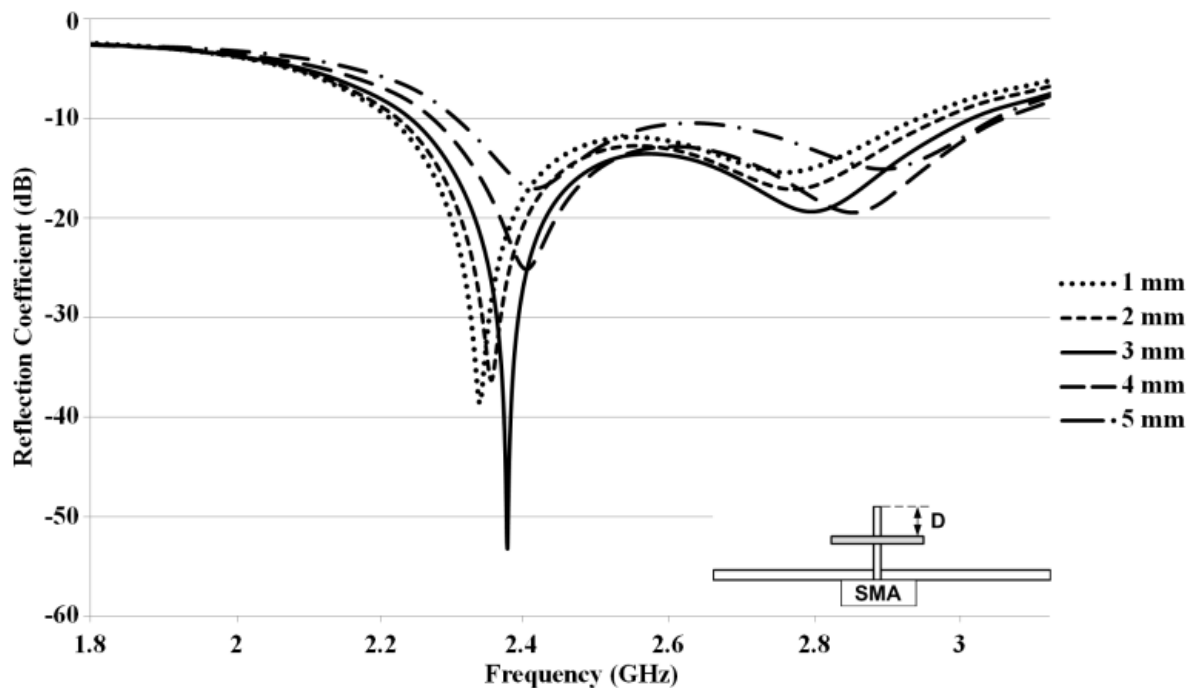


Fig. 5.19: Simulated  $S_{11}$  patterns versus varying distance between the insert and the cell.

As can be seen in Fig. 5.19, changing the distance between the solar cell and the metal insert has a serious effect on the  $S_{11}$  pattern. Similar to the effect of varying the insert

length, in Fig. 5.19, it can be seen that the first effect of varying the distance between these elements can be given as a shift in the operational frequency band. As given in Fig. 5.19, increasing the distance between the suspended solar cell and the insert shifts the operational frequency band of the cross-coaxial fed suspended solar patch antenna to a higher frequency. Secondly, up to  $D=3$  mm, increasing the distance between these two elements enhances the impedance matching. However, beyond  $D=3$  mm, significant deterioration in the  $S_{11}$  pattern is evident in Fig. 5.19. For this reason, the optimum distance between the cell and the insert was selected as  $D=3$  mm.

The effect of shorting the radiating element to the ground plane is also crucial for the design process. In view of this,  $S_{11}$  simulations were carried out with and without the shorting wire attached to the radiating element at the shorting point optimised in CST Microwave Studio as illustrated in Fig. 5.15(a). The reflection coefficients of solar patch antennas with and without the shorting wire are shown in Fig. 5.20. Examining Fig. 5.20, the solar patch without the shorting wire operates across the frequency band of 2.28-2.85 GHz, offering a bandwidth of 570 MHz. When a shorting wire was introduced at the shorting point illustrated in Fig. 5.15(a), an operating frequency band of 2.24-3.08 GHz was achieved, equating to a bandwidth of 840 MHz. This represents an increase in the -10 dB impedance bandwidth of the solar patch antenna by a factor of 32% in comparison to the solar patch antenna without the shorting wire.

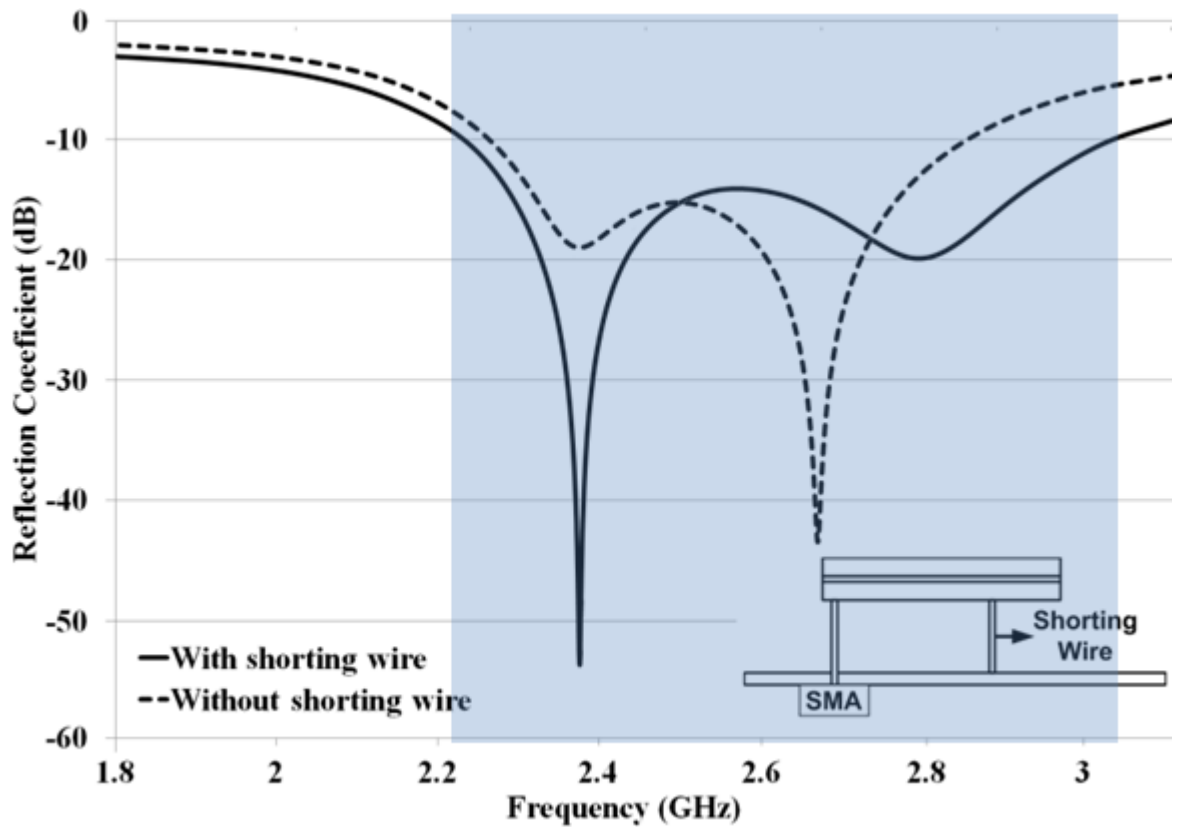


Fig. 5.20: Simulated  $S_{11}$  patterns with and without the shorting wire.

Similar to the far-field radiation pattern measurements of the photovoltaic antennas demonstrated until now, E-plane and H-plane far-field radiation pattern measurements of the proposed cross-coaxial fed solar patch antenna were carried out in an anechoic chamber with a signal generator power level of  $P_G=14$  dBm. The conical spiral antenna with a gain of  $G_T=4$  dBi was used as a reference antenna as demonstrated in Fig. 5.21.

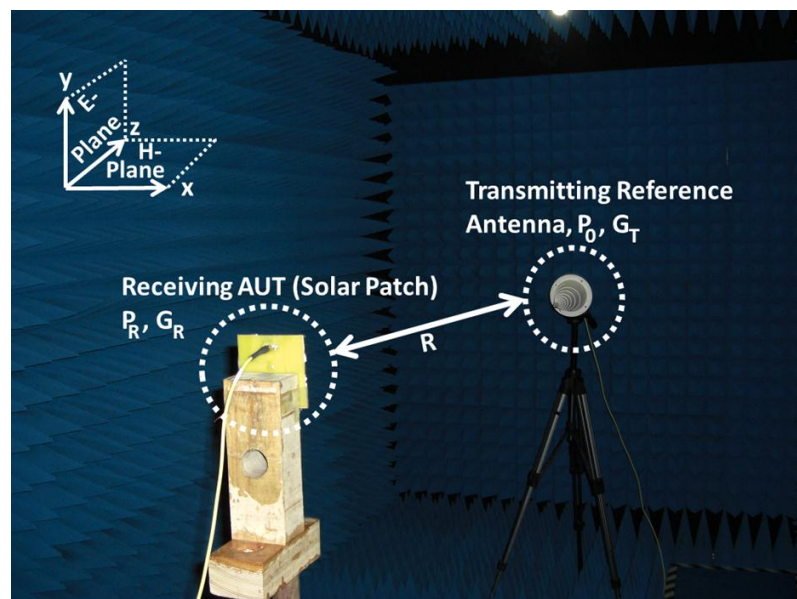


Fig. 5.21: Antenna far-field measurement set-up in the anechoic chamber.

In Fig. 5.21, the AUT is the proposed cross-coaxial fed solar patch antenna with a gain of  $G_R$  and received power level of  $P_R$ . The AUT was placed at a distance of  $R=3\text{m}$  from the reference conical spiral antenna and the measurements were taken over  $360^\circ$  in the E-plane and H-plane with a sampling angle of  $5^\circ$ . At each sampling angle, the received power level,  $P_R$ , was recorded and the gain values of the proposed solar patch antenna were calculated using Friis equation in equation (4.3) after taking the cable losses into account as given in equation (4.4). In Fig. 5.22(a), the measured normalised E-plane (y-z plane) far-field radiation patterns obtained at the frequencies of 2.45, 2.6 and 3 GHz are shown, whilst Fig. 5.22(b) and Table 5.3 illustrate the measured maximum E-plane gain values of the solar patch antenna across the operational frequency band.

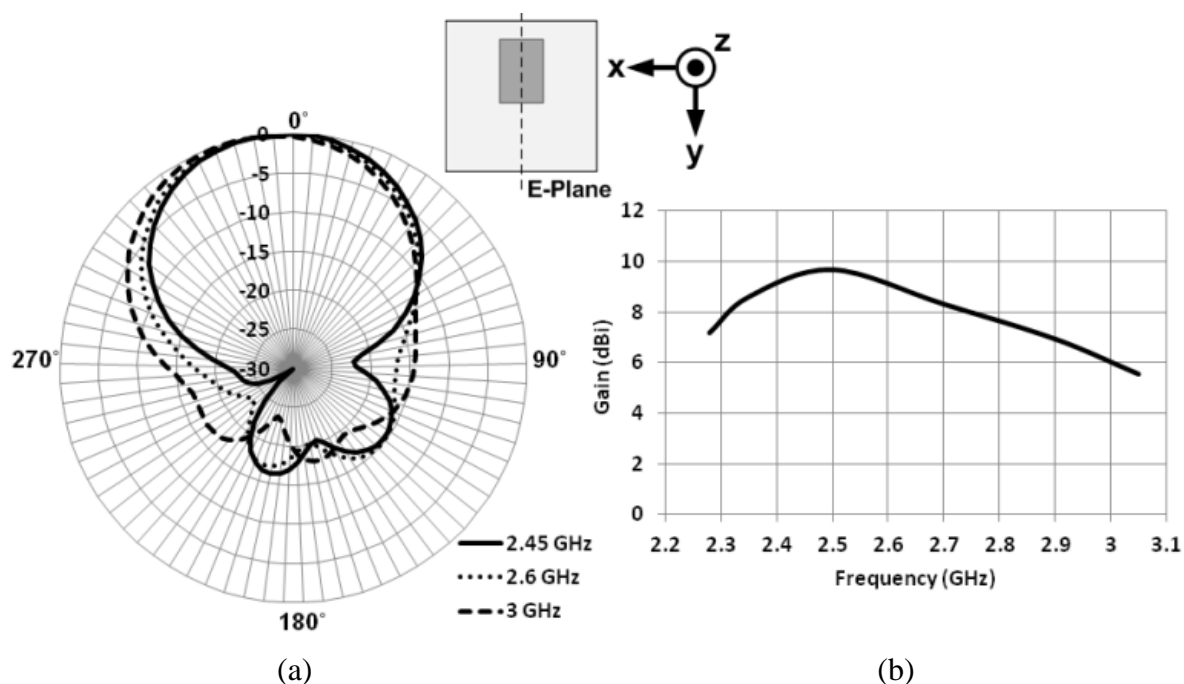


Fig. 5.22: E-plane far-field radiation (a) measured normalised E-plane radiation patterns at 2.45, 2.6 and 3 GHz (b) measured E-plane gain values across the operational frequency band.

Table 5.3: Measured maximum E-Plane gain values at selected frequencies.

Frequency (GHz)	$P_R$ (dBm)	$L_{\text{Cable}}$ (dB)	Measured E-Plane Gain (dBi)	Simulated E-Plane Gain (dBi)
2.3	-30.76	7.15	7.6	7.8
2.45	-29.58	7.42	9.6	9.9
2.6	-30.74	7.66	9.2	8.9
2.8	-33.29	7.97	7.6	7.5
3	-35.81	8.28	6	5.6

As demonstrated in Fig. 5.22(a), the cross-coaxial fed solar patch antenna has broadside E-plane far-field radiation patterns and offers an average maximum gain of 7.72 dBi across the operational frequency band in the E-plane, as illustrated in Fig. 5.22(b).

The measured normalised H-plane (x-z) far-field radiation patterns of the cross-coaxial fed solar patch antenna at 2.45, 2.6 and 3 GHz are demonstrated in Fig. 5.23(a) together with the maximum H-plane gain values given in Fig. 5.23(b) and Table 5.4.

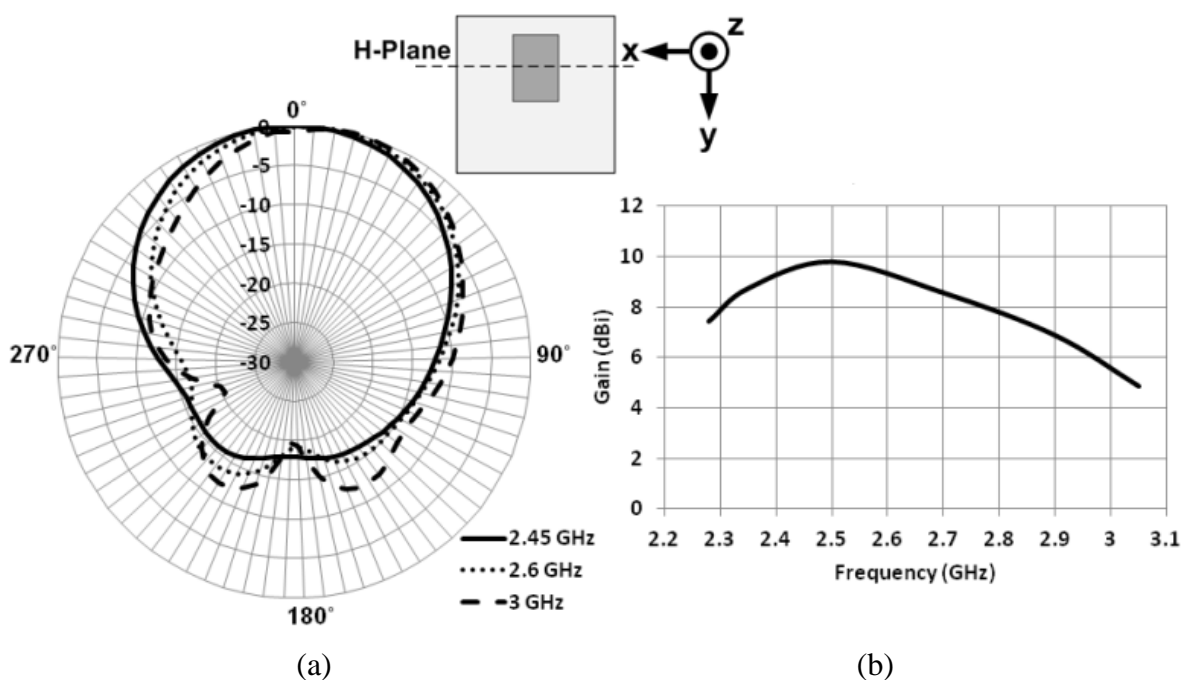


Fig. 5.23: H-plane far-field radiation (a) measured H-plane radiation patterns at 2.45, 2.6 and 3 GHz (b) measured H-plane gain values across the operational frequency band.

Table 5.4: Measured maximum H-plane gain values at selected frequencies.

Frequency (GHz)	$P_R$ (dBm)	$L_{Cable}$ (dB)	Measured H-Plane Gain (dBi)	Simulated H-Plane Gain (dBi)
2.3	-30.36	7.15	8	8.1
2.45	-29.58	7.42	9.6	9.9
2.6	-30.64	7.66	9.3	9
2.8	-33.13	7.97	7.7	7.5
3	-36.20	8.28	5.6	5.4

Similar to the measured E-plane far-field radiation patterns, the cross-coaxial fed solar patch antenna offers broadside H-plane far-field radiation patterns with an average maximum gain of 7.7 dBi across the operational frequency band as illustrated in Fig. 5.23(b). The difference between the measured maximum gain values in the E-plane and H-plane can be attributed to the proposed cross-coaxial feed, which introduces an asymmetry in the overall design of the antenna.

#### 5.4.2.2 Solar Performance

Solar performance measurements of the fabricated cross-coaxial fed suspended solar patch antenna were carried out in the metal halide solar simulator demonstrated in chapter 3. The solar simulator provides a colour temperature of 5200K with a uniform illumination intensity of  $1000 \text{ W/m}^2$  incident upon the solar antenna within the simulator fulfilling the requirements for the standard test conditions used for testing photovoltaic cells. Similar to the solar measurements of the photovoltaic antennas demonstrated until now, in order to determine the solar efficiency of the proposed solar antenna, short-circuit current, open-circuit voltage, and current and voltage at the maximum power point were measured when the DC terminals of the solar antenna were terminated in a group of resistors, from  $10 \Omega$  to  $2.7 \text{ k}\Omega$ , as a load. The solar measurement set-up of the cross-coaxial fed suspended solar patch antenna is illustrated in Fig. 5.24.

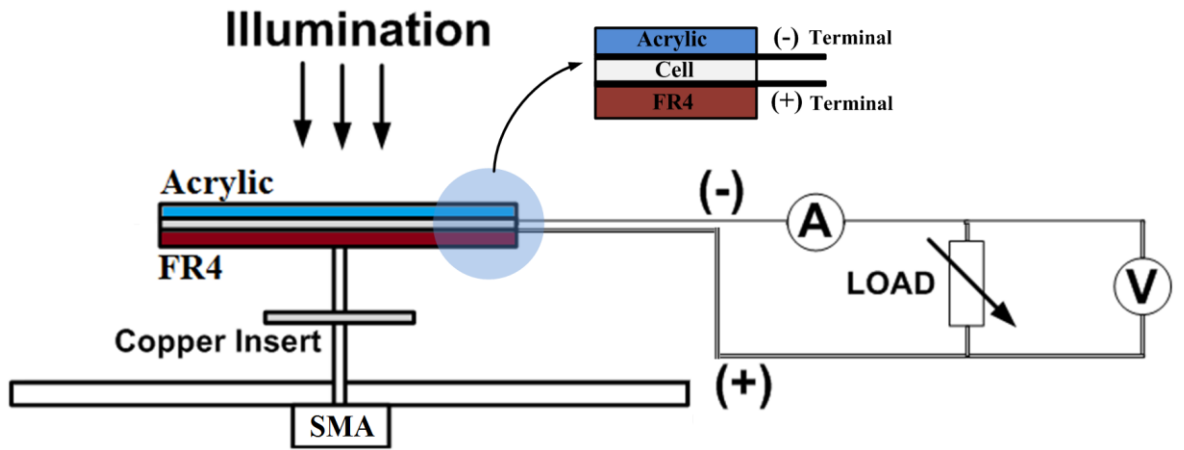


Fig. 5.24: Solar measurement of the cross-coaxial fed suspended solar patch antenna.

The measured I/V curve of the proposed solar patch antenna is illustrated in Fig. 5.25.

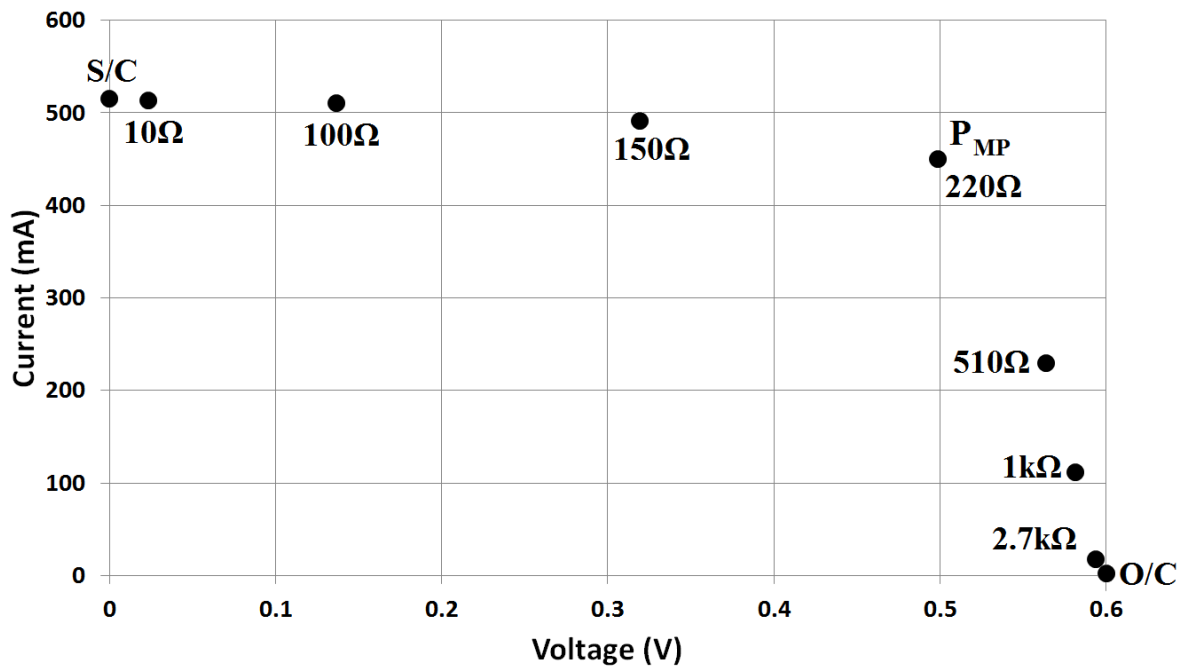


Fig. 5.25: Measured I/V curve of the solar antenna.

The measured solar performance readings of the solar patch antenna are summarised in Table 5.5.

Table 5.5: Solar measurement readings.

$V_{oc}$ (V)	$I_{sc}$ (mA)	$V_{Mp}$ (V)	$I_{Mp}$ (mA)	$P_{max}$ (mW)	$\eta$ (%)
0.601	511.6	0.5	449.5	225	13.9

As can be seen in Fig. 5.25 and Table 5.5, at the maximum power point in the I/V curve, where the generated DC power output is maximum, the voltage and current values were measured as  $V_{MP}=0.5$  V and  $I_{MP}=449.5$  mA, respectively, resulting in a DC power output of  $P_{MP}=225$  mW. Considering the total input solar intensity upon the solar patch antenna within the solar simulator calculated as  $P_{in}=1.62$  W, which is determined by the surface area of the cell, 36 mm x 45 mm, multiplied by the simulator illumination intensity, 1000 W/m<sup>2</sup>, the solar efficiency of the proposed cross-coaxial fed solar patch antenna was calculated as 13.9% using equation (3.13).

## 5.5 Solar Illumination Intensity and the RF Antenna Performance

Until now in this chapter, the use of solar cells as an RF radiating element has been demonstrated. It has been shown that in RF radiating element solar antenna integration topology, attention must be given to the establishment of isolation between the photovoltaic DC load connections and the RF antenna operation. This is due to the fact that the surface current distribution across the rear metal contact of integrated solar cells replacing the conventional copper patch is significantly affected by the DC connections, which become a part of the RF operation. This deteriorates the radiation characteristics of the antenna unless a DC/RF isolation method is applied, which was given in this chapter as:

- Introducing the DC connections between the solar cell and the DC load at the non-radiating edge, or
- Using a DC/RF isolation circuit providing a high RF impedance at the cell terminal whilst maintaining a DC short-circuit current path for the cell

generated DC current to flow to the load. This technique is required if the DC load needs to be connected to the solar cell at the antenna radiating edge.

Moreover, there are two more factors that need to be studied in order to ensure the RF stability of solar antennas using solar cells as an RF radiating element. The first factor is the effect of the variation in the illumination intensity on the cell conductivity, which was reported as 4.6% for a poly-Si solar cell under full illumination and no illumination in [35]. The second factor is the effect of the variation of the solar illumination intensity on the RF antenna performance due to the change in the number of freed electrons and therefore the amount of generated DC cell current. It is well-known that the solar illumination intensity is not constant and changes over time in a day and the weather conditions that the solar cells are required to operate might well be unpredictable. Therefore, the answer to the question of whether the change in the number of freed electrons (and therefore the cell current) over time in a day affects the radiation characteristics of a solar antenna using the solar cell as an RF radiating element needs to be investigated. To this end, consideration must be given in order to demonstrate the RF stability of solar antennas in which the solar cells are used as an RF radiating element in addition to their photovoltaic function. For this reason, two identical microstrip solar patch antennas, both of which use a poly-Si solar cell as an RF radiating element replacing the conventional microstrip patch, operating at the centre frequency of 2.5 GHz were fabricated. The terminals of the radiating poly-Si solar cells were terminated in a DC load, which is a  $220\Omega$  resistor, as demonstrated in Fig. 5.26.

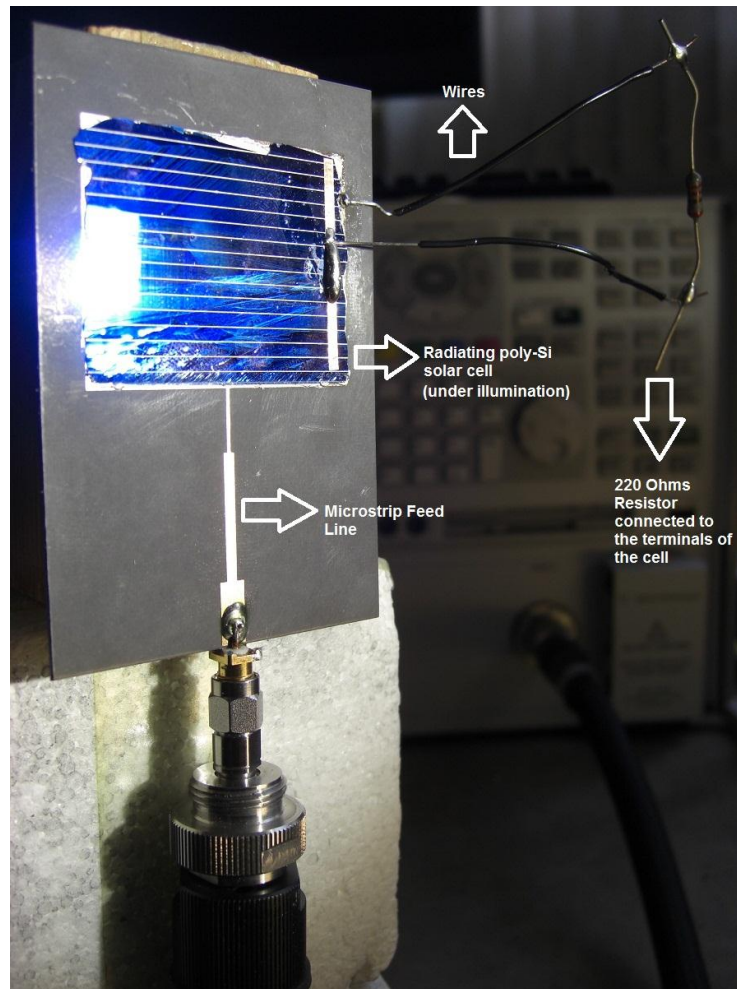


Fig. 5.26: Solar patch antenna terminated in a  $220\Omega$  DC load under varying illumination intensity.

The fabricated microstrip solar patch antennas operating as a transmitter and a receiver, respectively, were placed facing each other as illustrated in Fig. 5.27.

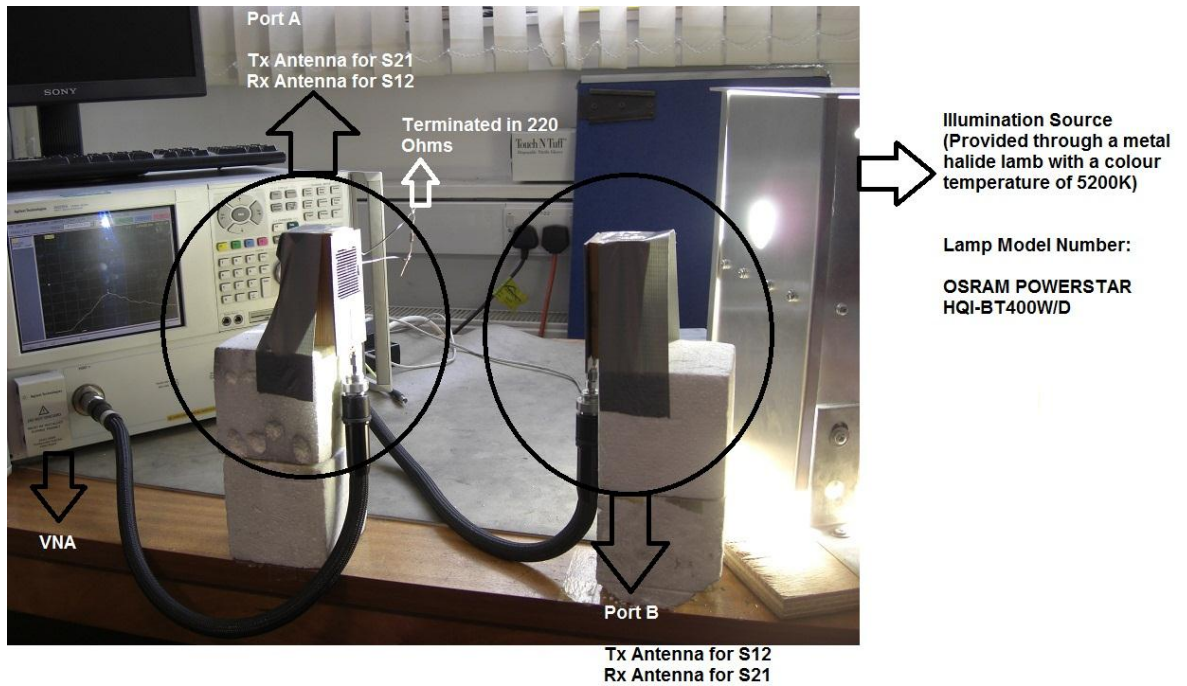


Fig. 5.27: Transmission coefficient and reflection coefficient measurement set-up under varying illumination intensity.

In the measurement set-up illustrated in Fig. 5.27, while the transmitting microstrip solar patch antenna was connected to the first port of the VNA, port A, the receiving antenna was connected to the second port of the VNA, port B. In the measurement set-up, the transmitting antenna was illuminated using a portable solar simulator through a hole as illustrated in Fig. 5.28.

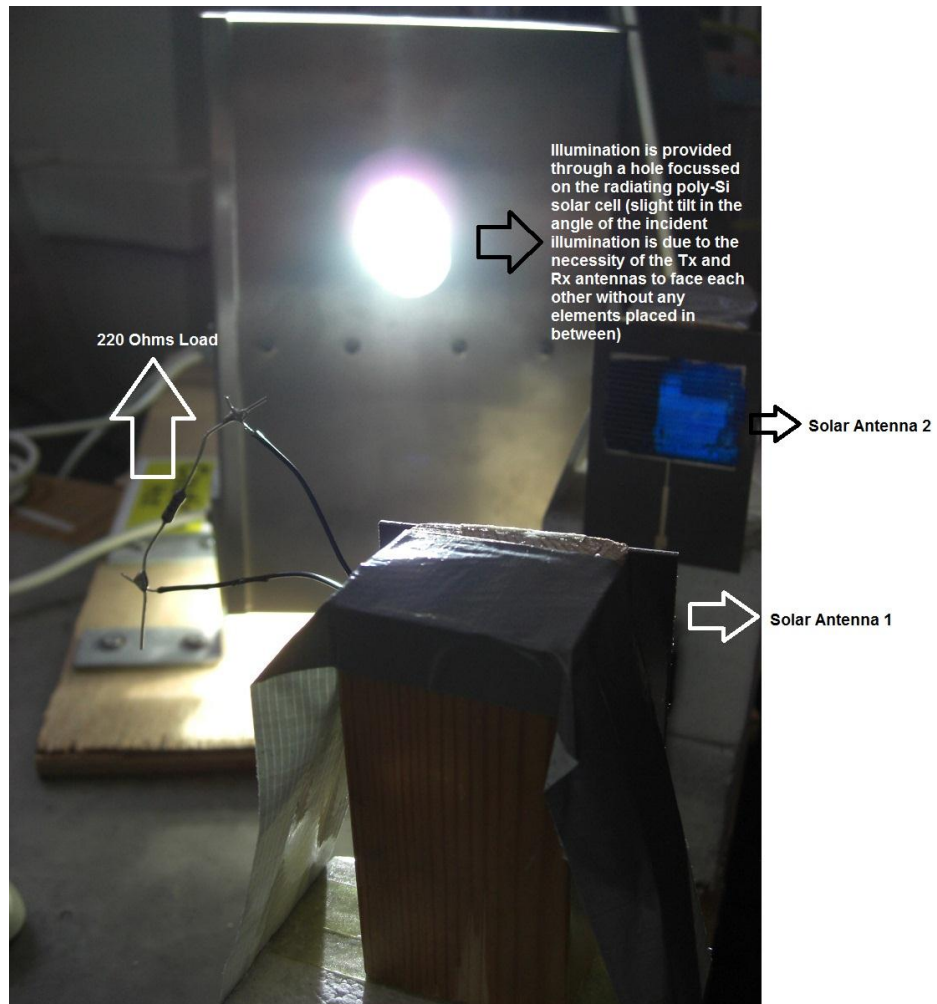


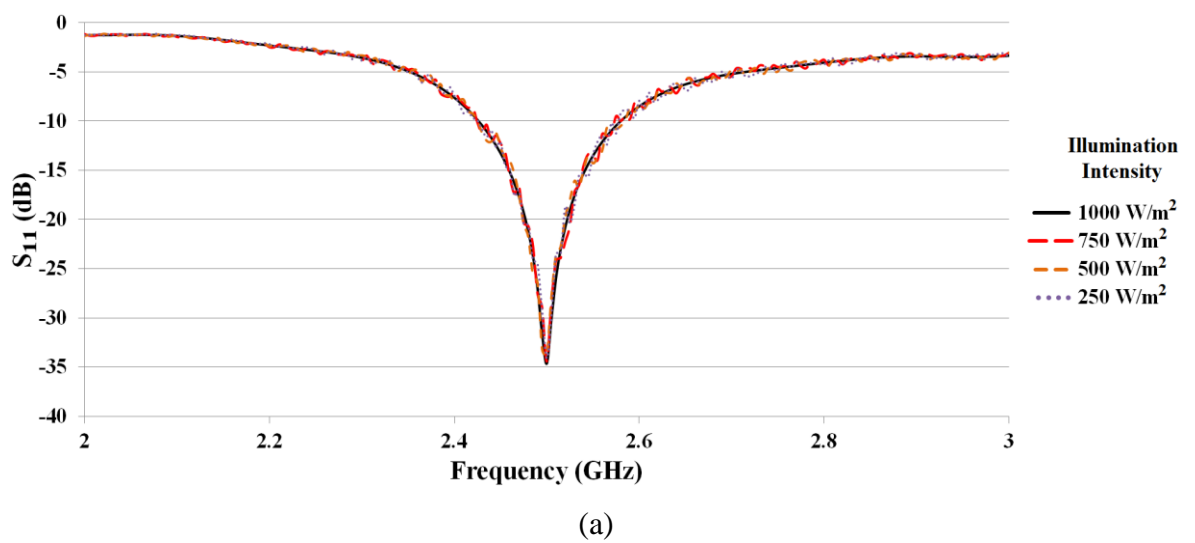
Fig. 5.28: Portable solar simulator illuminating the photovoltaic microstrip patch antenna.

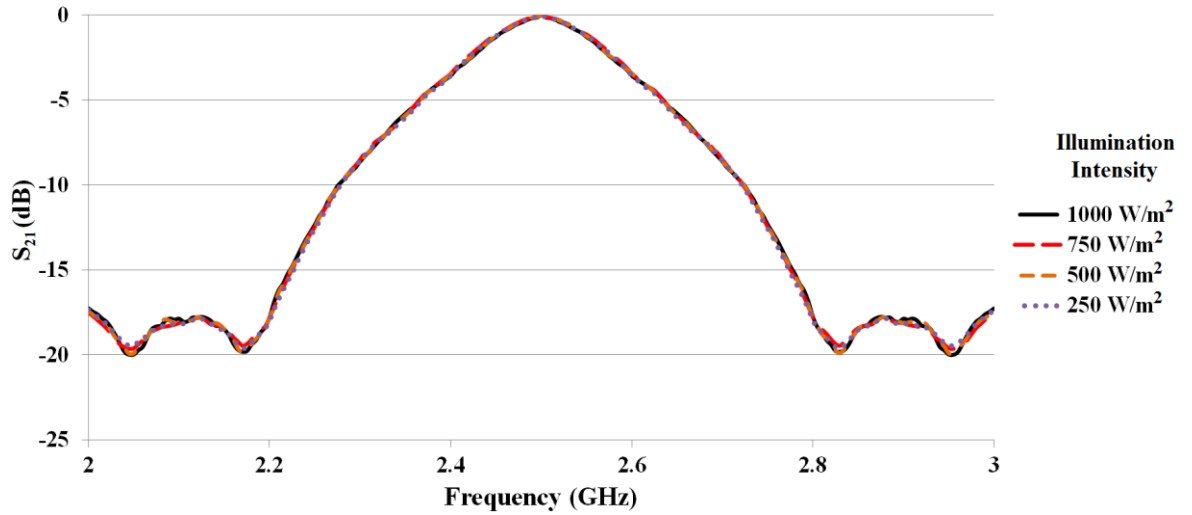
As the aim of this measurement is to demonstrate whether varying the solar illumination intensity affects the RF characteristics of solar antennas using solar cells as an RF radiating element, the illumination intensity provided by the portable solar simulator was varied in the range of  $250 \text{ W/m}^2$  -  $1000 \text{ W/m}^2$  and the  $S_{11}$  and  $S_{21}$  patterns were measured at each illumination intensity. For the determination of the illumination intensity, a light meter (TENMA 72-6693) was used as illustrated in Fig. 5.29.



Fig. 5.29: TENMA 72-6693 light meter.

The measured  $S_{11}$  and  $S_{21}$  patterns versus varying illumination intensity values are illustrated in Fig. 5.30.





(b)

Fig. 5.30: Measured S-parameter responses versus varying illumination intensities (a)  $S_{11}$  patterns (b)  $S_{21}$  patterns.

As can be seen in Fig. 5.30, no difference was observed in the  $S_{11}$  and  $S_{21}$  patterns obtained versus varying illumination intensities. This demonstrates the fact that the variation in the number of freed electrons under different illumination intensities does not affect the RF response of the measured photovoltaic patch antennas using the solar cells as an RF radiating element. This confirms the RF stability of photovoltaic antennas, which use solar cells as an RF radiating element and are required to operate under challenging weather conditions.

## 5.6 Summary

In this chapter, the RF radiating element solar antenna integration topology, which involves the use of solar cells as an RF radiating element in addition to their photovoltaic function, was investigated.

It was demonstrated that:

- RF radiating element solar antenna integration topology addresses the shading problem. In comparison to the use of solar cells as an RF ground plane demonstrated in chapter 4, using solar cells as an RF radiating element brings the advantage that the solar cells are not shaded by any RF components of the antenna.
- Due to the requirement for solar cells to be homogeneous in structure to achieve optimum solar performance, the RF radiating element solar antenna integration topology does not allow the modification of the RF radiating element, i.e. the solar

cell. Therefore, additional techniques requiring the modification of the RF radiating element to excite multiple  $TM_{mn}$  propagation modes, such as capacitive slot loading [59-83], to achieve multiband and wideband resonance response cannot be adopted in this integration topology. In this chapter, the challenge of achieving wideband resonance characteristics from photovoltaic patch antennas was partly addressed by using suspended antenna geometry and a modified cross-coaxial feeding structure.

- In comparison to the use of solar cells as an RF ground plane demonstrated in chapter 4, photovoltaic antennas using the RF radiating element photovoltaic integration topology produce less amount of DC power output. This is due to the smaller size of the RF radiating element in comparison to the size of the ground plane in a planar antenna.
- For the RF radiating element solar antenna integration topology demonstrated in this chapter, consideration must be given when it comes to terminating the integrated solar cell in a DC load. This is due to the fact that connecting a DC load to the terminals of the solar cell, whose rear contact replacing the conventional microstrip patch, significantly affects the RF surface current distribution unless the methods given below are applied:
  - The DC load must be connected to the cell terminals at the non-radiating edge, or
  - A DC/RF isolation circuit must be introduced if the DC load connection is required to be provided at the radiating edge.
- Variation in the solar illumination intensity does not change the reflection and transmission responses of a photovoltaic antenna in which the solar cells are used as an RF radiating element. This confirms the RF stability of solar antennas required to operate under challenging/unpredictable weather conditions.

# Chapter 6 – RF Stacked Parasitic Patch Element Solar Integration

## 6.1 Introduction

As demonstrated in chapter 4 and chapter 5, the existing solar antenna integration topologies have disadvantages from both antenna and photovoltaic perspectives. The RF ground plane solar antenna integration topology demonstrated in chapter 4 introduces the shading problem, which has the potential of significantly reducing the solar efficiency. The RF radiating element solar antenna integration topology demonstrated in chapter 5, on the other hand, makes it impossible for any modification techniques to be applied in the RF radiating element, i.e. the solar cell, due to the requirement for the integrated solar cells to be homogeneous in structure to achieve optimum solar performance.

This chapter proposes a novel solar antenna integration topology, which is the use of solar cells as a suspended stacked RF parasitic patch element in addition to their photovoltaic function. It demonstrates how the disadvantages associated with the existing solar antenna integration topologies can be overcome by using this proposed integration topology. This chapter also demonstrates the novel photovoltaic integration of a dual-polarised microstrip patch antenna for polarisation diverse applications. In addition, the demonstration of a photovoltaic microstrip patch array antenna capable of performing electronic beam-steering is also demonstrated for the first time in this thesis.

## 6.2 The Integration Topology

As described in chapter 4 and chapter 5, the solar antenna integration topologies studied in the literature have significant disadvantages, which can be given as follows:

- RF ground plane solar antenna integration topology: Solar cells as an antenna ground plane.
  - Shading caused by the opaque radiating element placed upon the ground plane, i.e. the solar cell. This challenge was addressed by meshing the radiating element at the expense of increasing the complexity of the fabrication process as demonstrated in chapter 4.

- RF radiating element solar antenna integration topology: Solar cell as an antenna radiating element.
  - Inability to modify the RF radiating element, i.e. the solar cell, to excite multiple  $TM_{mn}$  propagation modes in order to achieve multiband and wideband resonance characteristics. This is due to the requirement for the integrated solar cells to be homogeneous in structure to achieve optimum solar performance.

In this chapter, a novel RF stacked solar antenna integration topology addressing these challenges is proposed and investigated.

As demonstrated in Fig. 6.1, this technique is based upon the use of solar cells as a parasitic patch located above the radiating element. Such a design enables the geometry of the radiating element to be modified to provide multiband coverage.

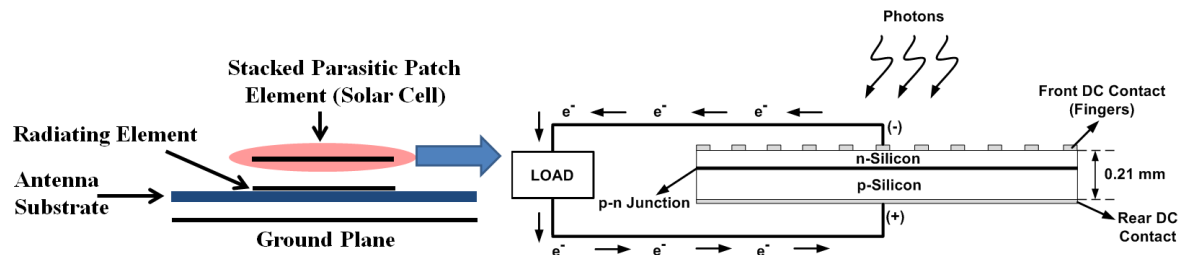


Fig. 6.1: RF stacked parasitic patch element solar antenna integration topology.

## 6.3 Solar Cell Stacked Modified Z-Double L-Slot Quad-Band PIFA

Following the demonstration of the suspended photovoltaic antennas using solar cells as an RF radiating element in chapter 5, this chapter introduces a new stacked solar antenna integration topology. In this section, the design of a solar cell stacked modified PIFA with a Z-double L-slot loaded radiating element is proposed for GSM 1800, 2.4 GHz band WLAN and 2.5/3.3/3.5 GHz band WiMAX networks. The significant improvement offered by this design is in the ability to modify the radiating element whilst incorporating the solar cell as a suspended parasitic patch. Moreover, the photovoltaic integration of a PIFA is studied for the first time in the literature. This brings the advantage of reducing the size of photovoltaic antennas due to the quarter-wavelength mode operation of PIFAs.

### 6.3.1 Solar PIFA Design

As illustrated in Fig. 6.1, the poly-Si solar cell consists of two metal contacts, a front grid and a rear solid, with a silicon layer in between. While from a photovoltaic perspective, the front and rear contacts represent the negative and positive terminals, respectively, from an RF point of view, the solid rear contact enables the cell to act as a homogenous metal plate. In this proposed design, the rear contact of the integrated poly-Si solar cell enables the cell to operate as a stacked RF parasitic patch suspended above the multi-slot radiating PIFA element.

The geometry of the proposed poly-Si solar cell stacked modified Z-double L-slot PIFA is shown in Fig. 6.2.

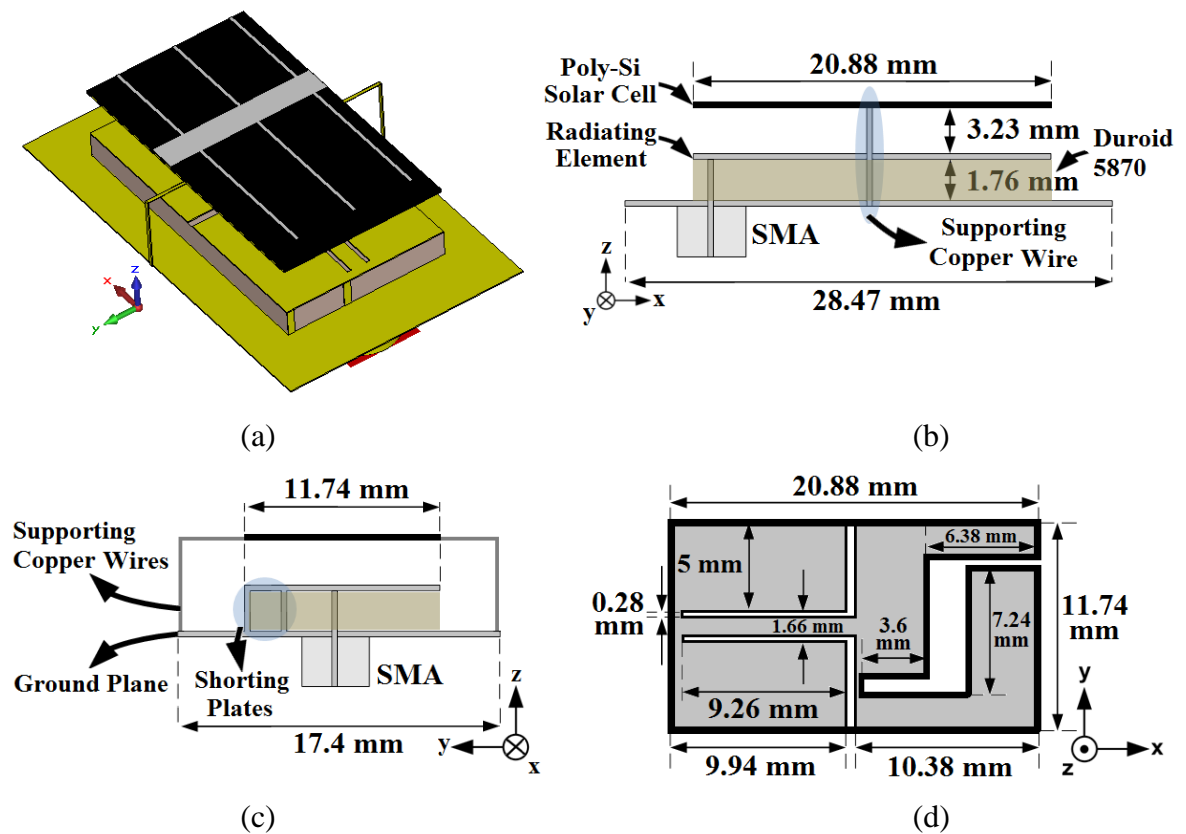


Fig. 6.2: Z-double-L slot loaded solar PIFA (a) overall view (b) side view (c) back view (d) radiating PIFA element top view.

The proposed solar PIFA was designed and optimised in CST Microwave Studio. For the fabrication of the antenna, a Stanley utility knife was used to cut the slots in the radiating PIFA element whilst the cut-out of the poly-Si solar cell was achieved using a diamond glass cutter. As illustrated in Fig. 6.2, the radiating PIFA element was printed upon a 1.76 mm thick RT/Duroid 5870 substrate,  $\epsilon_r=2.33$  and  $\tan\delta=0.0012$ . It consists of two

symmetric L-slots made in the centre with a Z-slot close to the top radiating edge in the x-axis, enabling the excitation of multiple  $TM_{mn}$  propagation modes to provide multiband coverage. It is short-circuited to the ground plane through two 0.5 mm thick shorting plates, which are introduced at the feeding edge and separated by a distance of 3.7 mm as illustrated in Fig. 6.2(c).

The poly-Si solar cell is suspended at 3.23 mm above the radiating PIFA element. The suspension of the stacked poly-Si solar cell was achieved using two copper wires on both sides as illustrated in Fig. 6.2, which are connected to the rear contact of the cell on top and the PIFA ground plane at the bottom. These wires act as a positive terminal from a photovoltaic point of view, and together with the negative terminal, i.e. the cell front grid, they are used to withdraw the electric current generated by the solar PIFA to a DC load connected to the cell terminals.

## 6.3.2 Simulation and Measurement Results

### 6.3.2.1 Antenna Performance

The  $S_{11}$  measurements of the fabricated solar PIFA were performed using a VNA, Agilent E8634B, whilst the simulations were carried out in CST Microwave Studio. The simulated and measured  $S_{11}$  patterns are shown in Fig. 6.3.

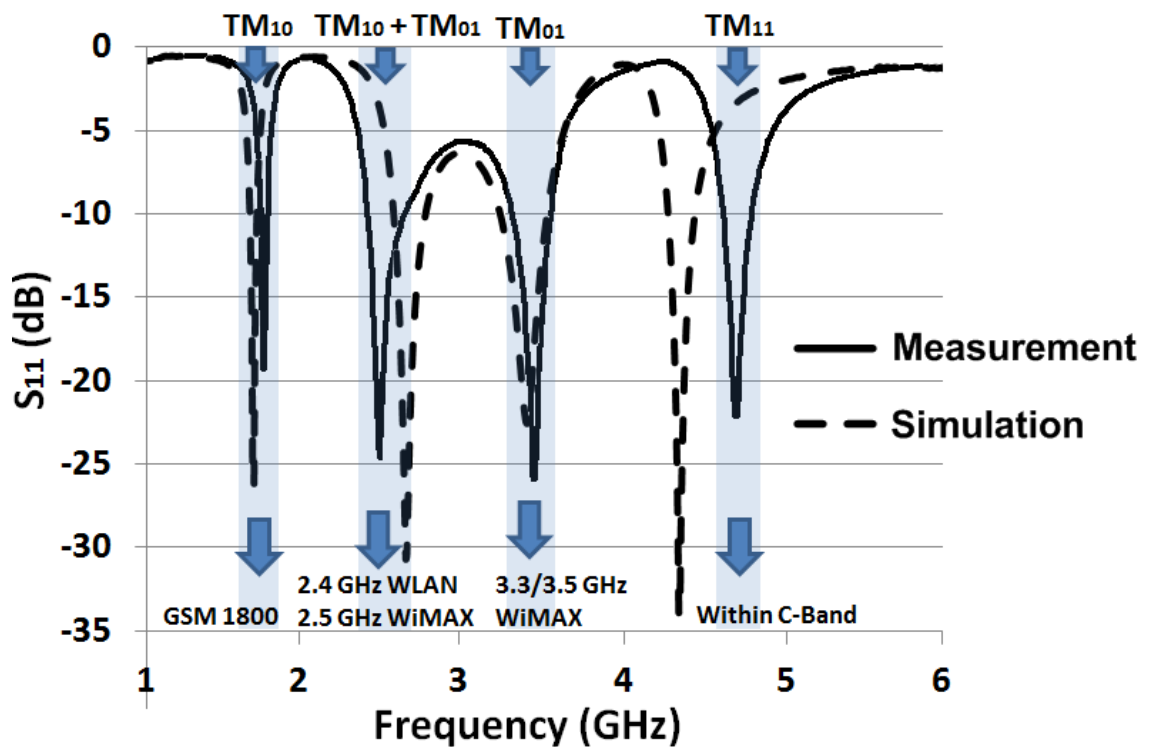


Fig. 6.3: Simulated and measured  $S_{11}$  patterns.

As demonstrated in Fig. 6.3, the proposed solar PIFA offers a quad-band resonance response and resonates at the measured centre frequencies of 1.79, 2.45, 3.4 and 4.75 GHz. The -10 dB impedance bandwidths centred at these resonance frequencies were obtained as 1.75-1.82 GHz (3.91%), 2.38-2.61 GHz (9.38%), 3.26-3.53 GHz (7.94%) and 4.66-4.83 GHz (3.58%), enabling the proposed solar PIFA to be employed in GSM 1800 (1.71-1.88 GHz), 2.4 GHz band WLAN (2.4-2.484 GHz), 2.5/3.3/3.5 GHz band WiMAX (2.5-2.7 GHz / 3.3-3.4 GHz / 3.4-3.6 GHz) and 4.75 GHz C-band networks. The obtained  $S_{11}$  performance of the proposed solar PIFA is summarised in Table 6.1.

Table 6.1: Analysis of the measured  $S_{11}$  performance.

<b>Resonance Frequency (GHz)</b>	<b>Frequency Band (GHz)</b>	<b>Bandwidth (MHz)</b>	<b>Bandwidth (%)</b>	<b>Networks</b>
1.79	1.75-1.82	70	3.91%	GSM1800
2.45	2.38-2.61	230	9.38%	2.4 GHz WLAN, 2.5 GHz WiMAX
3.4	3.26-3.53	270	7.94%	3.3/3.5 GHz WiMAX
4.75	4.66-4.83	170	3.58%	Within C-band

The quad-band resonance response demonstrated in Fig. 6.3 was achieved as a result of the introduced Z-double-L slots in the radiating PIFA element, enabling the excitation of multiple  $TM_{mn}$  propagation modes. For microstrip patch antennas,  $TM_{mn}$  propagation mode resonance frequencies can be calculated using equation (6.1) given below [176]:

$$f_{mn} = \frac{c}{2\sqrt{\epsilon_{\text{reff}}}} \sqrt{\left(\frac{m}{L_{\text{eff}}}\right)^2 + \left(\frac{n}{W_{\text{eff}}}\right)^2} \quad (6.1)$$

In equation (6.1),  $L_{\text{eff}}$  and  $W_{\text{eff}}$  represent the effective patch length and width while  $\epsilon_{\text{reff}}$  and  $c$  denote the effective substrate dielectric constant and the speed of light, respectively. However, for PIFAs, equation (6.1) cannot be used due to the quarter-wavelength

operation mode in comparison to the half-wavelength operation mode of microstrip patch antennas.

Therefore, in order to determine the  $TM_{mn}$  propagation modes introduced by the Z double-L slot loaded radiating PIFA element, equation (6.2) given below is used [177]:

$$f_{mn} = \frac{c}{4\sqrt{\epsilon_{reff}}} \sqrt{\left(\frac{m}{L_{eff}}\right)^2 + \left(\frac{n}{W_{eff}}\right)^2} \quad (6.2)$$

In equation (6.2),  $L_{eff}$  and  $W_{eff}$  represent the effective PIFA radiating element length and width determined by the Z-L slots modifying the surface current paths of the supported  $TM_{mn}$  propagation modes. The  $TM_{mn}$  propagation modes corresponding to the resonance frequencies demonstrated in Fig. 6.3 were calculated using equation (6.2) and are given in Table 6.2 together with the contribution of the proposed Z- L slots in the radiating PIFA element to the resonance bands.

Table 6.2: Slot types, contributed resonance bands and supported  $TM_{mn}$  propagation modes.

<b>Resonance Frequency (GHz)</b>	<b>Contributed Slots</b>	<b><math>L_{eff}</math> (mm)</b>	<b><math>W_{eff}</math> (mm)</b>	<b>Propagation Modes</b>
1.79	Z-Slot	27.46	15.44	$TM_{10}$
2.45	Z-Slot, Double L-Slot	23.21	13.05	$TM_{10}+TM_{01}$
3.4	Double L-Slot	18.35	10.31	$TM_{01}$
4.75	Double L-Slot	14.82	8.33	$TM_{11}$

As can be seen in Table 6.2, at the lower band, 1.79 GHz and 2.45 GHz, the effective length and width of the slot loaded radiating PIFA element exceed the physical size of the element,  $L=20.88$  mm and  $W=11.74$  mm. This is due to introduced Z-L slots widening the surface current path at the lower band enabling the excitation of multiple  $TM_{mn}$  propagation modes whilst the physical size of the radiating PIFA element remains the same. In order to demonstrate the effect of the proposed Z-L slot loading on the surface

current distribution across the modified radiating PIFA element, the simulated current distributions at the resonance frequencies of 1.79, 2.45, 3.4 and 4.75 GHz are illustrated in Fig. 6.4.

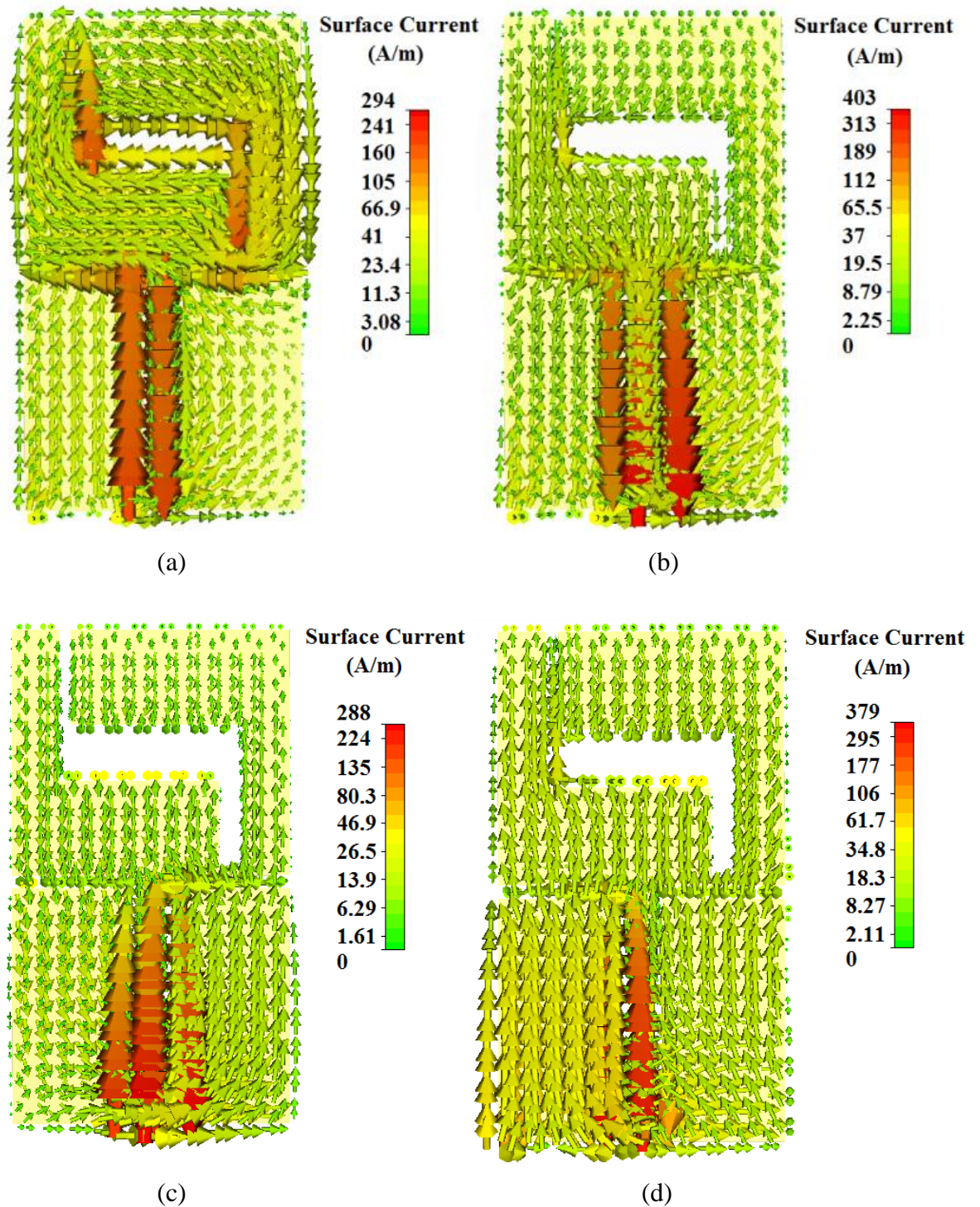
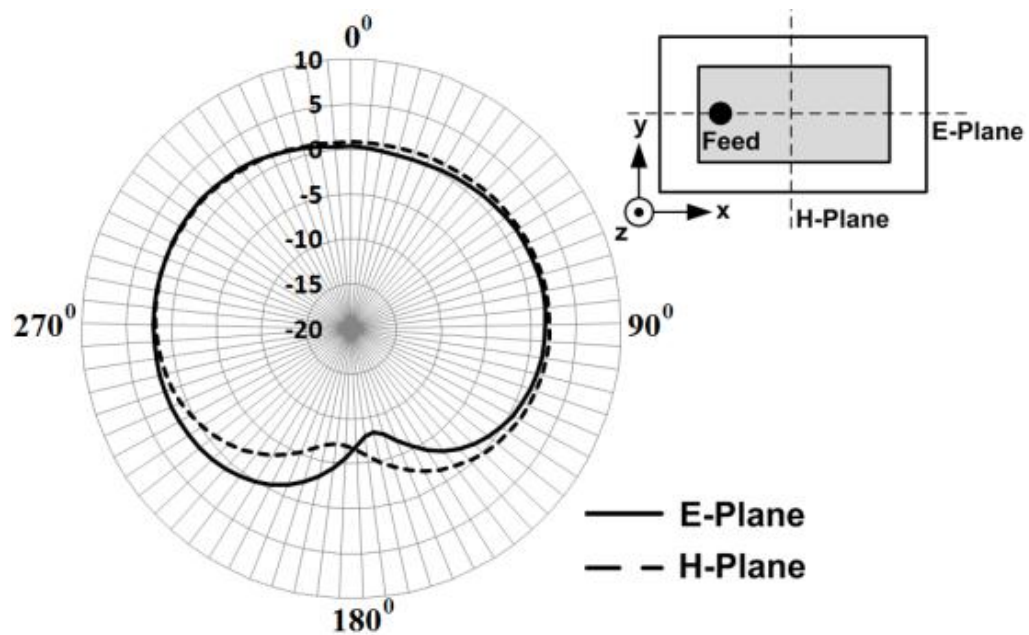


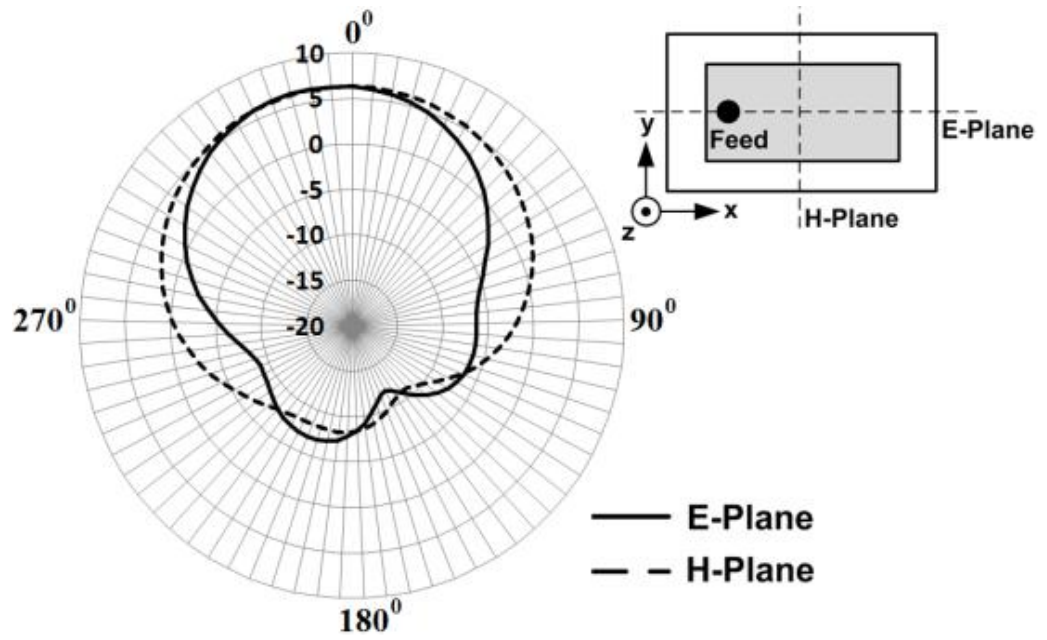
Fig. 6.4: Simulated surface current distributions on the Z-double-L slot loaded radiating PIFA element at the frequencies of (a) 1.79 GHz (b) 2.45 GHz (c) 3.4 GHz (d) 4.75 GHz.

As illustrated in Fig. 6.4, the surface current flows through the path determined by the introduced multi-slot pattern. The first resonance at the frequency of 1.79 GHz was obtained due to the existence of the proposed Z-slot whose contribution to the current distribution at this resonance band can clearly be seen in Fig. 6.4(a). Starting from the second resonance frequency, 2.45 GHz, the effect of the introduced double-L slot on the surface current distribution becomes dominant over the Z-slot as demonstrated in Fig. 6.4(b), (c) and (d). At these frequencies, the radiation mainly occurs within the proposed L-slot geometry, which reduces the electrical length of the radiating PIFA element compared to the electrical length at 1.79 GHz resulting in an increase in the resonance frequencies, which were obtained as 2.45, 3.4 and 4.75 GHz, respectively.

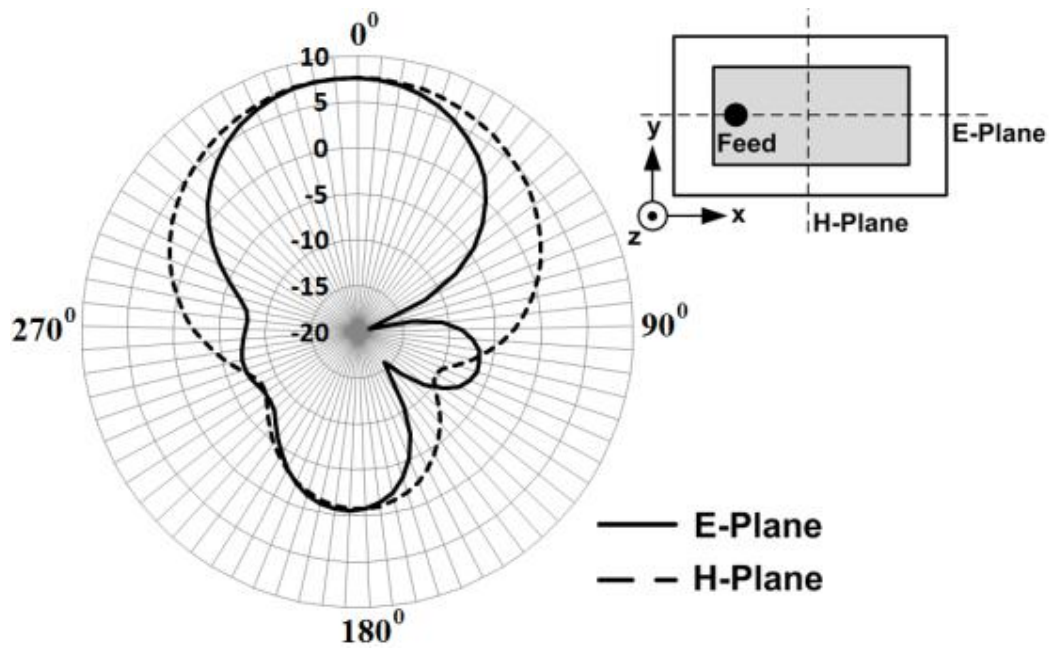
The E-plane and H-plane far-field radiation pattern measurements of the solar PIFA were performed in an anechoic chamber with a signal generator power level of  $P_G=14$  dBm. Similar to the radiation pattern measurements of the photovoltaic antennas demonstrated in the previous chapters, the conical spiral antenna with a gain of 4 dBi was used as a reference antenna for the measurements. The AUT was placed at a distance of  $R=3$  m from the reference conical spiral antenna and the measurements were taken over  $360^\circ$  in the E-plane and H-plane with a sampling angle of  $5^\circ$ . At each sampling angle, the received power,  $P_R$ , was measured and Friis equation given in equation (4.3) was then used to calculate the maximum gain values at each resonance frequency after taking the cable losses,  $L_{Cable}$ , into account as given in equation (4.4). The measured E-plane and H-plane far-field radiation patterns are shown in Fig. 6.5.



(a)



(b)



(c)

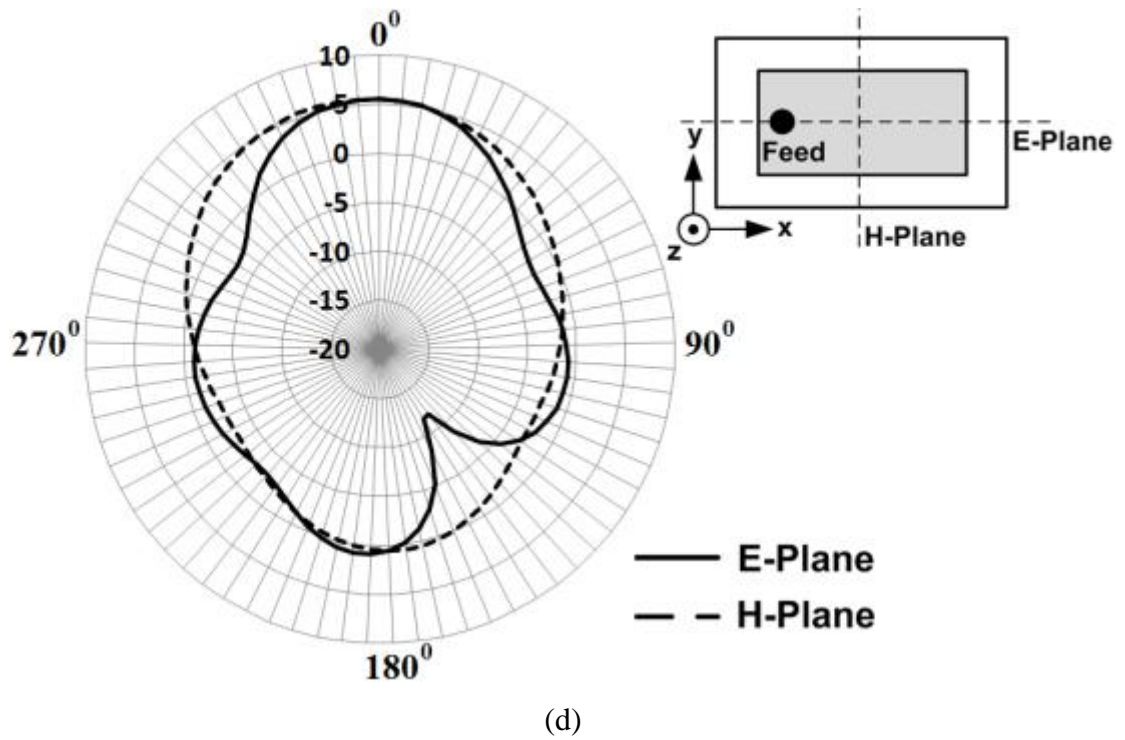


Fig. 6.5: Measured E-plane (x-z) and H-plane (y-z) far-field radiation patterns at (a) 1.79 GHz (b) 2.45 GHz (c) 3.4 GHz (d) 4.75 GHz.

As illustrated in Fig. 6.5, broadside far-field radiation patterns were obtained at the investigated resonance frequencies. Table 6.3 demonstrates the measured maximum gain values of the solar PIFA at the resonance frequencies of 1.79 GHz, 2.45 GHz, 3.4 GHz and 4.75 GHz.

Table 6.3: Measured maximum gain values of the solar PIFA.

Frequency (GHz)	$P_R$ (dBm)	$L_{Cable}$ (dB)	Measured Maximum Gain (dBi)	Simulated Maximum Gain (dBi)
1.79	-33.09	6.15	2.1	2.3
2.45	-32.78	7.41	6.4	6.1
3.4	-35.86	8.84	7.6	7.4
4.75	-42.32	10.61	5.8	6.3

As expected, the maximum gain of the PIFA increases with the increasing frequency up to 3.4 GHz. However, the maximum gain of the PIFA drops to 5.8 dBi at 4.75 GHz from 7.6 dBi at 3.4 GHz. This decrease in the maximum gain value can be attributed to the fact that the PIFA switches from  $TM_{01}$  propagation mode to  $TM_{11}$  propagation mode, which also presents increased surface wave losses reducing the gain.

### 6.3.2.2 Solar Performance

The solar performance measurements of the proposed solar PIFA were carried out in the metal halide solar simulator demonstrated in chapter 3. The simulator provides a uniform illumination intensity of  $1000 \text{ W/m}^2$  upon the solar PIFA, which is equivalent to the intensity used for the standard test conditions for testing photovoltaic cells. For the measurement of the I/V curve of the solar PIFA, similar to the solar antennas demonstrated until now, a group of resistors, from  $10\Omega$  to  $2.7\text{k}\Omega$ , were connected to the terminals of the stacked poly-Si solar cell and the current and voltage readings for each resistor were recorded. The measured I/V curve of the solar PIFA is illustrated in Fig. 6.6.

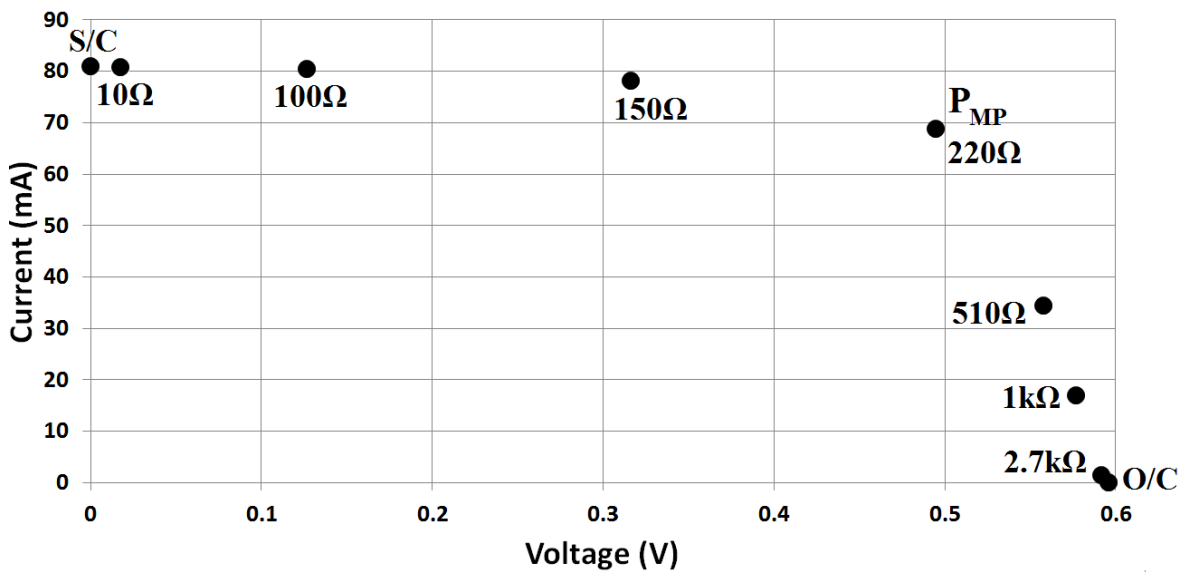


Fig. 6.6: Measured I/V curve of the solar PIFA.

As can be seen in Fig. 6.6, the open-circuit voltage and short-circuit current readings were measured as  $V_{OC}=0.596 \text{ V}$  and  $I_{SC}=80.85 \text{ mA}$ , respectively. At the maximum power point in the I/V curve in Fig. 6.6, where the generated DC power is maximum, the voltage and current were measured as  $V_{MP}=0.495 \text{ V}$  and  $I_{MP}=68.74 \text{ mA}$ , respectively, providing a generated maximum DC power output of  $P_{MP}=34 \text{ mW}$ . Considering the total illumination intensity of  $1000 \text{ W/m}^2$ , which provides an input illumination intensity of  $P_{in}=245 \text{ mW}$  determined by the total surface area of the poly-Si solar cell,  $2.45 \text{ cm}^2$  as illustrated in Fig.

6.2, the solar efficiency of the proposed solar PIFA was calculated as  $\eta=13.9\%$  from equation (3.13).

### 6.3.2.3 The Effect of Solar Integration on PIFA Performance

The  $S_{11}$  and E-plane and H-plane far-field radiation patterns of the proposed solar cell stacked PIFA were demonstrated in section 6.3.2.1. In order to determine the effect of integrating the poly-Si solar cell as an RF stacked parasitic patch element on the PIFA performance, two prototypes of the PIFA were designed in CST Microwave Studio.

- PIFA stacked with the poly-Si solar cell as demonstrated in Fig. 6.7,

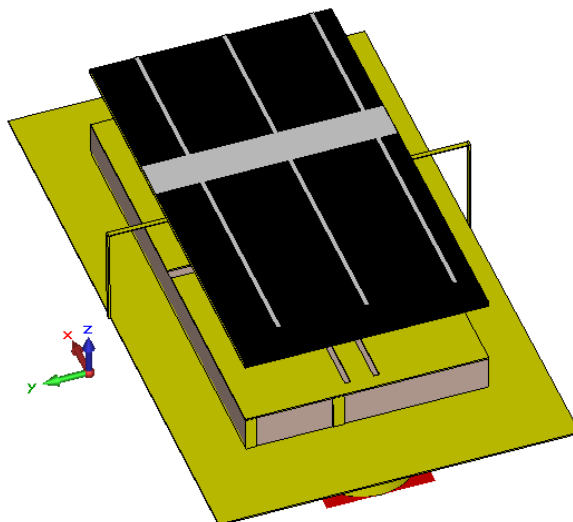


Fig. 6.7: PIFA with the suspended stacked poly-Si solar cell.

- PIFA without the stacked poly-Si solar cell as demonstrated in Fig. 6.8.

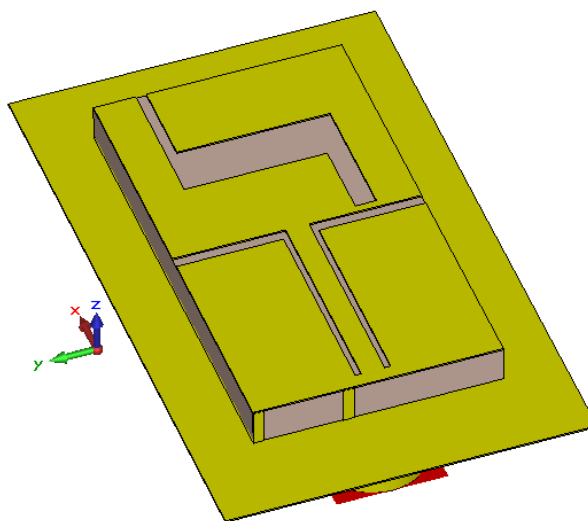


Fig. 6.8: PIFA without the poly-Si solar cell.

The simulated  $S_{11}$  patterns of the Z double-L slot PIFA with and without the stacked poly-Si solar cell are demonstrated in Fig. 6.9.

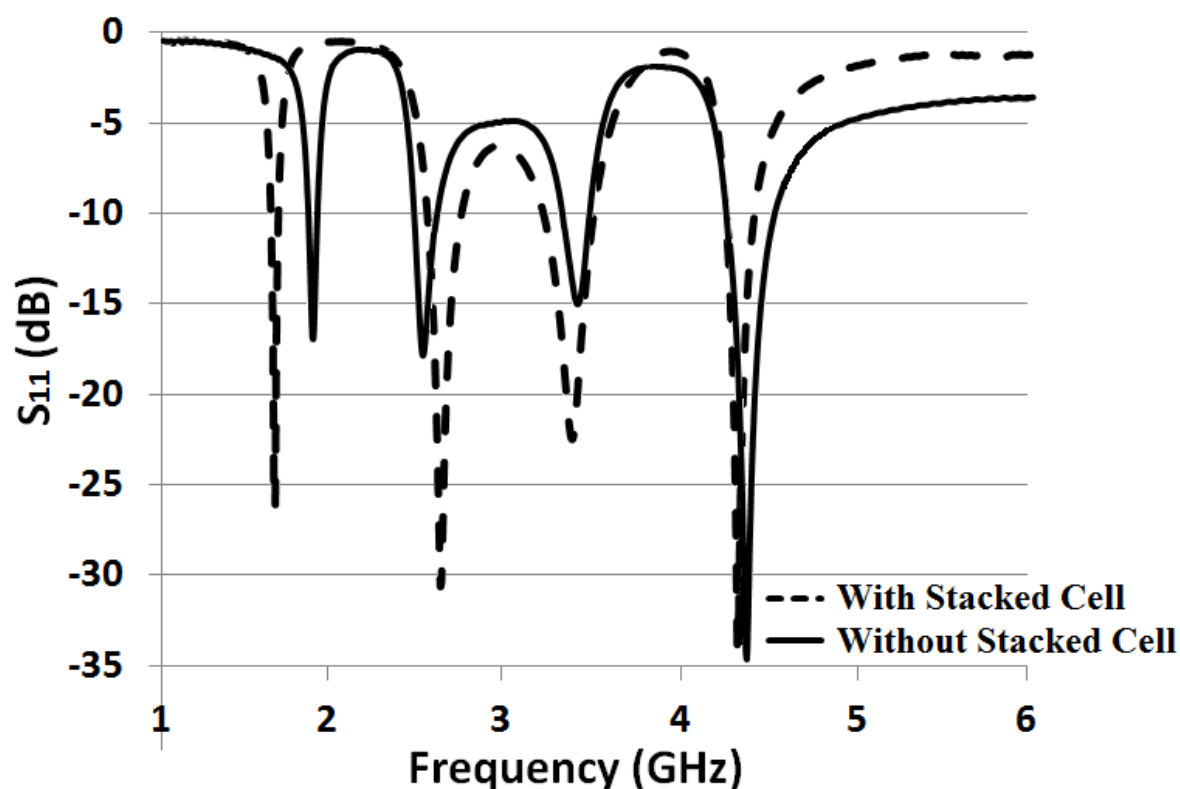
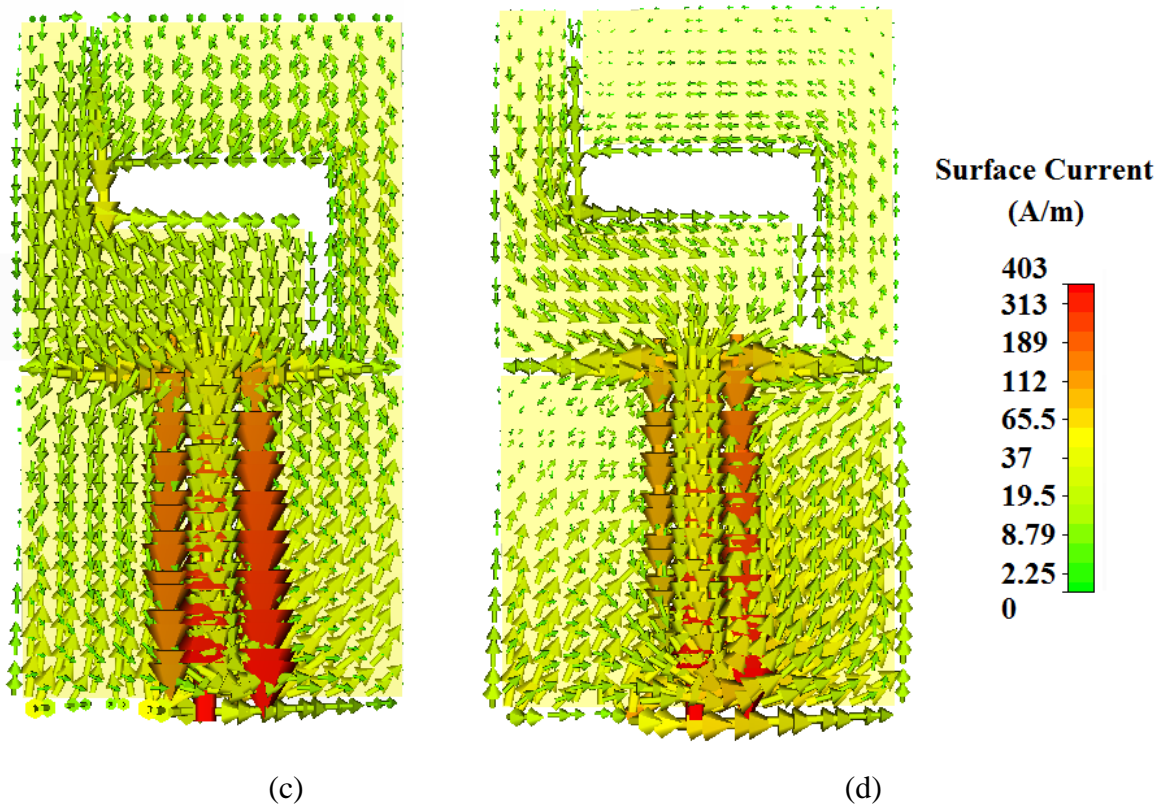
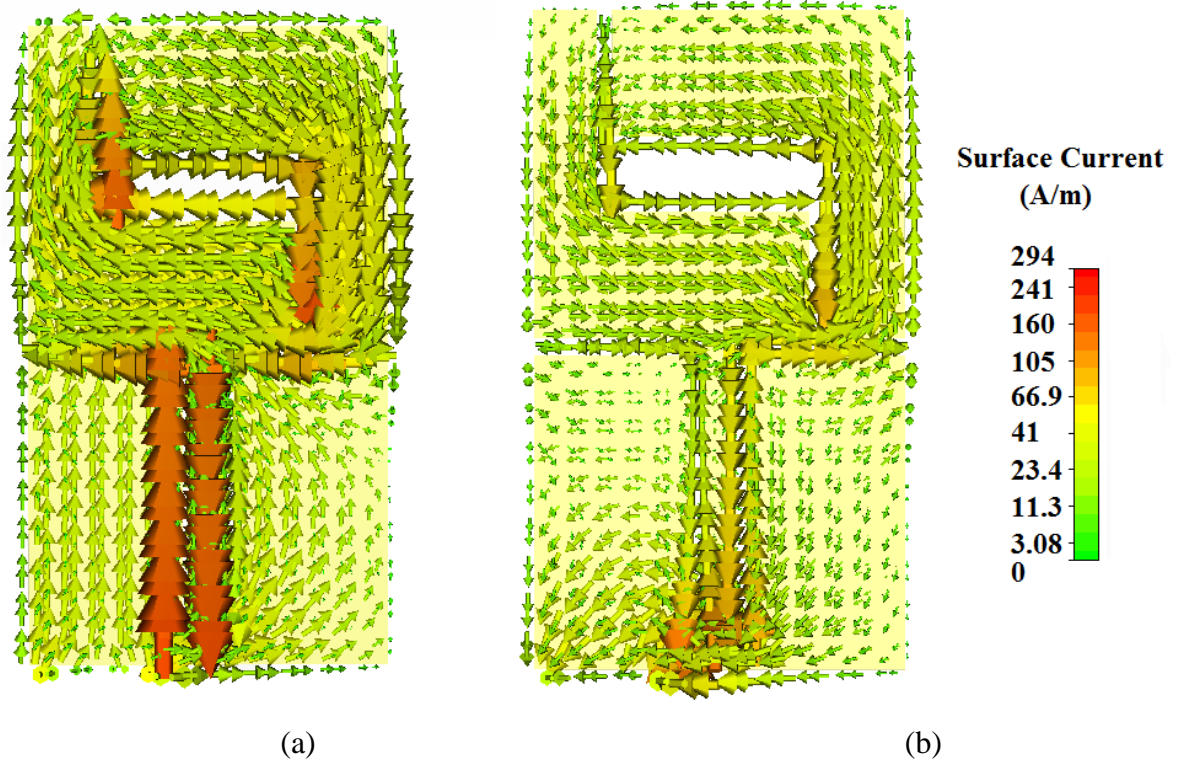


Fig. 6.9: Simulated  $S_{11}$  patterns of the Z-double-L slot loaded PIFA with and without the stacked poly-Si solar cell.

As can be seen in Fig. 6.9, the introduction of the poly-Si solar cell as an RF stacked parasitic patch element has a considerable effect on the resonance characteristics of the PIFA. The first conclusion to be drawn from Fig. 6.9 is that the quad-band resonance response is still present in the absence of the stacked poly-Si solar cell. It can be seen in Fig. 6.9 that the stacked poly-Si solar cell results in a frequency shift which is most pronounced for the first resonance band. Also, the introduction of the poly-Si solar cell as an RF stacked parasitic patch element widens the -10 dB impedance bandwidths at the second and third resonance bands of the PIFA, by a factor of 31.2% and 26.7%, respectively.

Following the investigation of the effect of the photovoltaic integration on the  $S_{11}$  response of the PIFA, the effect of the photovoltaic integration on the surface current distribution of the PIFA radiating element was also studied. For this reason, the surface current distribution of the PIFA was investigated when the stacked poly-Si solar cell was and was not present, respectively. Fig. 6.10 demonstrates the simulated surface current distributions

across the multi-slot radiating PIFA elements obtained for these two PIFA configurations at the resonance frequencies of 1.79 GHz, 2.45 GHz, 3.4 GHz and 4.75 GHz.



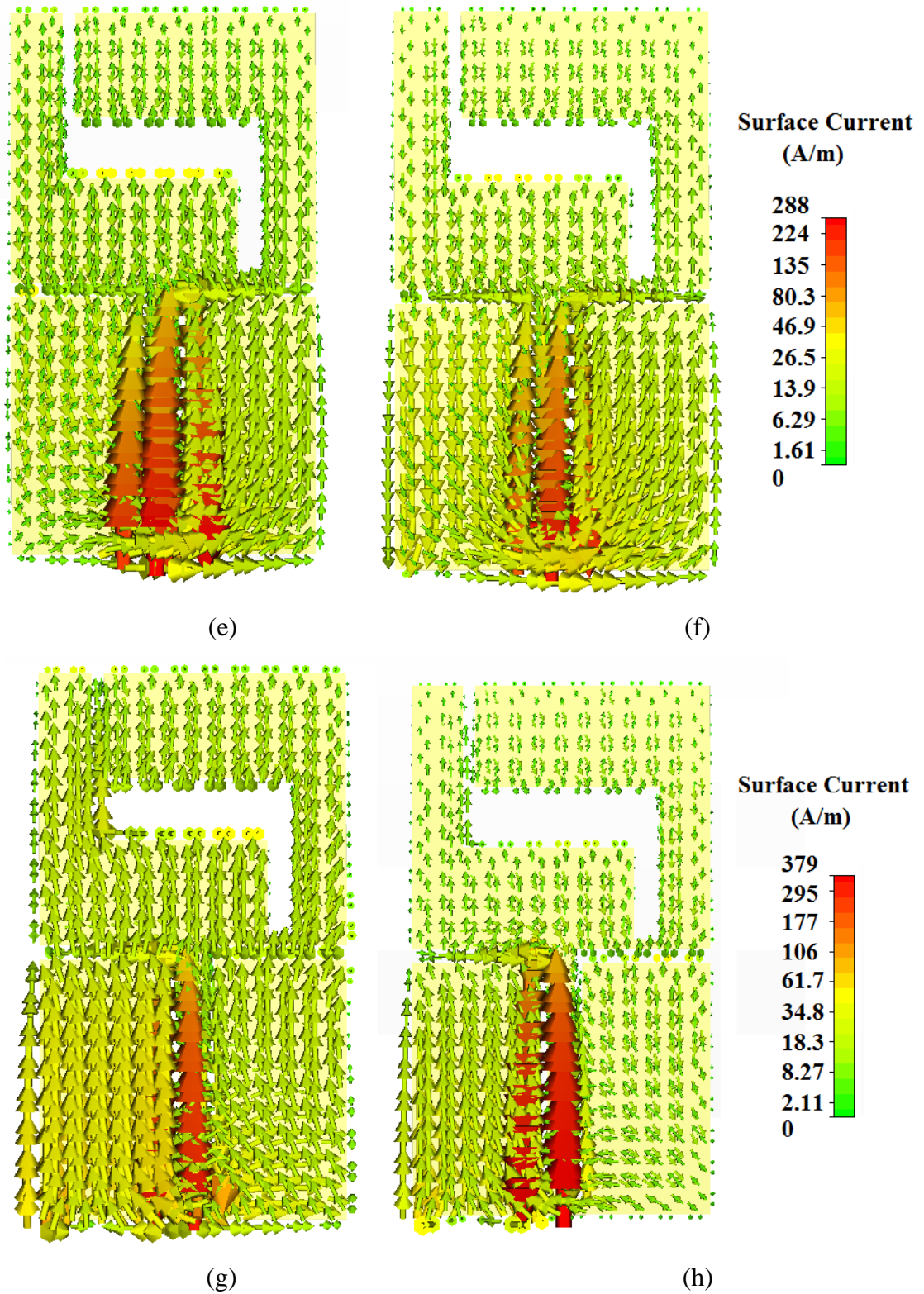


Fig. 6.10: Simulated surface current distributions. At 1.79 GHz (a) PIFA with the stacked poly-Si solar cell (b) PIFA without the poly-Si solar cell; at 2.45 GHz (c) PIFA with the stacked poly-Si solar cell (d) PIFA without the poly-Si solar cell; at 3.4 GHz (e) PIFA with the stacked poly-Si solar cell (f) PIFA without the poly-Si solar cell; at 4.75 GHz (g) PIFA with the stacked poly-Si solar cell (h) PIFA without the poly-Si solar cell.

As illustrated in Fig. 6.10, introduction of the poly-Si solar cell as an RF stacked parasitic patch element results in an increase in the amplitude of the surface current distribution and does not affect the direction of the surface current flow. This suggests that the use of the poly-Si solar cell as an RF stacked parasitic element does not change the polarisation of the integrated PIFA.

### 6.3.2.4 The Effect of the DC connections on PIFA Performance

In order for the stacked poly-Si solar cell to power a DC load, DC connections need to be introduced. The effect of the DC connections on the RF antenna response is required to be minimised in order to obtain stable RF characteristics from the proposed solar PIFA. In order to investigate the effect of the DC connections on the RF response of the solar PIFA, two prototypes of the PIFA were fabricated as demonstrated in Fig. 6.11:

- Solar PIFA with a DC load (a  $220\Omega$  resistor) connected to the stacked cell terminals at the PIFA radiating edge (parallel to the direction of the surface current as demonstrated in Fig. 6.11(a)),
- Solar PIFA with a DC load (a  $220\Omega$  resistor) connected to the stacked cell terminals at the PIFA non-radiating edge (perpendicular to the direction of the surface current as demonstrated in Fig. 6.11(b)).

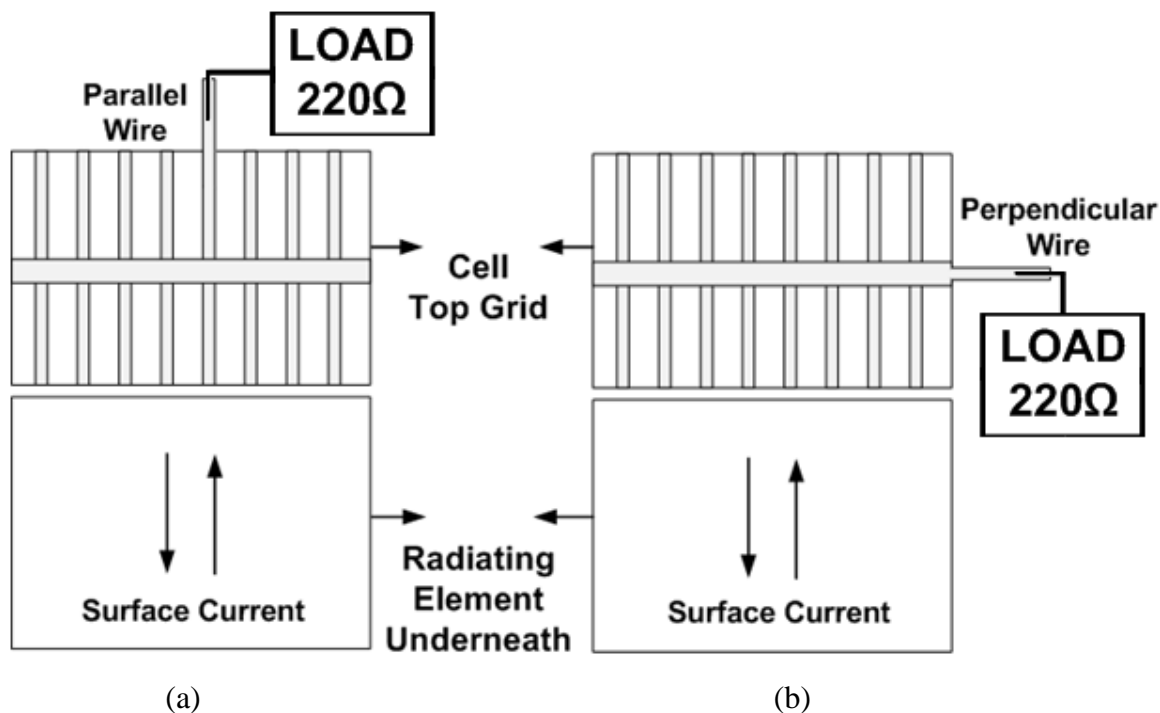


Fig. 6.11: The introduction of the DC load at the (a) radiating edge (b) non-radiating edge.

The measured  $S_{11}$  patterns are demonstrated in Fig. 6.12.

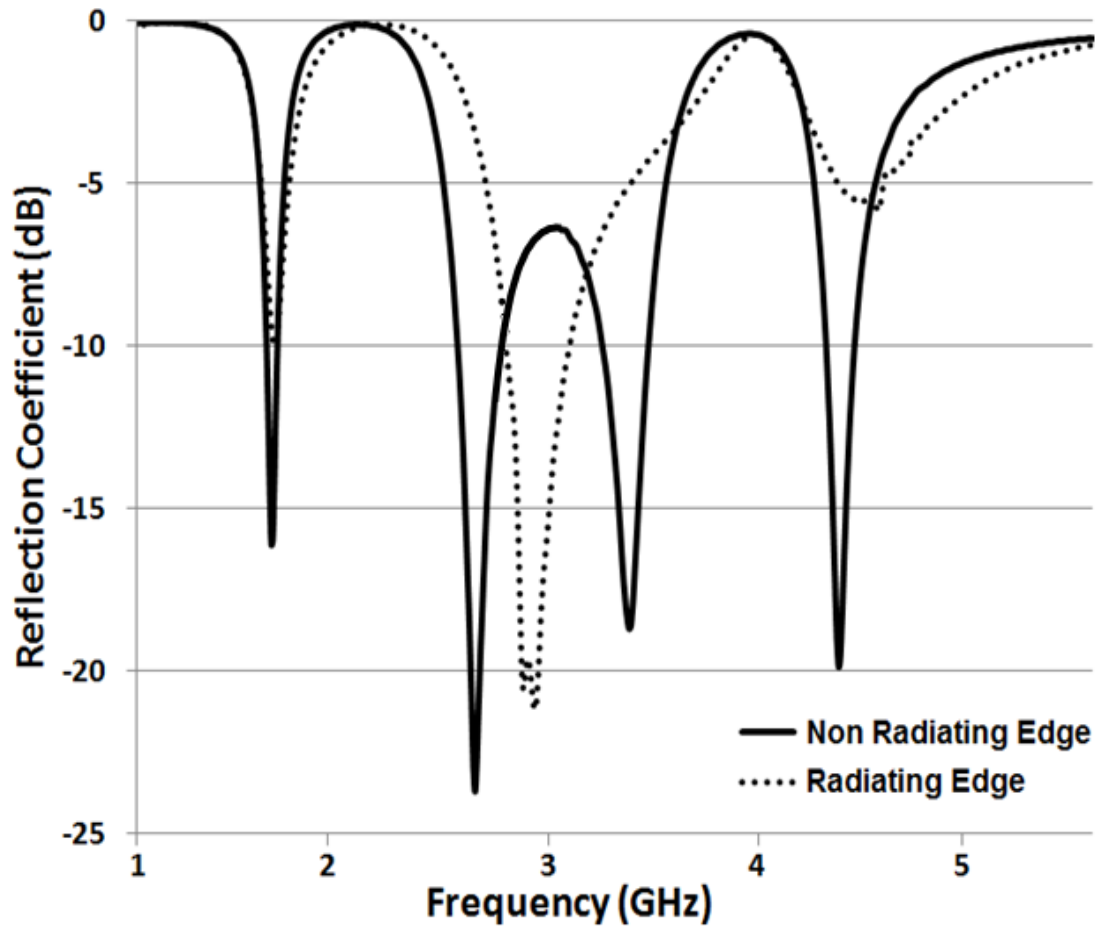


Fig. 6.12: Measured  $S_{11}$  patterns obtained when the DC load is introduced at the non-radiating and radiating edges, respectively.

As can be seen in Fig. 6.12, while the solar PIFA with the DC load connected to the terminals of the stacked parasitic poly-Si solar cell at the non-radiating edge of the PIFA maintains the quad-band resonance response, the introduction of the DC connections at the PIFA radiating edge seriously degrades the resonance characteristics. In comparison to the solar PIFA with the DC load at the non-radiating edge, the solar PIFA with the DC load at the radiating edge offers a single band operation resonating at 3 GHz, which makes it unsuitable for multiband WLAN and WiMAX applications.

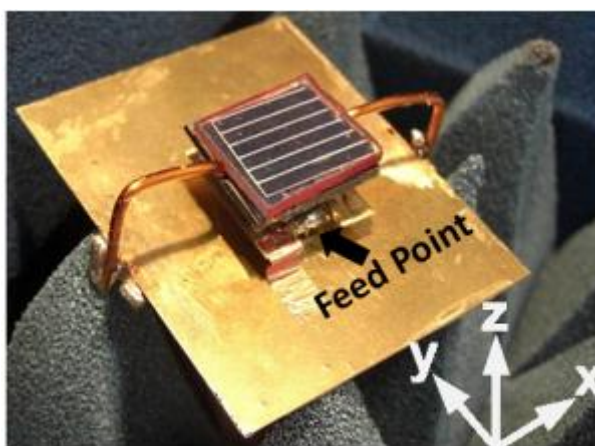
## 6.4 A Solar Cell Stacked Multi-Slot Quad-Band PIFA for GSM, WLAN and WiMAX Networks

It was demonstrated in section 6.3 that the proposed poly-Si solar cell stacked Z-double-L slot PIFA is suitable to be employed in GSM 1800, 2.4 GHz band WLAN and 2.5/3.3/3.5 GHz band WiMAX networks. However, it provides partial coverage for most of these

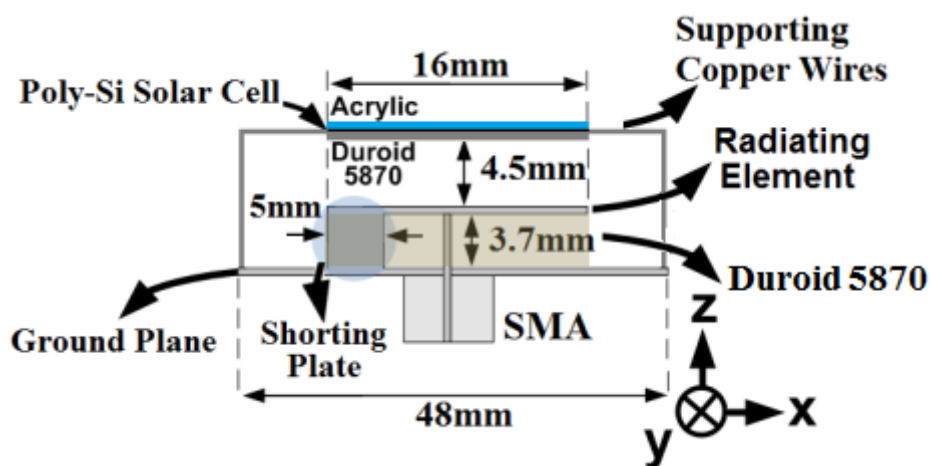
applications. In this section, a PIFA consisting of a W-L slot loaded radiating element stacked with a poly-Si solar cell in a similar manner to the solar PIFA demonstrated in the previous section is proposed for GSM 1800, 2.4 GHz band WLAN and 2.3/3.3/5.8 GHz band WiMAX networks, offering a full coverage for these applications.

## 6.4.1 Solar PIFA Design

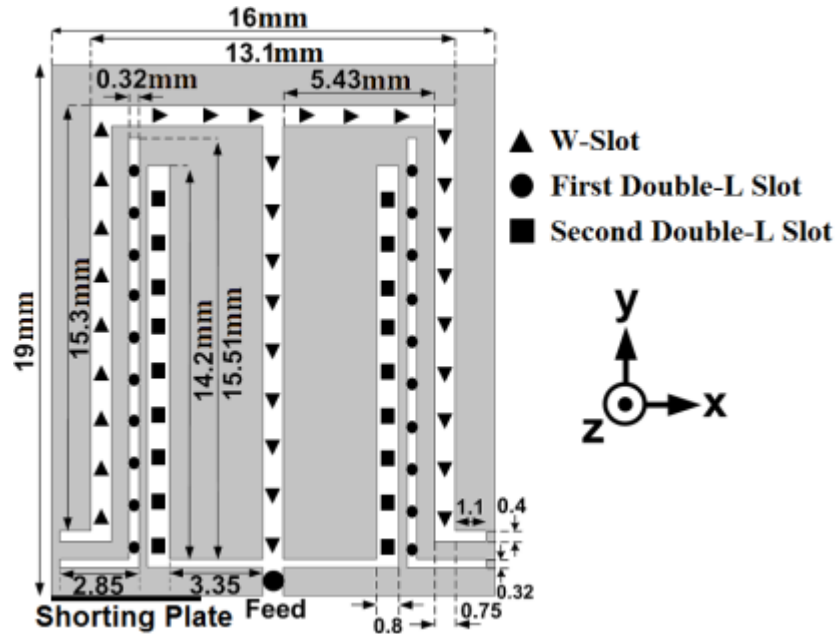
The geometry of the quad-band solar PIFA is shown in Fig. 6.13. The radiating PIFA element consists of W-shaped and L-shaped slots, enabling the excitation of multiple  $TM_{mn}$  propagation modes to achieve a multiband resonance response, which will be discussed in section 6.4.2.1.



(a)



(b)



(c)

Fig. 6.13: Fabricated W-L slot loaded solar PIFA (a) fabricated solar PIFA, overall view (b) fabricated solar PIFA, back view (c) W-L slot loaded radiating PIFA element, top view.

As illustrated in Fig. 6.13, The W-L slot loaded radiating PIFA element was printed upon an RT/Duroid 5870 substrate,  $\epsilon_r=2.33$  and  $\tan\delta=0.0012$ . The shorting plate was introduced at the feeding edge of the multi-slot radiating PIFA element and has a width of 5 mm. Suspended at 4.5 mm above the radiating PIFA element, the suspended poly-Si solar cell operating as an RF stacked parasitic patch element lies.

Different from the solar PIFA demonstrated in the previous section, the stacked poly-Si solar cell in this design was encapsulated. The encapsulation was achieved by placing the cell between an RT/Duroid 5870 substrate,  $\epsilon_r=2.33$ , at the bottom, and a transparent acrylic layer,  $\epsilon_r=3.6$ , on top. As illustrated in Fig 6.1, the rear DC contact of the cell is homogenous in structure and enables the cell to be used as an RF stacked parasitic patch element from an RF perspective. Similar to the solar PIFA demonstrated in the previous section, the suspension of the stacked cell was achieved through two supporting wires each placed on each side of the radiating PIFA element at the non-radiating edges as demonstrated in Fig. 6.13.

From an RF point of view, the proposed poly-Si solar cell stacked W-L slot loaded solar PIFA can be seen as a combination of two separate antennas in same dimensions. The first antenna is the PIFA with multi-slot loaded radiating element which operates in quarter-

wave mode and contributes to the radiation at the lower resonance bands below 3 GHz while the second antenna is the suspended stacked parasitic patch antenna which operates in half-wave mode and contributes to the radiation at the higher resonance bands beyond 3 GHz. The overall radiation characteristics of the proposed antenna are determined by the surface current distribution across the multi-slot loaded radiating PIFA element which also determines the induced current distribution across the surface of the stacked parasitic patch element, i.e. the rear contact of the solar cell.

## 6.4.2 Simulation and Measurement Results

### 6.4.2.1 Antenna Performance

The  $S_{11}$  pattern simulations of the proposed solar PIFA were performed in CST Microwave Studio while the measurements were taken using a VNA, Agilent E8634B. The simulated and measured  $S_{11}$  patterns are shown in Fig. 6.14.

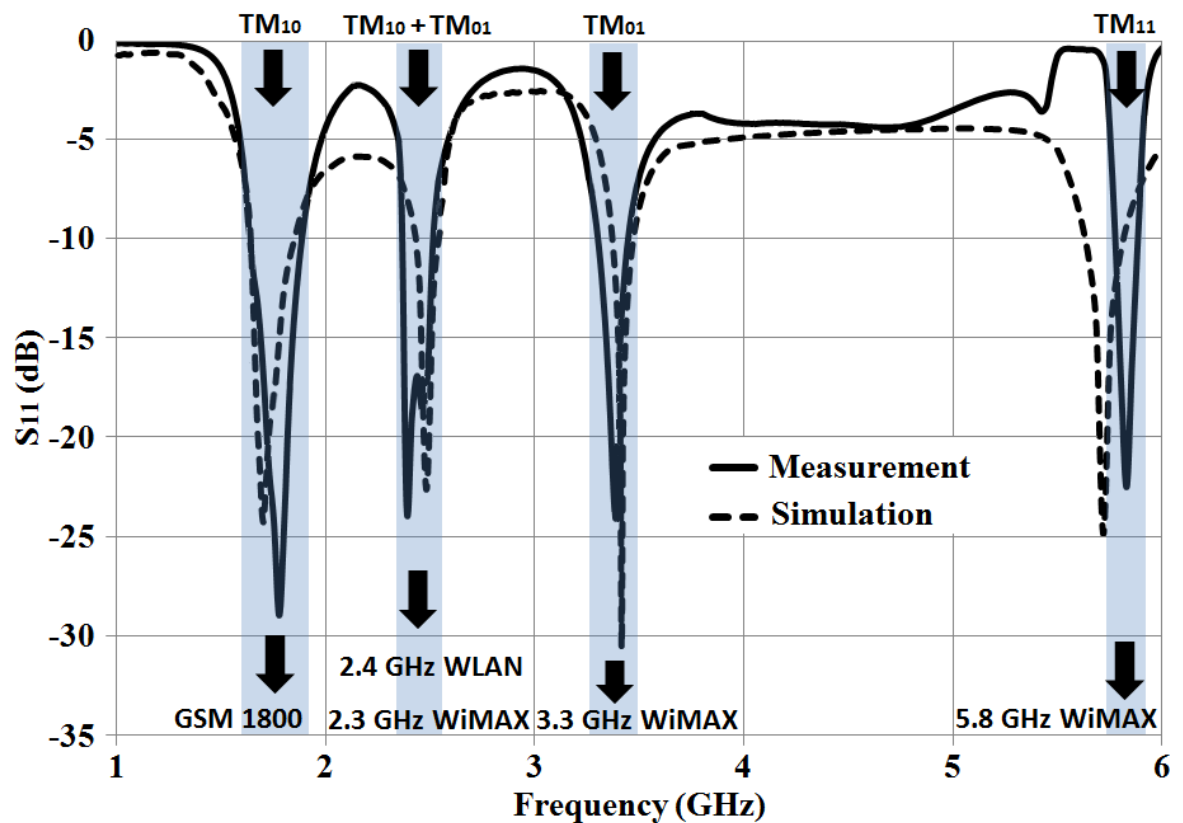


Fig. 6.14: Simulated and measured  $S_{11}$  patterns.

As illustrated in Fig. 6.14, the proposed solar PIFA offers a quad-band resonance response and operates across -10 dB impedance bands of 1.6-1.9 GHz, 2.3-2.52 GHz, 3.24-3.5 GHz and 5.7-5.9 GHz, fully covering the frequency bands of GSM 1800 (1.71-1.88 GHz), 2.4

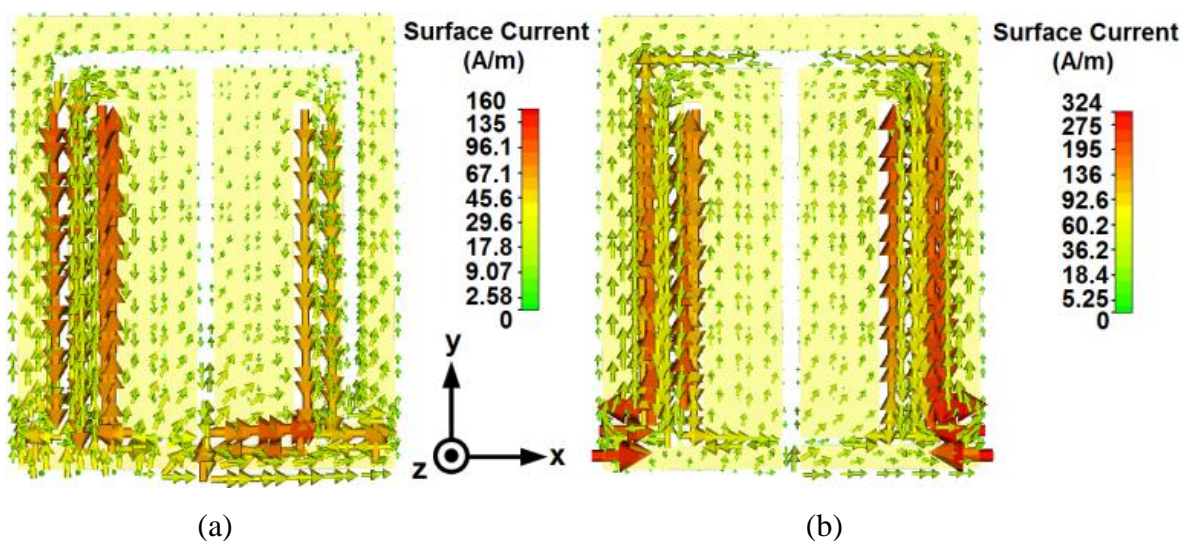
GHz band WLAN (2.4-2.484 GHz), and 2.3/3.3/5.8 GHz band WiMAX (2.3-2.4 GHz / 3.3-3.4 GHz / 5.725-5.825 GHz) networks simultaneously.

In order to determine the equivalent  $TM_{mn}$  propagation modes introduced by the W-L slot loading corresponding to the operational frequency bands demonstrated in Fig. 6.14, equation (6.2) was used. The supported  $TM_{mn}$  propagation modes, slot types and contributed resonance frequencies are summarised in Table 6.4.

Table 6.4: Slot types, contributed resonance bands and supported  $TM_{mn}$  propagation modes.

Resonance Frequency (GHz)	Contributed Slots	$L_{eff}$ (mm)	$W_{eff}$ (mm)	Propagation Modes
1.8	First Double-L	27.2	22.9	$TM_{10}$
2.4	W, First Double-L	22.3	18.73	$TM_{10}+TM_{01}$
3.4	W, Second Double-L	17.3	14.56	$TM_{01}$
5.8	W, Second Double L	13.1	11.03	$TM_{11}$

In order to demonstrate the contribution of the proposed W-L slots to the surface current distribution, the current distributions across the radiating PIFA element at the resonance bands of 1.8 GHz, 2.4 GHz, 3.4 GHz and 5.8 GHz were simulated in CST Microwave Studio and are shown in Fig. 6.15.



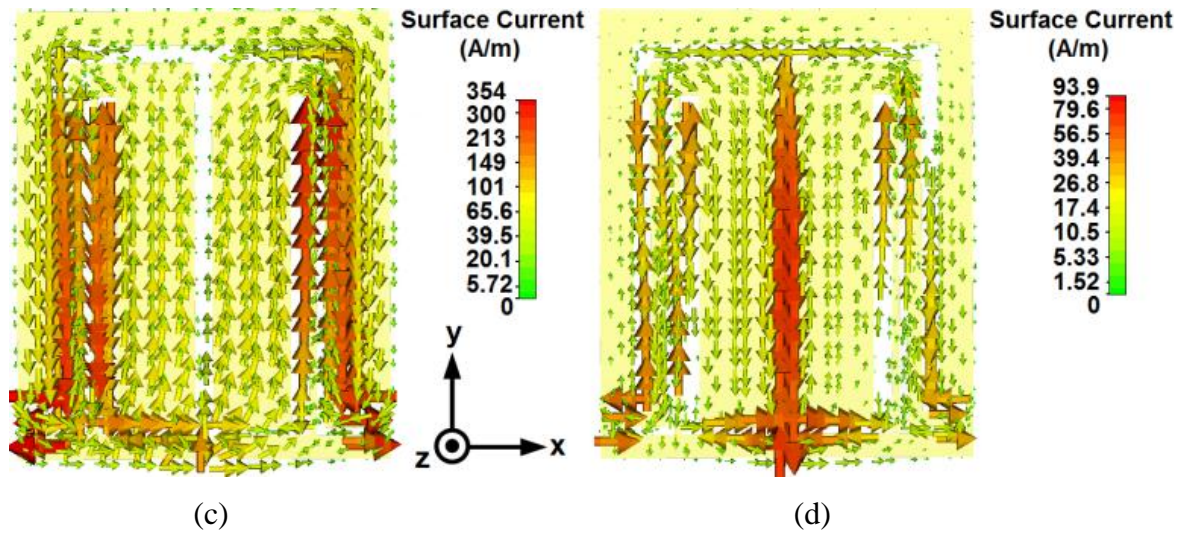


Fig. 6.15: Surface current distribution on the W-L slot loaded radiating PIFA element (a) 1.8 GHz (b) 2.4 GHz (c) 3.4 GHz (d) 5.8 GHz.

As can be seen in Fig. 6.15, the slot-loaded radiating PIFA element has its current distribution considerably strong in amplitude around the slot edges. While the first and second double-L slots play a significant role in the determination of the surface current paths at the frequencies of 1.8, 2.4 and 3.4 GHz, the W-slot with its central slot component along the y-axis is of considerable importance in the determination of the surface current path at the frequency of 5.8 GHz.

### 6.4.2.3 The Effect of Solar Integration on PIFA Performance

In section 6.3.2.3, the effect of the introduction of the poly-Si solar cell as an RF stacked parasitic patch element on the resonance response of the Z-L slot loaded PIFA was investigated. In this section, in addition to investigating the effect of the presence of the stacked poly-Si solar cell, the effect of two additional parameters on the antenna response of the PIFA is also investigated:

- The size of the stacked poly-Si solar cell,
- The distance of the cell from the radiating PIFA element.

The effect of these parameters on the  $S_{11}$  characteristics of the proposed PIFA is given in Table 6.5.

Table 6.5: Effect of size and distance of the stacked poly-Si solar cell on the resonance characteristics of the solar PIFA.

Band	Resonance (GHz)				-10 dB Bandwidth (%)			
	1 <sup>st</sup>	2 <sup>nd</sup>	3 <sup>rd</sup>	4 <sup>th</sup>	1st	2nd	3rd	4th
<b>Stacked Cell Size (mm)</b>								
12x15	1.875	2.45	-	-	14.4	7.6	-	-
16x19 (Optimum)	1.8	2.4	3.4	5.8	16.7	9.16	7.65	3.45
19x23	1.83	2.42	-	5.77	15.9	9.1	-	1.87
<b>Distance of the Cell from the PIFA (mm)</b>								
5.5	1.81	2.42	3.45	5.83	16.3	8.9	8.24	1.5
4.5 (Optimum)	1.8	2.4	3.4	5.8	16.7	9.16	7.65	3.45
3.5	1.775	2.365	3.295	-	16.5	9.34	6.78	-
No cell	1.85	2.47	3.48	5.74	15.4	7.8	1.4	1.1

As can be seen in Table 6.5,

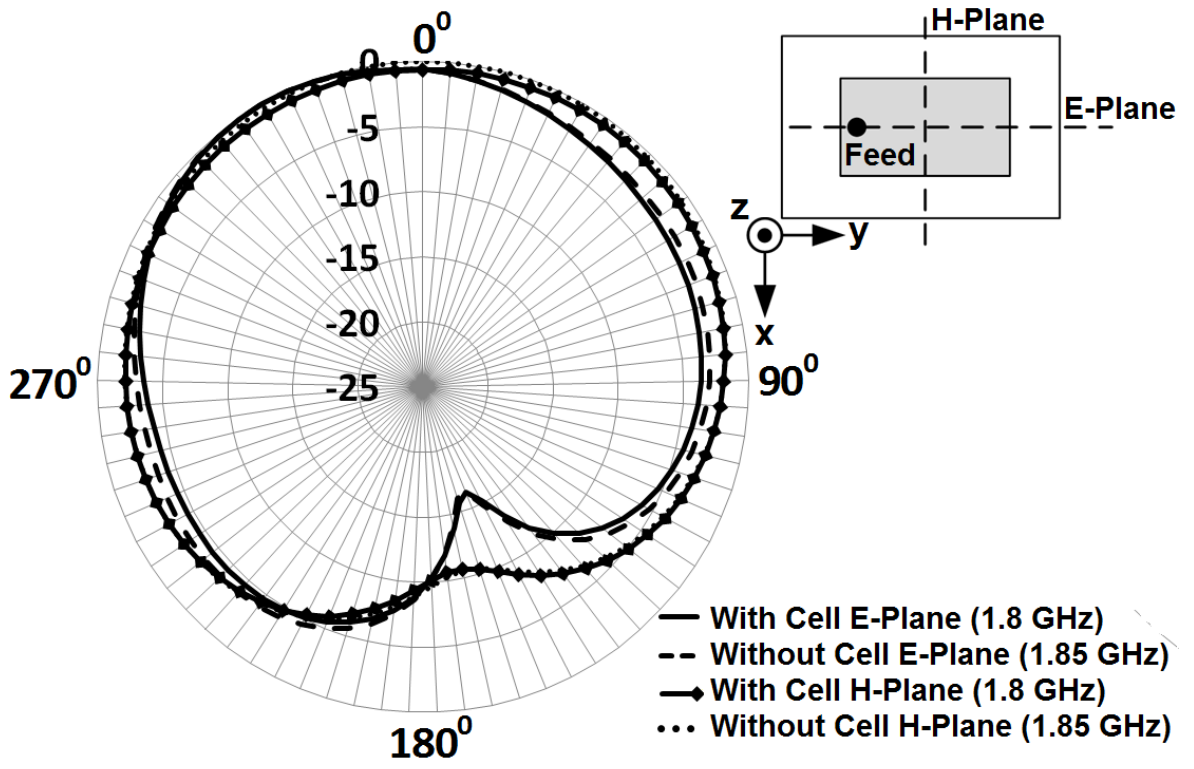
- Changing the distance between the radiating PIFA element and the stacked poly-Si solar cell has a significant effect on the  $S_{11}$  response of the PIFA. While the optimum quad-band response was observed when the separation between these two elements was selected as 4.5 mm, increasing the distance to 5.5 mm narrows the -10 dB impedance bandwidth at the fourth resonance band of the PIFA by 56.5%. In

the case of reducing the distance to 3.5 mm, on the other hand, the fourth resonance band was cancelled.

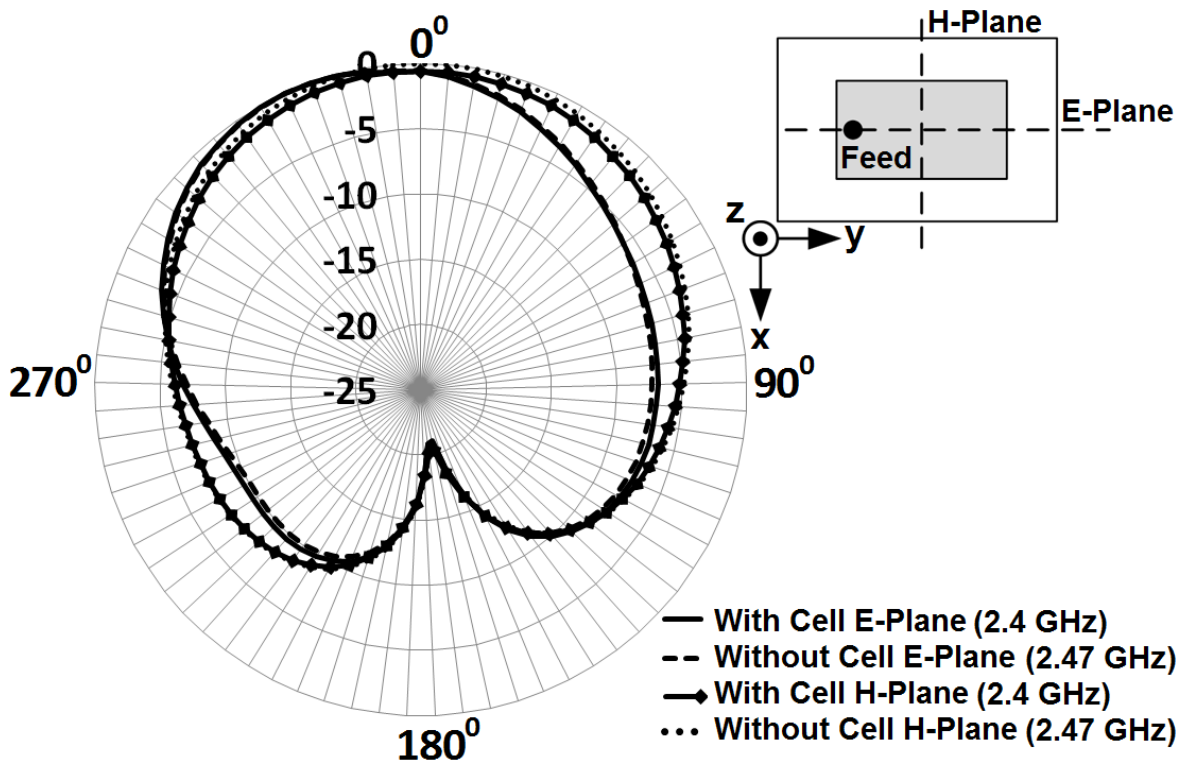
- Similarly, changing the size of the stacked poly-Si solar cell brings a significant effect on the resonance response of the PIFA. As can be seen in Table 6.5, the optimum quad-band response was obtained when the size of the solar cell was selected to be equal to the size of the radiating PIFA element, 16 mm x 19 mm. Reducing the size of the cell to 12 mm x 15 mm, i.e. by a factor of 40.8%, resulted in the third and the fourth resonances being cancelled. Increasing the size of the cell to 19 mm x 23 mm, i.e. by a factor of 43.8%, on the other hand, resulted in the third resonance band being cancelled and the fourth resonance band being significantly narrowed from 3.45% to 1.87%.

An interesting result was observed in the absence of the stacked poly-Si solar cell. As given in Table 6.5, the quad-band response of the PIFA is still present without the stacked poly-Si solar cell subject to minor shifts in the resonance frequencies. However, if attention is given to -10 dB impedance bandwidths at the resonance bands of the PIFA with and without the stacked poly-Si solar cell, it can be seen that the absence of the solar cell brings a significant deterioration in the  $S_{11}$  response of the PIFA by narrowing the impedance bandwidths of the third and the fourth resonance bands by 81.7% and 68.1%, respectively.

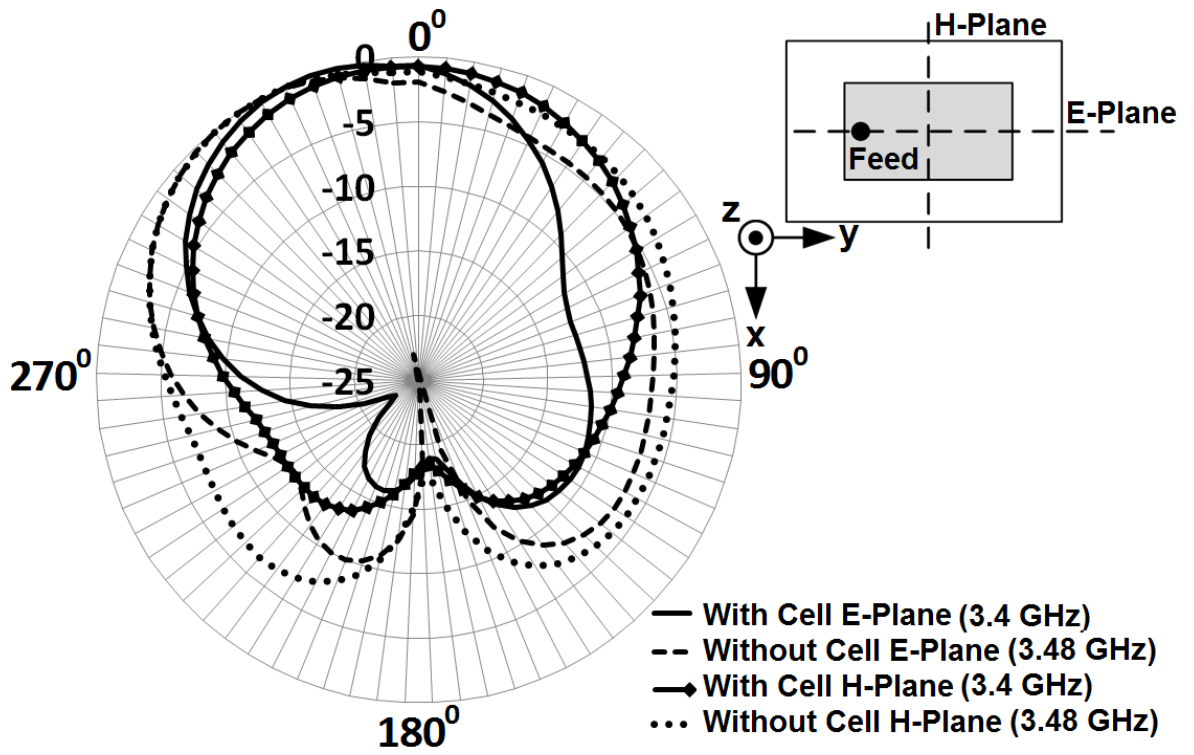
Similar to the solar antennas demonstrated until now, the conical spiral antenna with a gain of  $G_T=4$  dBi was used as a reference antenna for the measurement of the E-plane and H-plane far-field radiation patterns. The far-field radiation pattern measurements of the solar PIFA were performed in an anechoic chamber with a signal generator power level of  $P_G=14$  dBm. The AUT was placed at a distance of  $R=3$  m from the reference conical spiral antenna and the measurements in the E-plane and H-plane were taken over  $360^\circ$  with a sampling angle of  $5^\circ$ . At each sampling angle, the received power,  $P_R$ , was measured and Friis equation given in equation (4.3) was used to calculate the maximum gain values of the solar PIFA after taking the cable loss,  $L_{Cable}$ , into account as given in equation (4.4). The E-plane and H-plane far-field radiation patterns of the proposed solar PIFA were measured with and without the stacked poly-Si solar cell at the resonance frequencies of these two geometries given in Table 6.5 and are illustrated in Fig. 6.16.



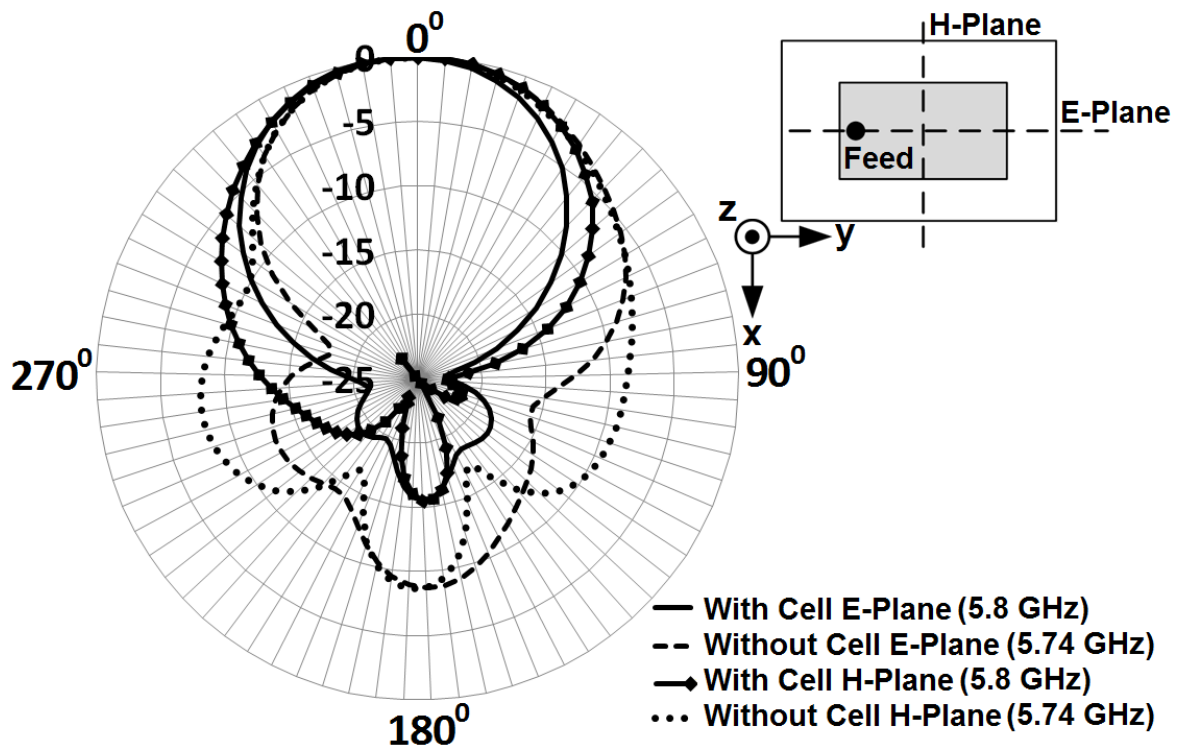
(a)



(b)



(c)



(d)

Fig. 6.16: Measured normalised E-Plane and H-Plane far-field radiation patterns with and without the stacked poly-Si solar cell at (a) first resonance (b) second resonance (c) third resonance (d) fourth resonance.

As illustrated in Fig. 6.16, the proposed solar PIFA has broadside E-plane and H-plane far-field radiation patterns at the investigated resonance frequencies. Whilst the effect of the absence of the stacked poly-Si solar cell on the far-field radiation patterns is negligible below 3 GHz, it has a considerable effect on the patterns at the higher bands above 3 GHz. This is due to the fact that, as explained earlier, from an RF perspective, the proposed W-L slot loaded poly-Si solar cell stacked solar PIFA can be thought as a combination of two antennas; a PIFA and a stacked parasitic patch antenna. Whilst below 3 GHz, the contribution to the radiation in the far-field comes mainly from the PIFA, above 3 GHz, the stacked parasitic patch antenna becomes more dominant. The measured maximum gain values given in Table 6.6 confirm this observation.

Table 6.6: Measured maximum gain values of the PIFA with and without the stacked poly-Si solar cell.

	With Solar Cell			Without Solar Cell			
Resonance Frequency (GHz)	Max. Gain (dBi)	$P_R$ (dBm)	$L_{Cable}$	Resonance Frequency (GHz)	Max. Gain (dBi)	$P_R$ (dBm)	$L_{Cable}$
1.8	2.3	-32.91	6.13	1.85	2.1	-33.53	6.31
2.4	4.7	-34.22	7.33	2.47	4.2	-35.09	7.45
3.4	7.1	-36.34	8.83	3.48	3.1	-40.67	8.95
5.8	5.5	-45.60	11.85	5.74	2.6	-48.34	11.77

If comparison needs to be made between the PIFAs with and without the stacked poly-Si solar cell, it can be seen in Table 6.6 that the PIFA presents similar maximum gain values regardless of the presence of the stacked poly-Si solar cell below 3 GHz. Above 3 GHz, however, the absence of the poly-Si solar cell has a considerable effect on the maximum gain values of the PIFA. Whilst the PIFA with the stacked poly-Si solar cell offers a maximum gain of 7.1 dBi at 3.4 GHz, the PIFA without the stacked parasitic poly-Si solar cell has a maximum gain of 3.1 dBi, equating to a decrease in the maximum gain performance by 56.3%. Similarly, at 5.8 GHz, whilst the PIFA with the stacked poly-Si solar cell has a maximum gain of 5.5 dBi, the PIFA without the stacked cell offers a

maximum gain of 2.6 dBi, corresponding to a decrease in the maximum gain performance by 52.7%.

### 6.4.2.2 Solar Performance

The solar performance measurements of the proposed solar PIFA were performed in the metal halide solar simulator demonstrated in chapter 3. Similar to the photovoltaic antennas demonstrated until now, a group of resistors, from  $10\Omega$  to  $2.7k\Omega$ , were connected to the terminals of the stacked poly-Si solar cell and the voltage and current values were measured for each resistor in order to obtain the I/V curve of the solar PIFA, which is demonstrated in Fig. 6.17.

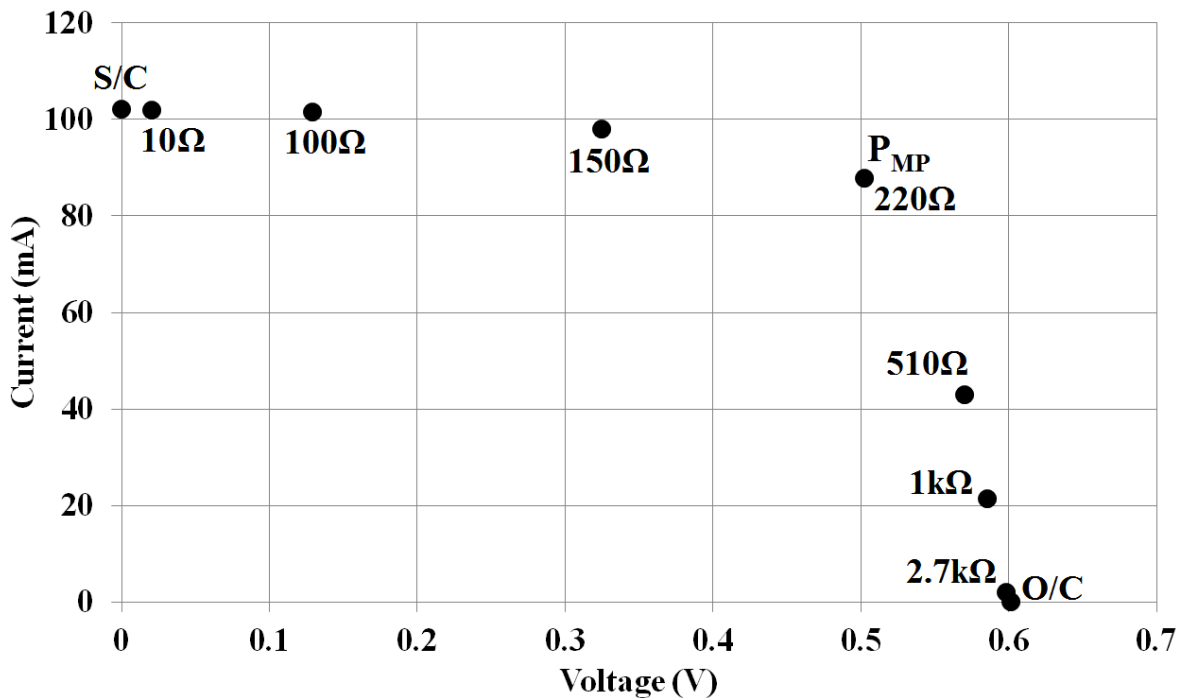


Fig. 6.17: Measured I/V curve of the solar PIFA.

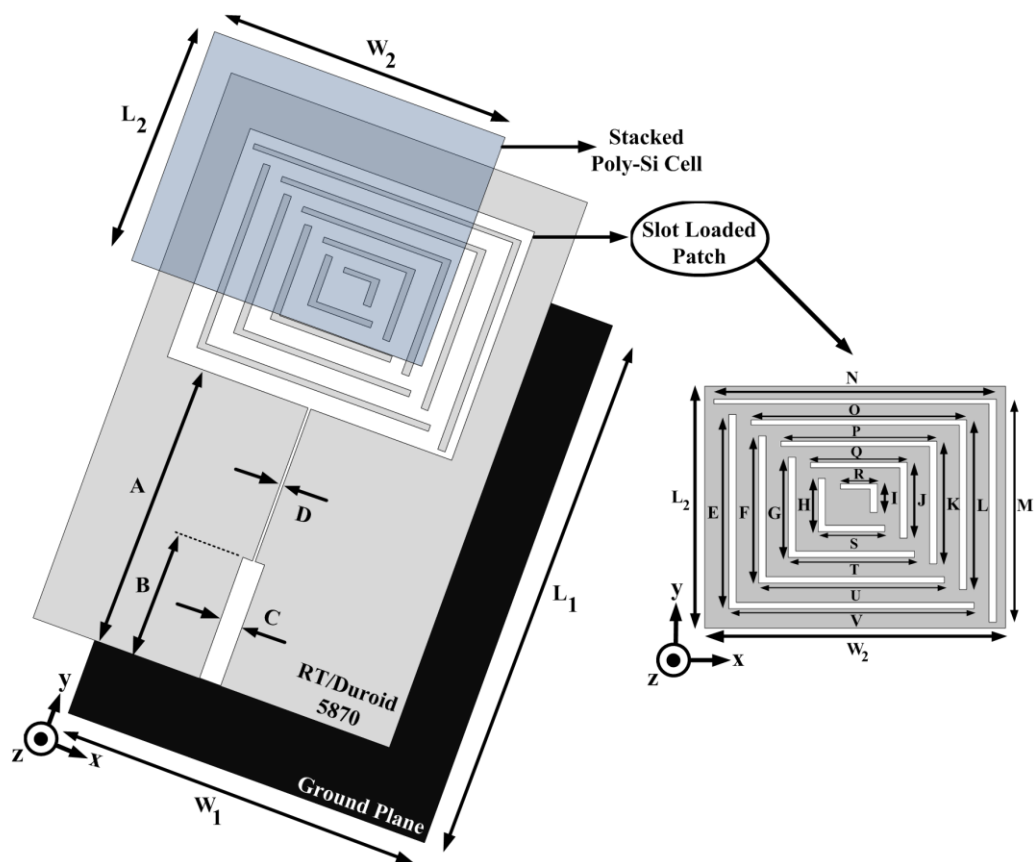
The open-circuit voltage and short-circuit current of the proposed solar PIFA were measured as  $V_{OC}=0.602$  V and  $I_{SC}=102$  mA, respectively. The voltage and current readings at the maximum power point were measured as  $V_{MP}=0.502$  V and  $I_{MP}=87.67$  mA, respectively, generating a DC power output of  $P_{MP}=44$  mW. Considering the input illumination intensity,  $P_{in}=0.304$  W, which is the total illumination intensity of the solar simulator,  $1000$  W/m<sup>2</sup>, multiplied by the surface area of the stacked poly-Si solar cell, 16 mm x 19 mm, the solar efficiency of the proposed solar PIFA was calculated as  $\eta=14.5\%$  from equation (3.13).

## 6.5 A Solar Cell Stacked Slot-Loaded Suspended Microstrip Patch Antenna for WLAN and WiMAX Networks

Although providing coverage for 2.3/2.5/3.3/3.5/5.8 GHz band WiMAX networks, the photovoltaic PIFAs demonstrated in the previous sections do not offer the potential to be employed in 5.2 GHz band WLAN networks. In order to address this challenge, in this section, a self-complementary shaped multiple-L slot loaded suspended microstrip patch antenna stacked with a poly-Si solar cell operating as an RF parasitic patch element is demonstrated for 2.4/5.2 GHz band WLAN networks. In addition to these networks, the proposed photovoltaic antenna also provides full coverage for 2.5/3.3/5.8 GHz band WiMAX networks.

### 6.5.1 Slot-Loaded Stacked Solar Patch Antenna Design

The proposed self-complementary shaped multiple-L slot loaded poly-Si solar cell stacked suspended microstrip solar patch antenna is demonstrated in Fig. 6.18.



(a)

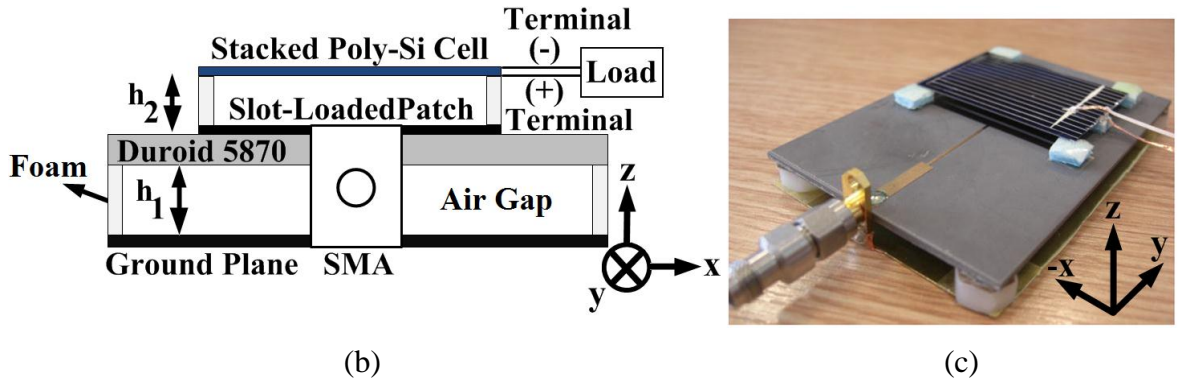


Fig. 6.18: Fabricated self-complementary shaped multiple-L slot loaded suspended microstrip patch antenna stacked with a poly-Si solar cell (a) Top view (b) back view (c) overall view. Dimensions (in mm):  $A=41.5$ ,  $B=18.3$ ,  $C=3.2$ ,  $D=0.38$ ,  $E=27.8$ ,  $F=21.1$ ,  $G=14.4$ ,  $H=7.6$ ,  $I=4.1$ ,  $J=10.8$ ,  $K=17.6$ ,  $L=24.3$ ,  $M=32$ ,  $N=40.5$ ,  $O=30.9$ ,  $P=22.3$ ,  $Q=13.8$ ,  $R=5.3$ ,  $S=9.5$ ,  $T=18.1$ ,  $U=26.6$ ,  $V=35.1$ ,  $W_1=60$ ,  $W_2=43$ ,  $L_1=90$ ,  $L_2=33$ ,  $h_1=6$ ,  $h_2=3$ , L-slot width=1.

As illustrated in Fig. 6.18, the modified patch together with the microstrip feed line was printed on a low-loss RT/Duroid 5870 substrate,  $\epsilon_r=2.33$  and  $\tan\delta=0.0012$ , which is suspended at 6 mm above the ground plane. The microstrip patch was loaded with self-complementary shaped multiple-L slots responsible for modifying the surface current distribution to excite multiple  $TM_{mn}$  propagation modes as demonstrated in section 6.5.2.1. The microstrip patch is stacked with a poly-Si solar cell suspended at 3 mm above the patch as illustrated in Fig. 6.18(b). In order to withdraw the current produced by the poly-Si solar cell to a DC load connected to the cell terminals, as shown in Fig. 6.18(b) and Fig. 6.18(c), copper wires with a diameter of 0.8 mm were connected to the positive and negative terminals of the poly-Si solar cell whose detailed structure is given in Fig. 6.1. The terminals of the stacked solar cell were terminated in a  $220 \Omega$  DC load, representing a conventional DC termination of a solar cell at the maximum power point. As illustrated in Fig. 6.1, the poly-Si solar cell consists of two metal contacts, a front grid (negative DC terminal) and a rear solid (positive DC terminal), together with a silicon layer in between. From an RF perspective, attention should be given to the rear metal contact of the cell, which is homogeneous in structure allowing the cell to be used as a suspended RF stacked parasitic patch element in addition to its photovoltaic function. Similar to the solar PIFAs demonstrated in the previous sections of this chapter, a significant challenge to be addressed here is the requirement of the effect of the DC load connections at the cell terminals on the RF antenna performance to be minimised, which was achieved by

connecting the DC load to the terminals of the stacked poly-Si solar cell at the non-radiating edge.

## 6.5.2 Simulation and Measurement Results

### 6.5.2.1 Antenna Performance

The simulated and measured  $S_{11}$  patterns are demonstrated in Fig. 6.19. The  $S_{11}$  simulations were performed in CST Microwave Studio while the measurements were taken using a VNA, Agilent E8364B.

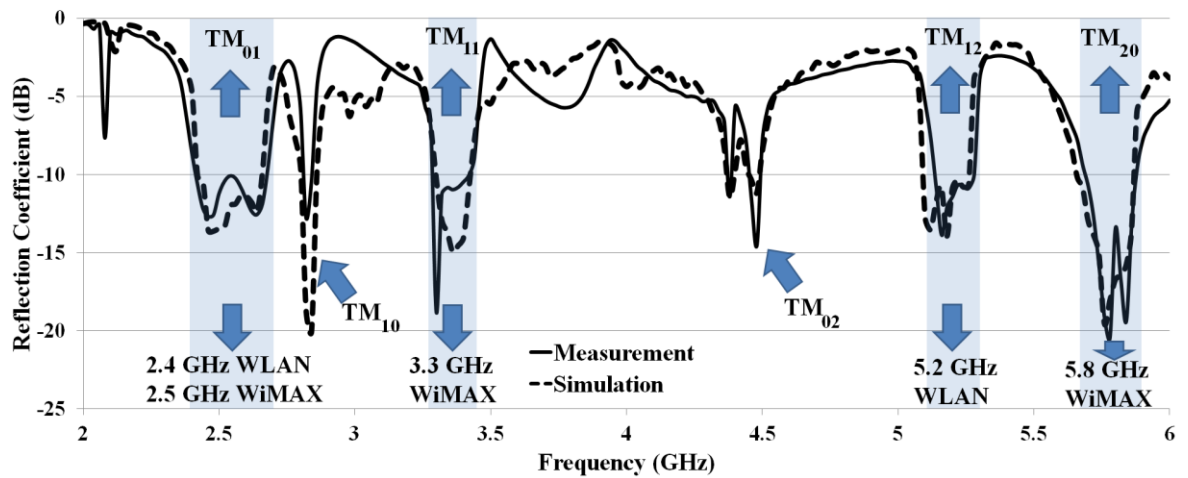


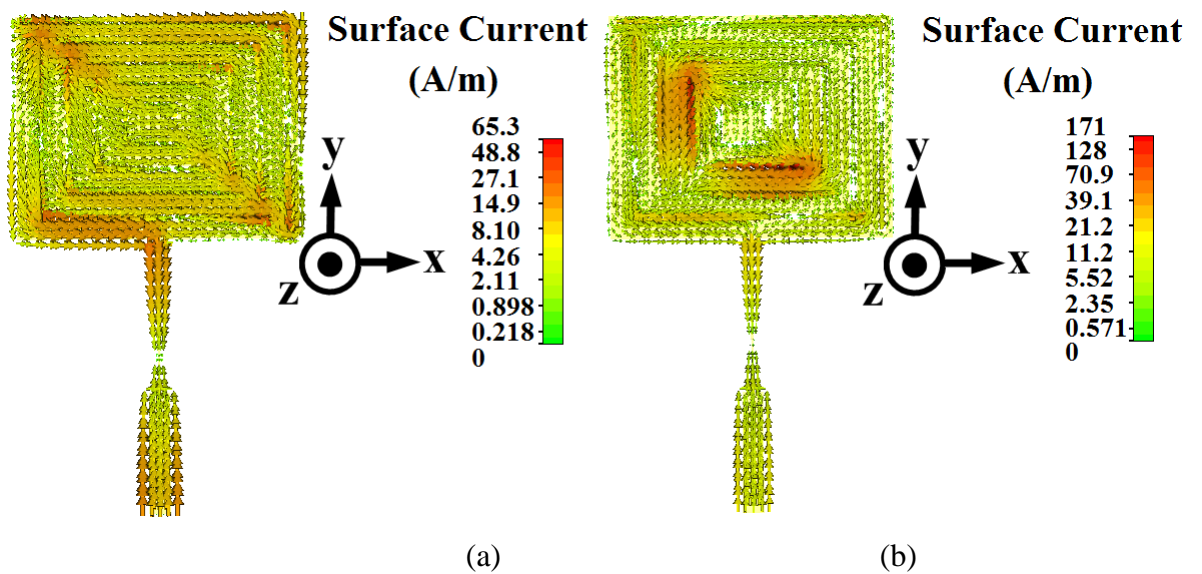
Fig. 6.19: Simulated and measured  $S_{11}$  patterns.

As can be seen in Fig. 6.19, there is good agreement between the simulated and measured  $S_{11}$  patterns. In order to determine the equivalent  $TM_{mn}$  propagation modes introduced by the self-complementary shaped multiple-L slot loading corresponding to the operational frequency bands demonstrated in Fig. 6.19, equation (6.1) was used [176]. Supporting the propagation modes  $TM_{01}$ ,  $TM_{10}$ ,  $TM_{11}$ ,  $TM_{02}$ ,  $TM_{12}$  and  $TM_{20}$  across the investigated frequency band of 2-6 GHz as given in Fig. 6.19, the proposed solar patch antenna operates at the measured frequency bands of 2.4-2.71 GHz, 3.29-3.44 GHz, 5.14-5.35 GHz and 5.68-5.88 GHz, respectively, providing full coverage at the frequency bands required for 2.4/5.2 GHz band WLAN (2.4-2.484 GHz / 5.15-5.35 GHz) and 2.5/3.3/5.8 GHz band WiMAX (2.5-2.7 GHz / 3.3-3.4 GHz / 5.725-5.825 GHz) networks. The  $S_{11}$  performance of the proposed solar patch antenna is summarised in Table 6.7.

Table 6.7: Measured  $S_{11}$  performance of the proposed solar patch antenna.

Resonance (GHz)	Frequency Band (GHz)	BW (%)	Covered Networks	$L_{eff}$ (mm)	$W_{eff}$ (mm)	Propagation Mode
2.5	2.4-2.71	12.4	2.4 GHz WLAN 2.5 GHz WiMAX	31.28	40.79	$TM_{01}$
3.3	3.29-3.44	4.5	3.3 GHz WiMAX	33.5	46.81	$TM_{11}$
5.2	5.14-5.35	4	5.2 GHz WLAN	34.18	44.59	$TM_{12}$
5.8	5.68-5.88	3.5	5.8 GHz WiMAX	33.81	44.07	$TM_{20}$

The simulated current distributions across the surface of the proposed multiple-L slot loaded suspended patch at the frequencies of 2.5, 3.3, 5.2 and 5.8 GHz are shown in Fig. 6.20.



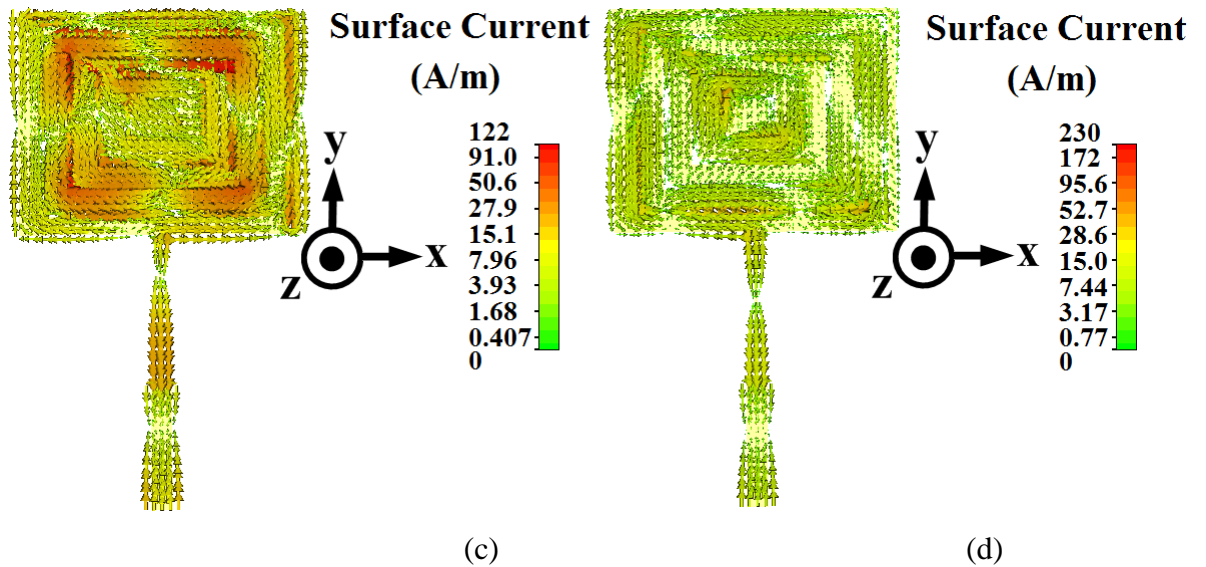
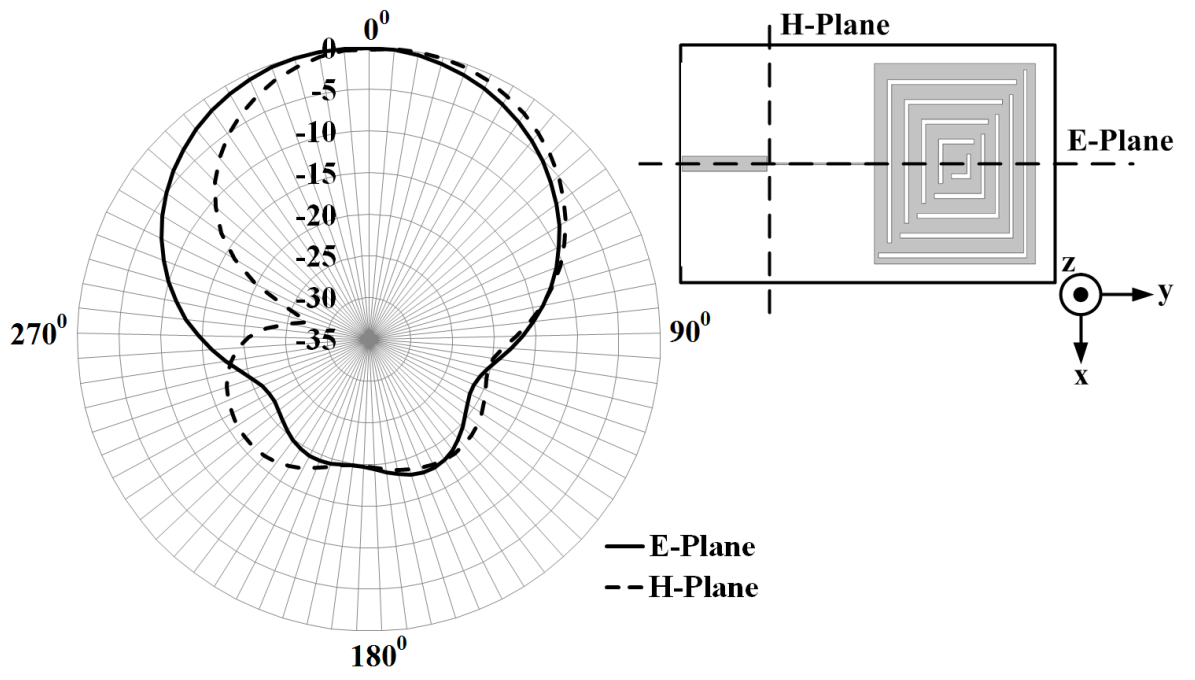


Fig. 6.20: Simulated current distributions across the self-complementary shaped multiple-L slot loaded suspended microstrip patch together with the feed line at (a) 2.5 GHz (b) 3.3 GHz (c) 5.2 GHz (d) 5.8 GHz.

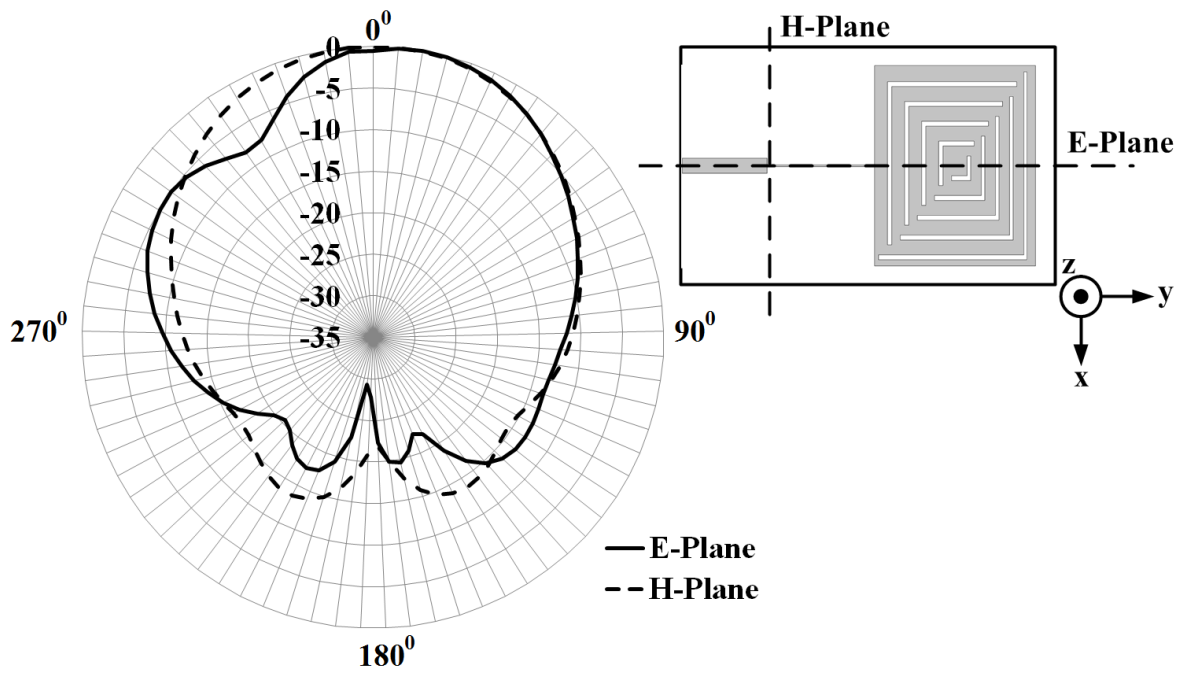
As can be seen in Fig. 6.20, the introduced self-complementary shaped multiple-L slots modify the current path across the patch surface. Whilst the slots at the patch centre play a significant role in the determination of the current paths of  $TM_{01}$ ,  $TM_{10}$  and  $TM_{11}$  propagation modes, the slots close to the edges have a considerable effect on shaping the current paths of  $TM_{02}$ ,  $TM_{12}$  and  $TM_{20}$  propagation modes.

The E-plane and H-plane far-field radiation pattern measurements were carried out in an anechoic chamber with a signal generator power level of  $P_G=14$  dBm. For the measurements, the conical spiral antenna with a gain of  $G_T=4$  dBi was used as a reference antenna placed at a distance of  $R=3$  m from the AUT. Similar to the far-field radiation pattern measurements of the photovoltaic antennas demonstrated until now, the received power by the AUT,  $P_R$ , was measured over  $360^\circ$  at  $5^\circ$  intervals in the E-plane and H-plane. The gain values were then calculated using Friis Equation given in equation (4.3) by taking the cable losses,  $L_{Cable}$ , given in equation (4.4) into account.

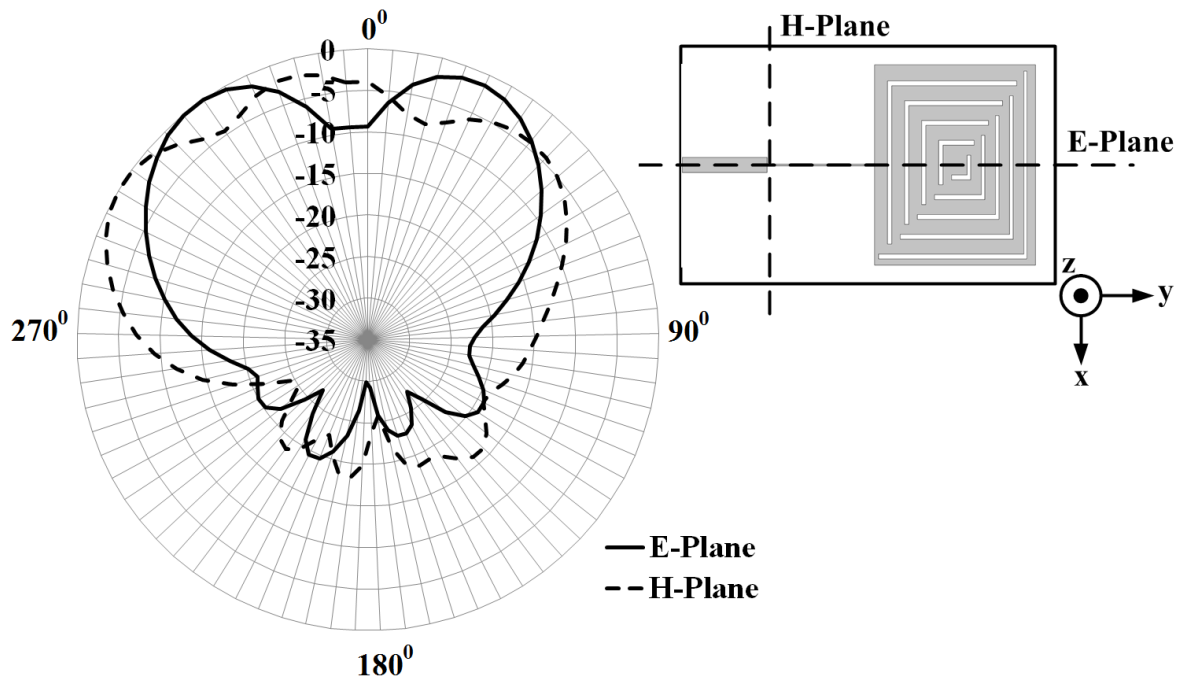
The measured normalised E-plane and H-plane far-field radiation patterns are demonstrated in Fig. 6.21.



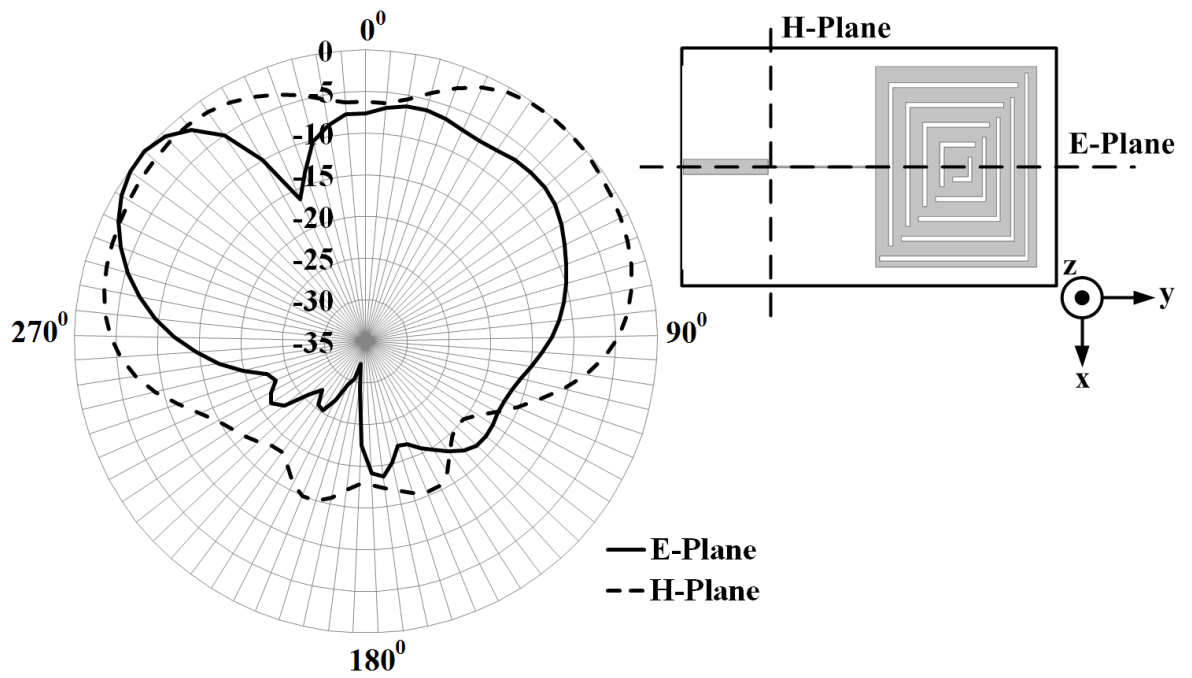
(a)



(b)



(c)



(d)

Fig. 6.21: Measured E-plane and H-plane far-field radiation patterns at (a) 2.5 GHz (b) 3.3 GHz (c) 5.2 GHz (d) 5.8 GHz.

As expected from  $TM_{01}$  propagation mode, the radiation is in the broadside direction at 2.5 GHz as demonstrated in Fig. 6.21(a). For  $TM_{11}$  mode at 3.3 GHz, broadside radiation is still present as illustrated in Fig. 6.21(b) replacing the conical off-broadside pattern of conventional rectangular microstrip patch antennas operating at  $TM_{11}$  mode [152]. This is

due to the modified current distribution along the width and the length of the proposed slot-loaded patch. If attention is given to Fig. 6.21(c), separation in the broadside radiation in the E-plane can clearly be seen enabling the proposed antenna to be used in multipath applications at this frequency. This separation is due to the nature of  $TM_{12}$ , which ideally introduces a null in the broadside direction. Similarly, at 5.8 GHz illustrated in Fig. 6.21(d), multipath conical radiation pattern with a separation in the near-broadside direction is present introduced by the propagation mode  $TM_{20}$ .

The measured maximum gain values of the proposed solar antenna are given in Table 6.8.

Table 6.8: Measured maximum gain values of the proposed solar patch antenna.

Frequency (GHz)	$P_R$ (dBm)	$L_{Cable}$ (dB)	Measured Max. Gain (dBi)	Simulated Max. Gain (dBi)
2.5	-30.94	7.49	8.49	8.2
3.3	-35.93	8.69	7.11	7.5
5.2	-40.06	11.16	9.4	9.1
5.8	-42.62	11.85	8.48	8.7

As given in Table 6.8, in comparison to the photovoltaic microstrip patch antennas demonstrated in the previous chapters, the proposed solar patch antenna using the RF stacked solar antenna integration topology demonstrates considerably higher maximum gain values. This is due to the presence of the stacked poly-Si solar cell operating as an RF parasitic patch element, which contributes to the radiation as a second radiator.

### 6.5.2.2 The Effect of Solar Integration on Antenna Performance

In this section, the effect of the photovoltaic integration on the RF antenna performance is studied by investigating the  $S_{11}$  responses of the proposed patch antenna with and without the stacked poly-Si solar cell, and the effect of DC load connections on the RF response of the antenna. In view of this, firstly,  $S_{11}$  measurements of the proposed antenna were taken with and without the stacked poly-Si solar cell and a comparison between the obtained results is made in Fig. 6.22.

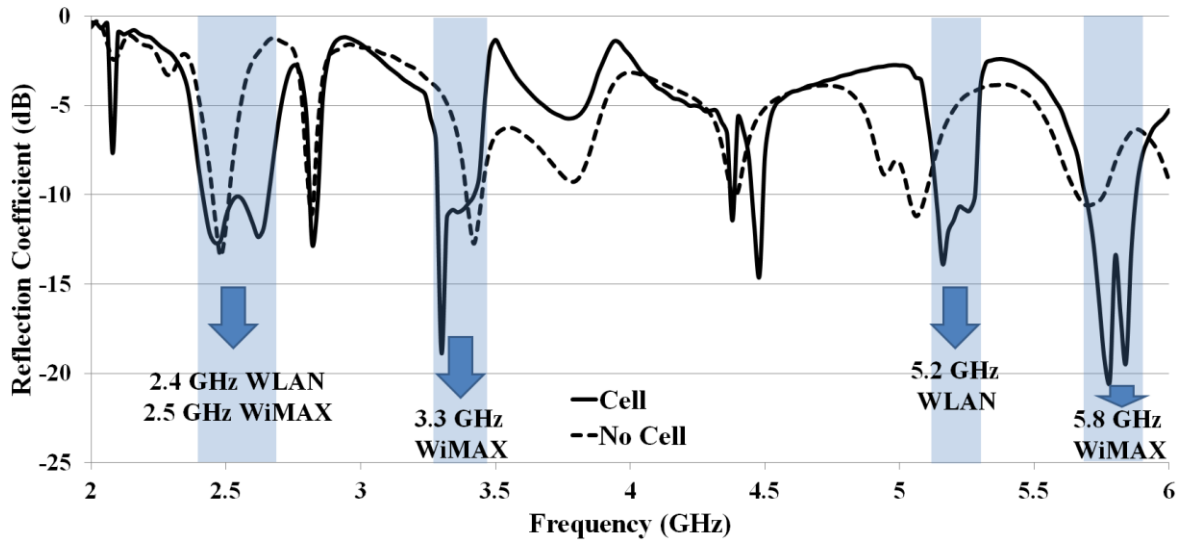


Fig. 6.22: Measured  $S_{11}$  patterns with and without the stacked poly-Si solar cell.

As can be seen in Fig. 6.22, due to the slot-loaded geometry, the antenna has a multiband resonance response regardless of the presence of the stacked poly-Si solar cell. However, the proposed poly-Si solar cell stacked geometry brings a considerable enhancement at the resonance bands enabling the antenna to provide a full coverage for 2.4/5.2 GHz band WLAN and 2.5/3.3/5.8 GHz band WiMAX networks in comparison to the microstrip patch without the stacked cell.

Secondly, the effect of DC load connections on the resonance response of the antenna was investigated by measuring the  $S_{11}$  patterns with and without the DC load connections. The measured  $S_{11}$  patterns are demonstrated in Fig. 6.23.

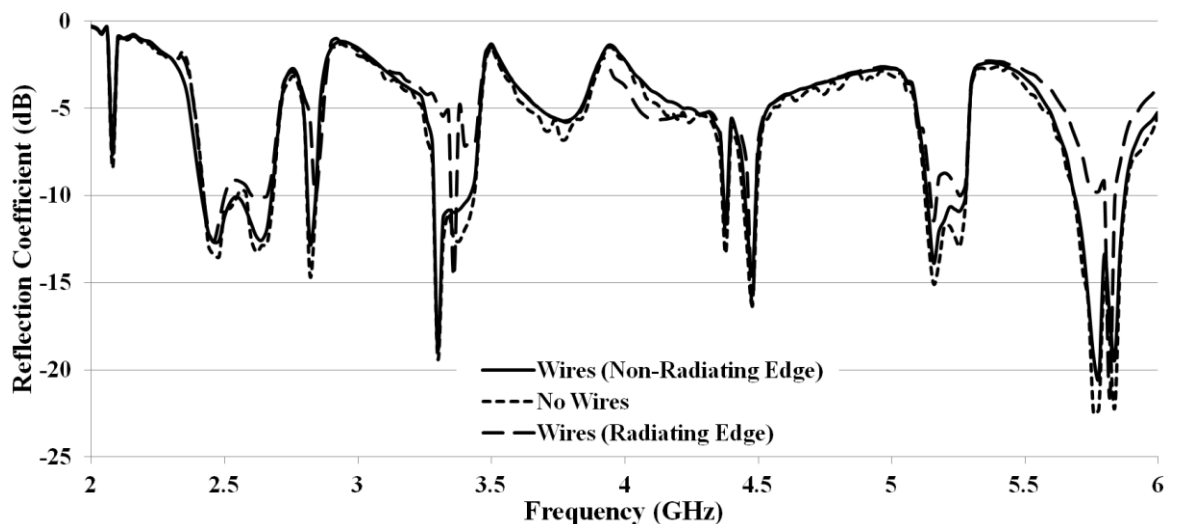


Fig. 6.23: Measured  $S_{11}$  patterns with and without DC wires connected to the terminals of the stacked poly-Si solar cell.

In Fig. 6.23, the difference between the  $S_{11}$  responses of the solar patch antenna with and without the DC connections is negligible when the DC load,  $220\Omega$ , is connected to the terminals of the stacked cell at the non-radiating edge, similar to the results demonstrated in the previous sections. Connecting the DC load to the terminals of the cell at the radiating edge, however, seriously degrades the  $S_{11}$  response of the antenna, especially at 3.3 GHz and 5.8 GHz resonance bands where the -10 dB impedance bandwidth is narrower by 75% and 40%, respectively, in comparison to the proposed non-radiating edge DC load connected design. This is due to the surface current across the rear contact of the stacked cell, which is induced by the slot loaded modified patch, to continue to flow through the DC load connections at the radiating edge, resulting in them being a part of the RF operation.

### 6.5.2.3 Solar Performance

Different from the solar antennas demonstrated until now, for the measurement of the solar performance of this solar patch antenna, a commercial solar simulator, Abet Sun 2000 [174], which was described in chapter 3, was used. The lack of the temperature control in the solar simulator made it not possible to measure the I-V curve at room temperature, all data were measured at  $32 \pm 3$  °C. Open-circuit voltage and short-circuit current were obtained as  $V_{OC}=0.57$  V and  $I_{SC}=463.8$  mA, respectively. The voltage and current at the maximum power point were measured as  $V_{MP}=0.46$  V and  $I_{MP}=379.2$  mA, resulting in a DC power output of  $P_{MP}=174.4$  mW. Considering the input illumination intensity of  $P_{in}=1.42$  W, which is determined by the total simulator solar illumination intensity of 1000 multiplied by the cell surface area, 33 mm x 43 mm, the solar efficiency was calculated as  $\eta=12.3\%$  calculated using equation (3.13).

## 6.6 Solar Cell Stacked Dual-Polarised Patch Antenna for 5.8 GHz band WiMAX Network

The photovoltaic antennas studied until now have linear polarisation and are not suitable for polarisation diversity applications. In a practical communication environment, due to the presence of various elements, the signal between the transmitter and receiver in the uplink and downlink undergoes diffraction, reflection and scattering during the propagation. This results in the signal in a communication link being received as a combination of different polarisations. Therefore, in a practical communication

environment, polarisation diversity, which is the transmitting of information on orthogonal polarisations, is an important factor to be considered in order to achieve communication between the transmitter and receiver. In view of this, whilst some work exists on the photovoltaic integration of circularly-polarised antennas [44, 53], no work has been performed on dual-polarised solar antennas in the literature. In addition to offering polarisation diversity, dual-polarisation antennas address the multipath fading problem and are capable of providing double transmission channels for frequency reuse communication systems [178].

In this section, the integration of a slant  $\pm 45^\circ$  dual-polarised microstrip patch antenna stacked with a poly-Si solar cell operating as an RF parasitic patch element is demonstrated. Due to the dual-polarised operation, a DC/RF isolation circuit, which was originally demonstrated in section 5.3, is used to connect the DC load to the stacked poly-Si solar cell.

### 6.6.1 Dual-Polarized Solar Patch Design

The proposed dual-polarized microstrip patch antenna stacked with a poly-Si solar cell is demonstrated in Fig. 6.24.

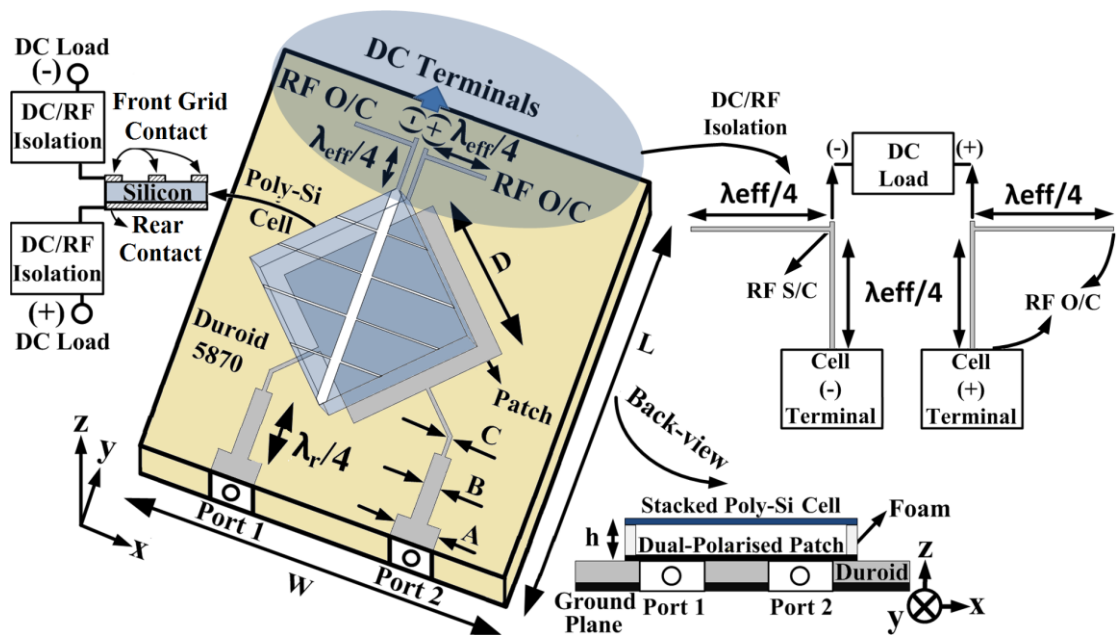


Fig. 6.24: Dual-polarised microstrip patch antenna stacked with a poly-Si solar cell with a DC/RF isolation circuit (Dimensions in mm:  $A=4.25$ ,  $B=1.64$ ,  $C=0.37$ ,  $D=15.2$ ,  $W=60$ ,  $L=62$ ,  $h=2$ ).

The square patch was printed upon a 1.5 mm thick low-loss RT/Duroid 5870 substrate,  $\epsilon_r=2.33$  and  $\tan\delta=0.0012$ , with a ground plane on the backside. The patch is fed through two microstrip transmission lines each consisting of a quarter-wavelength,  $\lambda_r/4$ , sub-transmission line matching the impedance at the patch edge, which was obtained as  $150\Omega$  in CST Microwave Studio, to the impedance of the input port,  $50\Omega$ . While port 1 is used for  $+45^\circ$  polarisation excitation of the patch, port 2 provides  $-45^\circ$  polarisation excitation. As illustrated in Fig. 6.24, the microstrip patch is stacked with a poly-Si solar cell, which is suspended at 2 mm above the printed patch. As can be seen in Fig. 6.24, the stacked poly-Si solar cell consists of two metal DC contacts, a front grid (negative terminal) and a rear solid (positive terminal), together with a silicon layer in between. If attention is given to the rear contact of the cell, it can be seen that it is homogeneous in structure and therefore has the potential to be used as a metal plate to be suspended above the microstrip patch to operate as an RF stacked parasitic patch element. However, a significant factor to be taken into account in this design is that the stacked solar cell is required to be terminated in a DC load whose effect on the RF antenna response must be minimised for optimum antenna performance. This cannot be achieved by simply connecting the DC load to the terminals of the stacked poly-Si solar cell at the non-radiating edges. This is due to the fact that for fundamental propagation modes,  $TM_{10}$  for  $+45^\circ$  polarisation and  $TM_{01}$  for  $-45^\circ$  polarisation, all edges are responsible for the RF radiation as the proposed dual-polarised solar patch antenna has two radiating edges for  $+45^\circ$  polarised excitation and the other two for  $-45^\circ$  polarised excitation. Therefore, in order to minimise the effect of the solar operation on the RF antenna response, a DC/RF isolation circuit connected to the negative and positive terminals of the stacked poly-Si solar cell is used as illustrated in Fig. 6.24.

The isolation circuit consists of two quarter-wavelength,  $\lambda_{eff}/4$ , microstrip transmission lines whose lengths are determined by the effective dielectric constant,  $\epsilon_{reff}$ , due to the suspended geometry of the stacked poly-Si solar cell resulting in  $\epsilon_{reff}=1.57$ . As illustrated in Fig. 6.24, theoretically, at the resonance frequency of 5.8 GHz, the open-ended transmission line in the x-axis produces an RF short-circuit at the other end, which is then converted to an RF open-circuit at the connection point to the stacked solar cell whilst a DC short-circuit line is maintained in order for the poly-Si solar cell generated DC current to flow to the DC load.

## 6.6.2 Simulation and Measurement Results

The S-parameters of the proposed dual-polarised solar patch antenna were measured using a VNA, Agilent E8364B, and are demonstrated in Fig. 6.25.

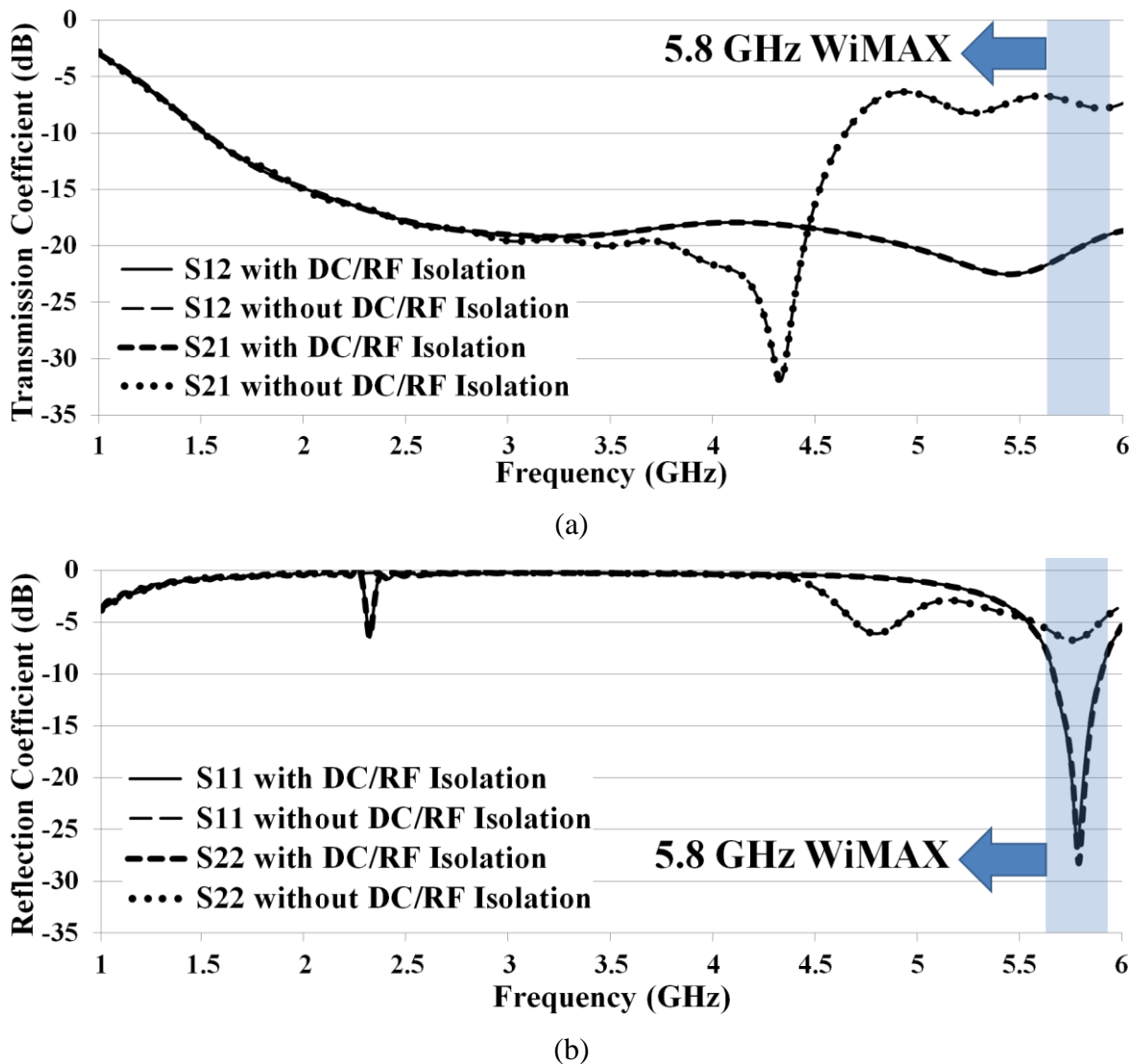


Fig. 6.25: Measured S-parameters of the dual-polarised solar patch antenna (a) transmission coefficient ( $S_{12}$  and  $S_{21}$ ) (b) reflection coefficient ( $S_{11}$  and  $S_{22}$ ).

As illustrated in Fig. 6.25(a), there is a considerable difference between the transmission coefficient responses when the antenna does and does not include the proposed DC/RF isolation circuit attached to the terminals of the stacked poly-Si solar cell. Whilst the solar patch with the DC/RF isolation circuit offers an isolation of -20 dB between the input ports at 5.8 GHz, in the absence of the DC/RF isolation circuit, the transmission coefficient level is almost -5 dB suggesting a poor isolation between the input ports. If attention is given to

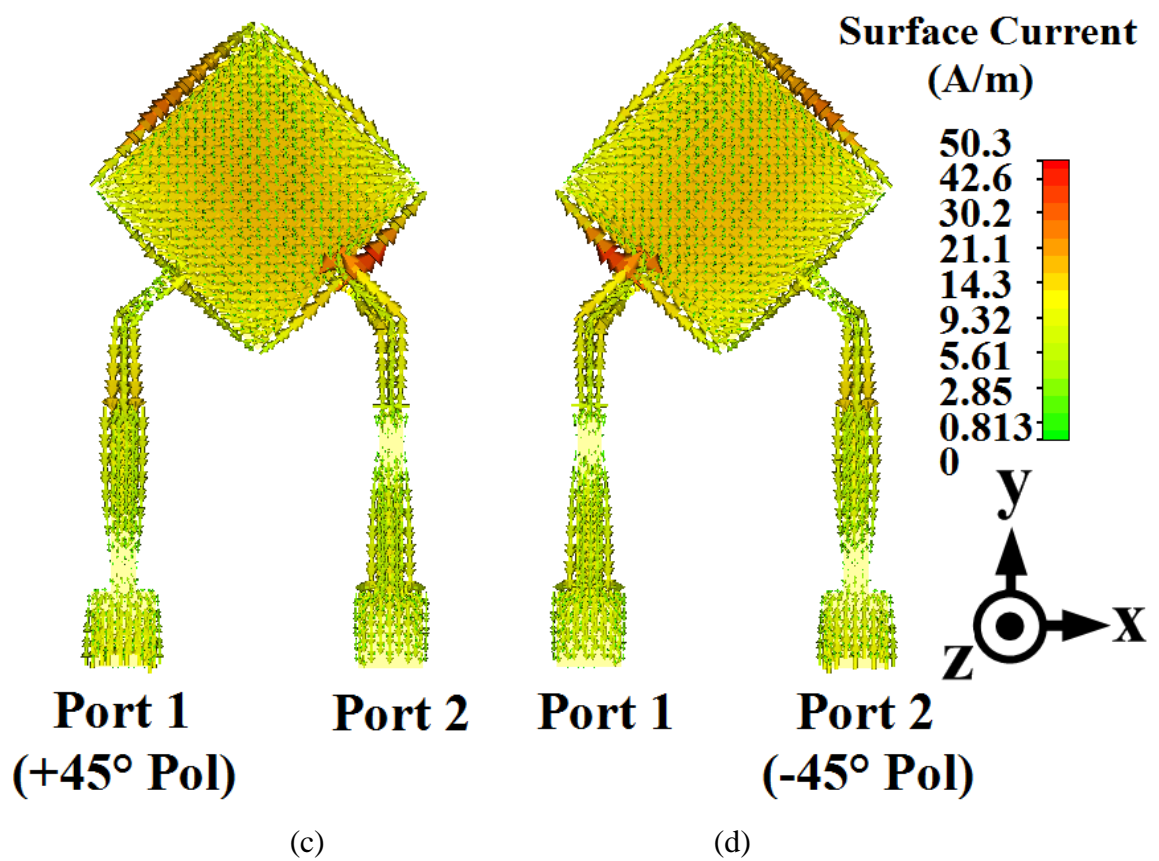
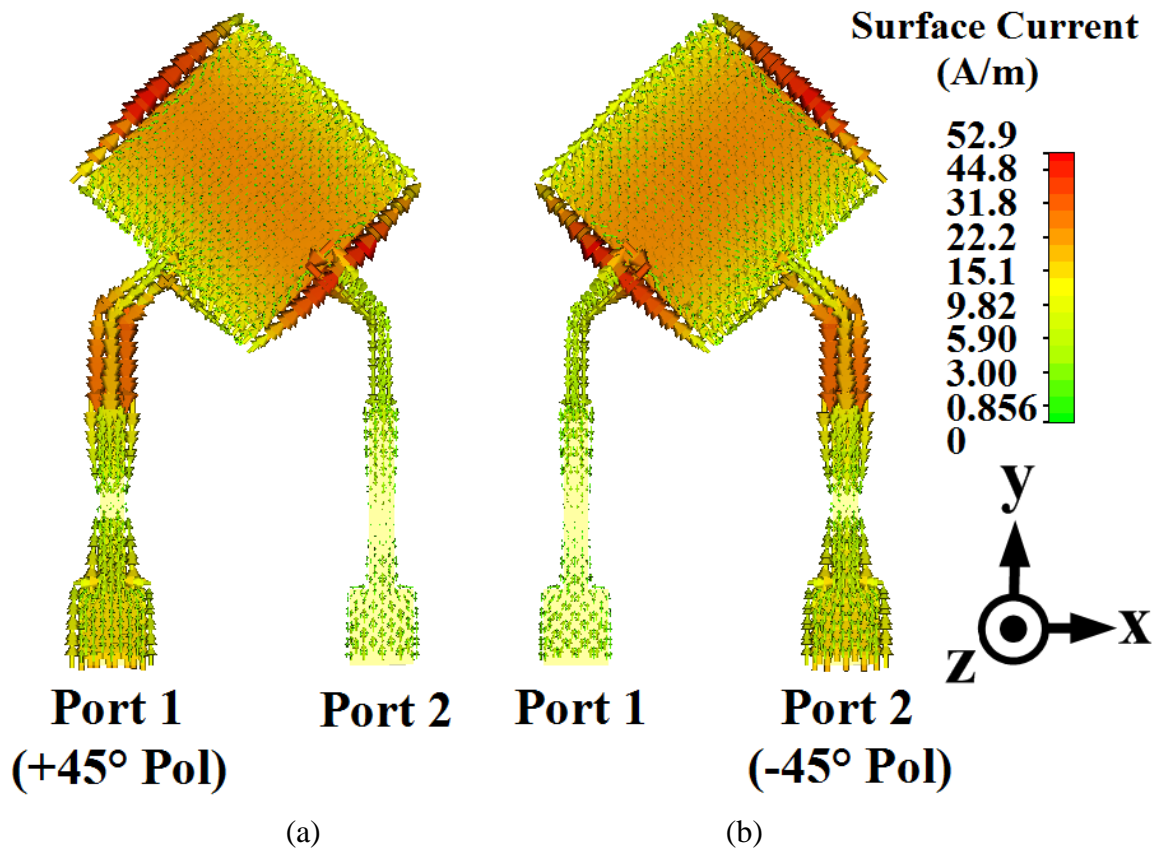
Fig. 6.25(b), it can be seen that the solar patch with the DC/RF isolation circuit operates across a measured -10 dB impedance band of 5.66-5.91 GHz whilst the absence of the isolation circuit results in a significant deterioration in the resonance response of the antenna with a reflection coefficient level of above -10 dB across the entire measured frequency band. From the S-parameter results demonstrated in Fig. 6.25, it is obvious that the proposed DC/RF isolation circuit has a significant importance to obtain an optimum RF response from the proposed dual-polarised solar patch antenna. In order to provide a better understanding of the reason behind the deterioration in the S-parameter response of the antenna in the absence of the DC/RF isolation circuit, the surface current distributions of:

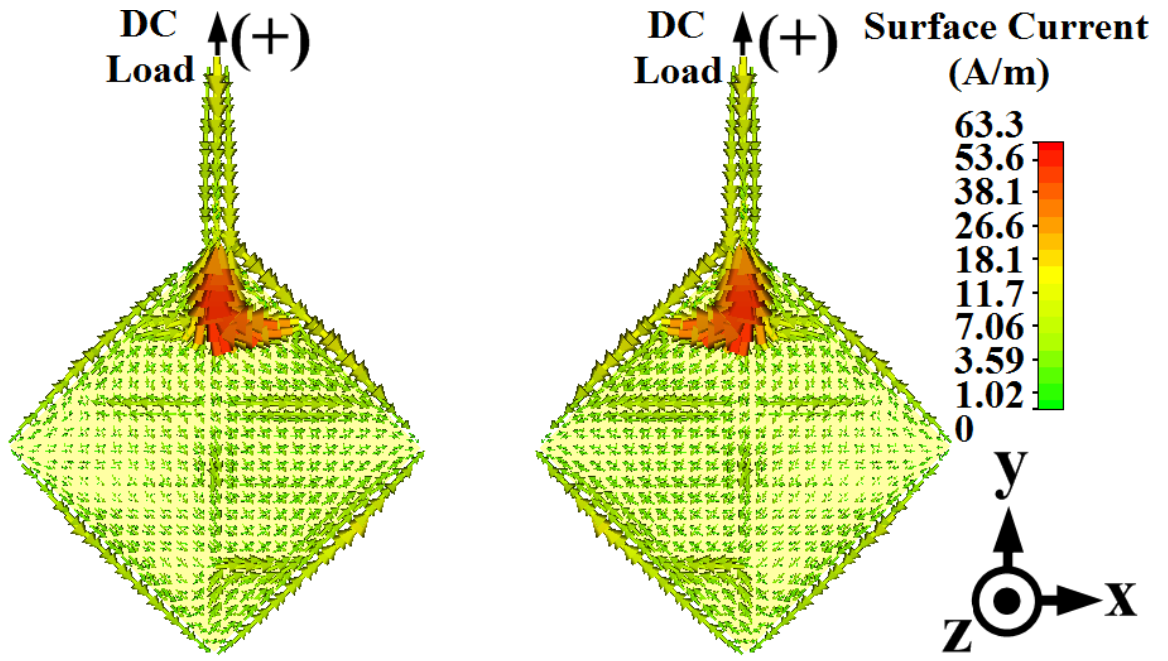
- Dual-fed microstrip patch,
- The rear DC contact of the stacked poly-Si solar cell,
- The front grid DC contact of the stacked poly-Si solar cell,

need to be investigated with and without the DC/RF isolation circuit. To this end, the surface current distributions of the elements given above were investigated:

- When the stacked poly-Si solar cell was terminated in a DC load,  $220\Omega$ , which was connected through the proposed DC/RF isolation circuit,
- When the stacked poly-Si solar cell was terminated in a DC load,  $220\Omega$ , which was connected without the DC/RF isolation circuit.

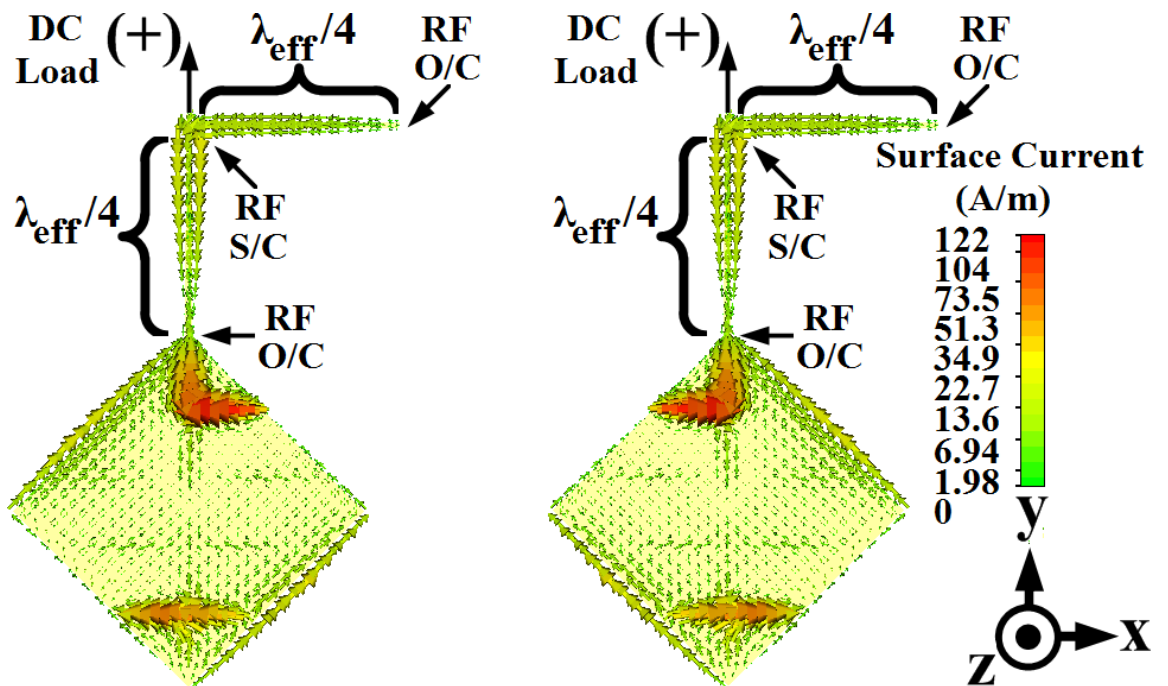
The obtained results are demonstrated in Fig. 6.26.





(e)

(f)



(g)

(h)

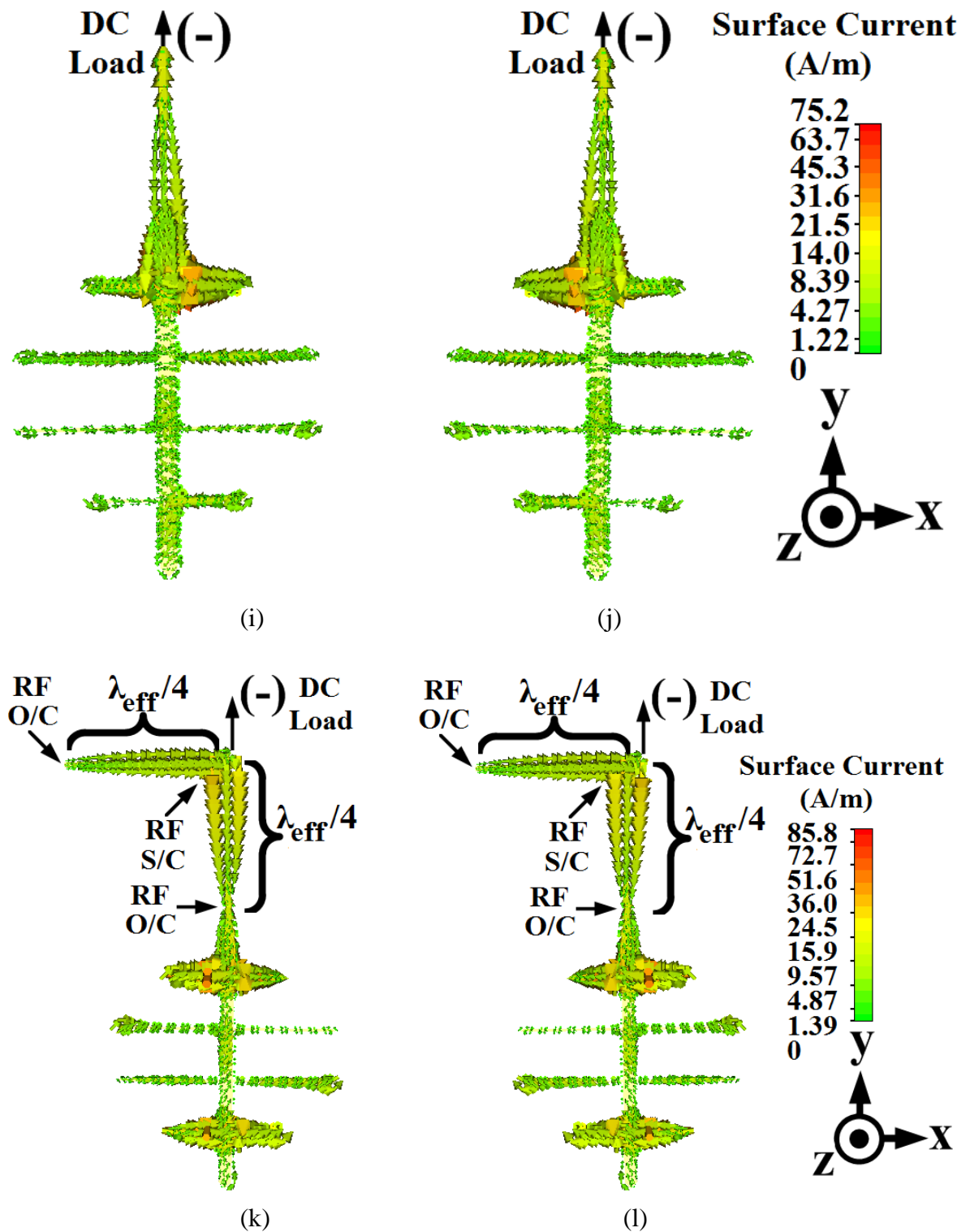
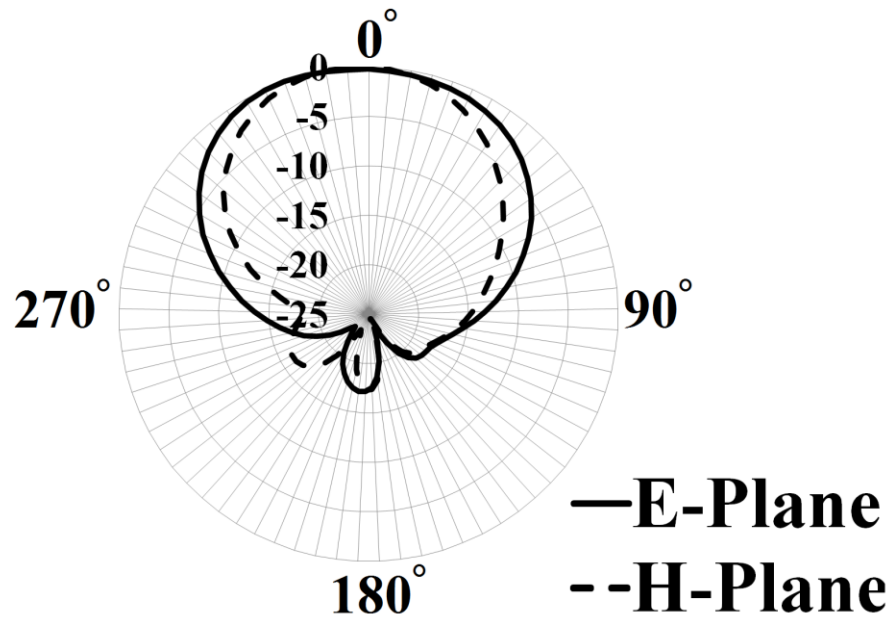


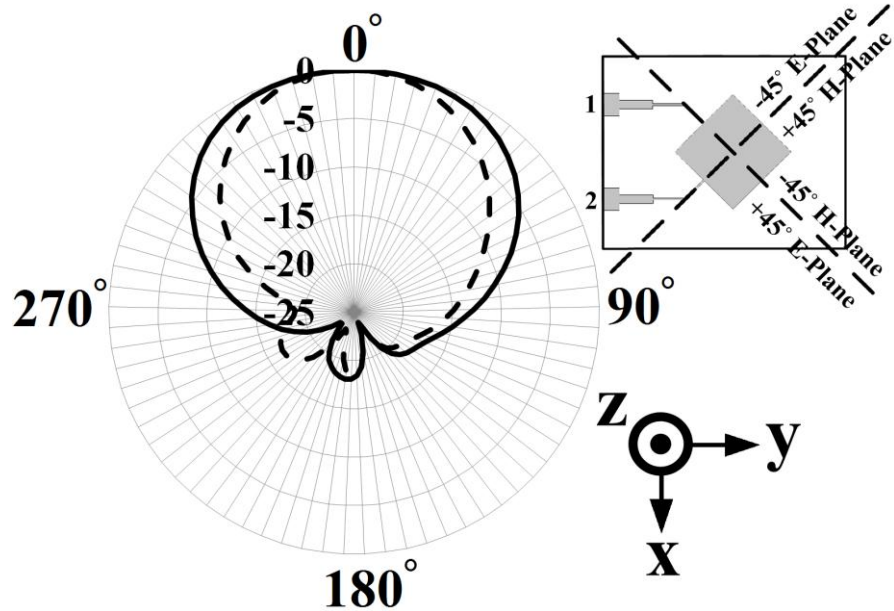
Fig. 6.26: Simulated surface current distributions (a, b) patch together with feed lines for  $+45^\circ$  and  $-45^\circ$  (with DC/RF isolation); (c, d) patch together with feed lines for  $+45^\circ$  and  $-45^\circ$  (no DC/RF isolation); (e, f) solar cell rear contact for  $+45^\circ$  and  $-45^\circ$  (no DC/RF isolation); (g, h) solar cell rear contact for  $+45^\circ$  and  $-45^\circ$  (with DC/RF isolation); (i, j) solar cell front grid for  $+45^\circ$  and  $-45^\circ$  (no DC/RF isolation); (k, l) solar cell front grid for  $+45^\circ$  and  $-45^\circ$  (with DC/RF isolation).

As can be seen in Fig. 6.26(a)-(d), the surface current distribution across the dual-fed microstrip patch changes dramatically in the absence of the proposed DC/RF isolation circuit. As the microstrip patch induces current across the surface of the rear DC contact of the stacked poly-Si solar cell, it is also expected to observe such a significant change in the current distribution across the rear cell surface when the DC/RF isolation circuit is not present. Current distributions given in Fig. 6.26(e)-(h) confirm this observation. If attention is given to Fig. 6.26(e) and Fig. 6.26(f), it can be seen that the induced RF surface current across the rear DC contact of the stacked cell continues to flow through the positive DC terminal connection of the load, making it a part of the RF operation. This results in a significant deterioration in the RF response of the proposed antenna. However, it can be seen in Fig. 6.26(g) and Fig. 6.26(h) that at the connection point to the stacked poly-Si solar cell, the proposed DC/RF isolation circuit chokes the RF current preventing the DC load and its conductive positive DC terminal connection from becoming a part of the RF operation whilst maintaining a DC path for the cell generated current. Fig 6.26(i)-(l) demonstrate the current distribution across the top grid of the stacked solar cell without and with the DC/RF isolation circuit. Similarly, whilst the negative DC terminal connection of the load attached to the front grid of the cell becomes a part of the RF operation in the absence of the DC/RF isolation circuit, it is RF isolated when the isolation circuit is introduced.

E-plane and H-plane far-field radiation patterns of the proposed solar antenna were measured for  $+45^\circ$  polarisation excited through the first port and  $-45^\circ$  polarisation excited through the second port, respectively. Similar to the far-field radiation pattern measurements of the solar antennas demonstrated until now, the E-plane and H-plane far-field radiation pattern measurements of the proposed dual-polarised solar patch antenna were carried out in an anechoic chamber with a signal generator power level of  $P_G=14$  dBm. For the measurements, the conical spiral antenna with a gain of 4 dBi was used as a reference antenna. The obtained E-plane and H-plane far-field radiation patterns are shown in Fig. 6.27.



(a)



(b)

Fig. 6.27: Measured E-plane and H-plane far-field radiation patterns (a) antenna fed through port 1 (+45° polarisation) (b) antenna fed through port 2 (-45° polarisation).

The antenna has a measured maximum gain of 7.6 dBi. As can be seen in Fig. 6.27, the E-plane and H-plane far-field radiation patterns obtained for +45° polarisation are very similar to the E-plane and H-plane far-field radiation patterns observed for -45° polarisation. This confirms the RF symmetry of the antenna for  $\pm 45^\circ$  polarisations despite the overall asymmetry introduced by the negative and positive DC load terminal connections. This was achieved by successfully isolating the DC terminal connections of

the stacked poly-Si solar cell from the RF response of the antenna by providing a high RF impedance at the cell terminals whilst maintaining DC short-circuit path for the cell generated DC current.

## 6.7 Beam Steering Solar Cell Stacked Dual-Polarised Microstrip Patch Array Antenna

From a photovoltaic perspective, optimum conditions for a given solar antenna occur when the solar antenna is directed towards the Sun at an optimal angle. This results in an ideal illumination intensity incident upon the solar cell within the antenna, which is required to obtain an optimum amount of generated DC power output. However, for the solar antennas studied until now, no discrimination has been made between the direction of the Sun and the direction of the target to be communicated with. For practical applications, however, these two directions are independent from each other and need to be dealt with separately. Whilst it is required for a solar antenna to be positioned in an optimum direction towards the Sun to achieve an optimal solar efficiency, from an RF perspective, the main lobe of the antenna should cover the target to be communicated with in order to achieve communication as demonstrated in Fig. 6.28.

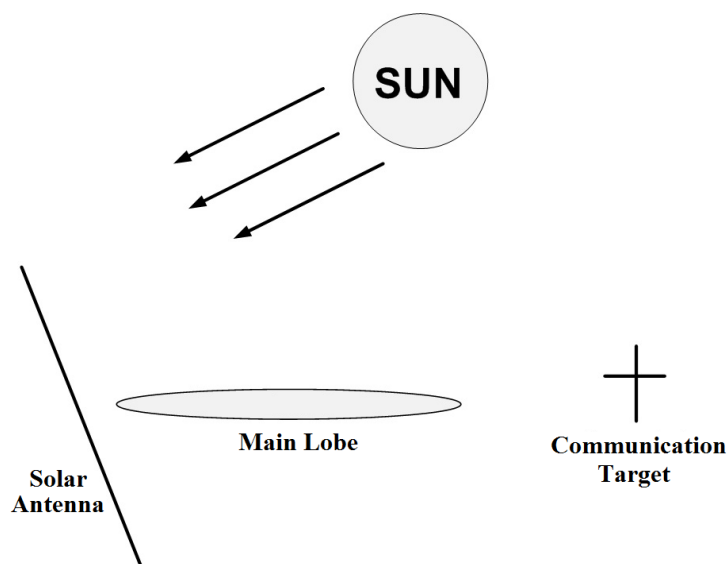


Fig. 6.28: A communication target positioned differently from the direction of the Sun.

This brings the challenge that the main lobe of the solar antenna needs to be directed towards the communication target without physically rotating the solar antenna. This challenge can be overcome by using a phase shift solar array antenna capable of electronically steering the beam in the direction of the communication target without

mechanically rotating the antenna. In view of this, in this section, the array version of the dual-polarised solar patch antenna demonstrated in the previous section is proposed for beam steering 5.8 GHz band WiMAX base stations for the first time in the literature.

## 6.7.1 Solar Array Antenna Design

The dual-polarised solar patch array antenna stacked with an array of suspended poly-Si solar cells is demonstrated in Fig. 6.29.

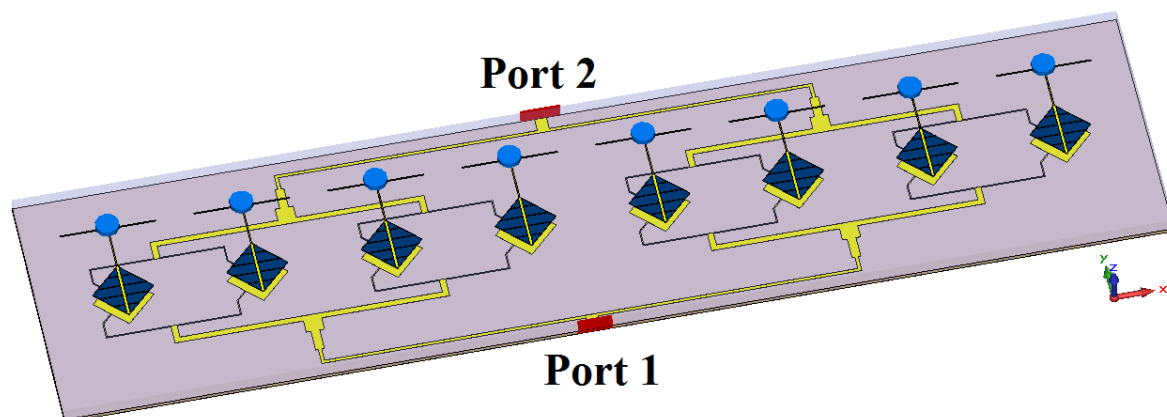


Fig. 6.29: Slant  $\pm 45^\circ$  dual-polarised microstrip patch array antenna stacked with an array of poly-Si solar cell.

As can be seen in Fig. 6.29, the array consists of eight dual-fed microstrip patches, each stacked with a poly-Si solar cell as illustrated in Fig. 6.30 in detail.

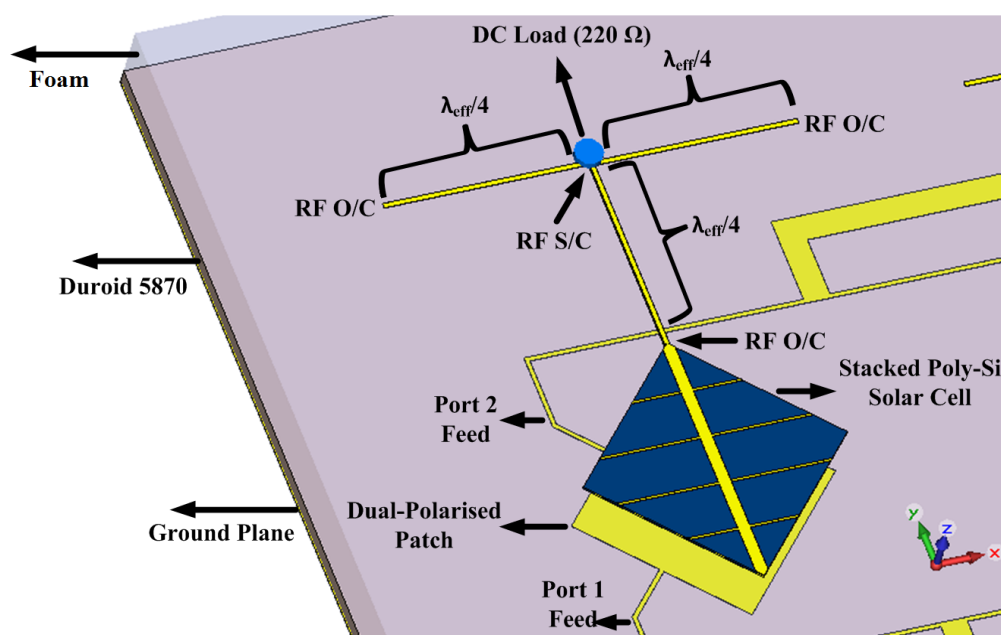


Fig. 6.30: A dual-polarised microstrip patch stacked with a poly-Si solar cell within the array.

As illustrated in Fig. 6.30, in order to achieve the suspension of the poly-Si solar cells, a sheet of expanded polystyrene foam,  $\epsilon_r=1.03$ , is placed between the microstrip patches and the stacked solar cells. As all edges contribute to the radiation in the far-field due to the dual-polarised operation, the DC load connections were introduced through a DC/RF isolation circuit as described in the previous section and can be seen in Fig. 6.30.

## 6.7.2 Simulation Results

The reflection coefficient simulations ( $S_{11}$  for port 1 and  $S_{22}$  for port 2) of the proposed solar array antenna were performed in CST Microwave Studio and are demonstrated in Fig. 6.31.

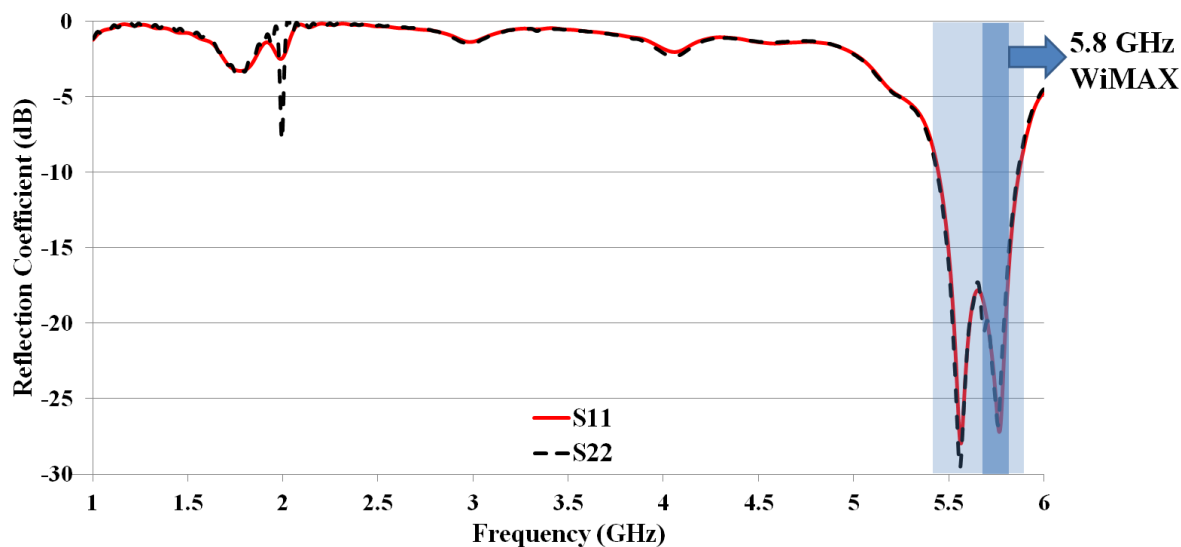


Fig. 6.31: Simulated  $S_{11}$  ( $+45^\circ$  polarisation, fed through port 1) and  $S_{22}$  ( $-45^\circ$  polarisation fed through port 2) patterns.

As demonstrated in Fig. 6.31, the solar patch array antenna offers identical reflection coefficient patterns when it is fed through port 1 ( $TM_{10}$  operation) and port 2 ( $TM_{01}$  operation). The solar patch array antenna operates across the frequency band of 5.42-5.9 GHz with a -10 dB impedance bandwidth of 480 MHz, fully covering 5.8 GHz band WiMAX network (5.725-5.825 GHz).

The simulated elevation (x-z) and azimuth (y-z) far-field radiation patterns of the proposed solar array antenna with no beam steering is applied are demonstrated in Fig. 6.32.

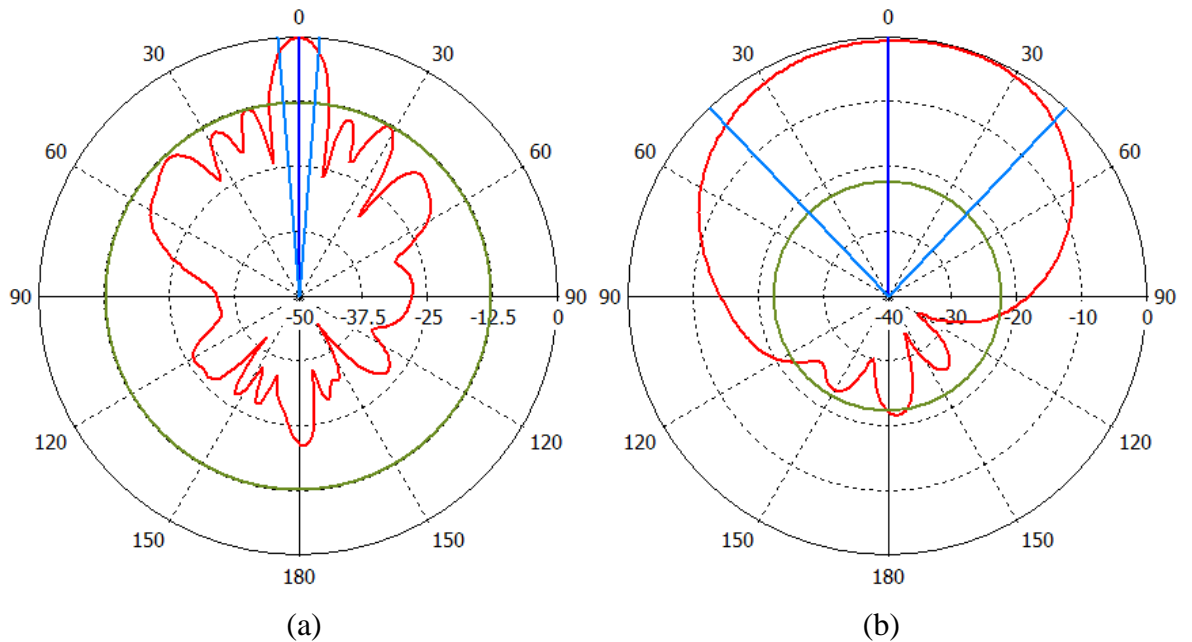


Fig. 6.32: Simulated far-field radiation patterns of the solar array antenna when no beam steering is applied (a) elevation (x-z) (b) azimuth (y-z).

As no beam steering is applied, in Fig. 6.32, the solar patch array antenna has broadside radiation patterns. For commercial WiMAX base station antennas, typical -3 dB azimuth and elevation beamwidths can be given as follows [179, 180]:

- 60° sector beamwidth:
  - -3 dB azimuth beamwidth:  $60^{\circ}$ - $62.5^{\circ}$
  - -3 dB elevation beamwidth:  $6.5^{\circ}$ - $7^{\circ}$
  - Gain: 17 dBi - 17.5 dBi
- 90° sector beamwidth:
  - -3 dB azimuth beamwidth:  $90^{\circ}$
  - -3 dB elevation beamwidth:  $6.5^{\circ}$ - $7^{\circ}$
  - Gain: 16.6 dBi – 17 dBi
- 120° sector beamwidth:
  - -3 dB azimuth beamwidth:  $120^{\circ}$
  - -3 dB elevation beamwidth:  $6.5^{\circ}$ - $7^{\circ}$
  - Gain: 15 dBi – 16 dBi

In Fig. 6.32, the -3 dB beamwidth of the solar patch array antenna was obtained as  $6.7^\circ$  in the elevation and  $88.7^\circ$  in the azimuth. This confirms the suitability of the proposed solar array to be employed in 5.8 GHz band  $90^\circ$  sector WiMAX base stations. As can be seen in Fig. 6.32(a), the sidelobe level of the antenna in the elevation plane is below -12.5 dB.

The simulated 3D far-field radiation pattern of the proposed solar array antenna is demonstrated in Fig. 6.33.

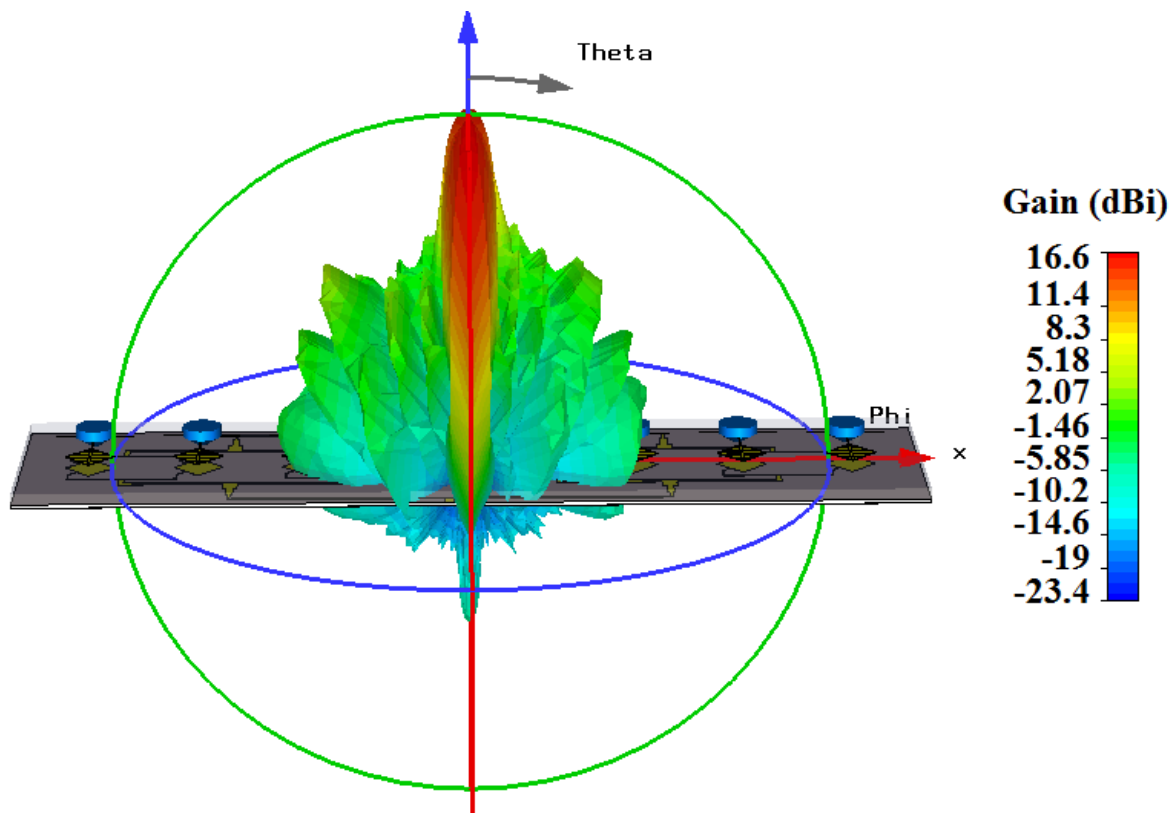


Fig. 6.33: Simulated 3D far-field radiation pattern of the solar array antenna when no beam steering is applied.

As illustrated in Fig. 6.33, the proposed solar patch array antenna has a maximum simulated gain of 16.6 dBi, which is in good agreement with typical gain values of commercial WiMAX base station antennas [179, 180]. As the proposed antenna is an eight-element array version of the single dual-polarised photovoltaic antenna with a measured maximum gain of 7.6 dBi demonstrated in section 6.6, the theoretical maximum gain that can be obtained from this array can be given as 16.63 dBi. Therefore, the simulated maximum gain of 16.6 dBi provides good agreement with this observation.

### 6.7.3 Beam Steering

The proposed microstrip solar patch array antenna consists of eight poly-Si solar cell stacked patch elements, all of which are placed linearly in the x-axis. As illustrated in Fig. 6.34, the spacing between the array elements was selected as 25.86 mm, which is a half-wavelength at 5.8 GHz.

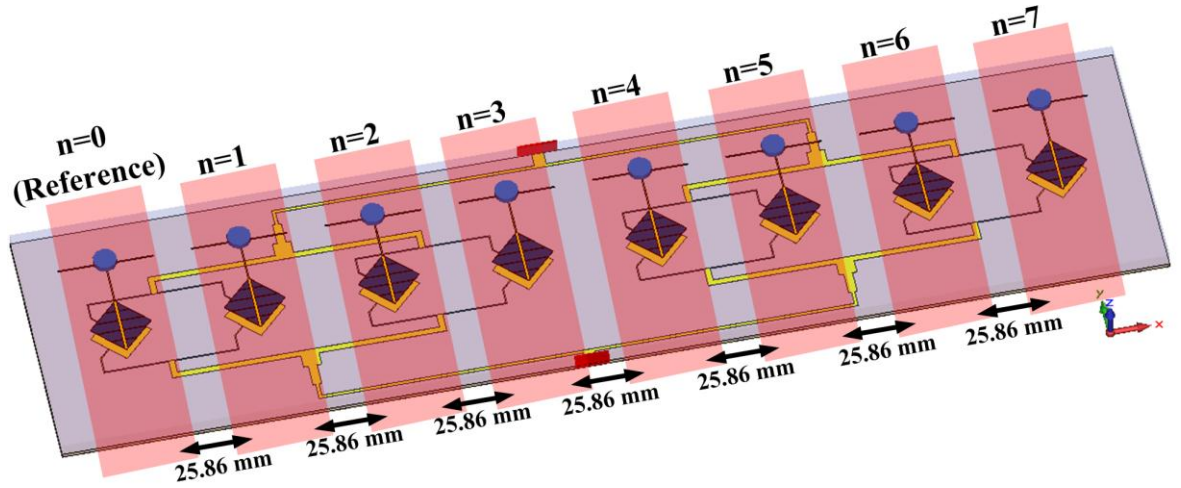


Fig. 6.34: Distance between array elements (no beam steering is applied).

Due to the separation of the array elements in the x-axis, the phase difference between the array elements in comparison to the reference element, which is element  $n = 0$  in Fig. 6.34, can be given as follows:

$$e^{jk_x dn}, \quad n = 0, 1, \dots, 7 \quad (6.2)$$

Where  $n$  is the number of the each patch within the array and  $n = 0$  indicates the reference patch highlighted in Fig. 6.34 while  $k_x$  is given by,

$$k_x = k \sin \theta \cos \phi \quad (6.3)$$

Due to the linear placement of the array elements in the x-axis,  $\phi$  in equation (6.3) is equal to  $0^\circ$  resulting in a phase difference between the array elements given as

$$e^{jkdnsin\theta}, \quad n = 0, 1, \dots, 7 \quad (6.4)$$

From equation (6.4), the array factor (AF) can be given as

$$AF = \sum_n a_n e^{jkdnsin\theta}, \quad n = 0, 1, \dots, 7 \quad (6.5)$$

In equation (6.5),  $a_n$  is the relative feed coefficient, which is unity due to the fact that no special weighting technique was applied in the proposed array design and therefore all feeding amplitudes of the patch elements within the array are equal. In order for the main lobe to be steered towards a desired angle,  $\theta_d$ , an external phase difference needs to be introduced for each element in the array to maximise the array factor at the desired steering angle.

For the sake of simplicity, if a new term,  $\psi$ , is introduced to represent the natural phase difference between the array elements,

$$\psi = kdn \sin \theta_d, \quad n = 0, 1, \dots, 7 \quad (6.6)$$

Then the array factor in equation (6.5) can be given as

$$AF = \sum_n a_n e^{j\psi}, \quad n = 0, 1, \dots, 7 \quad (6.7)$$

If  $\psi_n$  represents the external phase difference applied to each array element in order to maximise the array factor,

$$AF = \sum_n a_n e^{j(\psi - \psi_n)}, \quad n = 0, 1, \dots, 7 \quad (6.8)$$

Therefore, in equation (6.8), the array factor reaches its maximum when,

$$\psi = \psi_n \quad (6.9)$$

From equation (6.9), the external phase difference for each element can be determined as,

$$\psi_n = -kdn \sin \theta_d, \quad n = 0, 1, \dots, 7 \quad (6.10)$$

In order to achieve the external phase difference given in equation (6.10), depending upon the number of the array elements,  $n$ , the length of the microstrip feeding line needs to be increased by,

$$\Delta L_n = \frac{kdn\lambda \sin \theta_d}{2\pi}, \quad n = 0, 1, \dots, 7 \quad (6.11)$$

In a simpler form, equation (6.11) can be written as follows,

$$\Delta L_n = dn \sin \theta_d, \quad n = 0, 1, \dots, 7 \quad (6.12)$$

Equation (6.12) suggests that the external phase difference can be achieved by adjusting the length of the microstrip transmission lines feeding the patch elements within the array as demonstrated in Fig. 6.35.

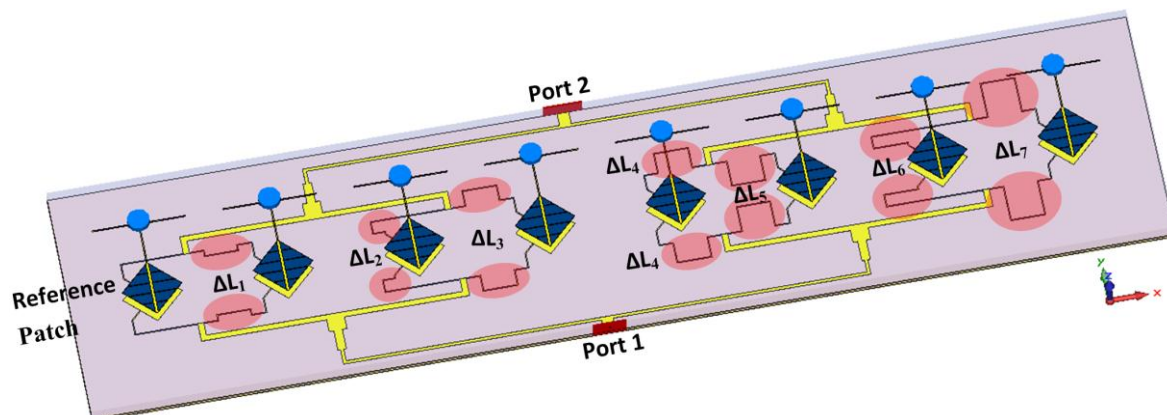


Fig. 6.35: Slant  $\pm 45^\circ$  dual-polarised microstrip patch array antenna with an external phase shift applied to each array element in order to steer the main lobe by  $10^\circ$  (phase shifters are highlighted).

In Fig. 6.35, the variation of the lengths of the microstrip transmission lines feeding the microstrip patches within the array can clearly be seen. The solar array demonstrated in Fig. 6.35 was designed to steer the main lobe of the antenna by  $10^\circ$  in the elevation plane (x-z). For applications where a dynamic electronic beam steering is required, phase shift modules introducing adjustable physical delay lines can be used [181]. The phase difference between the array elements, the external phase difference to maximise the array factor at  $10^\circ$  and the lengths of the transmission lines to achieve the external phase difference are given in Table 6.9.

Table 6.9: Beam steering parameters for the array elements.

Array Element Number ( $n$ )	Natural Phase Difference for $10^\circ$ Beam Steering ( $\psi = kdn \sin(10^\circ)$ )	External Phase Difference for $10^\circ$ Beam Steering ( $\psi_n = -kdn \sin(10^\circ)$ )	Increase in the Length of the Microstrip Feed Line ( $\Delta L_n = dn \sin(10^\circ)$ )
Reference ( $n = 0$ )	0	0	0
First Patch ( $n = 1$ )	$0.173\pi$	$-0.173\pi$	$0.0865\lambda$
Second Patch ( $n = 2$ )	$0.346\pi$	$-0.346\pi$	$0.173\lambda$
Third Patch ( $n = 3$ )	$0.519\pi$	$-0.519\pi$	$0.26\lambda$
Fourth Patch ( $n = 4$ )	$0.692\pi$	$-0.692\pi$	$0.346\lambda$
Fifth Patch ( $n = 5$ )	$0.865\pi$	$-0.865\pi$	$0.432\lambda$
Sixth Patch ( $n = 6$ )	$1.038\pi$	$-1.038\pi$	$0.519\lambda$
Seventh Patch ( $n = 7$ )	$1.211\pi$	$-1.211\pi$	$0.605\lambda$

The simulated elevation (x-z) and azimuth (y-z) far-field radiation patterns of the proposed solar array antenna when  $10^\circ$  beam steering is applied are demonstrated in Fig. 6.36.

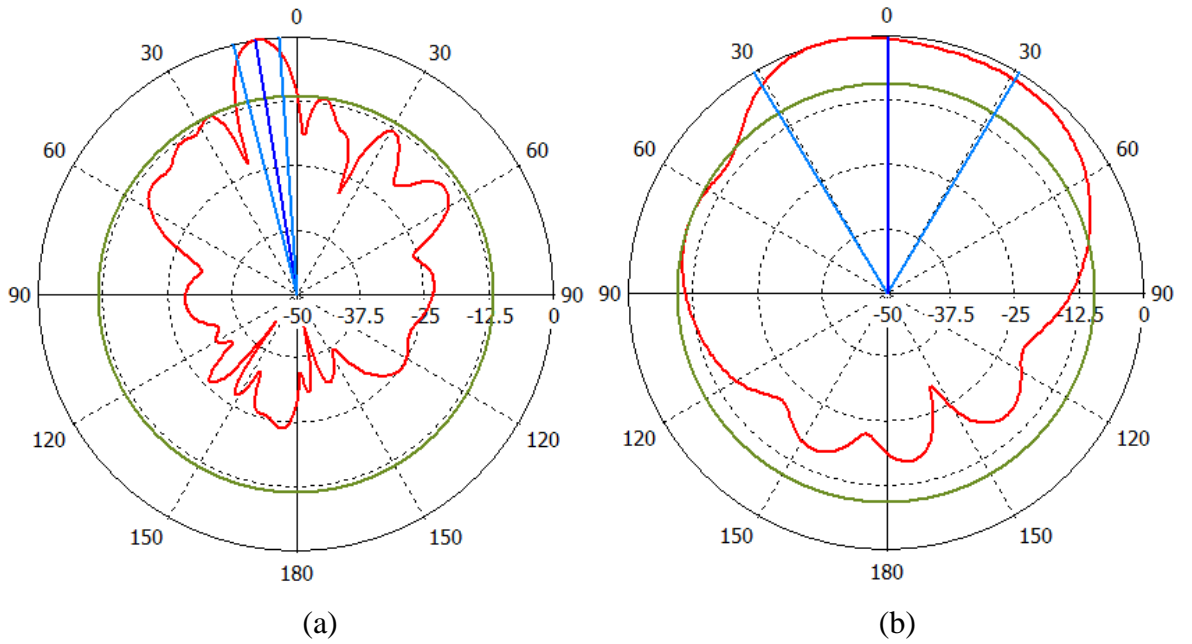


Fig. 6.36: Simulated far-field radiation patterns of the solar patch array antenna when  $10^\circ$  beam steering is applied in the elevation plane (x-z plane) (a) elevation (b) azimuth.

In Fig. 6.36, the effect of the beam steering applied along the elevation plane (x-z plane) is evident as the main lobe is not in the broadside direction but steered by  $10^\circ$ . The sidelobe level of the beam steered solar patch array remains below  $-12.5$  dB.

The simulated 3D far-field radiation pattern of the proposed solar patch array antenna with  $10^\circ$  beam steering is demonstrated in Fig. 6.37.

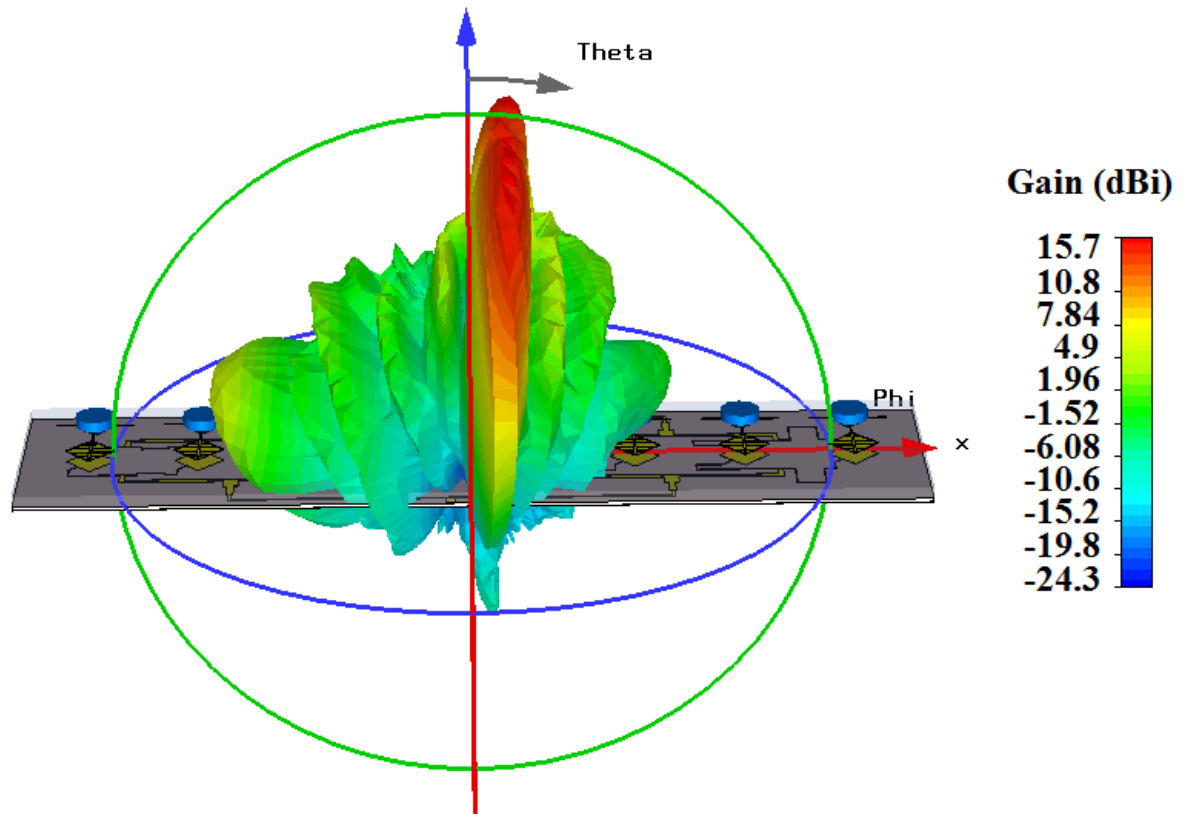


Fig. 6.37: Simulated 3D far-field radiation pattern of the solar array antenna when  $10^\circ$  beam steering is applied.

As can be seen in Fig. 6.37, the main lobe of the solar patch array antenna is steered by  $10^\circ$  in the elevation plane with a simulated maximum gain of 15.7 dBi, which is 0.9 dB less in comparison to the solar patch array antenna with no beam steering is applied.

## 6.8 Summary

In this chapter, a new stacked solar antenna integration topology was proposed as a promising alternative to the existing solar antenna integration topologies given as:

- Chapter 4 – RF ground plane solar antenna integration topology,
- Chapter 5 – RF radiating element solar antenna integration topology.

Moreover, for the first time in the literature, the integration of PIFAs with solar cells was carried out. In addition, novel study was performed on a dual-polarised microstrip solar patch antenna, which successfully addresses the challenge of using solar antennas for polarisation diverse communication systems. The novel array of the dual-polarised microstrip photovoltaic patch antenna was also demonstrated for applications where electronic beam steering is required.

It was demonstrated that:

- The proposed new RF stacked solar antenna integration topology successfully addresses the disadvantages of the existing solar antenna integration topologies, which can be given as:
  - RF ground plane solar antenna integration topology: As demonstrated in chapter 4, in this solar antenna integration topology, the solar cell operating as an RF ground plane is placed under an RF radiating element, which is opaque in structure. As a result of this, this solar antenna integration topology has the disadvantage of shading the integrated solar cell, i.e. the RF ground plane, and therefore significantly reducing the solar efficiency.
  - RF radiating element solar antenna integration topology: As demonstrated in chapter 5, in this solar antenna integration topology, the radiating element cannot be modified, such as capacitive slot loading, to achieve the excitation of multiple  $TM_{mn}$  propagation modes for multiband and wideband applications. This is due to the requirement for the solar cell, i.e. the RF radiating element, to be homogeneous in structure to achieve optimum solar performance.

The proposed suspended RF stacked solar antenna integration topology, which suggests the use of solar cells as an RF stacked parasitic patch element suspended above the RF radiating element, addresses these challenges by,

- Resulting in optimum solar operation performance by placing the solar cell above all other RF elements in a solar antenna design,
  - Enabling the modification of the RF radiating element due to the suspended geometry of the stacked solar cell.
- The proposed poly-Si solar cell stacked slant  $\pm 45^\circ$  dual-polarised microstrip solar patch antenna successfully addresses the requirement for WiMAX antennas to transmit information on orthogonal polarisations. Therefore, the demonstrated dual-polarised solar patch antenna has a significant potential to be employed in polarisation diverse WiMAX applications. It was demonstrated that, different from linearly-polarised solar antennas in which the DC connections can be introduced at the non-radiating edge, consideration must be given when it comes to introducing a

DC load in a dual-polarised solar antenna. This is due to the fact that for the dual polarised solar patch antenna demonstrated in this chapter, all edges contribute to the radiation (two edges for  $TM_{01}$  mode and the other two for  $TM_{10}$  mode) and therefore the DC load was connected to the terminals of the stacked poly-Si solar cell through a DC/RF isolation circuit. It was illustrated that the proposed DC/RF isolation circuit, which consists of quarter-wavelength microstrip transmission lines, successfully prevents the DC terminal connections from becoming a part of the RF operation ensuring the RF stability of the proposed dual-polarised solar patch antenna.

- For practical applications, whilst it is required for a solar antenna to be positioned in the direction of the sun at an optimal angle to achieve optimum solar performance, the target to be communicated with is located in a different position. This brings the challenge of being able to communicate with the communication target without physically rotating the solar antenna. This challenge was successfully addressed by designing an array of the proposed poly-Si solar cell stacked dual-polarised microstrip patch antenna for 5.8 GHz band WiMAX base stations. The designed photovoltaic array antenna is capable of steering the main lobe electronically in the direction of the communication target to provide an RF coverage whilst physically maintaining the position of the antenna.

# Chapter 7 - Conclusions and Future Work

## 7.1 Conclusions

In this research, the photovoltaic integration of microwave antennas has been demonstrated. In this framework, firstly, existing solar antenna integration topologies in the literature were analysed and classification of these topologies was performed as given below:

- Chapter 4 - The use of solar cells as an RF ground plane,
- Chapter 5 - The use of solar cells as an RF radiating element.

These integration topologies were investigated in detail and it was concluded that:

- RF ground plane solar antenna integration topology brings the shading problem from a photovoltaic perspective due to the alignment of the opaque RF radiating element, which is traditionally placed upon the ground plane, i.e. the solar cell, in a planar solar antenna.
  - A solution to this challenge was demonstrated in chapter 4 where meshing the RF radiating element and printing it on a transparent acrylic substrate was studied. It was demonstrated in chapter 4 that meshing the RF radiating element has the potential to offer an optical transparency of as high as 93.3% resulting in an observed enhancement of up to 42.5% in the solar efficiency in comparison to solar antennas in which conventional non-meshed optically opaque RF radiating elements are used. However, it should be noted that meshing the RF radiating element with a meshing line width of as small as 0.2 mm as demonstrated in chapter 4 requires special cutting equipment to be used, which increases the complexity and the cost of the antenna fabrication process.
- RF radiating element solar antenna integration topology ensures that the solar cells are placed above the antenna elements and therefore are not shaded by any RF components of the antenna. This results in optimum operation characteristics from a photovoltaic perspective. However, from an RF perspective, some well-known multiband/wideband techniques requiring the modification of the RF radiating element, such as loading the radiating element with capacitive slots to excite

multiple  $TM_{mn}$  modes, cannot be applied in this solar antenna integration topology. This is due to the requirement of ensuring the homogeneity of the solar cell structure to achieve optimum solar performance. This makes conventional microstrip patch antennas, which traditionally offer narrow -10 dB impedance bandwidths in the range of 3-5%, integrated with solar cells using the RF radiating element integration topology unsuitable to be employed in multiband and wideband applications, such as modern mobile, WLAN and WiMAX networks. Partial solutions to this challenge was demonstrated in chapter 5 by suspending the RF solar cell radiating element above the RF ground plane, which decreases the effective dielectric constant of the substrate and therefore increases the impedance bandwidth, and introducing a new cross-coaxial feed structure. Although impedance bandwidths of as high as 35% were achieved in chapter 5 as a result of this, the suspension technique has its own limits due to the potential of introducing surface waves reducing the radiation efficiency.

In order to provide a complete solution, a novel RF stacked solar antenna integration topology involving the use of solar cells as a stacked RF parasitic patch suspended above the RF radiating element was proposed in chapter 6. It was successfully demonstrated that the proposed stacked solar antenna integration topology has the potential to address the disadvantages of existing solar antenna integration topologies as given below:

- Suspension of the stacked solar cells above the RF radiating element enables the combined solar cells to operate without being shaded by any RF components of the antenna ensuring optimum solar performance.
- The suspended geometry of the stacked solar cells makes the modification of the RF radiating element underneath possible to achieve the excitation of multiple  $TM_{mn}$  propagation modes. This results in enhanced resonance characteristics for multiband and wideband mobile, WLAN and WiMAX networks as demonstrated in chapter 6.
- It was demonstrated in chapter 6 that in the proposed RF stacked solar antenna integration topology, the suspended stacked solar cells operate as a second RF radiating element contributing to the total radiation in the far-field and therefore enhancing the gain performance of the integrated antennas.

It is also for the first time in the literature that the integration of a PIFA with solar cells was performed. This brings the advantage for photovoltaic antennas being able to operate at a quarter-wavelength mode in comparison to the half-wavelength mode operation of traditional microstrip patch antennas.

In communication systems operating in challenging communication environments where the transmitted signal undergoes various diffractions, reflections and scattering, the polarisation of the signal during the transmission in the uplink and downlink can change significantly. This results in the received signal at the other end in a communication link being the sum of different polarisations. In view of this, the use of dual-polarised solar antennas has a significant potential to address this challenge. In this thesis, photovoltaic integration of dual-polarised microwave antennas was demonstrated for the first time in the literature. The proposed  $\pm 45^\circ$  slant dual-polarised microstrip solar patch antenna in chapter 6 has a significant potential to be employed in 5.8 GHz band polarisation diverse WiMAX applications. It was also illustrated in chapter 6 that different from linearly-polarised solar antennas for which a DC load can be introduced at the non-radiating edges with negligible effect on the RF response, all edges of dual-polarised solar patch antennas contribute to the radiation in the far-field. Therefore, a DC/RF isolation circuit must to be introduced between the cell terminals and the attached DC load in order to achieve stable antenna radiation characteristics.

For practical applications, as explained in chapter 6, whilst solar antennas are required to be oriented in the direction of the Sun at an optimal angle to achieve optimum solar performance, the target to be communicated with might be located at a different position. In order to achieve communication with the target, a solar antenna should provide coverage in the direction of the target whilst physically pointing at the direction of the Sun. This challenge can only be addressed by electronically steering the main lobe of the solar antenna without physical rotation, which can be achieved by using phased array solar antennas. In this thesis, this challenge has been addressed with the novel design of a photovoltaic microstrip patch array antenna consisting of an eight element dual-polarised linear phased patch array stacked with solar cells for 5.8 GHz band  $90^\circ$  sector WiMAX base stations. Using the proposed solar patch array, an electronic beam steering of  $10^\circ$  was achieved. It was illustrated that the proposed photovoltaic array offers -3dB beamwidths of  $88.7^\circ$  in the azimuth and  $6.7^\circ$  in the elevation planes making it a suitable candidate to be

employed in environmentally-friendly polarisation diverse 5.8 GHz band WiMAX base stations.

The solar illumination intensity undergoes variations during a day, resulting in a fluctuation in the number of freed electrons in a solar cell. This also results in a variation in the cell generated DC current whose effect on the RF performance of photovoltaic antennas needs to be investigated. Therefore, the investigation into the effect of the variation in the solar illumination intensity on the reflection and transmission coefficients of a solar patch antenna using a poly-Si solar cell as an RF radiating element was carried out in chapter 5. The S-parameter measurements performed under varying illumination intensities in the range of  $250 \text{ W/m}^2 - 1000 \text{ W/m}^2$  demonstrate that variations in the solar illumination intensity do not affect the RF response of the solar patch antenna ensuring the RF stability of photovoltaic antennas.

## 7.2 Future Work

Although aims given in chapter 1 were fully achieved, recommendations for future work can be given as follows:

- The photovoltaic antennas demonstrated in this research produce DC current and voltage resulting in a DC power output which can be used to power the communication systems in which these antennas can be built. Future work recommendation would be the investigation of oscillator circuits to convert the DC cell output to an RF signal output to be directly fed to the antenna input. This could be achieved by powering the circuit elements in an oscillator through the cell generated voltage and current. A challenge with this work would be the narrow tolerance requirements for the oscillator circuit elements in order to achieve an RF output at the resonance band of the photovoltaic antenna to be fed. This is due to the fact that even a small change in the value of the oscillator circuit elements would result in a significant change in the operational frequency band. This is especially crucial for single band solar antennas with narrow-band resonance characteristics. For multiband and UWB photovoltaic antennas demonstrated in this thesis, on the other hand, the oscillator would be required to produce an RF signal output over a wide frequency band covering the resonance bands of these antennas.
- The photovoltaic antennas investigated in this research consist of non-flexible crystalline silicon solar cells. In this framework, future work recommendation

would be the investigation of the integration of flexible thin-film solar cells with microwave antennas consisting of textile or paper based flexible dielectric substrates. The design of flexible photovoltaic antennas would have a significant potential to be employed in applications where flexibility is required, such as body-centric communication systems in military applications. A challenge regarding this work would be to achieve stable RF characteristics due to the variations in the resonance and far-field radiation characteristics with the flexible antenna geometry. Moreover, for body-centric applications, the losses of the living tissues in the human body would also be needed to be taken into account.

- Metamaterials are artificially engineered materials presenting unusual material properties that cannot be achieved using conventional materials available in nature. Research in this field has been attracting increasing attention, especially since the experimental realisation of double-negative metamaterials presenting simultaneous  $\epsilon$ -negative and  $\mu$ -negative responses by Smith *et. al.* in 2000 [182]. In view of this, future work recommendation would be the integration of metamaterials with photovoltaic antennas making use of the advantage of engineering the material properties to achieve further antenna size reduction and enhanced antenna resonance and radiation characteristics.

# References

- [1] J. C. Maxwell, "A dynamical theory of the electromagnetic field", *Philosophical Transactions of the Royal Society of London*, vol. 155, pp. 459-512, 1865.
- [2] R.S. Elliott, "The history of electromagnetics as Hertz would have known it", *IEEE Transactions on Microwave Theory and Techniques*, vol. 36, no. 5, pp. 806-823, 1988.
- [3] J.J. Carr, *Practical Antenna Handbook*, 4<sup>th</sup> edition, McGraw-Hill, 2001.
- [4] H.J. Visser, *Antenna Theory and Applications*, Wiley, 2012.
- [5] C.A. Balanis, *Antenna Theory Analysis and Design*, 3<sup>rd</sup> edition, Wiley, 2005.
- [6] J.D. Kraus, *Antennas*, 2<sup>nd</sup> edition, McGraw-Hill, 1988.
- [7] G. Kumar and K.P. Ray, *Broadband Microstrip Antennas*, Artech House, 2003.
- [8] L. Fraas and L. Partain, *Solar Cells: A Brief History and Introduction*, Wiley, 2<sup>nd</sup> edition, 2010.
- [9] "The history of solar", U.S. Department of Energy – Energy Efficiency and Renewable Energy, 2002.
- [10] R.G. Seippel, *Photovoltaics*, Reston, 1983.
- [11] D. Chapin, C. Fuller, and G. Pearson, "A new silicon p-n junction photocell for converting solar radiation into electrical power", *Journal of Applied Physics*, vol. 25, pp. 676-677, 1954.
- [12] A. Luque and S. Hegedus, *Handbook of Photovoltaic Science and Engineering*, 2<sup>nd</sup> edition, Wiley, 2003.
- [13] J. Nelson, *the Physics of Solar Cells*, Imperial College Press, 2003.
- [14] D. Jenny, J. Loferski, and P. Rappaport, "Photovoltaic effect in GaAs p-n junctions and solar energy conversion", *Physical Review*, vol. 101, pp. 1208-1209, 1956.
- [15] J. G. Harris, A. Shaban, D. Dolan, T. Sheffield, and E. Tal, "Cal Poly Sustainable power for Electrical Resources (SuPER) project," *North American Power Symposium (NAPS)*, pp. 1-6, Aug. 2011.

- [16] J. Szlufcik, S. Sivoththaman, J.F. Nlis, R.P. Mertens, and R.V. Overstraeten, "Low-cost industrial technologies of crystalline silicon solar cells," *Proceedings of the IEEE*, vol. 85, pp. 711-730, 1997.
- [17] S. Shafiee and E. Topal, "When will fossil fuel reserves be diminished?," *Energy Policy*, ELSEVIER, vol. 37, no. 1, pp. 181-189, Jan. 2009.
- [18] F. Xiaoming, W. Shaw, and I. Lee, "Layered clustering for solar powered wireless visual sensor networks", *9<sup>th</sup> IEEE International Symposium on Multimedia*, pp. 237-244, 2007.
- [19] R. Prasad and R. Mehrotra, "A solar powered telecom architecture for off-grid locations", *Technical Symposium at ITU Telecom World*, pp. 205-210, 2011.
- [20] E. Palm, F. Heden, and A. Zanma, "Solar powered mobile telephony", *2<sup>nd</sup> International Symposium on Environmentally Conscious Design and Inverse Manufacturing*, pp. 219-222, 2001.
- [21] W.G. McCoy, "Design of a superregenerative receiver for solar powered applications", *IEEE Transactions on Consumer Electronics*, vol. 38, pp. 869-873, 1992.
- [22] B. Gaudette, V. Hanumaiah, S. Vrudhula, and M. Krunz, "Optimal range assignment in solar powered active wireless sensor networks", *Proceedings IEEE INFOCOM*, pp. 2354-2362, 2012.
- [23] T. Kandasamy and J.K. Krishnan, "Multipath routing scheme in solar powered wireless sensor networks", *New Technologies, Mobility and Security*, pp. 1-5, 2008.
- [24] L. Wang, Y. Yang, D.K. Noh, H.K. Le, J. Liu, T.F. Abdelzaher, and M. Ward, "AdaptSens: An adaptive data collection and storage service for solar-powered sensor networks", *30<sup>th</sup> IEEE Real-Time Systems Symposium*, pp. 303-312, 2009.
- [25] J. D. Hagerty, "Radio telemetry buoy for long-range communication," United States Patent, Patent No.: US Patent 54522625452262, Sep. 1995.
- [26] R. Morais, J. B. Cunha, M. Cordeiro, C. Serodio, P. Salgado, and C. Couto, "Solar data acquisition wireless network for agricultural applications," in *Proceedings of 19<sup>th</sup> Convention of Electrical and Electronics Engineers in Israel*, Jerusalem, Israel, pp. 527–530, Nov. 1996.

- [27] X. Jiang, J. Polastre, and D. Culler, "Perpetual environmentally powered sensor networks," in *Proceedings of 4<sup>th</sup> International Symposium on Information Processing in Sensor Networks*, Los Angeles, USA, pp. 463–468, Apr. 2005.
- [28] D. R. Green, J. Ward, and N. Wyper, "Solar-powered wireless crosswalk warning system," United States Patent, Patent No.: US20050128105, Jun. 2005.
- [29] D. A. Baker, "Telemetry power system," United States Patent, Patent No.: US7199488, Apr. 2007.
- [30] G. E. Tompson, "Wireless, solar-powered, pavement temperature sensor," United States Patent, Patent No.: US7275864, Oct. 2007.
- [31] K. Isoyama, T. Ohkuma, and D. Kawasaki, "Power saving wireless telemetering system," United States Patent, Patent No.: US7301477, Nov. 2007.
- [32] S. Baglio, S. Gagliano, D. Neri, N. Savalli, and G. Tina, "Optimal design of photovoltaic systems for wireless sensor networks," *IEEE International Symposium on Industrial Electronics 2008 (ISIE 2008)*, pp. 2108–2113, Nov. 2008.
- [33] D. Honore, "Wireless solar entertainment system," United States Patent, Patent No.: US5551065, Aug. 1996.
- [34] M. Shaff, "Solar-powered mobile telephone," United States Patent, Patent No.: US7072696, Jul. 2006.
- [35] S.V. Shynu, M.J.R. Ons, P. McEvoy, M.J. Ammann, S.J. McCormack and B. Norton, "Integration of microstrip patch antenna with polycrystalline silicon solar cell", *IEEE Transactions on Antennas and Propagation*, vol. 57, pp. 3969-3972, Dec. 2009.
- [36] S. V. Shynu, M.-J. Roo Ons, M. J. Ammann, S. Gallagher, and Norton, B., "Inset-Fed Microstrip Patch Antenna with Integrated Polycrystalline Photovoltaic Solar Cell," *European Conference on Antennas and Propagation*, pp. 1-4, Nov. 2007.
- [37] S. V. Shynu, M. J. R. Ons, G. Ruvio, M. J. Ammann, S. McCormack, and B. Norton, "A microstrip printed dipole solar antenna using polycrystalline silicon solar cells," *IEEE Antennas and Propagation Society International Symposium*, pp. 1-4, Jul. 2008.

- [38] S. V. Shynu, M. J. Roo Ons, M. J. Ammann, S. McCormack, and Norton, B., "A metal plate solar antenna for UMTS pico-cell base station," *Loughborough Antennas and Propagation Conference*, pp. 373-376, Mar. 2008.
- [39] S. V. Shynu, M. J. Ammann, and B. Norton, "Quarter-wave metal plate solar antenna," *Electronics Letters*, vol. 44, no. 9, pp. 570-571, Apr. 2008.
- [40] T. W. Turpin and R. Baktur, "Meshed Patch Antennas Integrated on Solar Cells," *IEEE Antennas and Wireless Propagation Letters*, vol. 8, pp. 693-696, 2009.
- [41] M. J. Roo-Ons, S. V. Shynu, M. J. Ammann, S. J. McCormack, and B. Norton, "Transparent patch antenna on a-Si thin-film glass solar module," *Electronics Letters*, vol. 47, no. 2, pp. 85-86, Jan. 2011.
- [42] S. V. Shynu, M. J. Roo Ons, M. J. Ammann, S. McCormack, and B. Norton, "Dual band a-Si:H solar-slot antenna for 2.4/5.2GHz WLAN applications," *3<sup>rd</sup> European Conference on Antennas and Propagation*, pp. 408-410, Mar. 2009.
- [43] S. Vaccaro, P. Torres, J. R. Mosig, A. Shah, J.-F. Zurcher, A. K. Skrivervik, P. de Maagt, and L. Gerlach, "Stainless steel slot antenna with integrated solar cells," *Electronics Letters*, vol. 36, no. 25, pp. 2059-2060, Dec. 2000.
- [44] S. Vaccaro, J. R. Mosig, and P. de Maagt, "Two advanced solar antenna "SOLANT" designs for satellite and terrestrial communications," *IEEE Transactions on Antennas and Propagation*, vol. 51, no. 8, pp. 2028-2034, Aug. 2003.
- [45] W.-Y. Li, C.-Y. Wu, W.-J. Chen, and H.-H. Lin, "Internal LTE/WWAN handset antenna integrated with solar cells for performance improvement," *IEEE Antennas and Propagation Society International Symposium*, pp. 1-2, Jul. 2012.
- [46] T. Wu, R. Li, and M. M. Tentzeris, "A Scalable Solar Antenna for Autonomous Integrated Wireless Sensor Nodes," *IEEE Antennas and Wireless Propagation Letters*, vol. 10, pp. 510-513, 2011.
- [47] F. Giuppi, A. Georgiadis, S. Via, A. Collado, R. Vyas, M. M. Tentzeris, and M. Bozzi, "A 927 MHz solar powered active antenna oscillator beacon signal generator," *IEEE Topical Conference on Wireless Sensors and Sensor Networks*, pp. 1-4, Jan. 2012.

- [48] M. Danesh, and J. R. Long, "An Autonomous Wireless Sensor Node Incorporating a Solar Cell Antenna for Energy Harvesting," *IEEE Transactions on Microwave Theory and Techniques*, vol. 59, no. 12, pp. 3546-3555, Dec. 2011.
- [49] M. Danesh, and J. R. Long, "An autonomous wireless sensor node using a solar cell antenna for solar energy harvesting," *IEEE MTT-S International Microwave Symposium Digest*, pp. 1, Jun. 2011.
- [50] M. Danesh, J. R. Long, and M. Simeoni, "Small-area solar antenna for low-power UWB transceivers," *European Conference on Antennas and Propagation*, pp. 1-4, Apr. 2010.
- [51] M. Danesh and J. R. Long, "Compact solar cell ultra-wideband dipole antenna," *IEEE Antennas and Propagation Society International Symposium*, pp. 1-4, Jul. 2010.
- [52] S. Vaccaro, J. R. Mosig and P. de Maagt, "Making planar antennas out of solar cells," *Electronics Letters*, vol. 38, no. 17, pp. 945-947, Aug. 2002.
- [53] N. Henze, A. Giere, H. Fruchting, and P. Hofmann, "GPS patch antenna with photovoltaic solar cells for vehicular applications," *IEEE 58<sup>th</sup> Vehicular Technology Conference*, vol. 1, pp. 50-54, vol. 1, Oct. 2003.
- [54] N. Henze, M. Weitz, P. Hofmann, C. Bendel, J. Kirchhof, and H. Fruchting, "Investigation of planar antennas with photovoltaic solar cells for mobile communications," *15th IEEE International Symposium on Personal, Indoor and Mobile Radio Communications*, vol. 1, pp. 622-626, vol. 1, Sept. 2004.
- [55] F. Declercq, A. Georgiadis, H. Rogier, "Wearable aperture-coupled shorted solar patch antenna for remote tracking and monitoring applications," *Proceedings of the 5th European Conference on Antennas and Propagation*, pp. 2992-2996, Apr. 2011.
- [56] J. Huang and M. Zawadzki, "Antennas integrated with solar arrays for space vehicle applications," *5<sup>th</sup> International Symposium on Antennas, Propagation and EM Theory*, pp. 86-89, Aug. 2000.
- [57] S. Vaccaro, P. Torres, J. R. Mosig, A. Shah, A. K. Skrivervik, J.-F. Zurcher, P. de Maagt, and L. Gerlach, "Combination of antennas and solar cells for satellite communications," *Wiley Microwave and Optical Technology Letters*, vol. 29, no. 1, pp. 11-16, Apr. 2001.

- [58] W. Alomar, J. Degnan, S. Mancewicz, M. Sidley, J. Cutler, and B. Gilchrist, "An extendable solar array integrated Yagi-Uda UHF antenna for CubeSat platforms," *IEEE International Symposium on Antennas and Propagation*, pp. 3022-3024, Jul. 2011.
- [59] S. C. Gao, L.-W. Li, T.-S. Yeo, and M. S. Leong, "FDTD analysis of a slot-loaded meandered rectangular patch antenna for dual-frequency operation," *IEE Proceedings Microwaves, Antennas and Propagation*, vol. 148, no. 1, pp. 65-71, 2001.
- [60] Shivnarayan and B. R. Vishvakarma, "Analysis of slot loaded microstrip patch antenna," *IEEE Antennas and Propagation Society International Symposium*, vol. 3, pp. 2420-2423, vol. 3, Jun. 2004.
- [61] J. A. Ansari, S. K. Dubey, P. Singh, R. U. Khan, and B. R. Vishvakarma, "Analysis of V-slot loaded patch for wide-band operation," *Microwave and Optical Technology Letters*, vol. 50, no. 12, pp. 3069-3075, 2008.
- [62] S. Maci, G. B. Gentili, P. Piazzesi, and C. Salvador, "Dual-band slot-loaded patch antenna," *IEE Proceedings Microwaves, Antennas and Propagation*, vol. 142, no. 3, pp. 225-232, Jun. 1995.
- [63] J.-H. Lu and K.-L. Wong, "Slot-loaded, meandered rectangular microstrip antenna with compact dual frequency operation," *Electronics Letters*, vol. 34, no. 11, pp. 1048-1050, May 1998.
- [64] Y.-X. Guo, K. M. Luk, and K. F. Leez, "Dual-band slot-loaded short-circuited patch antenna," *IEEE Antennas and Propagation Society International Symposium*, vol. 3, pp. 1592-1595, vol. 3, Jul. 2000.
- [65] J.-H. Lu, "Dual-frequency operation of rectangular microstrip antenna with bent-slot loading," *Asia-Pacific Microwave Conference*, pp. 1343-1346, 2000.
- [66] J.-H. Lu, C.-L. Tang, and K.-L. Wong, "Novel dual-frequency and broad-band designs of slot-loaded equilateral triangular microstrip antennas," *IEEE Transactions on Antennas and Propagation*, vol. 48, no. 7, pp. 1048-1054, Jul. 2000.
- [67] K. U. Kiran, R. M. Vani, R. M. Ravi, and P. V. Hunagund, "Slot-loaded Rectangular Microstrip Antenna with Meandering Slots in the Ground Plane for Compact Broadband Dual-frequency Operation," *7<sup>th</sup> International Symposium on Antennas, Propagation & EM Theory*, pp. 1-4, Oct. 2006.

- [68] Y.-X. Guo, K. M. Luk, and K.-F. Lee, "Dual-band slot-loaded short-circuited patch antenna," *Electronics Letters*, vol. 36, no. 4, pp. 289-291, Feb. 2000.
- [69] M. Thomas, J. S. Roy, and B. Gupta, "Miniaturized slot loaded proximity-coupled microstrip antenna for WLAN," *International Conference on Communications and Signal Processing*, pp. 61-64, Feb. 2011.
- [70] M. S. El-Sallamy, M. Y. Omar, and D. Abdelaziz, "Tri-slot loaded Equilateral Triangular Microstrip Antenna for compact and dual-frequency operation," *National Radio Science Conference*, pp. 1-6, Mar. 2009.
- [71] R. C. Reddy T, and R. Bhattacharjee, "Investigation on L-slot loaded dual-band compact patch antenna," *IEEE Asia-Pacific Conference on Antennas and Propagation*, pp. 237-238, Aug. 2012.
- [72] C. Run-nan, L. Shu, H. Guan-long, and W. Jin-xiang, "Simulation and experimental research on the multi-band slot-loaded printed antenna," *12<sup>th</sup> IEEE International Conference on Communication Technology*, pp. 500-503, Nov. 2010.
- [73] J. A. Ansari, N. P. Yadav, A. Mishra, Kamakshi, and A. Singh, "Broadband rectangular microstrip antenna loaded with a pair of U-shaped slot," *International Conference on Power, Control and Embedded Systems*, pp. 1-5, 2010.
- [74] T. Dissanayake and K. P. Esselle, "Design of slot loaded band-notched UWB antennas," *IEEE Antennas and Propagation Society International Symposium*, vol. 1B, pp. 545-548, 2005.
- [75] N. P. Yadav, A. Mishra, P. Singh, J. A. Ansari, and B. R. Vishvakarma, "A broadband U-slot loaded circular disk patch antenna," *International Conference on Emerging Trends in Electronic and Photonic Devices & Systems*, pp. 317-319, Dec. 2009.
- [76] C. Vegni and F. Bilotti, "Parametric analysis of slot-loaded trapezoidal patch antennas," *IEEE Transactions on Antennas and Propagation*, vol. 50, no. 9, pp. 1291-1298, Sep. 2002.
- [77] C. Sim and C.-J. Chi, "A Slot Loaded Circularly Polarized Patch Antenna for UHF RFID Reader," *IEEE Transactions on Antennas and Propagation*, vol. 60, no. 10, pp. 4516-4521, Oct. 2012.

- [78] A. A. Deshmukh and G. Kumar, "Half U-slot loaded rectangular microstrip antenna," *IEEE Antennas and Propagation Society International Symposium*, vol. 2, pp. 876-879, Jun. 2003.
- [79] A. Mishra, S. Dubey, J. A. Ansari, B. R. Vishvakarma, "W-slot loaded patch antenna for dual-band operation," *International Conference on Emerging Trends in Electronic and Photonic Devices & Systems*, pp. 320-323, Dec. 2009.
- [80] P. K. Mishra, R. Raaj, P. Maddhyeshia, and R. K. Vishwakarma, "Design of Dual Band Slot Loaded Rectangular Microstrip Antenna for Global Positioning Satellite," *International Conference on Communication Systems and Network Technologies*, pp. 37-40, Apr. 2013.
- [81] A. K. Singh and M. K. Meshram, "Slot-Loaded Shorted Rectangular Microstrip Antenna for Dual Band Operation," *Asia-Pacific Microwave Conference*, pp. 1-4, Dec. 2007.
- [82] J. A. Ansari and A. Singh, Kamakshi, A. Mishra, "Analysis of L-strip feed slot loaded dual band microstrip patch antenna," *2<sup>nd</sup> International Conference on Computer and Communication Technology*, pp. 511-516, Sept. 2011.
- [83] A. E. Daniel and R. K. Shevgoankar, "Slot loaded rectangular microstrip antennas for tunable dual band operation," *IEEE Antennas and Propagation Society International Symposium*, vol. 1, pp. 257-260, vol. 1, Jun. 2004.
- [84] K.-L. Wong, *Planar Antennas for Wireless Communications*, Wiley-Blackwell, 2003.
- [85] W. Gosling, *Radio Antennas and Propagation*, Elsevier, 1998.
- [86] R. Garg, P. Bhartia, I. Bahl, and A. Ittipiboon, *Microstrip Antenna Design Handbook*, Artech House, 2000.
- [87] Z. N. Chen and M. Y. W. Chia, *Broadband Planar Antennas: Design and Applications*, Wiley-Blackwell, 2005.
- [88] J. R. James and P. S. Hall, *Handbook of Microstrip Antennas*, The Institution of Engineering and Technology, 2<sup>nd</sup> edition, 1989.
- [89] L. V. Blake and M. W. Long, *Antennas: Fundamentals, Design, Measurement*, 3<sup>rd</sup> edition, SciTech Publishing, 2009.

- [90] S. J. Orfanidis, *Electromagnetic Waves and Antennas*, August 2013, Chapter 17, <http://www.ece.rutgers.edu/~orfanidi/ewa/>
- [91] S. Saunders and A. A.-Zavala, *Antennas and Propagation for Wireless Communication Systems*, Wiley-Blackwell, 2<sup>nd</sup> edition, 2007.
- [92] IEEE standard definitions of terms for antennas, *IEEE Std 145-1993*, pp. 1-32, Apr. 2013.
- [93] G. Deschamps and W. Sichak, "Microstrip microwave antennas," *Proceedings of 3<sup>rd</sup> Symposium on USAF Antenna Research and Development Program*, October 18-22, 1953.
- [94] H. Gutton and G. Baissinot, "Flat aerial for ultra-high frequencies," French Patent No. 703113, 1955.
- [95] R. Munson, "Conformal microstrip antennas and microstrip phased arrays," *IEEE Transactions on Antennas and Propagation*, vol. 22, no. 1, pp. 74-78, Jan. 1974.
- [96] C. Garvin, R. Munson, L. Ostwald, and K. Schroeder, "Missile base mounted microstrip antennas," *IEEE Transactions on Antennas and Propagation*, vol. 25, no. 5, pp. 604-610, Sep. 1977.
- [97] C. Garvin, R. E. Munson, L. Ostwald, and K. Schroeder, "Low profile, electrically small missile base mounted microstrip antennas," *Antennas and Propagation Society International Symposium*, vol. 13, pp. 244-247, Jun. 1975.
- [98] R. Munson and G. Sanford, "Microstrip phased array developed for 5 GHz application," *Antennas and Propagation Society International Symposium*, 1977, vol.15, no., pp.72,75, Jun 1977
- [99] S.-B. Yeap and Z. N. Chen, "Microstrip Patch Antennas With Enhanced Gain by Partial Substrate Removal," *IEEE Transactions on Antennas and Propagation*, vol. 58, no. 9, pp. 2811-2816, Sept. 2010.
- [100] J. Volakis, *Antenna Engineering Handbook*, 4<sup>th</sup> edition, McGraw-Hill Professional, 2009.
- [101] S. Maci and G. B. Gentili, "Dual-frequency patch antennas," *IEEE Antennas and Propagation Magazine*, vol. 39, no. 6, pp. 13-20, Dec. 1997.

- [102] I. Papapolymerou, R. F. Drayton, and L. P. B. Katehi, "Micromachined patch antennas," *IEEE Transactions on Antennas and Propagation*, vol. 46, no. 2, pp. 275-283, Feb. 1998.
- [103] K. R. Carver and J. Mink, "Microstrip antenna technology," *IEEE Transactions on Antennas and Propagation*, vol. 29, no. 1, pp. 2-24, Jan. 1981.
- [104] R. B. Waterhouse, S. D. Targonski, and D. M. Kokotoff, "Design and performance of small printed antennas," *IEEE Transactions on Antennas and Propagation*, vol. 46, no. 11, pp. 1629-1633, Nov. 1998.
- [105] D. M. Pozar and D. H. Schaubert, *Microstrip Antennas: The Analysis and Design of Microstrip Antennas and Arrays*, Wiley-IEEE Press, May 1995.
- [106] R. Tomar, Y. M. M. Antar, and P. Bhartia, "Computer-aided-design (CAD) of suspended-substrate microstrips: An overview," *International Journal of RF and Microwave Computer-Aided Engineering*, vol. 15, no. 1, pp. 44-55, 2005.
- [107] V. Gupta, S. Sinha, S. K. Koul, and B. Bhat, "Wideband dielectric resonator-loaded suspended microstrip patch antennas," *Microwave and Optical Technology Letters*, vol. 37, no. 4, pp. 300-302, 2003.
- [108] P. H. Rao, M. R. Ranjith, and L. Naragani, "Offset fed broadband suspended plate antenna," *IEEE Transactions on Antennas and Propagation*, vol. 53, no. 11, pp. 3839-3842, Nov. 2005.
- [109] Z. N. Chen and M. Y. W. Chia, "Broad-band suspended probe-fed plate antenna with low cross-polarization levels," *IEEE Transactions on Antennas and Propagation*, vol. 51, no. 2, pp. 345-347, Feb. 2003.
- [110] Z. N. Chen, "Broadband suspended plate antenna with concaved center portion," *IEEE Transactions on Antennas and Propagation*, vol. 53, no. 4, pp. 1550-1551, Apr. 2005.
- [111] V. Gupta, S. Sinha, S. K. Koul, and B. Bhat, "Suspended microstrip patch antenna with dielectric resonator loading for enhanced bandwidth," *Asia-Pacific Microwave Conference*, pp. 1330-1334, 2000.

- [112] Q. Zhang, Y. Fukuoka, and T. Itoh, "Analysis of a suspended patch antenna excited by an electromagnetically coupled inverted microstrip feed," *IEEE Transactions on Antennas and Propagation*, vol. 33, no. 8, pp. 895-899, Aug. 1985.
- [113] R. Gardelli, G. La Cono, and M. Albani, "A low-cost suspended patch antenna for WLAN access points and point-to-point links," *IEEE Antennas and Wireless Propagation Letters*, vol. 3, no. 1, pp. 90-93, Dec. 2004.
- [114] L. F. Marzall, R. Schildberg, and J. C. da S Lacava, "High-performance, low-cross-polarization suspended patch array for WLAN applications," *IEEE Antennas and Propagation Society International Symposium*, pp. 1-4, Jun. 2009.
- [115] N. U. Lau and R. Sloan, "Broadband millimeter-wave suspended microstrip antenna array," *IEEE Antennas and Propagation Society International Symposium*, vol. 1, pp. 288-291, Jun. 2003.
- [116] S. Nirate, R. M. Yadahalli, K. K. Usha, R. M. Vani, and P. V. Hunagund, "Wideband gap-coupled suspended rectangular microstrip antenna," *International Conference on Recent Advances in Microwave Theory and Applications*, pp. 833-835, Nov. 2008.
- [117] X. N. Low, W. K. Toh, and Z. N. Chen, "Broadband suspended plate antenna for WiFi/WiMAX applications," *International Conference on Information, Communications & Signal Processing*, pp. 1-5, Dec. 2007.
- [118] D. Wojcik and M. Surma, "Low cost dual-polarized suspended microstrip antenna array for 5.8 GHz point-to-point links," *22<sup>nd</sup> International Conference Radioelektronika*, pp. 1-4, Apr. 2012.
- [119] M. Abbak, S. A. Rezaeieh, and I. Akduman, "Broad-band three layer suspended plate antenna," *Telecommunications Forum*, pp. 951-954, Nov. 2011.
- [120] B. A. Zeb and P. Meincke, "An air-supported wideband circularly polarized patch antenna," *IEEE International Symposium on Microwave, Antenna, Propagation and EMC Technologies for Wireless Communications*, pp. 427-429, Oct. 2009.
- [121] J.-K. Xiao, W.-N. Liu, and Q.-X. Chu, "A new PBG suspended patch antenna," *International Symposium on Antennas, Propagation and EM Theory*, pp. 229-232, Nov. 2008.

- [122] C. Karakus and M. F. Demirkol, "Suspended patch antenna with Z-type Strip Plate as broadband impedance transformer," *IEEE-APS Topical Conference on Antennas and Propagation in Wireless Communications*, pp. 47-49, Sept. 2011.
- [123] J. Lu, K. Zhenqi, and X. Zhu, "Broadband suspended patch antenna fed by co-planar double L-probes," *IEEE International Workshop on Antenna Technology*, pp. 80-83, Mar. 2012.
- [124] N. U. Lau, C. M. Gregory, and R. Sloan, "Broadband suspended patch antennas with ground taper transformer," *Electronics Letters*, vol.38, no.18, pp.1005,1006, 29 Aug 2002.
- [125] Y. Rahayu, R. Ngah, and T. A. Rahman, "Simulation of wideband inverted suspended patch antenna," *Asia-Pacific Conference on Applied Electromagnetics*, pp. 114-117, Dec. 2005.
- [126] J. Christ and U. Mahr, "Low-cost and wide-band suspended patch element using a three-dimensional dual-feeding section," *International Conference on Antennas and Propagation*, vol. 2, pp. 574-577, 2001.
- [127] J. Gao, K. Li, and H. Harada, "Wideband stacked microstrip patch antenna on thin PTFE substrate for millimeter-wave personal area network (mmWPAN)," *IEEE Antennas and Propagation Society International Symposium*, pp. 1-4, Jul. 2010.
- [128] V. Devaraj, K. K. Ajayan, and M. R. Baiju, "An Optimised Stacked E-Shaped Patch Antenna," *European Conference on Antennas and Propagation*, pp. 1-6, Nov. 2007.
- [129] M. Roshanaei and R. Faraji-Dana, "A New Quad-Band CPW-Fed Stacked Antenna for Wireless LAN Applications," *International Conference on Electromagnetics in Advanced Applications*, pp. 535-538, Sept. 2007.
- [130] J. A. Ansari, R. B. Ram, and N. P. Yadav, "Analysis of tunnel diode loaded stacked microstrip antenna," *International Conference on Recent Advances in Microwave Theory and Applications*, pp. 365-368, Nov. 2008.
- [131] S. Patil, and B. K. Kanaujia, "Tunable Stacked Circular Patch Microstrip Antenna," *International Conference on Computational Intelligence and Communication Networks*, pp. 740-744, Oct. 2011.

- [132] X. Zhang, T. Hong, and Z. Wang, "Dual-band stacked microstrip antenna using a parabolic-pedestal," *International Symposium on Antennas, Propagation and EM Theory*, pp. 144-147, Nov. 2008.
- [133] I. Ang and B.-L. Ooi, "A broad band stacked microstrip patch antenna," *Asia-Pacific Conference Proceedings Microwave Conference*, vol. 2, pp. 2, Dec. 2005.
- [134] E. Nishiyama, M. Aikawa, and S. Egashira, "Three-element stacked microstrip antenna with wide-band and high-gain performances," *IEEE Antennas and Propagation Society International Symposium*, vol. 2, pp. 900-903, Jun. 2003.
- [135] J.-H. Oh, Y.-P. Hong, and J.-G. Yook, "Dual circularly-polarized stacked patch antenna for GPS/SDMB," *IEEE Antennas and Propagation Society International Symposium*, pp. 1-4, Jul. 2008.
- [136] J. A. Ansari, S. K. Dubey, P. Singh, R. U. Khan, and B. R. Vishvakarma, "Stacked V-slot loaded patch antenna," *International Conference on Recent Advances in Microwave Theory and Applications*, pp. 508-510, Nov. 2008.
- [137] E. Nishiyama, S. Egashira, and A. Sakitani, "Stacked circular polarized microstrip antenna with wide band and high gain," *IEEE Antennas and Propagation Society International Symposium*, vol. 4, pp. 1923-1926, Jun. 1992.
- [138] R. G. Patil, A. Mukherjee, and A. B. Nandgaonkar, "Design of broadband two layer stacked Microchip Antenna with a folded plate pair for military band applications," *International Conference on Emerging Trends in Networks and Computer Communications*, pp. 418-420, Apr. 2011.
- [139] M. Khodier and C. G. Christodoulou, "A technique to further increase the bandwidth of stacked microstrip antennas," *IEEE Antennas and Propagation Society International Symposium*, vol. 3, pp. 1394-1397, Jul. 2000.
- [140] J. Wang, R. Fralich, C. Wu, and J. Litva, "Multifunctional aperture coupled stacked antenna," *IEEE Antennas and Propagation Society International Symposium*, vol. 2, pp. 727-730, Jun. 1991.
- [141] J. Bai, W. Chen, Y. Chen, and Z. Feng, "Stacked CP patch antenna with broad impedance and AR bandwidth," *International Symposium on Antennas and Propagation*, pp. 793-795, Jul. 2011.

- [142] S. Egashira and E. Nishiyama, "Stacked microstrip antenna with wide bandwidth and high gain," *IEEE Transactions on Antennas and Propagation*, vol. 44, no. 11, pp. 1533-1534, Nov. 1996.
- [143] M. Klemm and G. Troster, "Characterisation of an aperture-stacked patch antenna for ultra-wideband wearable radio systems," *International Conference on Microwaves, Radar and Wireless Communications*, vol. 2, pp. 395-398, May 2004.
- [144] D. M.-Syahkal and H. R. Hassani, "Characteristics of stacked rectangular and triangular patch antennas for dual band applications," *International Conference on Antennas and Propagation*, vol. 2, pp. 728-731, 1993.
- [145] B. L. Ooi and C. L. Lee, "Broadband air-filled stacked U-slot patch antenna," *Electronics Letters*, vol. 35, no. 7, pp. 515-517, Apr. 1999.
- [146] J. Dong, A. Wang, P. Wang, and Y. Hou, "A novel stacked wideband microstrip patch antenna with U-shaped parasitic elements," *International Symposium on Antennas, Propagation and EM Theory*, pp. 185-188, Nov. 2008.
- [147] V. Natarajan, E. Chettiar, and D. Chatterjee, "An ultra-wideband dual, stacked, U-slot microstrip antenna," *IEEE Antennas and Propagation Society International Symposium*, vol. 3, pp. 2939-2942, Jun. 2004.
- [148] A. Lamminen and J. Saily, "Wideband stacked patch antenna array on LTCC for W-band," *European Conference on Antennas and Propagation*, pp. 2962-2966, Apr. 2011.
- [149] W. C. Gibson, *The Method of Moments in Electromagnetics*, Chapman and Hall/CRC, 2007.
- [150] K. S. Kunz and R. J. Luebbers, *The Finite Difference Time Domain Method for Electromagnetics*, CRC Press, 1993.
- [151] J. Jin, *The Finite Element Method in Electromagnetics*, 2<sup>nd</sup> edition, Wiley-Blackwell, 2012.
- [152] K. F. Lee and K. M. Luk, *Microstrip Patch Antennas*, Imperial College Press, 2010.
- [153] K. F. Lee and W. Chen, *Advances in Microstrip and Printed Antennas*, Wiley-Blackwell, 1997.

- [154] R. B. Waterhouse, *Microstrip Patch Antennas: A Designer's Guide*, Springer, 2003.
- [155] H. Haberlin, *Photovoltaics System Design and Practice*, Wiley, 2012.
- [156] C. E. Backus, *Solar Cells*, IEEE Press, 1976.
- [157] S. J. Fonash, *Solar Cell Device Physics*, Academic Press, 1981.
- [158] R. J. Komp and J. Perlin, *Practical Photovoltaics: Electricity from Solar Cells*, 3<sup>rd</sup> edition, Aatec Publications, 1995.
- [159] S. R. Wenham, M. A. Green, M. E. Watt, R. Corkish, and A. Sproul, *Applied Photovoltaics*, 3<sup>rd</sup> edition, Earthscan Publishing, 2011.
- [160] C. Hu and R. M. White, *Solar Cells: From Basic to Advanced Systems*, McGraw-Hill, 1983.
- [161] A. McEvoy, L. Castaner, and T. Markvart, *Solar Cells*, 2<sup>nd</sup> edition, Elsevier, 2012.
- [162] P. Rappaport, "Single-crystal silicon", *Proceedings Workshop Photovoltaic Conversion of Solar Energy for Terrestrial Applications*, vol. 1, pp. 9-16, Oct. 1973.
- [163] P. A. Lynn, *Electricity from Sunlight*, Wiley, 2010.
- [164] P. J. Reddy, *Science and Technology of Photovoltaics*, 2<sup>nd</sup> edition, CRC Press, 2009.
- [165] T. L. Chu, "Polycrystalline silicon", *Proceedings Workshop Photovoltaic Conversion of Solar Energy for Terrestrial Applications*, vol. 1, pp. 17-21, Oct. 1973.
- [166] P. Rappaport, "The photovoltaic effect and its utilization", *Solar Energy*, vol. 3, no. 4, pp. 8-18, Dec. 1959.
- [167] M. A. Green, K. Emery, Y. Hishikawa, W. Warta, and E. D. Dunlop, "Solar cell efficiency tables (version 40)", *Progress in Photovoltaics: Research and Applications*, vol. 20, no. 5, pp. 606-614, Aug. 2012.
- [168] E. Manea, E. Bundianu, M. Purica, C. Podaru, A. Popescu, C. Parvulescu, A. Dinescu, A. Coraci, I. Cernica, and F. Babarada, "Front surface texturing processor for silicon solar cells", *International Semiconductor Conference*, vol. 1, pp. 191-194, 2007.

- [169] L. A. Dobrzanski and A. Drygala, "Surface texturing of multicrystalline silicon solar cells", *Journal of Achievements in Materials and Manufacturing Engineering*, vol. 31, no. 1, pp. 77-82, Nov. 2008.
- [170] M. Wolf, "A new look at silicon solar cell performance", *Energy Conversion*, vol. 11, pp. 63-73, Jun. 1971.
- [171] L. M. Fraas and L. D. Partain, *Solar Cells and Their Applications*, Wiley, 2010.
- [172] R. J. Van Overstraeten and R. P. Mertens, *Physics, Technology and Use of Photovoltaics*, Adam Hilger, Bristol, 1986.
- [173] Powerstar HQI,  
<https://www.darlas.gr/comersus/store/catalog/pf/datasheets/46567.pdf>
- [174] Sun 2000 Solar Simulators, Abet Technologies,  
[http://www.abettechnologies.com/images/stories/PDFs/Sun\\_2000\\_Solar\\_Simulators.pdf](http://www.abettechnologies.com/images/stories/PDFs/Sun_2000_Solar_Simulators.pdf)
- [175] G. Clasen and R. Langley, "Meshed patch antennas", *IEEE Transactions on Antennas and Propagation*, vol. 52, pp. 1412-1416, Jun. 2004.
- [176] A. A. Deshmukh, and K. P. Ray, "Analysis of Broadband Psi ( $\Psi$ )-Shaped Microstrip Antennas," *IEEE Antennas and Propagation Magazine*, vol. 55, no. 2, pp. 107-123, Apr. 2013.
- [177] K.-L Wong, *Compact and Broadband Microstrip Antennas*, Wiley-Interscience, 1<sup>st</sup> edition, 2002.
- [178] J.-J. Xie, X.-S. Ren, and Y.-Z. Yin, and J. Ren, "Dual-polarised patch antenna with wide bandwidth using electromagnetic feeds," *Electronics Letters*, vol. 48, no. 22, pp. 1385-1386, Oct. 2012.
- [179] WiMAX Antenna Catalog, Laird Technologies,  
<http://www.wpsantennas.com/pdf/Laird-WiMAX-Antenna-Catalog.PDF>.
- [180] Commercial – WiMAX and LTE Antennas, Cobham Antenna Systems,  
<http://www.european-antennas.co.uk/markets-commercial-wimaz.php>.

[181] M. Y.-W. Chia, T.-H. Lim, J.-K. Yin, P.-Y. Chee, S.-W. Leong, and C.-K. Sim,,  
"Electronic beam-steering design for UWB phased array," *IEEE Transactions on  
Microwave Theory and Techniques*, vol. 54, no. 6, pp. 2431-2438, Jun. 2006.

[182] D. R. Smith, W. J. Padilla, D. C. Vier, S. C. Nemat-Nasser, and S. Schultz,  
"Composite medium with simultaneously negative permeability and permittivity,"  
*Physical Review Letters*, vol. 84, no. 18, pp. 4184-4187, 2000.